Spectroscopic and Theoretical Studies of Two Anticancer Compounds

A thesis by publication
submitted in fulfilment of the requirements for the degree of
Doctor of Philosophy

by

Muhammad Khattab

Cell Biophysics
Centre for Microphotonics
Faculty of Science, Engineering and Technology
Swinburne University of Technology
Melbourne, Australia

2018

"Say: Are those equal, those who know and those who do not know? It is those who are endued with understanding that receive admonition." [Qur'an, 39:9]

Abstract

Tyrosine Kinase Inhibitors (TKIs) are small molecules that show antiproliferative activity against cancer cells. An understanding of the electronic and configurational structure of how a new TKI behaves in solution and when bound to its target tyrosine kinase is crucial for further drug development. However, the existing approaches such as NMR and X-ray crystallography require specialized equipment and/or restrictive conditions that obviate routine structure determination. Therefore in my study, an alternative approach which combines ultraviolet-visible spectroscopy with high level computational chemistry has been undertaken to determine the conformation and electronic properties of TKIs. In addition, the environment surrounding the immediate vicinity of the drug is explored with absorption and fluorescence spectroscopy. As a model system for TKIs, AG1478 and SKF86002 are examined which comprise two major pharmacophores for extensively used drugs in the clinic.

The literature review and introductory section are presented in *Chapter I*. Tyrosine kinase families are introduced since they exemplify an important anticancer target. The six types of tyrosine kinase inhibitors along with the two TKIs under study are discussed. The importance and applications of the applied methodologies of UV-Vis spectroscopy and computational chemistry are also introduced.

In *Chapter II*, the solvatochromism of AG1478 is discussed. The steady-state absorption and fluorescence measurements revealed a huge stokes shift in AG1478 spectrum by 4536-9210 cm^{-1} upon changing solvent strength. Linear solvation energy relationship models were applied to qualitatively and quantitatively define the solvent parameters responsible for altering the electronic configuration of AG1478.

In *Chapter III*, the conformational investigation of AG1478 structure is presented. The assignment of the two characteristic overlapping bands in AG1478 absorption spectrum was accomplished by coupling quantum chemical calculations to the experimental results. The *ca.* 330nm peak was assigned to a coplanar structure of AG1478 while the *ca.* 340nm band was assigned to a twisted structure where the aniline moiety is tilted by 49º relative to the quinazoline ring.

In *Chapter IV*, the effect of hydration on AG1478 structure and spectrum is discussed. The AG1478 solution in binary mixtures of acetonitrile:water disclosed an enhancement of AG1478 optical density upon increasing water fraction. While an intense fluorescence quenching (by 80%) was observed by addition of 2% v/v water. An unorthodox fluorescence enhancement of AG1478 was reported with increasing the temperature of the binary mixture in contrary to the observation of AG1478 in a neat acetonitrile solution. It was concluded that a potential AG1478-water complex(s) can be formed when water molecules are at the vicinity of AG1478. Theoretical calculations proposed that 3-5 water molecules can favorably bind to AG1478 planar and twisted structures resulting in a more energetically stable AG1478 hydrates exhibiting distinctive spectral properties.

In *Chapter V*, the impact of medium pH on AG1478 structure and spectrum is discussed. Studying AG1478 in media of different pH revealed dependence of AG1478 absorption on solution pH. Combined theoretical and experimental results unraveled existence of two twisted isomers of AG1478 (protonated at N1 and N3) in acidic solutions. While the neutral planar conformer predominates in pH 7-12. At pH≥ 13, a mixture of neutral and anionic conformers of the planar and twisted AG1478 structures can exist. Overall, absorption spectrum of AG1478 is an excellent reporter of the pH of its environment.

In *Chapter VI*, conformational flexibility of AG1478 and heterogeneity of its binding site are investigated for AG1478-protein complexes. Excitation spectra revealed existence of AG1478 in multiple conformations and the predominant conformation is exclusively dependent on the AG1478 environment (protein). Fluorescence and red edge excitation shift (REES) spectroscopy revealed the heterogeneity of AG1478 binding site. It was also found that the extent of ruggedness and polarity of AG1478 binding site is protein-dependent. Based on Reichardt model, the polarity of AG1478 binding site is estimated nearly equal to *N*-methylformamide and 1,4-dioxane for AG1478 in aminoglycoside phosphotransferase and MAPK14 respectively. A detailed analyses of literature X-ray data of AG1478 and its analogue in the two proteins were also performed and compared to our experimental results. Our theoretical calculations were consistent with our experimental results and literature demonstrating a reasonable reliability of using UV-Vis spectroscopy in probing AG1478 when bound to a target protein.

In *Chapter VII*, the solvatochromism and theoretical structural analysis of SKF86002 are discussed. The SKF86002 fluorescence spectrum was found sensitive to solvent polarity and H-bonding strength. Theoretical calculations showed that the spatial orientation of SKF86002 rings significantly alters its absorption spectrum. These findings indicated that SKF86002 conformation has an impact on the ground and excited states of SKF86002. A feature that can be exploited for monitoring SKF86002 in biological assays.

In summary, the conducted studies showed that the two TKIs, AG1478 and SKF86002, can be used as a reporter for their own environment. This can lay the ground for future studies on the two drug candidates in a more complex environments *in vitro* and *in vivo*.

Acknowledgment

First of all, I would like to thank **ALLAH** for enlightening my path and introducing me to the best people who helped me initiating and completing this work.

I would like to thank my parents **Khattab** and **Sanaa** and brothers **Ahmed** and **Mahmoud** who receive my deepest gratitude and love for their dedication and the many years of support during my whole life generally and postgraduate studies specifically which provided the foundation for this work.

Words can never express my deepest gratitude and appreciation to Prof. **Andrew Clayton** for his sincere supervision, continuous encouragement and beneficial comments in writing the thesis. I would like to record my gratitude to him not only for suggesting the research point but also for his constitutive guidance. I am heavily indebted to him for his supervision, the valuable time and unlimited valuable advice he gave to me which enabled this work to be completed. I really will miss the encouraging appellation "Champ" from him.

I would like to express my sincere gratitude and appreciation to Prof. **Feng Wang** "Head of Molecular Model Discovery Laboratory, Department of Chemistry and Biotechnology, Swinburne University" for her guidance, her supervision and assistance from the very early stage of this research.

Finally, I would like to thank everyone who was important to the successful realization of the thesis, as well as expressing my apology that I could not mention personally one by one.

Declaration

I, Muhammad Khattab, declare that this thesis entitled:

"Spectroscopic and Theoretical Studies of Two Anticancer Compounds"

- Contains no material which has been accepted for the award of any other degree or diploma, except where due reference is made in the text of the thesis,
- Contains, to the best of my knowledge, no material previously published or written by another person except where due reference is made in the text of thesis,
- Contains materials, in *Chapter VII*, performed by Madeline Van Dongen and published in her honours thesis, and
- Discloses the relative contributions of the respective workers or authors, where the work is based on a joint research or publications.

Muhammad Khattab

Cell Biophysics
Centre for Microphotonics
Faculty of Science, Engineering and Technology
Swinburne University of Technology
Melbourne, Australia

Table of Contents

List of Tables

List of Illustrations

Abbreviations

TKs	Tyrosine kinase**s**
TKIs	Tyrosine kinase inhibitor**s**
ALK	Anaplastic lymphoma receptor tyrosine kinase
NSCLC	Non-small cells lung carcinoma
AML	Acute myeloid leukemia
CML	Chronic myeloid leukemia
DDR	Discoidin domain receptor
EGFR	Epidermal growth factor receptor

EPHA	Ephrin type-A receptor
ALL	Acute lymphoid leukemia
EPHB	Ephrin type-B receptor
FGFR	Fibroblast growth factor receptor
FLT3	Fms-like tyrosine kinase 3
IGFR	Insulin growth factor receptor
CLL	Chronic lymphocytic leukemia
INSR	Insulin receptor
LTK	Leukocyte tyrosine kinase
NTRK	Neurotrophic tyrosine kinase
PDGFR	Platelet-derived growth factor receptor
ROR	Receptor tyrosine kinase-like orphan receptor
VEGFR	Vascular endothelial growth factor receptor
SdP	Catalán solvent dipolarity
SP	Catalán solvent polarizability
$\boldsymbol{\beta_1}$	Laurence solvent basicity
$\boldsymbol{\pi^*}$	Kamlet-Taft solvent polarity/polarizability
$\boldsymbol{\alpha}$	Kamlet-Taft solvent acidity
SA	Catalán solvent acidity
$\boldsymbol{\alpha_1}$	Laurence solvent acidity
$\boldsymbol{\beta}$	Kamlet-Taft solvent basicity
$\boldsymbol{E}$**(30)**	Reichardt transition energy
$\boldsymbol{E_T^N}$	normalized transition energy
SB	Catalán solvent basicity
F($\boldsymbol{\varepsilon}$**,**$\boldsymbol{n}$**)**	Reynold's reaction field
AN	Acceptor number
$\boldsymbol{\varepsilon}$	Dielectric constant
$\boldsymbol{\mu}$	Dipole moment
ES	Laurence electrostatic force parameter
DI	Laurence dispersion-induction parameter
n	Refractive index
$\boldsymbol{\eta}$	Viscosity

List of Publications

1. **Muhammad Khattab**, Feng Wang and Andrew H.A. Clayton, *UV–Vis spectroscopy and solvatochromism of the tyrosine kinase inhibitor AG-1478*, Spectrochim. Acta A Mol. Biomol. Spectrosc. 164 (**2016**), 128-32

2. **Muhammad Khattab**, Subhojyoti Chatterjee, Andrew H.A. Clayton and Feng Wang, *Two Conformers of a Tyrosine Kinase Inhibitor (AG-1478) Disclosed Using Simulated UV-Vis Absorption Spectroscopy*, New J. Chem. 40 (**2016**), 8296-304

3. **Muhammad Khattab**, Feng Wang and Andrew H.A. Clayton, *Micro-Solvation of Tyrosine-Kinase Inhibitor AG1478 Explored with Fluorescence Spectroscopy and Computational Chemistry*, RSC Adv. 7 (**2017**), 31725-35

4. **Muhammad Khattab**, Feng Wang and Andrew H.A. Clayton, *A pH-induced conformational switch in a tyrosine kinase inhibitor identified by electronic spectroscopy and quantum chemical calculations*, Sci. Rep. 7 (**2017**), 16271

5. **Muhammad Khattab**, Madeline Van Dongen, Feng Wang and Andrew H.A. Clayton, *Solvatochromism and linear solvation energy relationship of the kinase inhibitor SKF86002*, Spectrochim. Acta A Mol. Biomol. Spectrosc. 170 (**2017**), 226-33

6. Madeline Van Dongen, **Muhammad Khattab**, Feng Wang and Andrew H.A. Clayton, *Exploring optical reporting characteristics of drugs: UV-Vis spectra and conformation of tyrosine kinase inhibitor SKF86002*, New J. Chem. 41 (**2017**), 14567-73

7. **Muhammad Khattab**, Feng Wang and Andrew H.A. Clayton, *Conformational Plasticity in TKI-kinase Interactions Revealed with Fluorescence Spectroscopy and Theoretical Calculations*, (submitted paper)

Chapter I

General Introduction

1.1. Literature Review

Cancer is one of the most fatal diseases prevalent worldwide. It accounts for more than a hundred incurable illnesses which place a significant burden on patients, communities and the health care system. It is estimated to be responsible for one in eight deaths in the world [1, 2]. Generally, cancer is a rapid abnormal cellular growth owing to a malfunctioning inherited or acquired DNA. A secondary development of tumor growth often takes place distant from the cancer origin due to metastasis, which spreads the malfunctioning infected cells throughout the body through the blood and lymphatic systems [3-6]. Nowadays, a wide diversity of tumor therapies are available such as chemotherapy [7-9], hormonal therapy [10-12], radiotherapy [13-15], and surgery [16]. Nevertheless, exploring new targeted therapies with minimal side effects is the ultimate global goal.

For the targeted cancer therapies, small molecule inhibitors (SMIs) and monoclonal antibodies (mAbs) are good candidates targeting cancer cells via binding to specific intracellular domains or trans-membrane antigens, respectively [17]. One of the various targets for SMIs is tyrosine kinases (TKs) [18]. TKs are abundant enzymes located in mostly all human cells and are involved in activation of other enzymes and hormones through transfer of a phosphate group from adenosine triphosphate (ATP) to the tyrosine moiety of inactive target. Accordingly, protein phosphorylation, triggered by TKs, is essential for cell proliferation, differentiation, regulation, and apoptosis. However, it has been discovered that some oncoproteins depend also on the phosphorylation process for activation, proliferation, cell-invasion, and survival of tumor cells [19].

Tyrosine kinases play pivotal roles in signal transduction, cell proliferation, and homeostasis [20]. Three prominent signalling pathways are activated by TKs which are the Ras/Raf MAPK pathway, the phosphoinositol 3-kinase/Akt (PI3K/Akt) pathway and the JAK/STAT pathway. In some cancers, TK over-expression or mutation can cause alteration of its function, hence interruption of these signalling pathways. For example, TKs associated with cancer promote decreased apoptosis and increased cell proliferation. The disruption in cellular functions and homeostasis triggers cancer cells growth and development [21]. Examples of the oncogenic TKs with their associated cancers are compiled in **Table 1.1**.

Table 1.1. Oncogenic receptor tyrosine kinases in cancer; *adapted from [22]*.

Oncogenic RTK (Examples)	Cancer (Examples)	Oncogenic RTK (Examples)	Cancer (Examples)
ALK	NSCLC, colorectal cancer, breast cancer	**INSR**	Colorectal cancer, prostate cancer
AXL	Lung, colon, breast, AML, CML	**INSRR**	Neuroblastoma
CCK4 (PTK7)	Small cell lung cancer, breast cancer, gastric and colon cancer, AML	**KIT**	AML, melanoma, ovarian carcinoma
DDR1	NSCLC, breast cancer, AML, ovarian cancer	**LTK**	Gastric cancer, lymphoma and leukemia
DDR2	NSCLC, lung cancers, CML, breast cancer	**MER**	Glioblastoma, hepatocellular carcinoma
EGFR1 (ERBB1/HER1)	Breast cancer, hepatocellular carcinoma, brain cancer	**MET**	Hepatocellular carcinoma, CLL, breast cancer
EGFR2 (ERBB2/HER2)	Breast cancer, gastric adenocarcinomas	**MUSK**	Ovarian cancer
EGFR3 (ERBB3/HER3)	Breast cancer, ovarian cancer, Squamous cell lung cancer	**NTRK1 (TrkA)**	Colorectal cancer, breast cancer
EGFR4 (ERBB4/HER4)	Breast cancer, melanoma	**NTRK2 (TrkB)**	Neuroblastoma, astrocytoma
EPHA1	NSCLC, prostate cancer	**NTRK3 (TrkC)**	Neuroblastoma, breast cancer
EPHA2	Hepatocellular carcinoma. colorectal cancer, breast cancer	**PDGFRA**	Lung adenocarcinoma, gastrointestinal stromal tumors
EPHA3	Glioblastoma, lung cancer, melanoma, ALL	**PDGFRB**	Gastrointestinal stromal tumors, glioblastoma
EPHA4	NSCLC, gastric cancer	**RET**	NSCLC, medullary thyroid carcinoma
EPHA5	Breast cancer, hepatocellular carcinoma, ALL	**RON (MST1R)**	Pancreatic cancer, breast cancer, NSCLC
EPHB1	NSCLC, cervical cancer, ovarian Cancer	**ROR1**	CLL, ALL, AML, MCL, HCL, melanoma
EPHB2	Cervical cancer, breast cancer	**ROR2**	Hepatocellular carcinoma melanoma, colon cancer
EPHB3	NSCLC, breast cancer, colorectal cancer	**ROS1**	NSCLC, ovarian cancer
EPHB4	Melanoma, glioma, breast cancer	**RYK**	CML, ovarian cancer

FGFR1	Squamous cell lung cancer, breast cancer	**TIE**	Glioblastoma, breast tumor
FGFR2	Squamous cell lung cancer, breast cancer, thyroid cancer	**TEK**	Bladder cancer, glioblastoma, AML
FGFR3	Bladder cancer, squamous cell carcinoma	**TYRO3**	Melanoma, thyroid cancer, breast cancer, colon cancer
FLT3	AML, acute promyelocytic leukemia	**VEGFR1 (FLT1)**	Ovarian cancer, NSCLC, colorectal carcinoma
IGF1R	CLL, breast cancer, pancreatic cancer	**VEGFR2 (KDR)**	Renal cell carcinoma, breast cancer
IGF2R	Breast cancer, prostate cancer, colorectal carcinoma	**VEGFR3 (FLT4)**	Thyroid carcinoma, breast cancer

Because of the importance of protein kinases in cellular regulation, protein kinases pathways and inhibition mechanisms have been intensively and extensively studied by academia and pharmaceutical companies. Pharmaceutical research, directed toward designing and characterizing protein kinase inhibitors, has accelerated in the last decade, putting protein kinases as the second largest pharmaceutical target behind G-protein coupled receptors [23]. Accordingly, researches have been conducted to discover and develop SMIs capable of inhibiting or blocking the phosphorylation process mediated by kinases in cancer cells through three main approaches; a) Inhibiting ATP binding to the kinase's catalytic domain, b) Modifying the conformation of allosteric sites required for activation of certain kinases, and c) Blocking TKs dimerization, ligand binding or receptor internalization [24].

A myriad of tyrosine kinase inhibitors have been synthesized, having molecular weight average of about 500 Dalton [22]. They are classified as Type-I to Type-V inhibitors and covalent inhibitors depending on the nature of binding site of the protein kinase to which the inhibitor binds. The first generation of TKIs includes the first drugs developed and are mostly used as the first line medications. Drugs, demonstrating higher potency and tolerability in patients resistant to the first line treatment, are categorized as the second generation of TKIs. The third generation shows more efficacy against most types of mutations, including T315I mutation [25]. All types of tyrosine kinases are discussed in detail in the next section.

1.1.1. Types of Tyrosine Kinases

Historically, Src protein was discovered in 1911 by Rous, and is regarded as the oldest known oncogene. Later in 1980, the protein was isolated and characterized as the first tyrosine kinase [26, 27]. The isoquinoline sulphonamide derivatives were later developed by Hiroyoshi Hidaka as the first synthesized TKIs [28]. Genetically, the human genome encodes for two types of kinases, lipid kinases and protein kinases. Protein kinases are encoded by around 2% of genes in human kinome. Human kinome is the complete set of protein kinases encoded in its genome [23, 29]. Approximately, 518 kinase members comprise the protein kinase superfamily, from which eight subfamilies are emerged; tyrosine kinases (TK), tyrosine kinase-like (TKL), protein kinase A, protein kinase G and protein kinase C related (AGC), casein kinase 1 (CK1), Ca^{2+}/calmodulin-dependant kinase, STE20 STE11 STE7 related (STE), Cdk MAPK GSK and Cdk-like related (CMGC), and finally receptor guanylyl cyclase (RGC) [29]. All kinases exert the same function which is to facilitate the transfer of γ-phosphate group from the nucleoside triphosphate (ATP or GTP) to the hydroxyl group of amino acid moieties *viz.* serine, threonine or tyrosine of the protein substrate [30].

Of the isolated and characterized 90 tyrosine kinases, 58 receptor tyrosine kinases (RTKs) are grouped under 20 subfamilies, while the 32 non-receptor tyrosine kinases (nRTKs) are placed into 10 subfamilies, refer to **figures 1.1** and **1.2** [31]. As the name indicates, RTK is a transmembrane receptor consisting of an extracellular ligand-binding domain linked to an intracellular kinase domain, while nRTK is embedded into the cytoplasm or located superficially on the cytoplasmic membrane or translocated on the nucleus. The structure of RTK reveals an extracellular ligand-binding domain linked through a single transmembrane helix to a cytoplasmic ATP-binding domain. Upon agonist binding, dimerization or oligomerization of the RTK occurs which is essential for auto-phosphorylation [32]. In case of targeting a kinase with antagonist like tyrphostin, the tyrphostin binds to the cytoplasmic domain of RTK after crossing the plasma membrane. Consequently, it suppresses the catalytic activity of the enzyme through the interference with the binding of ATP or the natural substrate [33].

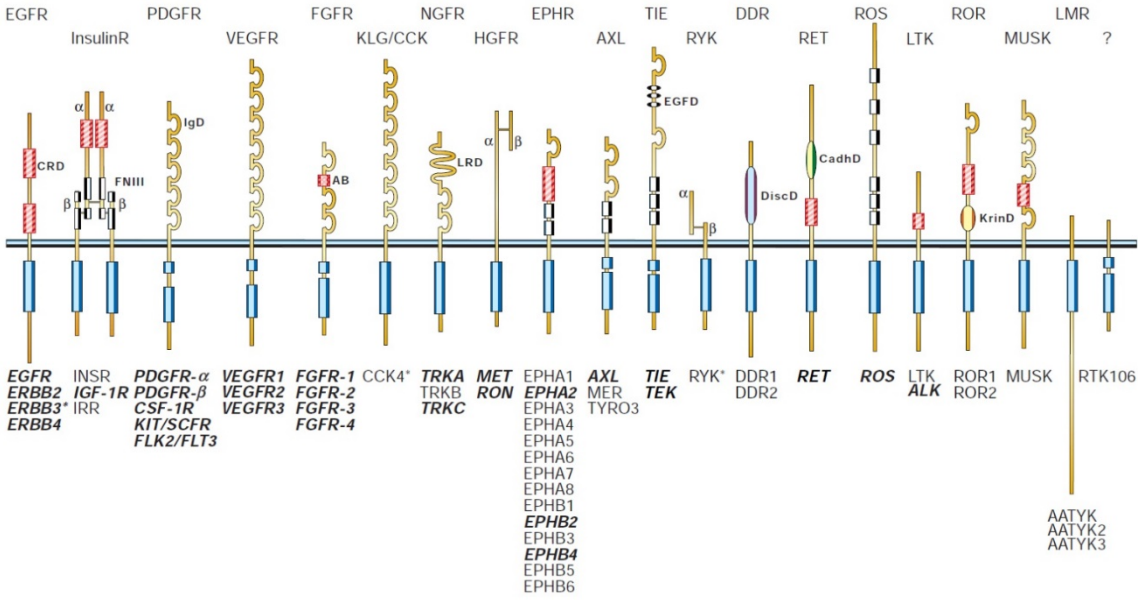

Figure 1.1. Domain organization of the 20 subfamilies of Human Receptor Tyrosine Kinases. The prototypic receptor for each family is indicated above the receptor, and the known members are listed below. *Reproduced with permission from the publisher of [34]*.

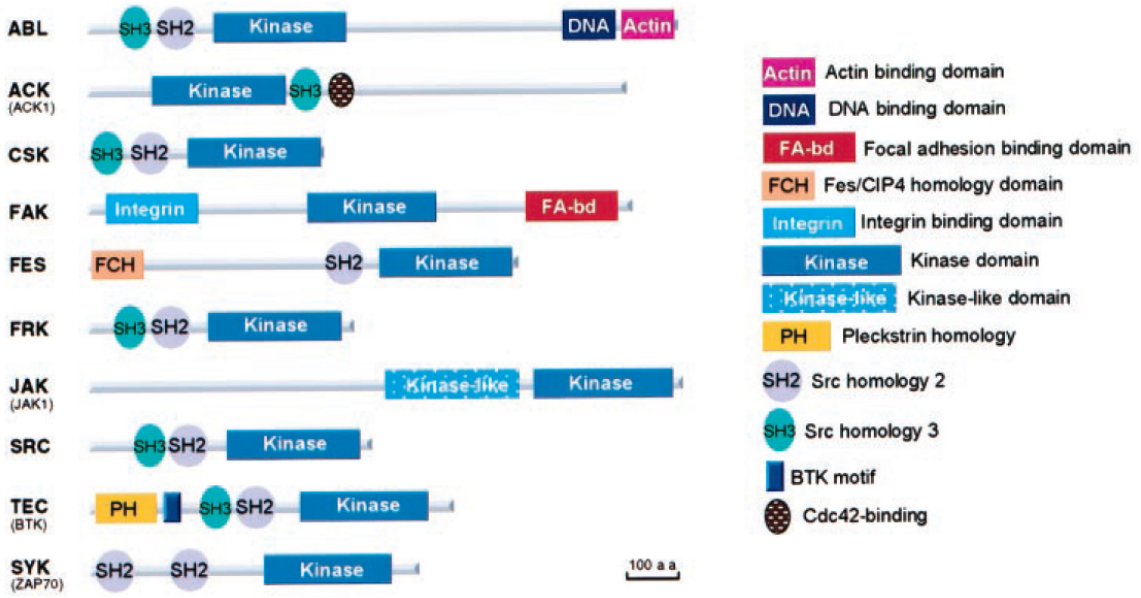

Figure 1.2. Domain organization of the 10 subfamilies of Human non-Receptor Tyrosine Kinases. A simple illustration of domain organization of 10 nRTKs, showing the amino terminus on the left side and the carboxyl terminus on the right side. *Reproduced with permission from the publisher of [31]*.

Over the past decade, over 130 inhibitors have undergone preclinical and clinical trials [35, 36]. Thirty-eight SMIs of kinase inhibitors have been approved by FDA for effective cancer treatment, all of them are either classified as Type I or II inhibitors [37, 38]. Classification of TKIs is based on the active kinase domain to which they bind, and to the reversibility of interaction as summarized in **Table 1.2**. Type I, Type II, Type III, Type IV, Type V and covalent inhibitors are the main classes of TKIs [39]. A brief description of the mechanism of binding of each type is provided below.

Table 1.2. Comparison between the different types of tyrosine kinase inhibitors; *adapted from [39]*.

	Type 1	**Type II**	**Type III**	**Type IV**	**Type V**	**Covalent inhibitor**
Binding mechanism	Reversible	Reversible	Reversible	Reversible	Reversible	Irreversible
Binding Site	ATP site	ATP site and DFG pocket	Allosteric (by ATP pocket)	Allosteric (substrate binding domain)	ATP site and substrate binding domain	ATP site
ATP-competitive	Yes	Yes	No	No	No	No
Selectivity	Low	High	Very High	Very High	The highest	Low

Type I inhibitors

ATP-competitive inhibitors represent the first type of TKIs. The structure of a type I inhibitor typically consists of a heterocyclic ring system residing in the purine binding site of the hinge region. Type I inhibitor serves as a scaffold bearing a side chain capable of binding with the hydrophobic region of kinase. It acts via binding to the phosphorylated active conformation "DFG-in" motif of tyrosine kinase, mimicking the purine ring of adenine moiety of ATP cofactor [40].

One to three H-bonds are formed during binding of the inhibitor to the ATP-binding site of a kinase. Furthermore, hydrophobic interactions can be observed at the adjacent hydrophobic region. The hydrophilic region targeted by the ribose moiety of ATP can be exploited in improving the inhibitor bioavailability by incorporating polar groups for increasing solubility in the blood serum [41]. On the other hand, type I inhibitors exhibit low selectivity toward kinases, thus more side effects are reported [42]. This is attributed to the highly conserved ATP-binding site in almost all kinases, making further development of selective/specific type I tyrphostins extremely difficult [43].

Type II inhibitors

Type II inhibitors are ATP competitive inhibitors which bind to the active site of non-phosphorylated kinase conformer. They display reversible interaction with both the ATP binding site and the hydrophobic region adjacent to the ATP pocket blocking the kinase in "DFG-out" state [44]. They exploit the conformational change in the phenylalanine residue of the activation loop to form one to three H-bonds with the lipophilic pocket of TKs. Therefore, type II inhibitors gain a higher degree of selectivity toward kinases superior to type I, because these interactions cannot take place in the phosphorylated "DFG-in" form of the enzyme [39].

Unlike type I, type II inhibitors attain selectivity through binding solely to the hydrophobic pocket created by DFG "out" motif, and preventing the kinase from adapting DFG "in" conformation. On the other hand, both type I and II are affected by mutations within the hinge region. For example, one of various clinically relevant mutations occurs when the threonine amino acid of the gatekeeper residue is mutated. The access to the ATP binding pocket is restricted resulting in resistance to the two types of inhibitors [45].

Type III (Allosteric) inhibitors

Allosteric inhibitors are non ATP-competitive inhibitors where the binding interaction occurs in a site other than ATP-binding site. Like type II inhibitors, type III inhibitors bind to the hydrophobic pocket created by DFG motif in the "out" state, but not extending into the hinge region as with type II. Stabilization of the inactive conformation of TK results in skewing of a glutamate residue in such a way preventing autophosphorylation of the protein [45]. However, this kind of interaction induces a conformational change of the ATP-binding site preventing autophosphorylation of TK [23].

The DFG motif is composed of three consecutive amino acids, Asp-Phe-Gly positioned close to the activation loop of TK enzyme. Aspartate and phenylalanine moieties can change their positions resulting in two different conformational states of TKs, "DFG-in" and "DFG-out". This conformational rearrangement creates an extremely important hydrophobic pocket, adjacent to ATP-binding domain, representing an attractive target for developing TKIs. The higher selectivity of type III inhibitors over Type I and II is attributed to the less conserved nature of amino acids surrounding the DFG domain, see **figure 1.3**. Despite higher selectivity, the poor aqueous solubility is the major problem of using type III tyrphostins. Several approaches are being developed to improve the pharmacokinetics and bioavailability of type III inhibitors [44].

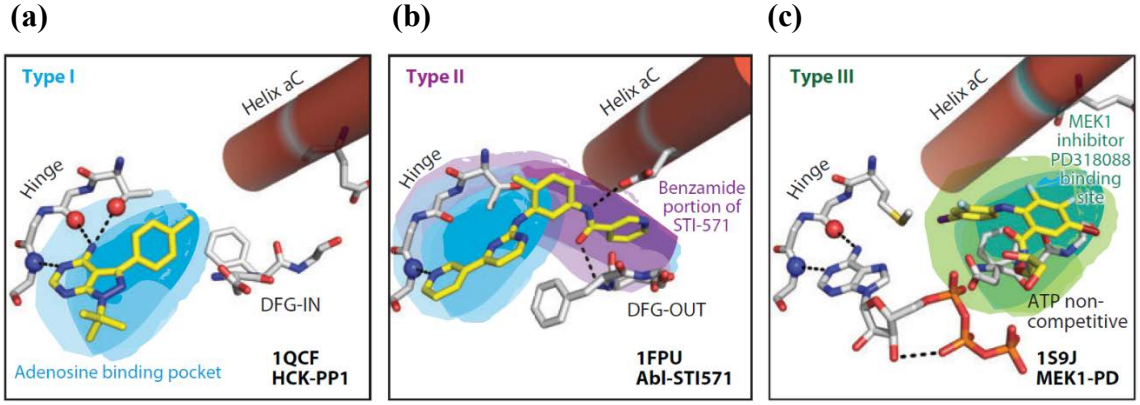

Figure 1.3. Type I, II, and III inhibitors bound to different conformational states of TKs (DFG-in and DFG-out conformers). *Reproduced with permission from authors of [46].*

(a) Type I inhibitor occupies adenosine binding pocket (blue) forming H-bonds with kinase hinge region (shown is the PP1 inhibitor docked into HCK (PDB ID 1QCF)). (b) Type II inhibitor induces a configurational change of DFG residue termed "DFG-out" where the D of DFG is flipped 180° relative to the active state confirmation (shown is STI-571 docked into Abl (PDB ID 1FPU)). (c) Type III inhibitor binds to a site adjacent to ATP binding pocket (green) (shown is the PD318088 inhibitor docked into MEK1 (PDB ID 1S9J))

Type IV (substrate-directed) inhibitors

The fact that only a small number of natural kinases substrates can bind unselectively to various kinases paved the way for developing a more selective type of TKIs. Type IV inhibitors can bind to the unique kinase substrate binding site offering a high degree of selectivity [39]. The substrate binding pockets of TKs are commonly less conserved than ATP-binding site. Since the natural kinases substrates exist in concentrations much lower than ATP concentrations, type IV inhibitors become more potent and more selective than other previously listed types of TKIs [28].

Further developments of type IV inhibitors are hindered by a variety of challenges. There is still a significant lack of data obtained for characterization and structure elucidation of the isolated TK proteins. Furthermore, the substrate binding site is often shallow and solvent exposed making rational design of new TKIs really difficult [45].

Type V inhibitors

All protein kinases are bisubstrate enzymes which bind to both specific protein substrate and the cofactor ATP. A worthy challenge is to search for inhibitors capable of targeting a specific kinase of more than 500 kinases discovered in human. A bisubstrate inhibitor is designed by linking an ATP-competitive small molecule to a non ATP-competitive ligand for the kinase of interest. By targeting two distinct binding sites on a tyrosine kinase, the selectivity, specificity, and potency of an inhibitor can be improved [47].

Type V inhibitors are divided into two subgroups, bisubstrate inhibitors (type Va) and bivalent inhibitors (type Vb). Type Va inhibitors target both the ATP binding site and the substrate binding pocket concurrently, while type Vb inhibitors target any two sites whether catalytic or regulatory. Thus, designing a type V inhibitor requires previous knowledge and understanding of the various types of TKIs and their protein targets [45].

Covalent inhibitors

Covalent inhibitors bind irreversibly via covalent bond to the catalytic nucleophile of kinase active site. Protein-binding takes place through trapping of cysteine moiety either by displacement of a good leaving group via S_N2 mechanism or through interacting with a Michael acceptor of the inhibitor molecule. This kind of suicide inhibition results in a longer duration of action [48].

Covalent inhibitors show a plethora of advantages of having longer dissociation half-lives, reducing the drug exposure, and minimizing the off-target effects [49]. Oral administration of covalent TKIs showed a potent antitumor efficacy in overexpressed ErbB receptors overcoming the double mutation L858R/T790M. The irreversible inhibitors can be used as a second-line treatment for patients with drug-induced resistance [50, 51].

In the last two decades, extensive research has been conducted to develop new generations of selective tyrosine phosphorylation inhibitors (Tyrphostins) with higher potency and resistance to TKs mutations. One of these promising tyrphostins is AG1478 which will be discussed next.

1.1.2. Tyrphostin AG1478

Several small molecule inhibitors have been synthesized and their inhibitory activity on the epidermal growth factor receptor was reported [52, 53]. Gazit and co-workers were the first to introduce "Tyrphostins" as a name for the class of compounds capable of blocking EGF-dependent autophosphorylation [53]. The hydroxyl-*cis*-benzylidene-malononitrile pharmacophore was responsible for the antiproliferative activity, whereas the molecular modification of this moiety led to more selective tyrosine kinase inhibitors [54]. Later, Barker synthesized and evaluated the antineoplastic activity of some quinazoline derivatives, where AG1478 proved itself as a potent drug candidate for leukemia, bladder, breast, colon, lung, ovarian, pancreatic, prostatic and rectal cancers.

The chemical structure and nomenclature of AG1478 are depicted in **figure 1.4**. Many preclinical studies on AG1478 have been conducted. AG1478 showed selectivity and efficacy toward hepatocellular carcinoma through inhibition of epidermal growth factor receptor [55]. It also inhibited autocrine growth in human lung and prostate cancer cell lines. It was also found that AG1478 can bind irreversibly to the extracellular-regulated kinase (ERK) and Akt/protein kinase B [56]. Cisplatin-resistant human lung adeno-carcinoma (A549/DDP) can be effectively treated by AG1478 since these cells were found more sensitive to AG1478 than A549 cell line [57]. AG1478 also inhibited the proliferation of nasopharyngeal carcinoma CNE2 cells without reducing expression of EGFR [58]. AG1478 with the retinoid derivative deguelin had a synergistic effect on inhibiting the head and neck squamous cell carcinoma (HNSCC). This was mediated through inhibition of Akt pathway in Ca9-22 and HSC-4 cell lines [59].

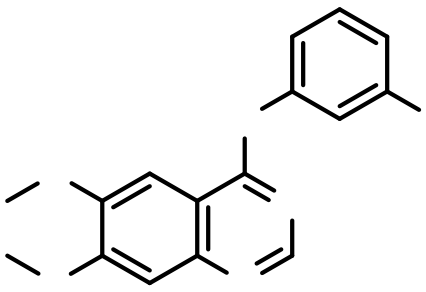

Figure 1.4. Chemical structure of *N*-(3-chlorophenyl)-6,7-dimethoxyquinazolin-4-amine (AG1478).

Not only is AG1478 a potent antitumor drug candidate, but it can also exert many pharmacological effects. For instance, AG1478 was found effective in reducing neutrophil infiltration and mucus hypersecretion in rat nasal epithelium *in vitro* which means AG1478 can also be used as an anti-inflammatory agent [60]. AG1478 also showed antiviral activity as it retarded viral replication of encephalo-myocarditis virus (EMCV) and hepatitis C virus (HCV). The antiviral activity was attributed to inhibition of a cellular target other than EGFR, that is, lipid kinase phosphatidylinositol 4-kinase III alpha (PI4KA) [61]. AG1478 promoted optic nerve protection and regeneration [62, 63]. It increased retinal ganglion cell survival in a chronic glaucoma model for seven months [62]. It also increased the neural regeneration in an optic nerve crush injury [63].

Due to the diverse biological functions of AG1478, it has been formulated in various dosage forms depending on the treatment target. For instance, the nanostructured lipid carriers loaded with AG1478 were prepared for the parenteral delivery of the drug to an infected liver [64]. Lavik and co-workers fabricated biodegradable polymeric microspheres achieving a sustained intraocular delivery of AG1478 over six months [63, 65].

Despite of the broad treatment spectrum of AG1478, some side effects have been reported for using AG1478 *in vivo*. For instance, acute interstitial pneumonia is one of the complications of the treatment with tyrosine kinase inhibitors targeting EGFR. It is due to the upregulation of interleukin-6, collagen and α–pectin [66]. Other complications include skin toxicity manifested by dry skin with pruritus, papular or pustular folliculitis and hair/nail abnormalities [67]. Preclinical studies of AG1478 on normomagnesemic rats reveal that AG1478 causes significant hypomagnesemia, oxidative stress and cardiotoxicity. Since the elderly and the hospitalized cardiac patients are more liable to hypomagnesemia, AG1478 with a magnesium-wasting side effect would trigger deleterious cardiovascular dysfunctions [68].

Study of the binding interactions between AG1478 and its target protein can be exploited to optimize drug efficacy and reduce side effects. AG1478, as one of TKIs, binds to the ATP binding site of protein kinases. It was designed to mimic the purine moiety of ATP cofactor, so that it can specifically bind to the ATP binding pocket [69]. It was found that

AG1478 binds selectively to EGFR/ErbB-1 inducing structural and functional abnormalities in the tyrosine kinase. AG1478 demonstrated alternation of the post-transitional processing (biosynthesis) of EGFR and disruption of EGFR glycosylation [70].

Since ATP-binding site is highly conserved and expressed in all kinases [43], studies on proteins other than EGFR have been conducted to unravel the mechanism of AG1478-protein binding. Aminoglycoside *O*-phosphotransferase APH(3`)Ia is one of the antibiotic kinase family which activates the antibiotic substrate through ATP-catalyzed phosphorylation. X-ray crystallography of the refined co-crystals of APH(3`)Ia with AG1478 was performed [71]. As represented in **figure 1.5**, the N(1) quinazolyl atom of AG1478 was found to form a H-bond with the amide of Ile101. The 6-methoxy group was docked in the vicinity of deoxyribose-binding site for ATP. While the 7-methoxy moiety accommodated the cavity formed by Pro102. The quinazoline core along with the *m*-chloroaniline moiety were found almost coplanar forming hydrophobic interactions with Phe53, Ile205 and Ile215 amino acids [71]. Topology of AG1478 and its binding site on APH(3`)Ia were found quite similar to the docking results of AG1478 into other protein kinases, providing the molecular evidence of the conserved binding between AG1478 and the ATP-binding pocket in all kinases [71].

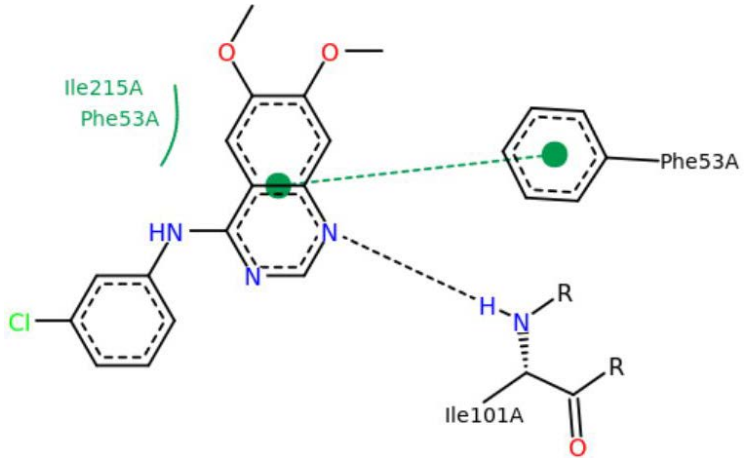

Figure 1.5. Representative 2D structure of AG1478 (PDB ID: 0TO) showing interactions with the surrounding amino acids in APH(3`)-Ia (PDB ID: 4FEX). The dashed line indicates hydrogen bonding while continuous green lines refer to the hydrophobic interactions; adapted from [72].

Unlike AG1478, SKF86002 is an imidazothiazole-based protein kinase inhibitor. SKF86002 represents another class of TKIs with a pronounced anti-inflammatory activity. In the next section, a deeper insight into SKF86002 structure and biological activities is provided.

1.1.3. SKF86002

Most pyridyl-imidazole derivatives were explored as potential MAPK inhibitors and were classified as non-steroidal anti-inflammatory drugs (NSAIDs), or more specifically, cytokine suppressive anti-inflammatory drugs (CSAIDs) [73, 74]. SKF86002 was first synthesized by Lantos *et al* in 1988 [73]. A few years later, it was reported to inhibit interleukin-1 beta and arachidonic acid metabolism [75]. The 2D chemical structure is depicted in **figure. 1.6**.

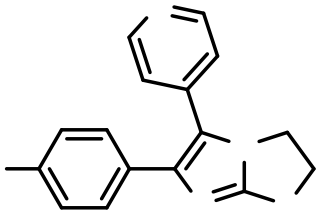

Figure 1.6. Chemical structure of 6-(4-fluorophenyl)-2,3-dihydro-5-(4-pyridinyl)-imidazo[2,1-b]thiazole (SKF86002).

The central pharmacophore connects to a vicinal pyridine and fluorophenyl rings. Several inhibitors fulfilling these criteria have been introduced to clinical trials [76]. The 4-fluorophenyl and 5-pyridyl ring moieties have been identified as being responsible for the interaction of SKF86002 with the ATP-binding pocket of MAP kinase [76, 77]. It was found that SKF86002 lacks intrinsic fluorescence but becomes fluorescent upon binding to MAPK. Hence, the crystals of SKF86002 with various kinases show a strong fluorescence [78]. Accordingly, the pan kinase inhibitor, SKF86002, has been demonstrated as a fluorescent tracer for binding of different ATP-competitive inhibitors to the target kinases [78]. However the fluorescent probing feature of SKF86002 have not been linked to the structural changes in SKF86002.

SKF86002 was also found to target the p38α MAP kinase. The p38α kinase is activated by phosphorylation in presence of ATP cofactor as a result of external stimuli [79]. Activation of p38α MAP kinase is associated with the release of proinflammatory cytokines, which are the key mediators of immune or inflammation process [79, 80]. By inhibiting the phosphorylation of p38α MAPK, SKF86002 can suppress the production of cytokines, hence the inflammation. Due to its relatively low affinity and specificity, SKF86002 can bind to other kinases such as PIM1, ASK1, AMPK and HCK [78].

Parker *et al* identified the crystal structure of apo-Pim1 complexed with SKF86002 (PDB ID: 4LL5) [78]. Crystallography of the structurally similar molecule, SB203580, suggested that the pyridyl nitrogen acts as a hydrogen bond acceptor for the backbone NH of Met109, while the neighbouring fluorophenyl has a less specific interaction with a hydrophobic pocket [76, 81]. Selig *et al* reported the great impact of conformational effects on the inhibitor potency which is caused by the steric hindrance of the S–methyl group in the well-known class of pyridyl thioimidazoles of SKF86002 derivatives [76].

The two TKIs, AG1478 and SKF86002, have been selected to conduct my research project. The question raised now is, *which techniques can be exploited, what kind of information can be extracted and how useful the information is?*

1.2. Absorption/Fluorescence Spectroscopy

Light plays a vital role in our daily lives. Without light, human beings cannot exist on the earth. Photosynthesis, a process where light is consumed for formation of C-H bonds, is a milestone for life for all creatures on the earth. Likewise, the scattering of sun's rays through raindrops to form a rainbow is a noticeable example of light interaction with matter, where the white light is separated into visible spectra of its primary colors. Light is an electromagnetic wave and the propagation of such waves relies on the generated electric and magnetic forces. However, in spectroscopy, only the effects exerted by the electric component of the light are of a major concern [82, 83].

In *optical spectroscopy*, light is used to probe properties of a compound which absorbs or transmits light over a certain range of wavelengths. While *spectrophotometry* is any technique that uses light to measure the concentration of a compound. One of the most well-known techniques for studying spectroscopy or spectrophotometry is the ultraviolet-visible (UV-Vis) spectroscopy. UV-Vis spectroscopy utilizes light in the near UV and visible regions of 200-800 nm [84]. Below a wavelength of 200 nm, the high energy photon is sufficient to induce ionization and photochemical decomposition. Meanwhile, only vibronic transitions are allowed using wavelengths above 800 nm as the photon energy becomes insufficient to promote electronic transitions [85].

Appropriate (quantized) photon energy promotes (*i.e.* excites) electrons in the valence shell of a molecule to the excited states producing an absorption and/or excitation spectrum. The main difference between absorption and excitation spectra is the technique of how it is recorded. To obtain an absorption spectrum, the monochromator collects the transmitted light from which absorption can be calculated. The excitation spectrum can only be recorded for fluorescent molecules where the emission wavelength is fixed while scanning the excitation monochromator over a specified wavelength range. In fluorescence spectroscopy, electrons are first excited by light of a specific wavelength to the excited states of a molecule. When radiation is emitted upon transitions of electrons from the first excited state to the ground state, the emission spectrum of a compound is obtained [86]. The optical responses, either absorbance or fluorescence are effectively used to obtain information about the electronic configuration of compounds or cells [87].

UV-Vis spectroscopy has become one of the most employed techniques due to its simplicity, sensitivity, accuracy, reliability, reproducibility [87]. Therefore, it is often the analytical method of choice in many research aspects *viz.* physical chemistry, biophotonics, forensic medicine and analytical chemistry. UV-Vis spectroscopy encompasses many techniques such as steady-state spectroscopy and red edge excitation shift (REES) spectroscopy. *Steady-state spectroscopy* is the spectroscopic techniques for measuring the optical density, fluorescence excitation and fluorescence emission using continuous irradiation by a beam of light. The absorption, excitation and emission spectra are measured as a function of wavelength [88, 89].

Red edge excitation shift (REES) spectroscopy is a reliable qualitative measure for the conformational heterogeneity of a fluorophore environment [90]. REES is a phenomenon where a low-energy excitation beam selectively excites discrete fluorophore molecules, hence potentially reflects the conformational equilibrium of a fluorophore ground and excited states [91, 92]. The emission wavelength becomes independent of excitation wavelength when the fluorescence lifetime is greater than environmental relaxation time. But in a rigid environment, the delayed solvent relaxation causes a blue-shifted fluorescence spectrum, when excited in the blue, due to emission from the solvent-unrelaxed excited state of the fluorophore. While a red-shifted emission is observed when the fluorophore is excited in the red due to the emission from solvent-relaxed state. Therefore, REES can be observed with fluorophores in viscous solutions or complexed with folded proteins [93, 94].

Steady-state absorption and fluorescence spectroscopy along with REES spectroscopy but to a lesser extent were exploited in my study. Some principal terms used in UV-Vis measurements are defined next. **Absorption/emission maximum** refers to the wavelength at which the maximum signal intensity of absorption/fluorescence is observed. The **bathochromic (red) shift** indicates the change in spectral band position of the absorption or emission spectrum to a longer wavelength. While the **hypsochromic (blue) shift** designates the change in band position to a shorter wavelength. The difference in energy between the absorption and emission maximum is denoted by **stokes shift**. The two most common causes of stokes shift are attributed to a) non-radiative decay to the lowest vibrational energy level of fluorophore excited state and b) the electron

occupies a higher vibrational level of fluorophore ground state upon releasing fluorescent photon. As a result of energy loss in a) or gain in b), the emission spectrum is red-shifted relative to the absorption spectrum [95].

The efficiency of light absorption by a compound is called the **extinction coefficient**. The greater the extinction coefficient is, the greater the absorbing power of a molecule is. Fluorescence **quantum yield** is indicative for the efficiency of emission process. It is defined as the ratio of emitted photons to absorbed photons. Therefore it is calculated relative to a strongly fluorescent reference compound and takes values from 0 to 1. The attenuation of emission signal is called **fluorescence quenching**. The quenching process is subdivided into dynamic quenching and static quenching. **Dynamic quenching** is attributed to collisions between fluorophore and quencher molecules. Fluorophore-ion complex formation (exciplex), aggregation of excited fluorophore molecules (excimer) and H-bond formation with fluorophore molecules can result in **static quenching**. Unlike dynamic quenching, the static quenching takes place in fluorophore ground state [95].

Compounds containing chromophores are capable of either absorbing or emitting a photon or both. Such compounds are called fluorophores or fluorochromes. When a fluorophore is irradiated with UV-Vis light, an electron from its outer shell is expelled to a higher electronic level (excited state). Since every electronic level has different vibrational and rotational levels, the absorption spectrum is a summation of all transitions from various levels in the electronic ground state (GS) to different levels in the electronic excited state (ES). Absorption and excitation processes are almost identical involving the transition of outermost electron from GS to ES. Therefore, absorption and excitation spectra are identical or nearly identical in most cases.

In order to measure a fluorescence (emission) spectrum, the wavelength of maximum absorption is preferably selected to illuminate the fluorophore. Transition (excitation) of outermost electron takes place from GS to ES on a sub-femtosecond time. This transition is usually followed by electronic relaxation to lower vibronic states from which a photon is released upon translocation of the excited electron back to the GS. This results in loss of part of the electron energy, hence the fluorescence spectrum is red shifted (lower in energy) relative to the absorption spectrum. Jablonski diagram (**figure 1.7**) illustrates

electronic transitions during absorption and fluorescence processes.

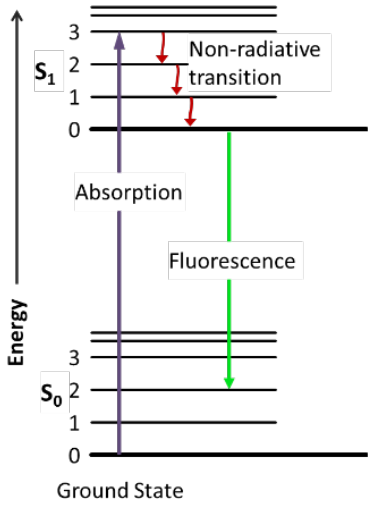

Figure 1. 7. Jablonski diagram for absorption and fluorescence process [96].

Since most of the tyrosine kinase inhibitors are small aromatic molecules, their extended conjugation and ionizable groups are often chromophores rendering them a good candidate for UV-Vis spectroscopy tool. Hence probing some of the physicochemical properties of TKIs becomes feasible [97]. In literature, UV-Vis spectroscopic measurements of TKIs have been explored utilizing a) the spectral change upon modifying the local environmental of TKI e.g. solvent polarity and pH [97-102], b) the fluorescence quenching of TKI or its protein complex [103-106], c) the TKI-catalyzed redox formation of a fluorescent dye [107], and d) a fluorescent dye for kinase labelling and probing [108]. However only a few UV-Vis spectroscopic studies have been reported for AG1478 and SKF86002 so far.

Clayton *et al* have employed fluorescence titration analysis to quantify the binding interaction between AG1478 mesylate salt, with and without cyclodextrin carrier, and human serum albumin (HSA) [109]. The increase in fluorescence quantum yield of AG1478 upon binding to albumin was measured at excitation wavelength of 350 nm. The steady-state fluorescence data were tested by a single-site and two-site models. The better fit to the two-site model speculated that AG1478 can interact with at least two different binding sites on albumin molecule. The combined fluorescence and ultracentrifugation data suggested formation of a ternary or higher order complexes between AG1478 and carrier protein [109]. In the next section, a brief introduction is given for the computational methods applied in this thesis.

1.3. Computational Chemistry

The golden rule in chemistry is "structure dictates properties". In spectroscopy, the electronic and structural information of a molecule is encoded in the measured spectra, which can only be decoded using quantum mechanics. In this thesis, a number of experimental spectroscopic measurements *i.e.* absorption and fluorescence spectroscopy are combined with quantum mechanical calculations, in order to reveal the structure-property relationship of AG1478 and SKF86002.

Computational chemistry is the use of mathematics and computer processing power to define the chemical and physical properties of a compound. The behaviour of an electron revolving around an atom in a molecule can be described by the Schrödinger equation. When the Schrödinger equation is solved for its energy and wavefunction, other properties of the molecule can be calculated.

Various approaches can address theoretical chemistry problems such as quantum mechanical methods and many other methods. Quantum mechanical methods are primarily concerned with computing the electronic properties and interactions at atomic level. The established methods of quantum chemistry are based on molecular orbital theory. Various quantum mechanical models such as density functional theory (DFT) have been progressively developed and built in a range of computational chemistry software for research use such as Gaussian package software. While the other computational methods deals with the formulation of analytical expressions, empirically and/or semi-empirically, for the properties of molecules and their reactions [110].

The quantum and classical mechanics as well as statistical physics and thermodynamics are the foundation for most of the computational chemistry theories and simulation software. These computational methods calculate the electronic and geometrical properties of atoms and molecules using quantum mechanics or other approximations. Computational chemistry software can be used for computing important molecular properties such as [110]:

- Bond length, bond angle, molecular volume and reaction energies
- Potential energy surfaces (PES)

- Structures of the ground-, excited- and transition-states
- Atomic charges, dipole moments and electrostatic potentials
- Transition energies and intensities for UV-Vis spectrum
- Vibrational frequencies (IR and Raman) and NMR chemical shifts
- Protein calculations (Docking)
- Rate constants for chemical reactions (Reaction kinetics)
- Thermodynamic calculations, e.g. Enthalpy, Entropy, energy of activation, ...etc
- Many other molecular and bulk physical and chemical properties

Methods derived, in part or in whole, from the basic laws of quantum mechanics are studied under a more specific discipline of computational chemistry called *quantum chemistry*. Quantum chemistry is divided into two broad areas depending on how the wavefunction in Schrödinger equation is treated. The *electronic structure* approaches (employed in this thesis) which treat a molecule nuclei as stationary particles surrounded by moving electrons. While *chemical dynamics* methods (not employed in thesis) simulate molecular behaviour over time for both electrons and nuclei. It combines laws of quantum physics (quantum dynamics) or classical newtonian mechanics (molecular dynamics) or a combination of both (semi-classical dynamics) [111].

To perform a quantum chemical computation, one has to set up a *model chemistry*. A model chemistry defines all calculation specifications such as theoretical method, basis set, density fitting set, solvation model,….etc. One important thing to be considered is to employ the identical model chemistry for comparing the chemical and physical properties of the ground state (GS) and the excited state (ES) energies of the same molecule or for a comparative study of different molecules [111].

Theoretical methods, referred to as *levels of theory*, compile different approximations to Schrödinger equation with varying accuracy, resource requirement and computational cost. Families of theoretical models include Hatree-Fock, semi-empirical methods, Moller-Plesset perturbation theory, density functional theory, coupled cluster methods and compound models. Only density functional theory is discussed here, since it is exclusively employed in all calculations in the thesis [111].

Density functional theory (DFT) has been used extensively for computational calculations on medium and large size molecules (20-200 atoms) [112, 113]. It is the most widely applied model for calculating ground state properties of molecules and clusters. Due to continuous improvements of exchange-correlation functionals [114, 115], DFT becomes the most reliable model and the blockbuster approach in chemistry and physics [116]. To account for the excited state properties of molecules, time-dependent (TD) nature of electromagnetic waves has to be taken into account in solving Schrödinger equation [117]. This leads to *time-dependent DFT* which is increasingly employed owing to its outstanding accuracy/cpu-cost ratio [116].

The second component of a model chemistry is the *basis set*. A basis set compiles a group of mathematical functions for defining the quantum mechanical wavefunction of a molecular system. Basis sets assign a collection of basis functions to each atom within a molecule. Each basis function is composed of a linear combination of numerous gaussian functions, known as primitives, giving a mathematical approximation for electronic orbitals. Larger basis sets impose fewer constraints on the probability of finding an electron around the nucleus. The fewer constraints leads to a more accurate description of a molecular wavefunction, but with a higher computational cost [111].

Given that the electron probability distribution within an isolated atom is completely different than in a molecule. Quantum Chemists prompted to define multiple functions with different gaussian exponents known as zeta values. To represent the polarization of electronic orbitals, consideration of higher angular momentum is required to account for formation of molecular bonds. Three major sets of basis sets are currently used which are split-valence, polarized and diffuse functions. *Split-valence* denotes basis sets where valence orbitals are defined by two or more basis functions of different size but retaining the same orbital shape. In *polarized* basis sets, orbitals with a higher angular momentums definition are used. For instance, polarized basis sets add “d” functions to carbon atoms. A larger sized versions of s- and p-type functions are used in *diffuse* functions. Basis sets with added diffuse functions are ideal for modelling systems where electrons are relatively far from the nucleus such as in anions, excited states and molecules with lone pairs of electrons [111].

The basis set, used mainly in the thesis, is 6-311+G* which is equivalent to 6-311+G(d). It stands for the 6-311G split valence basis set with one additional polarization function (d) on heavy atoms (non-hydrogen atoms) and diffuse function (+) on heavy atoms. The 6-311G is a triple zeta function where the core orbitals are represented by 6 contracted gaussian-type orbitals (GTO), the inner part of the valence atomic orbitals is composed of 3 contracted GTO and each of the medial and outer part of valence orbitals is described by 1 GTO. So the main model chemistry employed in my thesis is B3LYP/6-311+G* that showed a reasonable high accuracy and computational cost for the studied small and medium sized molecules [118-123].

Since molecular properties can vary with even small changes in molecular structure, it is necessary to locate the equilibrium geometry of a studied molecule. A *geometry optimization* (energy minimization) locates a point on a *potential energy surface* (PES) of a molecule where the forces on nuclei are almost zero. A geometry optimization must be followed by a frequency calculation to evaluate whether the optimized structure is a *true local minimum* or a *saddle point* (transition structure) [111]. The PES scan of AG1478 molecules showed one local minimum structure besides the global minimum structure, as can be seen in **figure 1.8**. The local minimum structure (A) has the anilino moiety tilted relative to the quinazoline ring while the global minimum (B) is in a planar form. In the local minimum (twisted) structure, the characteristic intramolecular H-bond is broken and this is proposed the reason behind destabilization of the twisted structure by 1.58 kcal/mol relative to the planar structure. This will be discussed in detail in *Chapter III*.

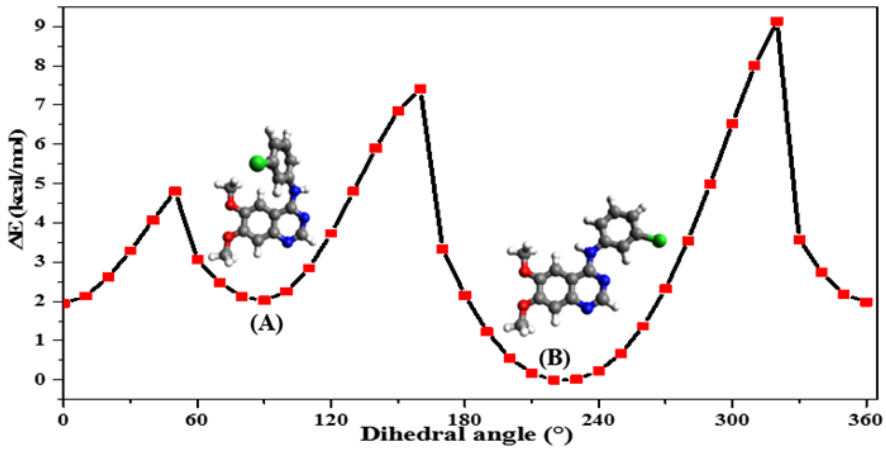

Figure 1.8. A potential energy surface scan of AG1478 (***Ch. III***).

The next calculation is td-DFT calculation to predict the absorption spectrum in question and to compare it with the observed spectrum. A significant deviation of absorption maximum (λ_{max}) from experiment is emerged due to simulating the molecule in isolation (vacuum). Since the solution environment has a significant impact on the calculated chemical properties of a molecule, therefore the chemical environment should be considered. Hence energy re-optimization of a molecule is performed in a selected solvent followed by td-DFT calculations.

To simulate experimental condition, the surrounding medium of a studied molecule can be treated by two different approaches. *Explicit* and *implicit* models are mainly used in DFT and td-DFT theories. In the former, all molecules of a solvent are explicitly treated so that hydrogen-bond formation between solvent and fluorophore is taken into account. In the latter, the solvent is treated as dielectric structureless continuum giving the same macroscopic properties of the solvent as in experiments [116, 124]. One of the most well-known schemes of implicit models is the *conductor-like polarizable continuum model* (CPCM). Despite the continuum models lack a description of the specific solute-solvent interactions such as H-bonding, ion pairing and π-interactions, solvent effects are adequately calculated with relatively limited computational cost [116].

By applying a model chemistry, the electronic absorption (excitation) transition energies with the corresponding oscillator strengths are obtained. The electronic transitions represented by vertical bars when fitted to gaussian model gives the characteristic (polynomial shape) absorption spectrum. Various features can be calculated which cannot be obtained experimentally. For instance, the molecular orbital contribution is easily calculated for each electronic transition. In addition, the absorption spectra from the global minimum structure and local minima structures can be calculated individually which helps in assigning the experimental spectrum with the appropriate geometrical conformer of the molecule.

In consideration of computational chemistry importance, it has been used in the last two decades for prediction of the electronic and molecular properties of many compounds. Literature revealed that computational chemistry applications provided a reliable platform for studying tyrosine kinase inhibitors and their target proteins [125-127].

We have noticed that a quite few computational studies were conducted on AG1478 and SKF86002 molecules. Santillan and co-workers have investigated some of the structural and electronic properties of AG1478 with other TKIs [128]. The structure of AG1478 was optimized using AM1 calculations and allowing two free rotations around the NH linker. The conformational analysis revealed that AG1478 adopts a fully coplanar conformation, hence the loss in chirality of NH moiety. The study was also concerned with calculating the net atomic charges of AG1478 heteroatoms. In addition, studies on the influence of substituents on the atomic charge of NH linker were performed on other TKIs sharing the same quinazoline pharmacophore with AG1478. The dipole moment, electron affinity and ionization potential were also calculated [128].

Later, molecular dynamics simulations were performed for TKIs tested *in vitro* against Myt1 kinase [129, 130]. In these studies, AG1478 docking into the binding pocket of the well-defined Myt1 kinase was investigated using single protein-ligand complex model. The inhibitory constant (K_i) value was estimated at 26μM [130]. Several docking parameters were calculated, however AG1478 conformation was not tackled in the article. Thus, understanding the inherent conformational flexibility of AG1478 and when it binds to a target protein is our concern.

Due to scarcity of quantum mechanical studies of the structure and property relationship of AG1478 and SKF86002, the current research aimed to employ the experimental UV-Vis spectroscopy and computational chemistry to unravel some properties of the two anticancer drug candidates. Our study demonstrated that combination of UV-Vis spectroscopy and theoretical calculations is a powerful tool to identify conformational signature of a fluorophore accounting for its absorption spectrum. In addition, determination of atomic charges and electronic transitions become feasible which cannot be obtained by experiments. For example, each of the theoretical global minimum (planar) structure and local minimum (twisted) structure of AG1478 gives only one major electronic transition in 300-360 nm region. This transition is due to the transition from the highest occupied molecular orbital to the lowest unoccupied molecular orbital (HOMO-LUMO transition). Thus the simulated spectra of AG1478 structures demonstrated that the experimental spectrum is ascribed to two conformers, rather than one structure, of AG1478 (planar and twisted rotamer), as can be seen in **figure 1.9**.

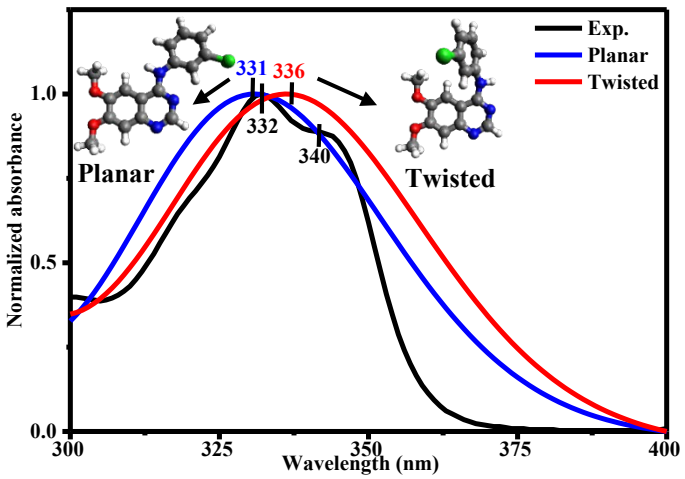

Figure 1.9. Normalized spectra of the observed and calculated absorption in the 300-400 nm region of AG1478 in methanol using B3LYP/6-311+G* model. The calculated spectrum of AG1478 planar conformer coincides with the 332 nm experimental band (-1 nm) while the twisted rotamer of AG1478 shows good agreement (-4 nm) relative to the measured band at 340nm (***Ch. III***).

It is worth mentioning that only absorption spectra are calculated in the thesis. Fluorescence spectrum calculation is somehow complex and tedious, and td-DFT model cannot accurately describe the electron transitions from ES to GS. Other methods such as CCSD are developed to allow electron relaxation to the lowest vibronic state of ES from which the electron returns to the GS. Therefore the calculated fluorescence spectrum is shifted to longer wavelength (lower energy) relative to the absorption spectrum due to the energy loss during electron relaxation. Generally, computational chemistry is indeed a useful tool for calculating chemical and physical characteristics of a molecule with avoiding usage of harsh chemicals. In the next section, aims and motivations of the thesis are listed.

1.4. Objectives of the Thesis

1.4.1. Aims and Motivations

An understanding of the structure of how a new TKI behaves in solution and when bound to its target tyrosine kinase is crucial for further drug development. However, existing approaches such as X-ray crystallography or nuclear magnetic resonance (NMR) require specialized equipment and/or restrictive conditions that obviate structure determination *in vitro* and *in vivo*. Therefore I propose, in this thesis, an alternative approach which combines UV-Vis spectroscopy with high level computational chemistry to explore the electronic and structural changes encountered for the two TKIs, AG1478 and SKF86002. My studies pave the way for understanding the structural requirements of drug-protein interactions of two different chromophores targeting the pharmaceutically important ATP-binding pocket. This might help in exploring the mechanism of remedial functions and lessening side effects. The aims and outcomes of my study are listed as follows:

Aim 1: To investigate the change in **AG1478** conformation upon varying medium polarity, H-bond strength, hydrophilicity, pH and temperature. The results will help to define AG1478 structure and polarity of AG1478 binding pocket in two protein kinases APH(3`)Ia and MAPK14. In more detail, we aimed to:

- Determine the dependence of absorption and fluorescence spectra of AG1478 on medium polarity using various solvent models (experimentally)
- Determine the structure of AG1478 conformations and assign the UV-Vis spectrum to the corresponding conformer (computationally)
- Study the effect of water molecules and solution pH on AG1478 conformation and spectra (experimentally and computationally)
- Examine AG1478 conformation and the physicochemical nature of AG1478-binding pocket in complex with proteins (experimentally and computationally)

Aim 2: To determine the fluorescence and conformational characteristics of **SKF86002**. This would help to clearly understand and define SKF86002 role in probing ATP-competitive inhibitor candidates of MAPK.

Overall, my study gives deep insights into the spatial and electronic characteristics of two different classes of the promising TKIs. The findings would pave the way for exploring and understanding the binding interactions of two anticancer candidates at the atomic and molecular levels. This would open the door for lead optimization and designing new generations of TKIs with higher potency/selectivity and resistance to EGFR mutations.

1.4.2. Thesis Outline

The overall structure of thesis takes the form of eight chapters, outlined as follows:

Chapter I. The introduction begins with providing an overview of the development of tyrosine kinase inhibitors and highlighting the various types of TKIs. A brief introductory section on UV-Vis absorption and fluorescence spectroscopy, and computational chemistry are also given. The objectives of the thesis are presented at the end.

Chapter II. A detailed examination of the absorption and fluorescence spectra of AG1478 in twenty-one solvents of different polarity and hydrogen-bonding strength is presented. Solvatochromic analyses using different solvent models are also performed.

Chapter III. A detailed computational study of AG1478 conformations and absorption spectra in different solvents are discussed.

Chapter IV. This chapter demonstrates the intermolecular interaction between AG1478 and water and the structural characterization of AG1478-hydrates.

Chapter V. The different prototropic states of AG1478 are experimentally and theoretically studied in the context of this chapter.

Chapter VI. This chapter displays the conformational flexibility of AG1478-protein complex using fluorescence and REES spectroscopy. It also includes analyses of the previously published X-ray data of crystals of AG1478 and its analogue. Information about AG178 conformation, AG1478-protein free-energy landscape and polarity of the binding pocket are discussed.

Chapter VII. It provides a detailed solvatochromic study on SKF86002 (experimental) along with the conformational analysis of its structure (computational).

Chapter VIII. It gives a summary of the thesis research outlining the importance and outcome of the study.

Chapter II

Solvatochromism of AG1478

Over the last few decades, studies on the photophysical properties of fluorescent probes have been the subject of intensive investigation owing to their potential applications in fluorescence sensors, optoelectronics and biomedical imaging [131-133]. It was found that the optical spectroscopic measurements of a fluorophore can be influenced by the change in physicochemical properties of the surrounding medium. Solvatochromism is the term used to define this phenomenon and firstly introduced by Hantz-schlater [134]. The change in compound absorption/emission spectrum is manifested by one or more alternations in the band position, intensity or shape [135-139]. The hypsochromic (blue) shift of the fluorescence band relative to the absorption band is commonly known as negative solvatochromism. While positive solvatochromism is the term given for the bathochromic (red) shift of the fluorescence band [140].

Solvent affects the structure and spectroscopic behavior of a fluorophore. Generally, solvatochromism is observed due to the differential solvation of the ground and excited states of a fluorophore. Despite its wide applications, the process of solvatochromism remains ambiguous due to the complex coupling of many static and dynamic interactions [141]. In negative solvatochromism, the molecule in its ground state is more stabilized than in the excited state upon increasing solvent polarity. When the excited state is more stabilized than the ground state, it results in a positive solvatochromism [140].

Solvatochromism is commonly used in many research aspects to characterize the nature of bulk environment [141]. Studying solvent effects on a fluorophore is commonly utilized to estimate the photophysical properties of a fluorophore. Fluorophore interaction with its environment can be triggered through specific interactions between fluorophore and solvent molecules e.g. H-bond formation and non-specific interactions. Electrostatic interactions, driven by the change in solvent dipole moment, refractive index, relative permittivity (formerly known as dielectric constant), polarizability and viscosity, can induce a significant change in fluorophore electronic configuration and spectrum [142].

A number of empirical solvent models have been developed for the solvatochromic analysis of organic molecules. It can be divided into approaches in which solute-solvent interaction is driven solely by solvent polarity/polarizability terms and models that account for solvatochromic effects by a colligative non-specific and specific interactions. In the later approach, a separate analysis of the polarity contribution and H-bonding interaction is feasible [143]. Linear solvation energy relationship (LSER) models have been proven to reliably define the interactions between solute and solvent molecules. Models developed by Bilot-Kawski [144] Lippert-Abboud-Mataga (L-M) [145, 146], Bakhshiev [147] and Kawski-Chamma-Viallet [148, 149] are among the most commonly used LSER models for solvatochromism analysis. In some cases, these models can demonstrate linear correlations between the measured spectral parameter of a fluorophore and the empirical solvent polarity function [150, 151].

The solvent scale proposed by Reichardt, *et al* [152] is more favourably used for studying solvatochromic dyes. It can also account for specific solute-solvent interactions because of using betaine probe as a reference which has H-bond acceptor and donor sites [140]. The microscopic solvent polarity $E_T(30)$ is defined as the transition energy ($kcal.mol^{-1}$) of the pyridinium-*N*-phenoxide betaine dye for the longest wavelength band measured in a defined solvent [140]. While the normalized parameter E_T^N has been developed considering water and tetramethylsilane as the extreme polar and non-polar reference solvents, respectively [153]. Owing to the fact that betaine dye forms H-bonds with protic solvents [154, 155], both $E_T(30)$ and E_T^N scales are more adopted for the evaluation of fluorophore solvatochromism in both aprotic and protic solvents.

Abboud-Abraham-Kamlet-Taft (AAKT) model is one of the empirical methods used to quantify solute-solvent interactions [156]. By using AAKT model, solvent parameters can be quantified using the equation $\upsilon = \upsilon_0 + a\alpha + b\beta + s\pi$, where α and β measure the hydrogen bond donating and accepting ability of the solvent and π refer to solvent polarity/polarizability. One major drawback of AAKT scale is that the π^* parameter does not separate dipolarity and polarizability of solvent effect [157-159]. To overcome this limitation, Catalán has reparametrized the linear solvation energy relationship into a more robust model [160]. Another database of solvent parameters has been recently proposed by Laurence *et al*, describing the empirical solute-solvent interactions. Approximately, 300 solvents were used for establishment of this novel database [161].

Hereafter, we investigate the potential of AG1478 as a fluorescent reporter of its own environment. To this end, we have carried out a detailed examination of the absorption and fluorescence spectra of AG1478 in twenty-one solvents of different polarity and hydrogen-bonding strength. Detailed solvatochromic analyses using different solvent models were also performed.

This chapter is presented in the form of the published paper, **Muhammad Khattab**, Feng Wang and Andrew H.A. Clayton, *UV–Vis spectroscopy and solvatochromism of the tyrosine kinase inhibitor AG-1478*, Spectrochim. Acta A Mol. Biomol. Spectrosc. 164 (2016), 128-32.

Spectrochimica Acta Part A: Molecular and Biomolecular Spectroscopy 164 (2016) 128–132

Contents lists available at ScienceDirect

Spectrochimica Acta Part A: Molecular and Biomolecular Spectroscopy

journal homepage: www.elsevier.com/locate/saa

UV–Vis spectroscopy and solvatochromism of the tyrosine kinase inhibitor AG-1478

Muhammad Khattab [a], Feng Wang [b,*], Andrew H.A. Clayton [a,*]

[a] Centre for Micro-Photonics, Faculty of Science, Engineering and Technology, Swinburne University of Technology, Melbourne, Victoria 3122, Australia
[b] Molecular Model Discovery Laboratory, Department of Chemistry and Biotechnology, School of Science, Faculty of Science, Engineering and Technology, Swinburne University of Technology, Melbourne, Victoria 3122, Australia

ARTICLE INFO

Article history:
Received 15 December 2015
Received in revised form 24 March 2016
Accepted 4 April 2016
Available online 12 April 2016

Keyword:
UV–Vis spectroscopy
Solvatochromism
AG-1478
Tyrosine kinase inhibitor

ABSTRACT

The effect of twenty-one solvents on the UV–Vis spectrum of the tyrosine kinase inhibitor AG-1478 was investigated. The absorption spectrum in the range 300–360 nm consisted of two partially overlapping bands at approximately 340 nm and 330 nm. The higher energy absorption band was more sensitive to solvent and exhibited a peak position that varied from 327 nm to 336 nm, while the lower energy absorption band demonstrated a change in peak position from 340 nm to 346 nm in non-chlorinated solvents. The fluorescence spectrum of AG-1478 was particularly sensitive to solvent. The wavelength of peak intensity varied from 409 nm to 495 nm with the corresponding Stokes shift in the range of 64 nm to 155 nm (4536 cm^{-1} to 9210 cm^{-1}). We used a number of methods to assess the relationship between spectroscopic properties and solvent properties. The detailed analysis revealed that for aprotic solvents, the peak position of the emission spectrum in wavenumber scale correlated with the polarity (dielectric constant or $E_T(30)$) of the solvent. In protic solvents, a better correlation was observed between the hydrogen bonding power of the solvent and the position of the emission spectrum. Moreover, the fluorescence quantum yields were larger in aprotic solvents as compared to protic solvents. This analysis underscores the importance of polarity and hydrogen-bonding environment on the spectroscopic properties of AG-1478. These studies will assume relevance in understanding the interaction of AG-1478 *in vitro* and *in vivo*.

1. Introduction

Cancer is a fatal proliferative disease causing a high rate of mortality. Mutation or over-expression of protein tyrosine kinases such as the epidermal growth factor receptor is linked to over 20% of cancers [1,2]. Tyrosine kinases play an important role in protein phosphorylation necessary for cell division, differentiation, signal transduction, and regulation [3]. Nevertheless, the functioning of many oncogenic proteins depends on kinase-catalyzed phosphorylation; hence blocking tyrosine kinase activity in tumor cells was and is still a promising strategy to halt tumor growth [2,3]. Pharmaceutical research, directed toward designing and characterizing protein kinase inhibitors, has recently accelerated, putting protein kinases as the second largest pharmaceutical research target behind G-protein coupled receptors [4].

In the 1980s, Gazit et al., synthesized a series of small molecule tyrosine kinase inhibitors called "Tyrphostins" [2]. These compounds showed promising *in vitro* and *in vivo* antiproliferative activity and gained global interest due to their potent and broad biopharmaceutical activities [5].

While these studies and others are very encouraging, some cancers appear to develop resistance to long-term tyrosine kinase inhibitor treatment. Understanding the spatial and temporal distribution of tyrosine kinase inhibitors is therefore of paramount importance to see whether these drugs are getting to the target of interest. An important step in this process is to first determine whether the inhibitors have spectral signatures that might assist in determining the relevant targets and interactions.

Photophysical studies have recently received much attention, since the spectral parameters are very sensitive to the change in microenvironment [8]. Environment-sensitive fluorophores are a special class of chromophores that could allow for deeper understanding of biological binding and function of candidate drugs. They can demonstrate changes in electronic configuration upon binding to target proteins, hence acting as biological marker for screening small molecule inhibitors [6,7]. 2-Propionyl-6-dimethylaminonaphthalene (PRODAN)

Abbreviations: AG-1478, tyrphostin 4-(3-chloroanilino)-6,7-dimethoxyquinazoline; UV–Vis, ultraviolet-visible light; *R*, Pearson's correlation coefficient; R^2, coefficient of determination; *tert*-But, *tert*-butanol; 1-But, 1-butanol; allyl, allyl alcohol; iPrOH, 2-propanol; EtOH, ethanol; MeOH, methanol; EG, ethylene glycol; Gly, glycerol; NMF, *N*-methylformamide; Diox, 1,4-dioxane; Tol, toluene; $CHCl_3$, chloroform; EtAc, ethylacetate; DCM, dichloromethane; DCE, 1,2-dichloroethane; Pyd, pyridine; Act, acetone; ACN, acetonitrile; DMF, *N*,*N*-dimethylformamide; DMSO, dimethylsulfoxide.

* Corresponding authors.
E-mail addresses: mkhattab@swin.edu.au (M. Khattab), fwang@swin.edu.au (F. Wang), aclayton@swin.edu.au (A.H.A. Clayton).

http://dx.doi.org/10.1016/j.saa.2016.04.009
1386-1425/

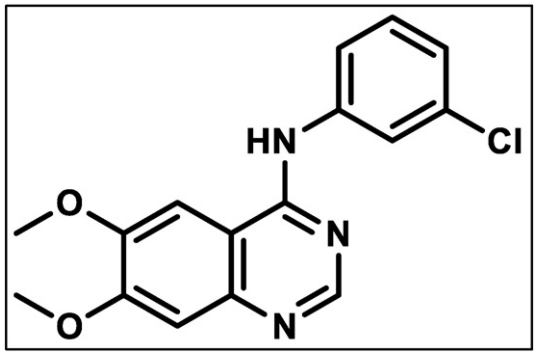

Fig. 1. Molecular structure of *N*-(3-chlorophenyl)-6,7-dimethoxyquinazolin-4-amine (AG-1478).

[8], 4-dimethylamino phthalimide (4-DMAP) [9], and 4-amino-1,8-naphthalimide derivatives [10] are well known applied examples of biological probes.

The present investigation is concerned with the tyrphostin AG-1478, with the molecular structure depicted in Fig. 1. *In vitro* studies demonstrated its reversible ATP-competitive inhibition on EGFR kinase domain [11]. Moreover, AG-1478 has structure similarities with Erlotinib and Gefitinib, which implies its potent antitumor application [12,13]. The focus of this study is to investigate the potential of AG-1478 as a fluorescence reporter of its own environment. To this end, we have carried out a detailed examination of the absorption and fluorescence of AG-1478 in twenty-one solvents of different polarity and hydrogen-bonding strength. Our analysis reveals that the fluorescence of AG-1478 is sensitive to *both* the polarity and hydrogen-bonding environment of the solvent. We therefore anticipate its use as a reporter of environment *in vitro* and *in vivo*.

2. Experimental

2.1. Materials

Solvents used in the experiments were selected to cover a broad range of dielectric constants (from 2.2 to 182.4) and proticity. Twenty-one solvents of spectroscopic or HPLC grade were used. Dimethyl sulfoxide, cyclohexane, dichloromethane, ethanol, 2-propanol and 1-butanol were purchased from Sigma-Aldrich Pty Ltd. Methanol, *tert*-butanol, *N*-methylformamide, ethylene glycol, allyl alcohol, pyridine, acetonitrile, *N*,*N*-dimethylformamide, 1,2-dichloroethane, 1,4-dioxane, ethylacetate, chloroform, acetone, toluene, glycerol and 9,10-diphenylanthracene were purchased from Thermo Fisher Scientific Inc. Tyrphostin AG-1478 was obtained from Sapphire Bioscience Pty Ltd. A matched pair of quartz cuvette was purchased from Starna Pty Ltd with a path length of 1 cm.

Table 1
Electronic UV–Vis absorption and emission maxima of AG-1478 in selected aprotic solvents (non-polar & polar). Stokes shifts are calculated in wavelength and wavenumber units.

Solvent[a]	Absorbance			Emission[b]	Stokes shift	
	λ_1	λ_2	λ_3	λ_{em}	$\lambda_{em} - \lambda_1$ (nm)	$\Delta\nu$ (cm^{-1})
Diox	342.5	329	–[c]	441.5	99	6547
Tol	–[c]	–[c]	–[c]	409.5	–[c]	–[c]
$CHCl_3$	350.5	–[c]	256	440.5	90	5829
EtAc	340	327	252	442.5[d]	102.5	6813
DCM	342	329	249	438[d]	96	6409
DCE	352	–[c]	255	–[c]	–[c]	–[c]
Pyd	345	330	–[c]	409	64	4536
Act	343.5	336	–[c]	456.5	113	7206
ACN	342	328	248	476.5	134.5	8253
DMF	342	331	–[c]	465.5[d]	123.5	7757
DMSO	346	332	–[c]	475.5[d]	129.5	7871

[a] Solvents are listed in order of increasing dielectric constants.
[b] Fluorescence excitation at 350 nm using slit width = 6.
[c] Not determined.
[d] Slit width = 3.

Table 2
Electronic UV–Vis absorption and emission maxima of AG-1478 in selected polar protic solvents. Stokes shifts are calculated in wavelength and wavenumber units.

Solvent[a]	Absorbance			Emission[b]	Stokes shift	
	λ_1	λ_2	λ_3	λ_{em}	$\lambda_{em} - \lambda_1$ (nm)	$\Delta\nu$ (cm^{-1})
tert-But	341	329	248	480.5	139.5	8514
1-But	345	333	248	484	139	8324
Allyl	343.5	334	250	430	86.5	5856
iPrOH	343	331.5	249	487.5	144.5	8642
EtOH	344	332	249	489	145	8620
MeOH	340	332	249	495	155	9210
EG	342	332	276	445.5	103.5	6793
Gly	–[c]	334	255	448	114[d]	7619
Water	–[c]	336	250	–[c]	–[c]	–[c]
NMF	343.5	330	261	487.5	144	8599

[a] Solvents are listed in order of increasing dielectric constants.
[b] Fluorescence excitation at 350 nm using slit width = 6.
[c] Not determined.
[d] Fluorescence excitation at 350 nm using slit width = 3 nm.

2.2. Methods

All solutions of AG-1478 were prepared on the same day for absorbance, excitation and emission measurements. Quartz cuvette was loaded with a fixed concentration (3 μM) of AG-1478. The electronic absorption spectra of AG-1478 were recorded at room temperature (293 K) on a Perkin-Elmer LAMBDA 1050 UV/Vis/NIR spectrophotometer. The absorbance at 300–360 nm band was typically <0.1. Excitation and emission measurements were conducted on a Perkin Elmer LS55 Fluorescence Spectrometer at 293 K. Spectra were scanned with three replicates at a speed of 266.75 nm/min for absorption spectra and 200 nm/min for both excitation and emission spectra. The background absorbance, scatter and fluorescence were corrected using blank samples containing solvent only. Fluorescence quantum yields were measured relative to 9,10-diphenylanthracene as a reference ($\Phi_F = 1$) in a cyclohexane solution [14].

3. Results and discussion

3.1. Absorbance and fluorescence spectra

The photophysical properties of AG-1478 are collected in Tables 1, 2 and 3. A typical absorption spectrum of AG-1478, recorded in *tert*-butanol, is displayed in Fig. 2. The absorption spectrum of AG-1478

Table 3
Fluorescence quantum yield (Φ) and molar absorptivity (ε_{max}) in L mol^{-1} cm^{-1} of AG-1478 in aprotic solvents (left panel) and in protic solvents (right panel).

Solvent	Φ	ε_{max} ($\times 10^4$)[a]	Solvent	Φ	ε_{max} ($\times 10^4$)[a]
Diox	0.029	2.68	*tert*-But	0.043	1.49
Tol	0.057	–[b]	1-But	0.012	4.28
$CHCl_3$	0.012	1.89	Allyl	0.005	2.20
EtAc	0.047	7.69	iPrOH	0.002	3.01
DCM	0.028	9.11	EtOH	0.005	3.19
DCE	–[b]	1.17	MeOH	0.001	2.95
Pyd	0.001	1.88	EG	0.005	1.53
Act	0.105	0.87	Gly	0.055	1.06
ACN	0.085	0.88	Water	–[b]	2.58
DMF	0.022	8.23	NMF	0.010	2.31
DMSO	0.016	7.70			

[a] Calculated using Beer-Lambert law (ε = A/lC), where A = maximum absorbance at λ_2, l = path length (1 cm), C = concentration in mol·L^{-1}.
[b] Not determined.

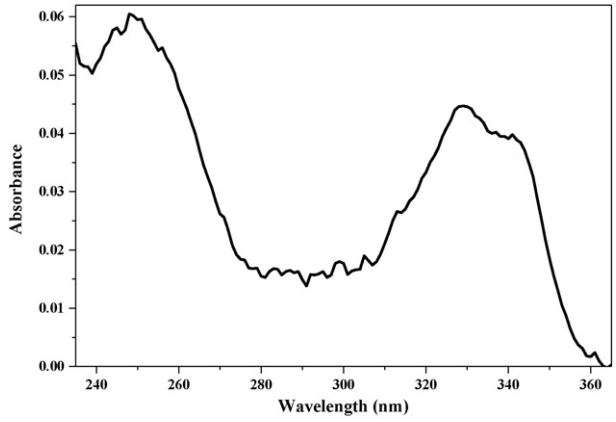

Fig. 2. Representative absorption spectrum of AG-1478 solution in *tert*-butanol.

consists of two partially-overlapping bands in the 300–360 nm region ($\lambda_{max1} \approx 340$ nm; $\lambda_{max2} \approx 330$ nm) and a shorter-wavelength band near 250 nm. The two low energy bands exhibited changes in spectral position and in relative absorbance in different solvents (Tables 1 and 2, Fig. 3a, b). The λ_{max1} varied from 340 to 346 nm, and λ_{max2} varied from 327 to 336 nm. We were unable to find a single solvent parameter that could account for the changes in peak positions or peak intensities in the absorption spectra as noted in Supplementary materials Table S1.

The emission spectra, recorded at excitation wavelength 350 nm, are shown in Fig. 4. In general, the fluorescence spectra were broad and unstructured but displayed quantum yields and peak positions that varied significantly (*i.e.* by a factor of 100 in quantum yield, and shifts in emission maxima up to (0.5 eV). The wavelength of peak intensity varied from 409 nm to 495 nm with the corresponding Stokes shift in the range of 64 nm to 155 nm (4536 cm^{-1} to 9210 cm^{-1}). The magnitudes of the Stokes shift are indicative of a large electronic rearrangement in the excited-state relative to the ground state.

To explore the relationship between spectroscopy and solvent polarity we plotted the emission maximum (in wavenumber) against the solvent polarity function $E_T(30)$. As can been seen in Fig. 5, a negative correlation between emission wavenumber and $E_T(30)$ was found for the selected aprotic solvents ($R = -0.89$, $R^2 = 0.79$, slope $= -196.34$ and intercept $= 30085.90$). Protic solvents were also negatively correlated with $E_T(30)$ but with a different slope and intercept to the aprotic solvents ($R = -0.86$, $R^2 = 0.74$, slope $= -40.48$ and intercept $= 22568.11$). The Stokes' shift was also correlated with the solvent polarity function $E_T(30)$ which enabled a calculation of the dipole moment difference between excited-state and ground state. For the aprotic solvents this dipole moment difference was calculated to be 3.6 ± 0.4 D (with slope = 5660 ± 1430 cavity radius = 4.2 A, $R = 0.87$) while for protic solvents the dipole moment difference was smaller at 1.6 ± 0.6 D (slope = 1279 ± 890, cavity radius 4.2 A, $R = 0.62$). The different dependencies of emission wavenumber on solvent polarity for protic and aprotic solvents and the correspondingly different calculated dipole moment differences provides evidence that hydrogen-bonding interaction plays some role in the excited state of AG-1478, in addition to solvent polarity.

Solvent polarity functions developed by Lippert-Mataga [15,16], Bakhshiev [17] and Kawski-Bilot [18,19] were also tested. Correlations between AG-1478 Stokes shift in aprotic solvents and polarity functions of Lippert and Bakhshiev models were obtained with $R = 0.69$ and 0.76, respectively. While $R = -0.76$ for the plot between the mean summation of absorption and emission wavenumber and Kawski function. For protic solvents, Lippert-Mataga plot showed a positive correlation with $R = 0.83$, however very weak correlations were observed using other two models $R < 0.5$. Therefore, we can conclude that solvent H-donating strength play significant role in the photophysics of AG-1478.

To account for the hydrogen-bonding and polarity solvent effects on the emission of AG-1478, we used the Kamlet-Taft linear solvation relationship. According to this model, a given spectroscopic observable can be parameterized in terms of a linear combination of the solvent polarity/polarizability, solvent acidity and solvent basicity. For 14 of the solvents, we found a linear correlation between AG-1478 emission wavenumber and Kamlet-Taft solvent parameters *viz*,

$$\nu_{em}(\alpha,\beta,\pi) = 24714 - 1596\alpha - 2319\beta - 1855\pi \left(R^2 = 0.93\right). \quad (1)$$

The analysis in Eq. (1) reveals that the hydrogen-bond donating power and hydrogen bond accepting strength of the solvent account for 28% and 40% of the solvent effects on AG-1478 emission, while solvent polarity accounts for 32% of the solvent effects.

The quantum yields of AG-1478 in different solvents are listed in Table 3. Generally, the fluorescence quantum yield values of AG-1478 were found comparatively low, varying from 0.001 to 0.105, relative to a solution of 9,10-diphenylanthracene in cyclohexane. In most cases, larger quantum yields were observed with aprotic solutions than with protic solutions. This observation points to the possibility of a hydrogen bonding effect between a hydrogen bond donor solvent and the tyrosine kinase inhibitor AG-1478.

In accordance with this proposal, it was found that the quantum yield of AG1478 emission in protic solvents was negatively correlated ($R = -0.82$) with the hydrogen-bond donating power of the solvent (from Kamlet and Taft). This observation suggests that hydrogen bond formation from the solvent to the AG1478 may cause an additional non-radiative decay path for the excited-state of AG-1478 and thereby a decrease in fluorescence quantum yield. It was also found that solvent viscosity positively correlated with the quantum yield of AG-1478 in protic solvents with $R = 0.86$, as summarized in Supplementary materials Table S2. This observation suggests that the rate of molecular rearrangement of solvent molecules in the solvation shell of AG-1478 plays significant role in stabilization of emissive state and retardation of non-radiative decay. Taken together, these results suggest that the

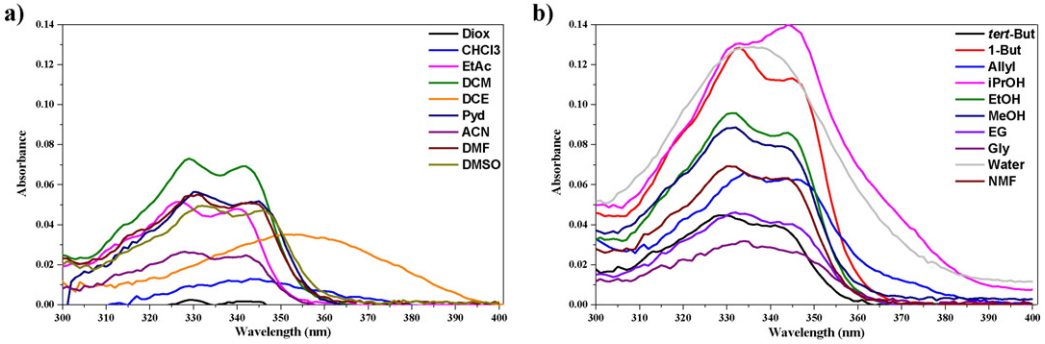

Fig. 3. Absorbance spectra of AG-1478 measured at concentration of 3 μM in the selected a) aprotic solvents and b) protic solvents at room temperature.

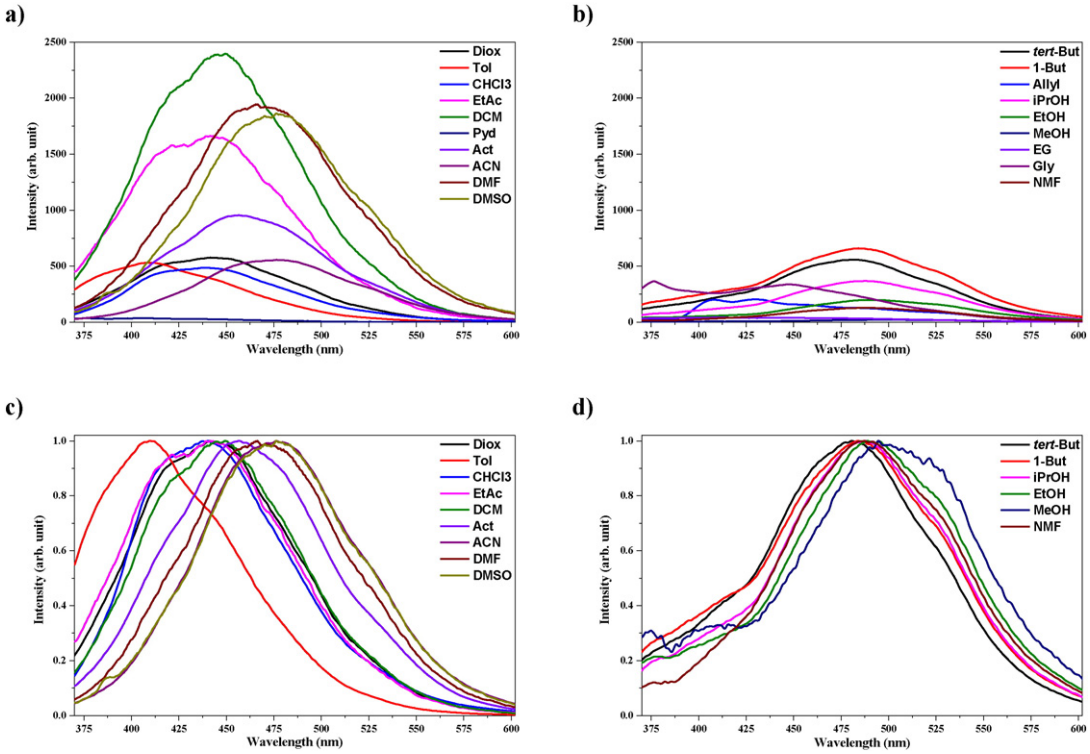

Fig. 4. Emission spectra (λ_{exc} = 350 nm) of AG-1478 measured at concentration of 3 μM in the selected a) aprotic solvents and b) protic solvents at room temperature; the normalized emission spectra for c) aprotic solvents and d) protic solvents.

strength and dynamics of solute-solvent interactions may play an important determinant of the emission quantum yield of AG1478. Determination of the relative effects on radiative and non-radiative processes will require further investigations using time-resolved spectroscopy.

With aprotic solvents, a correlation between quantum yield and dispersion induction (DI) solvent parameter, developed by Laurence et al. [20], was observed with $R = -0.88$. Correlations were also established for quantum yield with solvent refractive index (n) and solvent polarity (SP) of Catalán scale [21] with R values −0.87 and −0.84, respectively. Altogether, the intrinsic (solute) and extrinsic (solute-solvent) electrostatic interactions are required for stabilization of the emissive state. Which means polarity, polarizability and induction polarization play prominent role in variability of AG-1478 quantum yield in aprotic solvents.

In order for tyrosine kinase inhibitors to be effective, they must be able to bind to the cognate tyrosine kinase with high affinity without significantly interacting with other cellular components such as membranes, carbohydrates, nucleic acids or other proteins. At the organismal level, the bioavailability of tyrosine kinase inhibitors is also important and binding to plasma proteins, such as serum albumin, may increase the half-life of the tyrosine kinase inhibitors in sera. The results shown here suggest that AG-1478 fluorescence is well-suited as a spectroscopic marker of interactions of AG-1478 with other biological macromolecules. For example, in a previous study the fluorescence from AG-1478 was found to increase markedly upon interaction of AG-1478 with human serum albumin [22]. This is in line with the strong dependence of AG-1478 fluorescence on polarity and hydrogen-bonding environment.

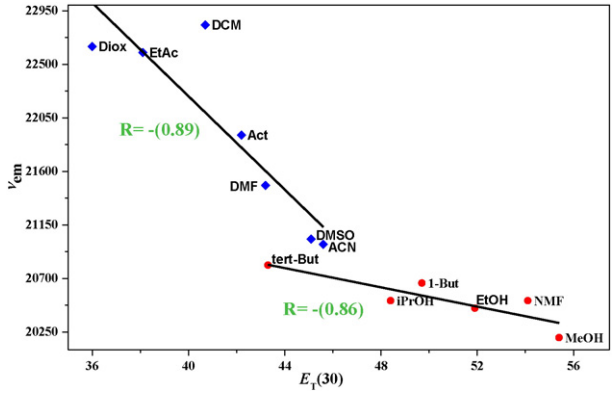

Fig. 5. The correlation of Reichardt solvent transition energy parameter with the emission maxima in wavenumber for aprotic solvents (blue squares) and protic solvents (red circles).

4. Conclusion

Solvent polarity and hydrogen-bonding interactions are both important factors in studying the solvatochromism of AG-1478. The change in optical density and band shape proves that the solvent can have a measurable effect on UV-absorbance of AG-1478 and the electronic stabilization of its ground state. Fluorescence spectral analyses showed that solvent hydrogen-bonding plays important role in solvatochromism, showing synergistic effect with solvent polarity in stabilizing the excited state. Fluorescence quantum yields were found to be influenced by solvent H-bond donor ability, being higher in aprotic than in protic solvents.

Acknowledgment

M. Khattab acknowledges Swinburne University Postgraduate Research Award (SUPRA).

Appendix A. Supplementary data

Supplementary data to this article can be found online at http://dx.doi.org/10.1016/j.saa.2016.04.009.

References

[1] P. Yaish, A. Gazit, C. Gilon, A. Levitzki, Blocking of EGF-dependent cell proliferation by EGF receptor kinase inhibitors, Science 242 (1988) 933–935.
[2] A. Gazit, P. Yaish, C. Gilon, A. Levitzki, Tyrphostins I: synthesis and biological activity of protein tyrosine kinase inhibitors, J. Med. Chem. 32 (1989) 2344–2352.
[3] C.J. Tsai, R. Nussinov, The molecular basis of targeting protein kinases in cancer therapeutics, Semin. Cancer Biol. 23 (2013) 235–242.
[4] R. Eglen, T. Reisine, Drug discovery and the human kinome: recent trends, Pharmacol. Ther. 130 (2011) 144–156.
[5] V. Kannappan, P. Vidhya, V. Sathyanarayanamoorthi, Quantum mechanical study of solvation analysis on some nitrogen containing heterocyclic compounds, J. Mol. Liq. 207 (2015) 7–13.
[6] J.R. Lakowicz, Topics in Fluorescence Spectroscopy: Volume 4: Probe Design and Chemical SensingSpringer Science & Business Media 1994.
[7] W.C. Shakespeare, SH2 domain inhibition: a problem solved? Curr. Opin. Chem. Biol. 5 (2001) 409–415.
[8] B.E. Cohen, T.B. McAnaney, E.S. Park, Y.N. Jan, S.G. Boxer, L.Y. Jan, Probing protein electrostatics with a synthetic fluorescent amino acid, Science 296 (2002) 1700–1703.
[9] G. Saroja, T. Soujanya, B. Ramachandram, A. Samanta, 4-Aminophthalimide derivatives as environment-sensitive probes, J. Fluoresc. 8 (1998) 405–410.
[10] I. Grabchev, J.M. Chovelon, X. Qian, A copolymer of 4-*N*,*N*-dimethylaminoethylene-*N*-allyl-1,8-naphthalimide with methylmethacrylate as a selective fluorescent chemosensor in homogeneous systems for metal cations, J. Photochem. Photobiol. a-Chem. 158 (2003) 37–43.
[11] R.B. Lichtner, A. Menrad, A. Sommer, U. Klar, M.R. Schneider, Signaling-inactive epidermal growth factor receptor/ligand complexes in intact carcinoma cells by quinazoline tyrosine kinase inhibitors, Cancer Res. 61 (2001) 5790–5795.
[12] C.L. Arteaga, T.T. Ramsey, L.K. Shawver, C.A. Guyer, Unliganded epidermal growth factor receptor dimerization induced by direct interaction of quinazolines with the ATP binding site, J. Biol. Chem. 272 (1997) 23247–23254.
[13] A. Levitzki, A. Gazit, Tyrosine kinase inhibition: an approach to drug development, Science 267 (1995) 1782–1788.
[14] I.B. Berlman, Oj Steingra, Further evidence of a hidden singlet transition in biphenyl, J. Chem. Phys. 43 (1965) 2140–2141.
[15] E. Lippert, Dipolmoment Und Elektronenstruktur Von Angeregten Molekulen, Zeitschrift Fur Naturforschung Part a-Astrophysik Physik Und Physikalische Chemie 10 (1955) 541–545.
[16] N. Mataga, Y. Kaifu, M. Koizumi, Solvent effects upon fluorescence spectra and the dipole moments of excited molecules, Bull. Chem. Soc. Jpn. 29 (1956) 465–470.
[17] N.G. Bakhshiev, Universal intermolecular interactions and their effect on the position of the electronic spectra of molecules in 2-component solutions .7. Theory (general case for isotopic solution), Opt Spektrosk. 16 (1964) 821–832.
[18] L. Bilot, A. Kawski, Zur Theorie Des Einflusses Von Losungsmitteln Auf Die Elektroenspektren Der Molekule, Zeitschrift Fur Naturforschung Part a-Astrophysik Physik Und Physikalische Chemie A 17 (1962) 621-&.
[19] A. Chamma, P. Viallet, Determination of dipole moment of molecule in singlet excited state - application to indole, benzimidazole and indazole, Comptes Rendus Hebdomadaires Des Seances De L Academie Des Sciences Serie C 270 (1970) 1901-&.
[20] C. Laurence, J. Legros, A. Chantzis, A. Planchat, D. Jacquemin, A database of dispersion-induction DI, electrostatic ES, and hydrogen bonding alpha 1 and beta 1 solvent parameters and some applications to the multiparameter correlation analysis of solvent effects, J. Phys. Chem. B 119 (2015) 3174–3184.
[21] J. Catalan, Toward a generalized treatment of the solvent effect based on four empirical scales: dipolarity (SdP, a new scale), polarizability (SP), acidity (SA), and basicity (SB) of the medium, J. Phys. Chem. B 113 (2009) 5951–5960.
[22] A.H.A. Clayton, M.A. Perugini, J. Weinstock, J. Rothacker, K.G. Watson, A.W. Burgess, E.C. Nice, Fluorescence and analytical ultracentrifugation analyses of the interaction of the tyrosine kinase inhibitor, tyrphostin AG1478-mesylate, with albumin, Anal. Biochem. 342 (2005) 292–299.

Supplementary materials

Table S1. List of Pearson's correlation coefficient (R) and coefficient of determination (R^2) of the best fitted line (sorted in descending order) of correlations drawn between absorption, emission and stokes shift wavenumbers and solvent parameters under study

Plot description	Protic[a]			Aprotic[b]	
	R	R^2		*R*	R^2
SdP/$\Delta\nu$[c]	0.98[c]	0.97	**ε/ν_{em}**	-(0.96)	0.91
SP/$\Delta\nu$[c]	-(0.96)[c]	0.92	**μ/ν_{em}**	-(0.94)	0.89
β_1/ν_{em}	0.95	0.91	**$E(30)/\nu_{em}$**	-(0.89)	0.79
π^*/ν_{em}	-(0.94)	0.89	**E_T^N/ν_{em}**	-(0.89)	0.79
α/ν_{em}	-(0.92)	0.85	**ES/ν_{em}**	-(0.89)	0.79
SA/ν_{em}	-(0.92)	0.84	**$\varepsilon/\Delta\nu$**	0.87	0.76
α_1/ν_{em}	-(0.89)	0.79	**$\mu/\Delta\nu$**	0.85	0.73
β/ν_{em}	0.89	0.78			
$E(30)/\nu_{em}$	-(0.86)	0.74			
E_T^N/ν_{em}	-(0.86)	0.74			
SB/ν_{em}	0.86	0.73			
F(ε,n)/ν_{em}	-(0.85)	0.72			
AN/ν_{ab}	-(0.84)	0.72			
SdP/ν_{em}	-(0.84)	0.71			

SdP (Catalán solvent dipolarity); SP (Catalán solvent polarizability); β_1 (Laurence solvent basicity); π^* (Kamlet-Taft solvent polarity/polarizability); α (Kamlet-Taft solvent acidity); SA (Catalán solvent acidity); α_1 (Laurence solvent acidity); β (Kamlet-Taft solvent basicity); $E(30)$ (Reichardt transition energy); E_T^N (normalized transition energy); SB (Catalán solvent basicity); F(ε,n) (Reynold's reaction field); AN (acceptor number); ε (dielectric constant); μ (dipole moment); and ES (Laurence electrostatic force parameter)

[a] aforementioned protic solvents excluding ethylene glycol, glycerol, allyl alcohol, and water

[b] aforementioned aprotic solvents excluding pyridine, toluene, chloroform, and 1,2-dichloroethane

[c] NMF data is not available

Table S2. Pearson's correlation coefficient (R) and coefficient of determination (R^2) of the best fitted line of correlations drawn between quantum yield (QY) and solvent parameters under study

Plot description	Aprotic[a]			Protic[b]	
	R	R^2		R	R^2
QY/DI	- (0.88)	0.78	**QY/*η***	0.86	0.73
QY/*n*	- (0.87)	0.76	**QY/*α***	- (0.82)	0.67
QY/SP	- (0.84)	0.71	**QY/AN**	- (0.81)	0.65

DI (Laurence dispersion-induction parameter); n (refractive index); SP (Catalán solvent polarizability); η (viscosity); α (Kamlet-Taft solvent acidity); and AN (acceptor number)

[a] aforementioned protic solvents excluding ethylene glycol, glycerol, allyl alcohol, and water

[b] aforementioned aprotic solvents excluding pyridine, toluene, chloroform, and 1,2-dichloroethane

Chapter III

Geometric and Electronic Characterization of AG1478

In the previous chapter, we revealed that polarity and H-bond strength of medium have a great impact on the spectra of AG1478. In this chapter, we reveal how the geometric structure of AG1478 can affect the measured spectra. Our density functional theory (DFT) based quantum mechanical calculations reported two conformers of AG1478 with a small energy difference. As such, the finding of AG1478 conformer pair helped to assign the two peaks of the measured absorption spectra to the two discovered conformers.

We utilized DFT to perform a potential energy surface scan of AG1478 in its ground electronic state. Results revealed that AG1478 has two distinct conformations with different anisotropic characteristics. The most stable structure, the global minimum structure, has the aniline and quinazoline moieties coplanar (in the same plane). The second structure, a local minimum structure, is a twisted rotamer where the aniline group is tilted by *ca*. 49º with respect to quinazoline plane. By employing time-dependent DFT, we calculated the absorption spectrum for each conformer. We have used B3LYP/6-311+G* model chemistry to compute the UV-Vis spectra because this model have given reliable results in a good agreement with the experiment [162-165]. The simulated spectra aided us to understand the electronic configuration of AG1478. The lowest energy absorption peak at 340-346 nm is ascribed to the $S_0 \rightarrow S_1$ transition of the twisted conformer. While the absorption band in 327-336 nm range is attributed to the $S_0 \rightarrow S_1$ transition of the planar structure of AG1478.

This chapter is presented in the form of the published paper, **Muhammad Khattab**, Subhojyoti Chatterjee, Andrew H.A. Clayton and Feng Wang, *Two Conformers of a Tyrosine Kinase Inhibitor (AG-1478) Disclosed Using Simulated UV-Vis Absorption Spectroscopy*, New J. Chem. 40 (2016), 8296-304

NJC

PAPER

Cite this: *New J. Chem.*, 2016, **40**, 8296

Two conformers of a tyrosine kinase inhibitor (AG-1478) disclosed using simulated UV-Vis absorption spectroscopy†

Muhammad Khattab,[a] Subhojyoti Chatterjee,[b] Andrew H. A. Clayton*[a] and Feng Wang*[b]

AG-1478 (*N*-(3-chlorophenyl)-6,7-dimethoxy-4-quinazolinamine) shows promising *in vitro* and *in vivo* antiproliferative activity and has gained global interest due to its potent and broad biopharmaceutical activities. An important step towards understanding its spatial and temporal distribution is to determine whether the inhibitors have spectral signatures that might assist in determining the relevant targets and interactions. Its UV-Vis absorption spectra in various solutions have been measured [Khattab *et al.*, *Spectrochimica Acta A*, 2016, **164**, 128]. The present study correlates the UV-Vis spectral signatures with the structure of the drug. Two stable conformers AG-1478**B** and AG-1478**A** with close energy values (ΔE = 1.58 kcal mol^{-1}) were located on the potential energy surface through rotation of the single C–N bond of the C–NH–C chain of the drug. The present density functional theory (DFT) study reveals that both conformers contribute to the measured UV-Vis absorption spectrum of AG-1478. The conformers, AG-1478**B** and AG-1478**A**, were subjected to further study using molecular orbital theory. It is found that although the conformers are close in energy, the anisotropic properties, such as the shape in three dimensional (3D) space, the dipole moment and the orbitals, are apparently different. The excess orbital energy spectrum (EOES) indicates that six core orbitals exhibit significant conformational changes, exhibiting the signatures of the N atoms, *i.e.*, the NH linker $N_{(25)}$ and the quinazoline $N_{(12)}$. The valence orbitals with significant configurational changes are either due to the local distribution (30a) or delocalization (46a, 76a and 82a (highest occupied molecular orbital (HOMO))).

Received (in Montpellier, France) 17th June 2016,
Accepted 4th August 2016

DOI: 10.1039/c6nj01909a

www.rsc.org/njc

1. Introduction

Due to the high prevalence of gene mutations, cancer becomes intolerant to many known inhibitors. Dysregulation of the epidermal growth factor receptor (EGFR) family is associated with a large number of epithelial cancers so the signalling pathway has, therefore, become a major target for drug discovery.[1] For this reason, several types of known inhibitors with various degrees of selectivity, such as quinazoline based anti-HER2 (human epidermal growth factor receptor 2), have been synthesized.[2–4] Quinazolines were designed to mimic epidermal growth factor receptor (EGFR or ErbB-1) targeted chemotherapies,[3,4] such as Gefitinib, Erlotinib and Lapatinib,[2–4] as well as tyrphostin 4-(3-chloroanilino)-6,7-dimethoxyquinazoline (AG-1478, Fig. 1).

Tyrphostin *N*-(3-chlorophenyl)-6,7-dimethoxyquinazolin-4-amine (AG-1478; CAS 175178-82-2) is a competitive small molecule tyrosine kinase inhibitor (TKI) of the adenosine triphosphate (ATP) binding site in the EGFR/HER1 kinase domain. It is a highly potent and specific small molecule inhibitor of EGFR (ErbB1) tyrosine kinase[5,6] and a potential anticancer agent.[5,7,8] For example, AG-1478 demonstrated potent antiproliferative activities against various cancer cell lines both *in vitro* and *in vivo*.[9–11] It was found to augment the cellular sensitivity to other cytotoxic drugs such as Doxorubicin and Cisplatin.[12,13] The effective inhibitory concentration of AG-1478 is within a nanomolar range and is sufficient to inhibit the overexpressed tyrosine kinases.[14] In xenograft models obtained from a nude mouse tumor, AG-1478 inhibited the proliferation of a human glioma xenograft that showed an increased number of mutant EGFRs. It sensitized the cells of the xenograft to the cytotoxicity of Temozolomide and Cisplatin. It synergistically enhanced the efficacy of the monoclonal antibody mAb 806.[7,15] Other studies demonstrated that AG-1478 is able to lessen the radio immunotherapy dose required to kill squamous cancer cells in mouse xenografts.[16] The preliminary pharmacokinetics and pharmacodynamics

[a] *Centre for Micro-Photonics, Faculty of Science, Engineering and Technology, Swinburne University of Technology, Melbourne, Victoria 3122, Australia. E-mail: aclayton@swin.edu.au*
[b] *Molecular Model Discovery Laboratory, Department of Chemistry and Biotechnology, School of Science, Faculty of Science, Engineering and Technology, Swinburne University of Technology, Melbourne, Victoria 3122, Australia. E-mail: fwang@swin.edu.au*

† Electronic supplementary information (ESI) available. See DOI: 10.1039/c6nj01909a

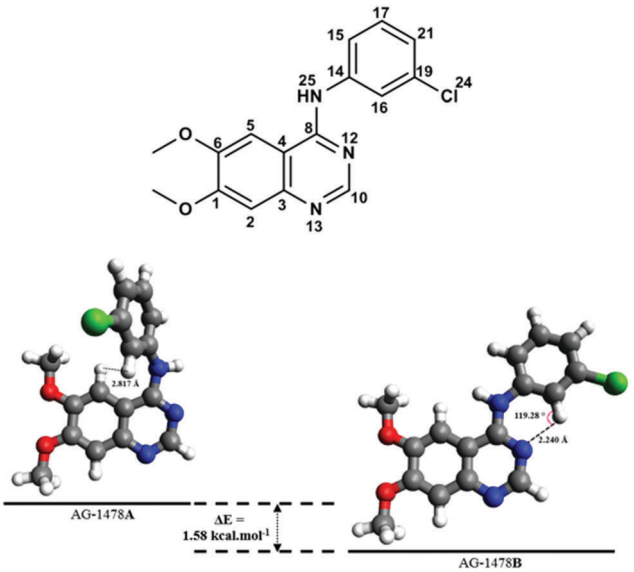

Fig. 1 The chemical two dimensional (2D) structure of *N*-(3-chlorophenyl)-6,7-dimethoxyquinazolin-4-amine (Tyrphostin AG-1478). In the lower panel, the three-dimensional ball and stick molecular models of the two most stable conformers of AG-1478 in vacuum are shown; (a) the local minimum (conformer A) showing the steric hindrance between $C_{(5)}$–H and $C_{(16)}$–H and (b) the global minimum (conformer B) showing the bond length and angle of a potential six-membered intramolecular H-bond. The atomic numberings are shown in the 2D structure.

data of AG-1478 have been preclinically evaluated in mice using drug/β-cyclodextrin formulations.[17]

The important chemical features of AG-1478, required for its binding affinity[4] and potent activity toward EGFR, include the topology of quinazoline nitrogens and the NH linker.[18] Being synthesized to mimic the purine moiety of the kinase cofactor (ATP), AG-1478 can bind to the ATP-active site of a protein forming one to three H-bonds with the 'hinge region' of protein. Extra interactions dominated by the hydrophobic chlorophenyl side chain were also predicted.[19] It was observed to covalently bind to the sulfhydryl group of Cys773 of EGFR.[20] The two methoxyl groups were incorporated to increase the aqueous solubility and were discovered to interact with the kinase hydrophilic region, which anchors the ribose moiety of ATP.[19]

Many biomolecules such as quinazoline based derivatives are inherently fluorescent.[1,4,21] The conjugated aromatic core of AG-1478 renders it a good candidate for studying its electronic absorption experimentally. Moreover, AG-1478 possesses five H-acceptor sites and one H-donor group, which are proposed to have a dramatic impact on the molecular structure and electronic transitions. As a result, it is important to study its topology and electron density distribution; hence, a rationale for the UV-Vis absorbance patterns of AG-1478 can be reached.[21] In addition, the moiety of AG-1478 is contained in the EGFR/HER1 family of inhibitors such as gefitinib, erlotinib, lapatinib *etc.*[4] Study of the UV-Vis absorption spectroscopy *in silico* at the molecular level will help one to understand the major UV-Vis absorption band at approximately 330 nm of the same class of drugs. It provides information on shifting the absorption band (and therefore the color of the spectra) by changing the highest occupied molecular orbital-lowest unoccupied molecular orbital (HOMO–LUMO) gap through modifications of its molecular structure, which hereby provides the foundation for rational drug design; the same principles have been applied in other molecular studies.[22,23]

Limited studies of the UV-Vis absorption spectra of drugs have been carried out at molecular level.[4,24,25] In this paper, the UV-Vis absorption spectrum of AG-1478 in methanol solution is studied *in silico* using quantum mechanical time-dependent density functional theory (TD-DFT) in order to correlate the structure and property relationship. The theoretical calculations together with our earlier experimental measurements[1] shed light on the molecular structure and spectral properties of TKI AG-1478.

2. Computational details

Density functional theory (DFT) based Becke three-parameters Lee–Yang–Parr hybrid functional (B3LYP)[26] in combination with the 6-311+G(d) basis set was employed in the calculations. The geometry of AG-1478 was originally optimized using the B3LYP/6-31G(d) model and reoptimized using the B3LYP/6-311G(d) model. The UV-Vis spectrum in methanol solution was calculated using TD-DFT and the conductor-like polarizable continuum model (CPCM).[27] Absorption UV-Vis spectra in methanol solution were calculated for the lowest 60 excited states of singlet–singlet transitions. Absorption profiles were simulated using a half-width half-maximum (HWHM) of 4428 nm (0.28 eV). All calculations were performed using a Gaussian 09 computational chemistry package[28] on the Swinburne University Supercomputing Facility.

3. Results and discussion

3.1. Discovery of AG-1478B (global) and AG-1478A (local) from potential energy scan

The 2D chemical structures and nomenclature of the AG-1478 (CAS 175178-82-2) are given in Fig. 1 (top). The quinazoline and the chlorophenyl rings are connected through a single bond NH linker, $C_{(8)}$–$N_{(25)}$H–$C_{(14)}$. A full geometry optimization using the DFT based B3LYP/6-311G(d) model leads to a minimum structure of AG-1478, *i.e.*, AG-1478**A**. The single C–N bonds of the NH linker are able to rotate to produce possible rotational conformers. As a result, based on the AG-1478**A** structure, a potential energy scan that rotates the $N_{(25)}$–$C_{(14)}$ bond while freezing the whole structure led to a more stable global minimum structure, AG-1478**B**. Fig. 2 presents the potential energy curve locating the two minimum energy structures of AG-1478**A** and AG-1478**B**.

Fully relaxed reoptimizations of the AG-1478**A** and AG-1478**B** structures were carried out. Shown as 3D structures in Fig. 1, the "global minimum" energy structure of AG-1478**B** is deduced to be more energetically stable than the local minimum energy structure AG-1478**A** conformer by a small energy difference

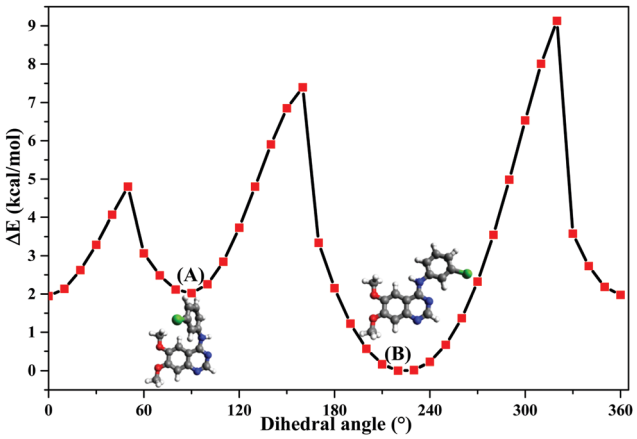

Fig. 2 Potential Energy Scan (PES) curve of AG-1478 through rotation of the $\angle N_{(12)}–C_{(8)}–N_{(25)}–C_{(14)}$ angle of AG-1478**A** using the B3LYP/6-311G* level of theory.

Table 1 Comparison of the selected geometrical parameters and other properties of the AG-1478**B** (global) and AG-1478**A** (local) structures using the B3LYP/6-311+G(d) model

Parameters	AG-1478**B**	AG-1478**A**
$R1^a$	8.370	8.368
$R2^a$	8.442	8.449
$R3^a$	8.206	8.200
Bond length (Å)		
$C_{(3)}–N_{(13)}$	1.367	1.363
$C_{(8)}–N_{(12)}$	1.324	1.327
$C_{(8)}–N_{(25)}$	1.376	1.393
$C_{(10)}–N_{(12)}$	1.351	1.348
$C_{(10)}–N_{(13)}$	1.310	1.314
$C_{(14)}–N_{(25)}$	1.406	1.412
$C_{(6)}–O_{(28)}$	1.356	1.354
$C_{(29)}–O_{(28)}$	1.419	1.421
$C_{(19)}–Cl_{(24)}$	1.761	1.760
$C_{(3)}–C_{(4)}$	1.416	1.422
Bond angle (°)		
$N_{(12)}–C_{(8)}–N_{(25)}$	119.57	114.59
$C_{(16)}–C_{(14)}–N_{(25)}$	124.42	122.60
$C_{(8)}–N_{(25)}–C_{(14)}$	131.92	128.12
$C_{(6)}–O_{(28)}–C_{(29)}$	118.66	118.38
Dihedral angle (°)		
$C_{(4)}–C_{(8)}–N_{(25)}–C_{(14)}$	−180.00	49.19
$C_{(4)}–C_{(8)}–N_{(25)}–H_{(26)}$	0.02	−163.46
$N_{(12)}–C_{(8)}–N_{(25)}–C_{(14)}$	0.00	−135.49
$N_{(12)}–C_{(8)}–N_{(25)}–H_{(26)}$	−179.97	11.86
$C_{(15)}–C_{(14)}–N_{(25)}–C_{(8)}$	179.94	−167.44
$C_{(15)}–C_{(14)}–N_{(25)}–H_{(26)}$	−0.08	46.23
$C_{(16)}–C_{(14)}–N_{(25)}–C_{(8)}$	−0.07	14.52
$C_{(16)}–C_{(14)}–N_{(25)}–H_{(26)}$	179.91	−131.82
$\langle R^2 \rangle$ (a.u.)	10395.1156	7611.6811
μ (D)	5.83	3.08
E (E_h)	−1393.276879	−1393.274497
ZPE (kcal mol^{-1})	173.51499	173.59588
E + ZPE (E_h)	−1393.000366	−1392.997854
HOMO–LUMO gap (eV)	4.25	4.26
Rotational const. A (GHz)	0.5882	0.3470
B (GHz)	0.1126	0.1855
C (GHz)	0.0946	0.1447

[a] Perimeters of the hexagon rings.[29]

of 1.58 kcal mol^{-1}. Table 1 compares the selected geometries and other electronic properties of the two conformers, such as ring perimeters,[29] electronic spatial extent, dipole moment, rotational constants and HOMO–LUMO energy gaps. For the complete list of geometric parameters, see Table S1 in the ESI.†

The major differences between the two conformers are obtained due to the rotation of the $N_{(25)}–C_{(14)}$ bond locally, which does not apparently affect the other bond lengths or most of the bond angles. For example, the ring perimeter of the three aromatic rings changes by less than 0.01 Å. The variations of the bond angles local to the NH linker are also small. Only the NH linker related dihedral angles changed significantly (all include $N_{(25)}$). For example, the dihedral angle of $C_{(4)}–C_{(8)}–N_{(25)}–C_{(14)}$ exhibited significant conformational changes from planar to twisted by 49.19°. In addition, the proposed hydrogen bond in AG-1478**B** as marked in Fig. 1 could contribute to its further stability. A possible H-bond between the $C_{(16)}–H\cdots N_{(12)}$ of AG-1478**B** (bond length = 2.24 Å) helps to stabilize the AG-1478**B** structure and to adapt the flat configuration as shown in Fig. 1. Breaking this H-bond needs approximately 5 kcal mol^{-1} energy as indicated in Fig. 2.

Folding over the NH linker changes the shape of the AG-1478**B** structure and leads to the reduction of its size and dimensions in space. For example, the electronic spatial extent $\langle R^2 \rangle$, which conveys roughly the molecular volume (size) of a molecule, changes significantly from the $\langle R^2 \rangle$ of 10 395 a.u. (AG-1478**B**) to 7,612 a.u. (AG-1478**A**). The difference in molecular size was also revealed by their rotational constants at equilibrium. The rotational constants of A, B and C of conformer AG-1478**B** were given by 0.5882 GHz, 0.1126 GHz and 0.0946 GHz, whereas the same rotational constants for the AG-1478**A** rotamer were calculated as 0.3470 GHz, 0.1855 GHz and 0.1447 GHz, respectively. In addition, one of the most noticeable property divergences between the two rotamers is the change in the dipole moment. Dipole moment values of 5.83 D and 3.08 D were calculated for AG-1478**B** and AG-1478**A**, respectively. As a result, the structural changes between AG-1478**A** and AG-1478**B** would cause one of them to dock appropriately into the protein active pocket. The lowest energy conformer is not necessarily the most potent drug; however, the higher energy conformer of a drug can be more potent as found in azidothymidine (AZT).[30]

3.2. Spectral signatures of AG-1478A (local minimum conformer) in the UV-Vis spectra

The conjugated ring system of AG-1478 makes it a good candidate for studying its UV-Vis spectrum. The measured UV-Vis absorption spectrum in the region of 200–400 nm of AG-1478 in methanol solution is compared with the simulated spectra of the conformers in Fig. 3. Four bands at 222 nm, 249 nm, 332 nm and 340 nm were determined from the measured UV-Vis spectrum (black) of AG-1478 in methanol solution. As seen in the measured spectrum, the bands form two clusters, which were distinctly separated from each other. In the same figure, the simulated UV-Vis spectra of AG-1478**A** (red) and AG-1478**B** (blue) in the region of 200–400 nm are also presented in this figure.

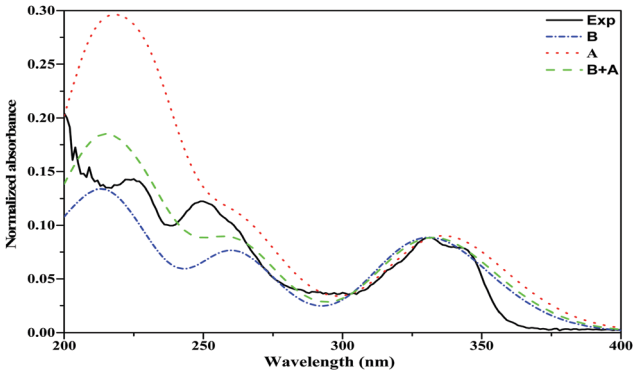

Fig. 3 The observed (solid, black) and calculated (dashed, colored) UV-Vis spectra of AG-1478 in methanol using B3LYP/6-311+G*. The calculated spectrum of AG-1478**B** coincides with the high energy absorption band of the experimental spectrum (−1 nm) and contributes significantly to the 249 and 222 nm bands. The theoretical spectrum of AG-1478**A** shows a good agreement (−4 nm) with the measured band at 340 nm. AG-1478**A** contributes more to the 222 nm band than to 249 nm band. The combination spectrum (green) qualitatively simulates the experimental spectrum.

Table 2 Comparison of the experimental and theoretical UV-Vis absorption spectral maxima (λ, nm) of AG-1478 in two sets of different solvents[1]

Solvent	Dielectric constant (ε)	AG-1478**B**[a] λ_1	AG-1478**A**[a] λ_2	Exp.[21] λ_1	Exp.[21] λ_2
Protic:					
Methanol	32.61	331	336	332	340
Ethanol	24.85	331	336	332	344
2-Propanol	19.26	331	336	333	343
tert-Butanol	12.47	331	336	329	341
1-Butanol	17.33	331	337	333	345
N-MFA	181.56	332	337	330	343.5
Aprotic:					
Ethylacetate	5.98	330	336	327	340
Acetonitrile	35.68	331	336	328	342
DCM	8.93	331	337	329	342
DMF	37.21	332	337	331	342
Pyridine	12.97	332	337	330	345
DMSO	46.82	332	337	332	346

[a] TD-DFT/B3LYP/6-311+G(d) model.

Interestingly, the more stable conformer AG-1478**B** showed three bands at approximately 212 nm, 258 nm and 331 nm, whereas the less stable conformer, AG-1478**A** exhibited two bands at 219 nm and 336 nm, respectively. Indeed, the measured AG-1478 spectrum seems to contain the collective features of AG-1478**A** as well as AG-1478**B**, as shown in Fig. 3 (green spectrum). As a result, superposition of the spectra (red and blue) of the two conformers (green) presents reasonably the experimental UV-Vis spectrum (black) of AG-1478.[21] This indicates that both the AG-1478**A** and AG-1478**B** structures appear in the solution phase and contribute to the spectral properties of AG-1478, and, hence, may affect its protein binding and biological functions.

Table 2 compares the measured[21] and calculated major bands (above 300 nm) of the UV-Vis spectra of AG-1478 in various protic and aprotic solvents. The TD-DFT calculations were performed for the UV-Vis spectra of AG-1478**B** and AG-1478**A** using the CPCM model *in silica*. As seen in this table, the measured major band is a broad band consisting of two bands λ_1 and λ_2 with approximately 10 nm splitting. The simulated major band of AG-1478**B** represents the measured band at λ_1 well, whereas the simulated major band of AG-1478**A** reproduces the measured λ_2 band. The simulated wavelength maxima of AG-1478**B** were calculated as $\lambda = 331 \pm 1$ nm, while those of AG-1478**A** were given by $\lambda = 336 \pm 1$ nm in various solutions. For instance, the UV-Vis spectrum of AG-1478 in methanol solution revealed a band maximum at λ_1 of 332 nm, which agrees well with the theoretical value of AG-1478**B** at 331 nm, whereas a band maximum of AG-1478**A** at $\lambda_2 = 336$ nm well reproduces the measured value of 340 nm. It is noted that all the calculations were carried out at 0 K, whereas the measurements were obtained at room temperature.

The UV-Vis absorption spectrum of a compound is the result of transitions among the occupied molecular orbitals and the virtual orbitals.[31] Fig. 4 reports the TD-DFT simulated UV-Vis

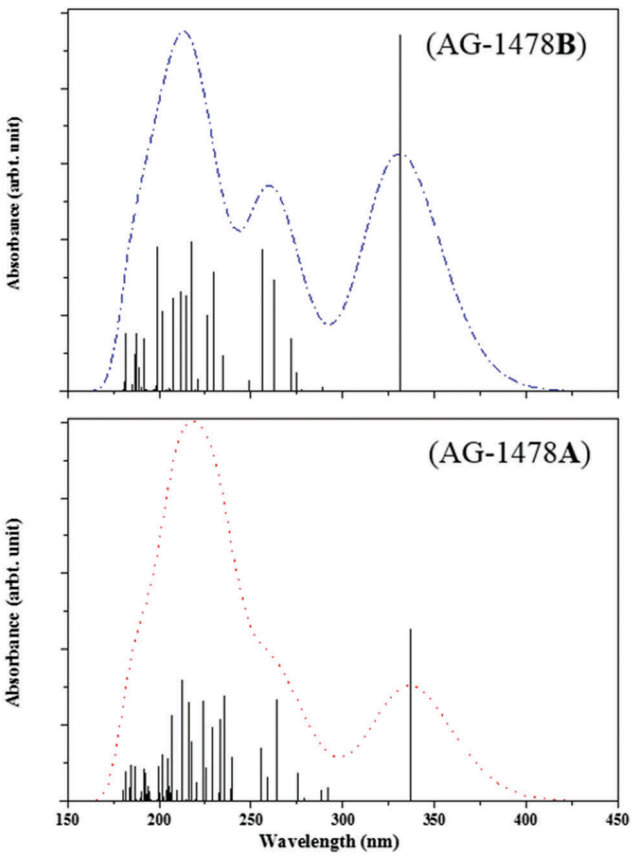

Fig. 4 Simulated UV-Vis spectra of AG-1478 in methanol at the B3LYP/6-311+G* level of theory showing the oscillator strength of electronic transitions as vertical solid lines. (HWHH = 0.28 eV).

spectra of AG-1478**B** and AG-1478**A** in methanol solution in a broader region of 150–450 nm. The major transitions with oscillator strength $f > 0.20$ are given in Table 3. As shown in the spectra, the major band at wavelengths longer than 300 nm is the result of a strong single transition (as shown by the

Table 3 Transitions of the absorption bands maxima of AG-1478**B** and AG-1478**A** with oscillator strengths ($f > 0.20$) and electronic transition configurations (>5%) (nm)[a]

AG-1478**B**			AG-1478**A**		
Excitation energy (nm)	Oscillator strength	Major contributions	Excitation energy (nm)	Oscillator strength	Major contributions
331.02	0.6533	H → L (97%)	336.65	0.3148	H → L (96%)
262.55	0.2051	H−1 → L (35%) H → L+1 (26%) H → L+2 (22%) H−2 → L+1 (5%)	212.74	0.2206	H−3 → L+2 (34%) H−5 → L (26%) H → L+6 (13%)
256.23	0.2591	H → L+3 (85%)			
230.14	0.2190	H−2 → L+1 (45%) H−1 → L+1 (10%) H−1 → L+3 (10%) H−3 → L (7%)			
217.69	0.2726	H−1→L+3 (48%) H→L+8 (17%) H−2→L+2 (11%) H−2→L+1 (6%)			

[a] B3LYP/6-311+G(d) model.

calculated vertical spectral line) in AG-1478**B** and AG-1478**A**, respectively. For example, the transition at 331.02 nm ($f = 0.65$) of AG-1478**B**, and at 336.65 nm of AG-1478**A** ($f = 0.31$) are both dominated by the HOMO–LUMO transitions with major contributions of 97% and 96%, respectively, as indicated in Table 3.

The band at 331 nm with a larger oscillator strength of 0.65 for AG-1478**B** and the other band at 336 nm with a smaller oscillator strength of 0.31 for AG-1478**A** qualitatively represent the measured overlapping bands at 332 nm and 340 nm (refer to Fig. 3). Other bands in the region under 300 nm are contributions from many other transitions among the low energy frontier orbitals, such as HOMO−*N* and LUMO+*M*, where *N* and *M* are small integers (1, 2,...8), representing low energy levels (transitions shown in Table 3 are those >5%). The band positions in this region cannot be determined simply using any single transitions, but need to be determined by the same fitting program used for experimental measurements. However, we simply determine the positions at the top of the peak positions at 212 nm and 258 nm for AG-1478**B** and 219 nm for AG-1478**A**.

Fig. 3 and 4 suggest that the measured UV-Vis spectrum of the AG-1478 in methanol solution could be a mixed contribution of the AG-1478 conformers dominated by AG-1478**B** and AG-1478**A**, as they are the most energetically stable and therefore the most populated conformers in the experimental conditions. The present calculation using the Boltzmann distribution at the experimental room temperature of 298.15 K gives the approximate ratio of 93% and 7% for AG-1478**B** and AG-1478**A**, respectively, indicating that at room temperature, AG-1478**A** can be less populated *in vitro*.

Fig. 5 provides the frontier orbital diagrams (from HOMO−2 to LUMO+2) of AG-1478**B** and AG-1478**A** calculated in methanol solution, together with their corresponding orbital density distributions. As shown in this figure, the energy gaps between the HOMO and the LUMO are very small (4.25 eV for AG-1478**B** and 4.26 eV for AG-1478**A**). The frontier orbitals and their energies of AG-1478**B** and AG-1478**A** are in good agreement with the calculated electronic transitions in Table 3. The smaller the $\Delta\varepsilon$ energies between the virtual orbitals (LUMO+*M*) and the occupied orbitals (HOMO−*N*), the larger the probability of the transitions.

As shown in Fig. 5 and Table 3, the HOMO–LUMO energy gaps of AG-1478**B** and AG-1478**A** are the minimum energies needed for transitions from the occupied to the virtual orbitals. Therefore, HOMO → LUMO transitions dominate the absorption bands of AG-1478**B** and AG-1478**A** at 331.02 nm (97%) and at 336.65 nm (96%), respectively. However, other orbitals energies, such as HOMO−1, are very different between the two conformers. For example, the HOMO−1 → LUMO transitions need 4.25 + 0.76 eV for AG-1478**B** and 4.26 + 0.63 eV for AG-1478**A**. As indicated in Table 3, the large contributions from the transitions in this region are due to a number of other transitions among low lying frontier orbitals, such as the band at 262.55 nm of AG-1478**B** due to four major transitions, HOMO−1 → LUMO (35%), HOMO → LUMO+1 (26%), HOMO → LUMO+2 (22%) and HOMO−2 → LUMO+1 (22%).

3.3. Electronic property differences between the AG-1478B and AG-1478A conformers

It is no surprise that in many potent drugs, the less stable conformer can often be more potent, depending on the shape of the drug conformer *in vivo*.[30] It is therefore important to understand the electronic structural differences and their shape between AG-1478**A** and AG-1478**B**, which may relate to their properties such as drug potency. Molecular electrostatic potential (MEP) maps that estimate the electronic density distribution of two conformers are depicted in Fig. 6. The electron density changes from negative (red) to positive (blue). The distributions of the MEP are quite different: AG-1478**B** is flat and AG-1478**B** is not. The latter (AG-1478**A**) is more packed as the chlorophenyl ring folds over in AG-1478**A**. The highly condensed electron density areas are localized over the atoms with electron lone pairs. For example, the regions around $Cl_{(24)}$, $N_{(12)}$, $N_{(13)}$, $O_{(28)}$ and $O_{(27)}$ in AG-1478**B** show a more dense electron localization. However in AG-1478**A**, the twisting of the chlorophenyl ring lessens only the electron density around $Cl_{(24)}$ as shown in Fig. 6. The most significant change between AG-1478**B** and AG-1478**A** is the shape – when

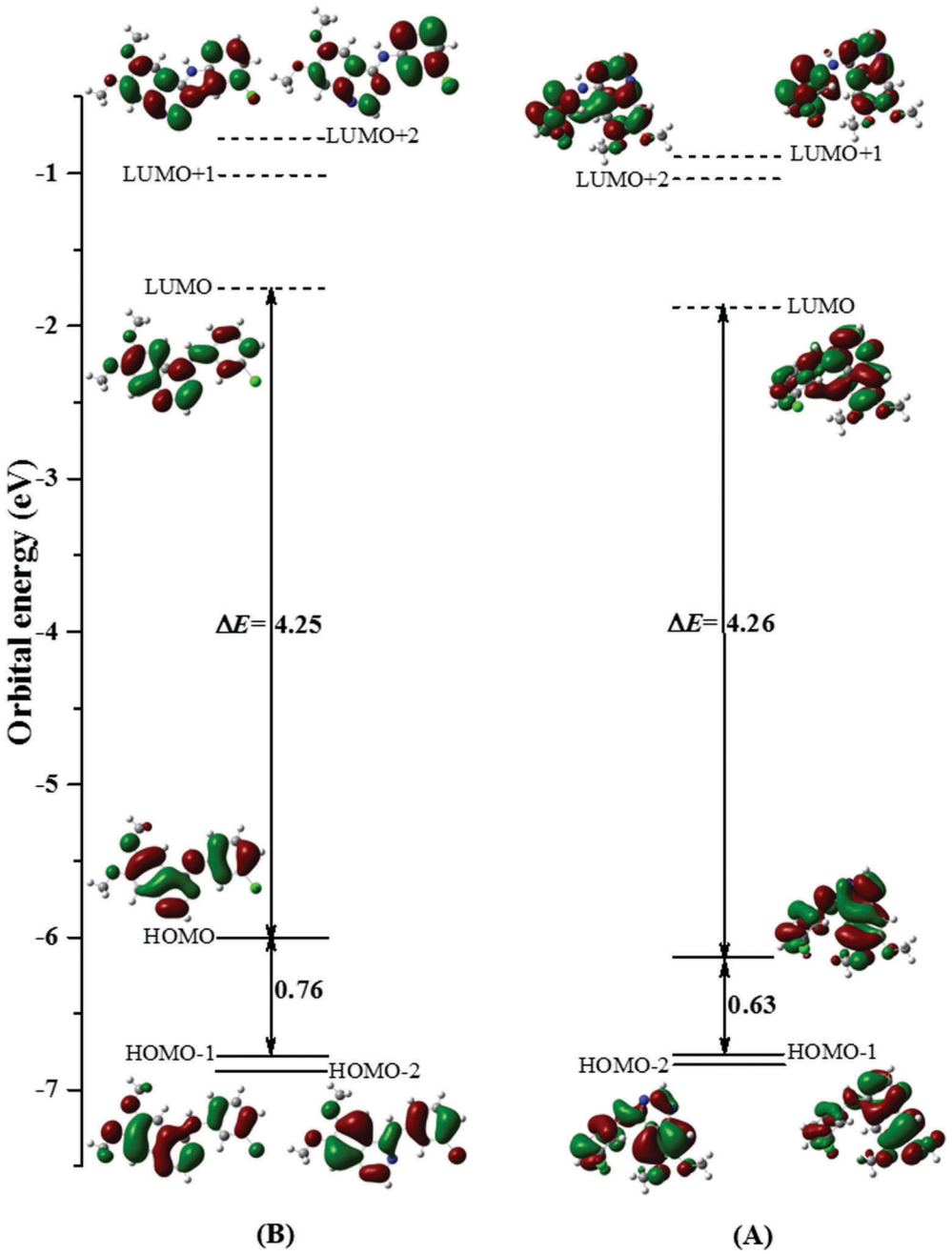

Fig. 5 Energy differences (in eV) between the HOMOs and LUMOs of AG-1478 in methanol at the B3LYP/6-311+G* level of theory. The positive electron density is shown in green, while the negative one is shown in red.

the chlorophenyl ring folds over in AG-1478**A**, it makes the N atoms, $N_{(25)}$ and $N_{(12)}$, with a larger potential in space for binding.

The conformation results in different electron distribution and therefore the hydrogen bond networks of AG-1478**A** and AG-1478**B**. For this reason, the natural bond orbital (NBO) charges for all heavy (no hydrogen) atoms are compared for two conformers and are given in Fig. S2 in the ESI.† As seen in this figure, negative charges are significantly accumulated on the nitrogens and oxygens. The NBO charges of all the Ns and Os of AG-1478**B** are over $-0.50e$, whereas the NBO charge on chlorine Cl is rather small at $-0.020e$. In AG-1478**A**, a noticeable increase in the electron density of $N_{(25)}$ is obtained due to the localization of the lone pair of electrons. The NBO charges of $-0.559e$ and $-0.605e$ were calculated for $N_{(25)}$ of AG-1478**B** and AG-1478**A**, respectively, indicating that this nitrogen atom in the local minimum energy conformer AG-1478**A** may be a strong electron donor for binding.

It is desirable to understand which orbitals are responsible for the conformation changes of AG-1478 in addition to their shape. The measured UV-Vis spectrum in methanol solution suggests that the AG-1478 can be a mixture of two conformers, AG-1478**B** and AG-1478**A**. For this reason, the recently developed

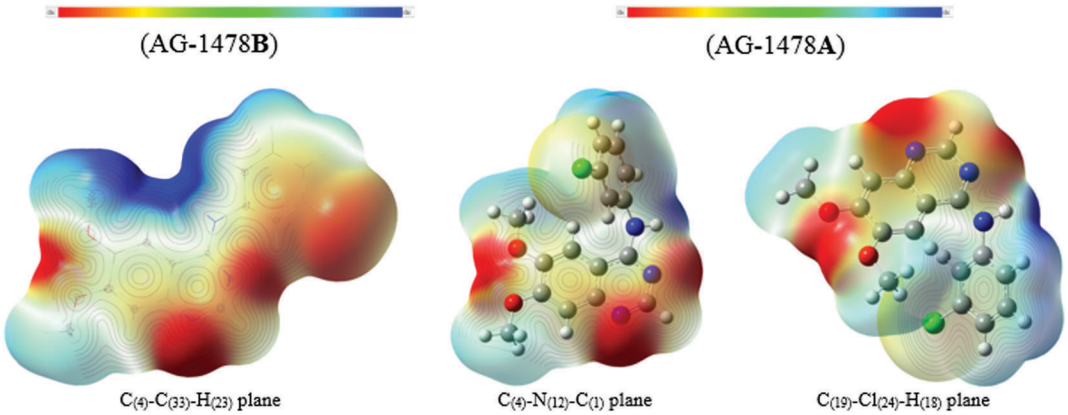

Fig. 6 Comparative molecular electrostatic potential (MEP) maps of AG-1478**B** in methanol solution (left); and AG-1478**A** (middle and right).

excess orbital energy spectrum (EOES)[32] has been applied to identify the orbital dependent changes of the two conformers. Fig. 7 reports the EOES of AG-1478 using $\Delta\varepsilon_i = \varepsilon_i^A - \varepsilon_i^B$, where ε_i^A is the ith orbital energy of AG-1478**A** and ε_i^B is the ith orbital energy of AG-1478**B**.

The ground electronic state of AG-1478 has 82 occupied molecular orbitals, with 26 core orbitals and 56 valence orbitals. The EOES of AG-1478 shows the near distribution of the orbital energy differences around the 0-line. The short red dashed lines in the EOES at $\Delta E \pm 1.58$ kcal mol^{-1} indicate the total electronic energy difference between AG-1478**A** and AG-1478**B**. As shown in the EOES spectrum, approximately one third of the occupied orbitals (24 MOs) have an orbital energy difference larger than their conformational energy difference, $|\Delta\varepsilon_i| > 1.58$ kcal mol^{-1}, indicating that the conformational change induced orbital changes are significant and cannot be neglected.

The EOES exhibits that some orbitals experience profound changes (outside the ± 2.5 kcal mol^{-1} range) with respect to the conformational changes. A total of six such orbitals show significant conformational changes: two core MOs, 4a and 5a, that is, MO4 and MO5, and four valence MOs (30a, 46a, 76a and 82a), as indicated in Fig. 7. The orbital density distributions of these six MOs of the two conformers are given in Fig. 8. Interestingly, it is further discovered that among the core orbitals with significant changes, MO4 (4a) is dominated by $N_{(25)}$ of the NH linker and MO5 is dominated by the quinazoline nitrogen $N_{(12)}$ (see Fig. 1 for the numbering). The former MO4(4a) is part of the NH linker, which rotates to form AG-1478**A** and the latter MO5(5a) is involved in hydrogen bonding with H–$C_{(16)}$ of the chlorophenyl ring, that is, $N_{(12)}\cdots$H–$C_{(16)}$ (refer to Fig. 1). Hence, the hydrogen bond indeed has a noticeable impact on the core shell structure of the compounds.[33] The valence orbitals that exhibit significant energy changes as identified by the EOES are either local at the NH linker area, such as orbital 30a, or delocalized in the entire molecule, such as orbitals 46a, 76a and 82a (HOMO), where the conformation of AG-1478**B** and AG-1478**A** influences the electronic distribution and the apparently different molecular structures of AG-1478**B** and AG1478A in 3D space indeed warrant such differences. Finally, the chlorine Cl atom does not significantly contribute to conformational changes.

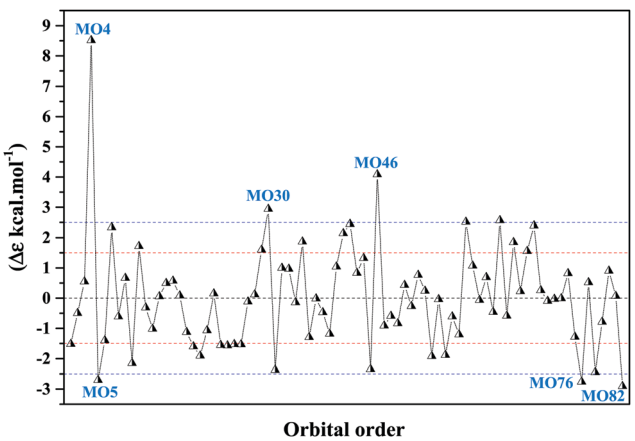

Fig. 7 Excess orbital energy spectrum (EOES) of AG-1478 in methanol ($E_A - E_B$) at the B3LYP/6-311+G* level of theory (The x-axis is the orbital order from the innermost orbital as MO1 to the HOMO as MO82).

4. Conclusions

UV-Vis absorption spectra of TKI AG-1478 in methanol solution have been calculated using TD-DFT. Potential energy scans led to the disclosure of a stable conformer AG-1478**B** and a less stable conformer AG-1478**A** with a small energy difference of 1.58 kcal mol^{-1}. The simulated UV-Vis spectrum of AG-1478 is the contribution of AG-1478**B** and AG-1478**A** conformers, which well reproduces the four measured spectral bands at 222 nm, 249 nm, 332 nm and 340 nm. As the shape of the drug plays an important role in the drug potency, further quantum mechanical study of the AG-1478 conformers revealed that properties such as shape (electronic spatial extent, rotational constants and MEP), dipole moment and electronic transitions are indeed different. EOES[32] indicates that six occupied orbitals exhibit substantial conformational changes. Among them, two core orbitals (MO4 and MO5) reveal that the signature of the $N_{(25)}$ linker

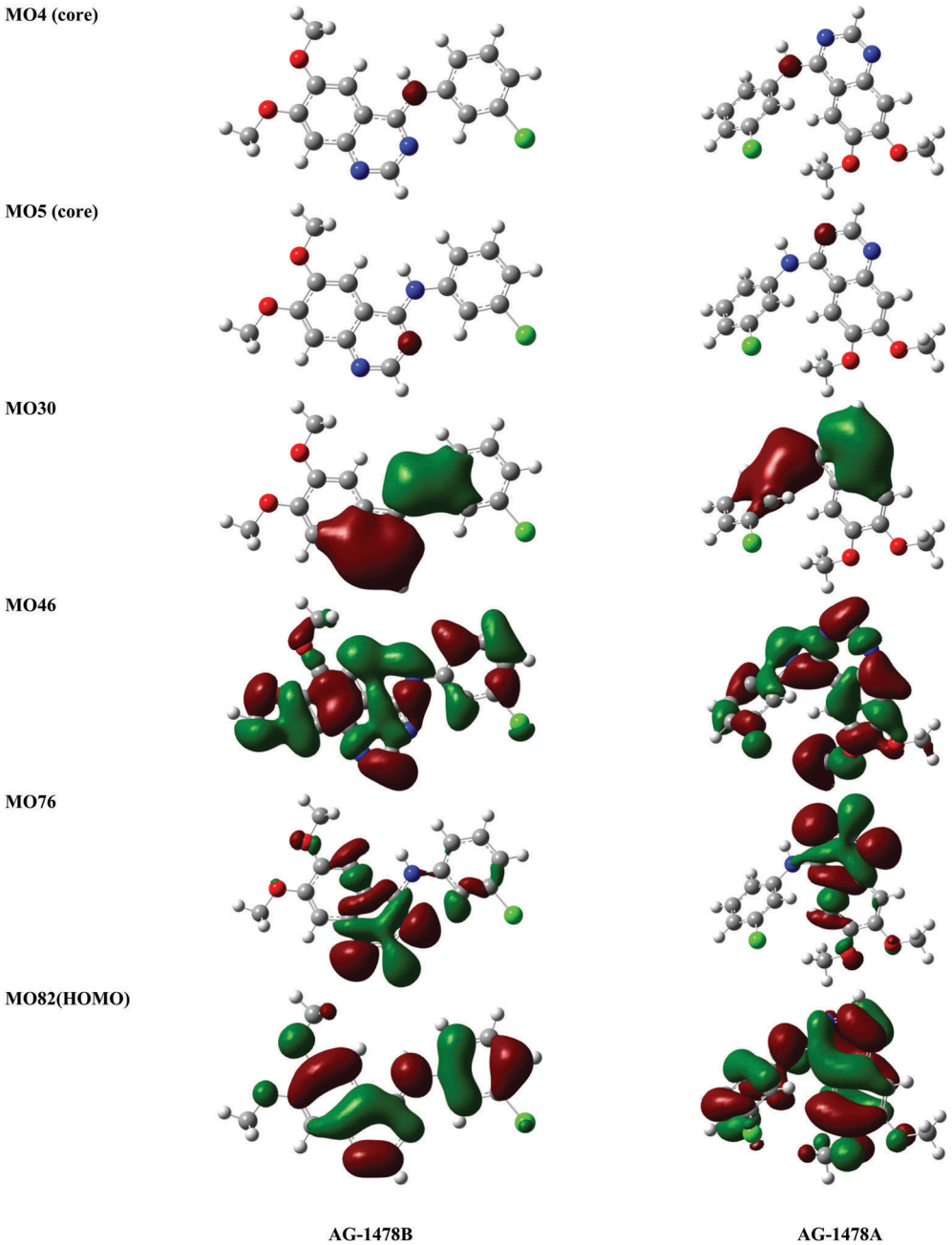

Fig. 8 Orbital charge densities of selected orbitals where energy differences between orbitals of two conformers are more than 2.5 kcal mol^{-1} in Fig. 7.

and the quinazoline $N_{(12)}$ are responsible for such conformational changes. The valence orbitals with significant conformational changes are either due to the local distribution at the NH linker (30a) or delocalization (46a, 76a and 82a(HOMO)), which all contribute to the UV-Vis spectra of AG-1478.

Acknowledgements

M. Khattab acknowledges the Swinburne University Postgraduate Research Award (SUPRA). FW acknowledges supercomputer support from Swinburne University of Technology.

References

1 A. H. A. Clayton, M. A. Perugini, J. Weinstock, J. Rothacker, K. G. Watson, A. W. Burgess and E. C. Nice, *Anal. Biochem.*, 2005, **342**, 292–299.
2 M. Arkin and M. M. Moasser, *Curr. Opin. Anti-Infect. Invest. Drugs*, 2008, **9**, 1264–1276.
3 M. M. Sadek, R. A. Serrya, A. H. N. Kafafy, M. Ahmed, F. Wang and K. A. M. Abouzid, *J. Enzyme Inhib. Med. Chem.*, 2014, **29**, 215–222.
4 J. N. Wilson, W. Liu, A. S. Brown and R. Landgraf, *Org. Biomol. Chem.*, 2015, **13**, 5006–5011.

5 A. Levitzki and A. Gazit, *Science*, 1995, **267**, 1782–1788.
6 T. J. Powell, H. Ben-Bassat, B. Y. Klein, H. Chen, N. Shenoy, J. McCollough, B. Narog, A. Gazit, Z. Harzstark, M. Chaouat, R. Levitzki, C. Tang, J. McMahon, L. Shawver and A. Levitzki, *Br. J. Dermatol.*, 1999, **141**, 802–810.
7 T. G. Johns, R. B. Luwor, C. Murone, F. Walker, J. Weinstock, A. A. Vitali, R. M. Perera, A. A. Jungbluth, E. Stockert, L. J. Old, E. C. Nice, A. W. Burgess and A. M. Scott, *Proc. Natl. Acad. Sci. U. S. A.*, 2003, **100**, 15871–15876.
8 H. R. Tsou, N. Mamuya, B. D. Johnson, M. F. Reich, B. C. Gruber, F. Ye, R. Nilakantan, R. Shen, C. Discafani, R. DeBlanc, R. Davis, F. E. Koehn, L. M. Greenberger, Y. F. Wang and A. Wissner, *J. Med. Chem.*, 2001, **44**, 2719–2734.
9 G. Partik, K. Hochegger, M. Schorkhuber and B. Marian, *J. Cancer Res. Clin. Oncol.*, 1999, **125**, 379–388.
10 A. Shushan, N. Rojansky, N. Laufer, B. Y. Klein, Z. Shlomai, R. Levitzki, Z. Hartzstark and H. Ben-Bassat, *Hum. Reprod.*, 2004, **19**, 1957–1967.
11 X. F. Zhu, Z. C. Liu, B. F. Xie, Z. M. Li, G. K. Feng, D. Yang and Y. X. Zeng, *Cancer Lett.*, 2001, **169**, 27–32.
12 W. Lei, J. E. Mayotte and M. L. Levitt, *Anticancer Res.*, 1999, **19**, 221–228.
13 M. Nagane, A. Levitzki, A. Gazit, W. K. Cavenee and H. J. Huang, *Proc. Natl. Acad. Sci. U. S. A.*, 1998, **95**, 5724–5729.
14 A. Gazit, J. Chen, H. App, G. McMahon, P. Hirth, I. Chen and A. Levitzki, *Bioorg. Med. Chem.*, 1996, **4**, 1203–1207.
15 M. Nagane, Y. Narita, K. Mishima, A. Levitzki, A. W. Burgess, W. K. Cavenee and H. J. Huang, *J. Neurosurg.*, 2001, **95**, 472–479.
16 F. T. Lee, A. J. Mountain, M. P. Kelly, C. Hall, A. Rigopoulos, T. G. Johns, F. E. Smyth, M. W. Brechbiel, E. C. Nice, A. W. Burgess and A. M. Scott, *Clin. Cancer Res.*, 2005, **11**, 7080s–7086s.
17 A. G. Ellis, M. M. Doherty, F. Walker, J. Weinstock, M. Nerrie, A. Vitali, R. Murphy, T. G. Johns, A. M. Scott, A. Levitzki, G. McLachlan, L. K. Webster, A. W. Burgess and E. C. Nice, *Biochem. Pharmacol.*, 2006, **71**, 1422–1434.
18 A. J. Bridges, *Curr. Med. Chem.*, 1999, **6**, 825–843.
19 Y. Liu and N. S. Gray, *Nat. Chem. Biol.*, 2006, **2**, 358–364.
20 M. Mohammadi, G. McMahon, L. Sun, C. Tang, P. Hirth, B. K. Yeh, S. R. Hubbard and J. Schlessinger, *Science*, 1997, **276**, 955–960.
21 M. Khattab, F. Wang and A. H. Clayton, *Spectrochim. Acta, Part A*, 2016, **164**, 128–132.
22 N. Mohammadi, P. J. Mahon and F. Wang, *J. Mol. Graphics Modell.*, 2013, **40**, 64–71.
23 N. Mohammadi and F. Wang, *J. Mol. Model.*, 2014, **20**, 2177–2185.
24 M. B. Santillan, F. Tomas-Vert, J. M. Aullo, E. A. Jauregui and G. M. Ciuffo, *Cell. Mol. Biol.*, 2003, **49**, 929–937.
25 K. Wichapong, A. Rohe, C. Platzer, I. Slynko, F. Erdmann, M. Schmidt and W. Sippl, *J. Chem. Inf. Model.*, 2014, **54**, 881–893.
26 A. D. Becke, *J. Chem. Phys.*, 1993, **98**, 5648–5652.
27 M. Cossi, N. Rega, G. Scalmani and V. Barone, *J. Comput. Chem.*, 2003, **24**, 669–681.
28 G. W. T. M. J. Frisch, H. B. Schlegel, G. E. Scuseria, M. A. Robb, J. R. Cheeseman, G. Scalmani, V. Barone, B. Mennucci, G. A. Petersson, H. Nakatsuji, M. Caricato, X. Li, H. P. Hratchian, A. F. Izmaylov, J. Bloino, G. Zheng, J. L. Sonnenberg, M. Hada, M. Ehara, K. Toyota, R. Fukuda, J. Hasegawa, M. Ishida, T. Nakajima, Y. Honda, O. Kitao, H. Nakai, T. Vreven, J. A. Montgomery, Jr., J. E. Peralta, F. Ogliaro, M. Bearpark, J. J. Heyd, E. Brothers, K. N. Kudin, V. N. Staroverov, R. Kobayashi, J. Normand, K. Raghavachari, A. Rendell, J. C. Burant, S. S. Iyengar, J. Tomasi, M. Cossi, N. Rega, J. M. Millam, M. Klene, J. E. Knox, J. B. Cross, V. Bakken, C. Adamo, J. Jaramillo, R. Gomperts, R. E. Stratmann, O. Yazyev, A. J. Austin, R. Cammi, C. Pomelli, J. W. Ochterski, R. L. Martin, K. Morokuma, V. G. Zakrzewski, G. A. Voth, P. Salvador, J. J. Dannenberg, S. Dapprich, A. D. Daniels, Ö. Farkas, J. B. Foresman, J. V. Ortiz, J. Cioslowski and D. J. Fox, *Revision C.01*, Gaussian, Inc., Wallingford CT, 2010.
29 F. Wang, M. T. Downton and N. Kidwani, *J. Theor. Comput. Chem.*, 2005, **4**, 247–264.
30 F. F. Chen and F. Wang, *Molecules*, 2009, **14**, 2656–2668.
31 J. R. Mulder, C. F. Guerra, J. C. Slootweg, K. Lammertsma and F. M. Bickelhaupt, *J. Comput. Chem.*, 2016, **37**, 304–313.
32 S. Islam and F. Wang, *RSC Adv.*, 2015, **5**, 11933–11941.
33 G. Chen, J. Damasco, H. Qiu, W. Shao, T. Y. Ohulchanskyy, R. R. Valiev, X. Wu, G. Han, Y. Wang, C. Yang, H. Agren and P. N. Prasad, *Nano Lett.*, 2015, **15**, 7400–7407.

Electronic Supplementary Material (ESI) for New Journal of Chemistry.

Supplementary Materials

Two Conformers of a Tyrosine Kinase Inhibitor (AG-1478) Disclosed Using Simulated UV-Vis Absorption Spectroscopy

Muhammad Khattab[a], Subhojyoti Chatterjee[b], Andrew H. A. Clayton[a*] and Feng Wang[b*]

[a]*Centre for Micro-Photonics, Faculty of Science, Engineering and Technology, Swinburne University of Technology, Melbourne, Victoria 3122, Australia*

[b]*Molecular Model Discovery Laboratory, Department of Chemistry and Biotechnology, School of Science, Faculty of Science, Engineering and Technology, Swinburne University of Technology, Melbourne, Victoria 3122, Australia*

*Corresponding author: fwang@swin.edu.au

aclayton@swin.edu.au

Table S1: Molecular parameters of AG-1478 obtained by geometry reoptimization using the B3LYP/6-311+G* model of the three local minimum structures of PES at 6-311G*

Parameters	AG-1478B	AG-1478A	Parameters	AG-1478B	AG-1478A
Bond length (Å)			**Bond angle (°)**		
$C_{(1)}$-$C_{(2)}$	1.3750	1.3748	$C_{(2)}$-$C_{(1)}$-$C_{(6)}$	119.64	119.83
$C_{(1)}$-$C_{(6)}$	1.4365	1.4402	$C_{(2)}$-$C_{(1)}$-$O_{(27)}$	125.31	125.23
$C_{(1)}$-$O_{(27)}$	1.3510	1.3498	$C_{(6)}$-$C_{(1)}$-$O_{(27)}$	115.04	114.93
$C_{(2)}$-$C_{(3)}$	1.4166	1.4176	$C_{(1)}$-$C_{(2)}$-$C_{(3)}$	121.16	120.95
$C_{(2)}$-$H_{(7)}$	1.0816	1.0815	$C_{(1)}$-$C_{(2)}$-$H_{(7)}$	121.96	122.02
$C_{(3)}$-$C_{(4)}$	1.4163	1.4216	$C_{(3)}$-$C_{(2)}$-$H_{(7)}$	116.88	117.02
$C_{(3)}$-$N_{(13)}$	1.3666	1.3627	$C_{(2)}$-$C_{(3)}$-$C_{(4)}$	119.38	119.21
$C_{(4)}$-$C_{(5)}$	1.4208	1.4209	$C_{(2)}$-$C_{(3)}$-$N_{(13)}$	118.26	118.51
$C_{(4)}$-$C_{(8)}$	1.4392	1.4269	$C_{(4)}$-$C_{(3)}$-$N_{(13)}$	122.36	122.25
$C_{(5)}$-$C_{(6)}$	1.3766	1.3743	$C_{(3)}$-$C_{(4)}$-$C_{(5)}$	118.96	119.23
$C_{(5)}$-$H_{(9)}$	1.0827	1.0795	$C_{(3)}$-$C_{(4)}$-$C_{(8)}$	115.34	115.18
$C_{(6)}$-$O_{(28)}$	1.3555	1.3536	$C_{(5)}$-$C_{(4)}$-$C_{(8)}$	125.71	125.54
$C_{(8)}$-$N_{(12)}$	1.3235	1.327	$C_{(4)}$-$C_{(5)}$-$C_{(6)}$	121.12	120.82
$C_{(8)}$-$N_{(25)}$	1.3764	1.3928	$C_{(4)}$-$C_{(5)}$-$H_{(9)}$	120.74	119.32
$C_{(10)}$-$H_{(11)}$	1.0870	1.0868	$C_{(6)}$-$C_{(5)}$-$H_{(9)}$	118.14	119.85
$C_{(10)}$-$N_{(12)}$	1.3505	1.3479	$C_{(1)}$-$C_{(6)}$-$C_{(5)}$	119.73	119.85
$C_{(10)}$-$N_{(13)}$	1.3101	1.3136	$C_{(1)}$-$C_{(6)}$-$O_{(28)}$	114.89	114.82
$C_{(14)}$-$C_{(15)}$	1.406	1.4023	$C_{(5)}$-$C_{(6)}$-$O_{(28)}$	125.38	125.32
$C_{(14)}$-$C_{(16)}$	1.4016	1.4005	$C_{(4)}$-$C_{(8)}$-$N_{(12)}$	121.30	121.57
$C_{(14)}$-$N_{(25)}$	1.4059	1.4118	$C_{(4)}$-$C_{(8)}$-$N_{(25)}$	119.13	123.66
$C_{(15)}$-$C_{(17)}$	1.3873	1.3896	$N_{(12)}$-$C_{(8)}$-$N_{(25)}$	119.57	114.59
$C_{(15)}$-$H_{(18)}$	1.0869	1.0852	$H_{(11)}$-$C_{(10)}$-$N_{(12)}$	115.17	115.51
$C_{(16)}$-$C_{(19)}$	1.3910	1.3904	$H_{(11)}$-$C_{(10)}$-$N_{(13)}$	116.99	117.08
$C_{(16)}$-$H_{(20)}$	1.0776	1.0818	$N_{(12)}$-$C_{(10)}$-$N_{(13)}$	127.84	127.4
$C_{(17)}$-$C_{(21)}$	1.3942	1.3945	$C_{(8)}$-$N_{(12)}$-$C_{(10)}$	117.43	117.42
$C_{(17)}$-$H_{(22)}$	1.0849	1.085	$C_{(3)}$-$N_{(13)}$-$C_{(10)}$	115.74	115.93
$C_{(19)}$-$C_{(21)}$	1.3894	1.3905	$C_{(15)}$-$C_{(14)}$-$C_{(16)}$	119.14	119.27
$C_{(19)}$-$Cl_{(24)}$	1.7611	1.7602	$C_{(15)}$-$C_{(14)}$-$N_{(25)}$	116.44	118.1
$C_{(21)}$-$H_{(23)}$	1.0827	1.0828	$C_{(16)}$-$C_{(14)}$-$N_{(25)}$	124.42	122.6
$N_{(25)}$-$H_{(26)}$	1.0061	1.0126	$C_{(14)}$-$C_{(15)}$-$C_{(17)}$	120.66	120.27
$O_{(27)}$-$C_{(33)}$	1.4231	1.4228	$C_{(14)}$-$C_{(15)}$-$H_{(18)}$	119.80	119.39
$O_{(28)}$-$C_{(29)}$	1.4185	1.4214	$C_{(17)}$-$C_{(15)}$-$H_{(18)}$	119.54	120.34
$C_{(29)}$-$H_{(30)}$	1.0881	1.0881	$C_{(14)}$-$C_{(16)}$-$C_{(19)}$	118.69	119.21
$C_{(29)}$-$H_{(31)}$	1.0954	1.0943	$C_{(14)}$-$C_{(16)}$-$H_{(20)}$	120.14	120.85
$C_{(29)}$-$H_{(32)}$	1.0954	1.0949	$C_{(19)}$-$C_{(16)}$-$H_{(20)}$	121.18	119.93
$C_{(33)}$-$H_{(34)}$	1.0879	1.0879	$C_{(15)}$-$C_{(17)}$-$C_{(21)}$	120.81	120.97
$C_{(33)}$-$H_{(35)}$	1.0941	1.0942	$C_{(15)}$-$C_{(17)}$-$H_{(22)}$	119.54	119.56
$C_{(33)}$-$H_{(36)}$	1.0941	1.0942	$C_{(21)}$-$C_{(17)}$-$H_{(22)}$	119.65	119.46
Bond angle (°)			**Dihedral angle (°)**		
$C_{(16)}$-$C_{(19)}$-$C_{(21)}$	122.86	122.15	$C_{(4)}$-$C_{(8)}$-$N_{(12)}$-$C_{(10)}$	0.00	-3.5
$C_{(16)}$-$C_{(19)}$-$Cl_{(24)}$	118.23	118.62	$N_{(25)}$-$C_{(8)}$-$N_{(12)}$-$C_{(10)}$	180.00	-178.93
$C_{(21)}$-$C_{(19)}$-$Cl_{(24)}$	118.91	119.22	$C_{(4)}$-$C_{(8)}$-$N_{(25)}$-$C_{(14)}$	-180.00	49.19
$C_{(17)}$-$C_{(21)}$-$C_{(19)}$	117.84	118.1	$C_{(4)}$-$C_{(8)}$-$N_{(25)}$-$H_{(26)}$	0.02	-163.46
$C_{(17)}$-$C_{(21)}$-$H_{(23)}$	121.40	121.34	$N_{(12)}$-$C_{(8)}$-$N_{(25)}$-$C_{(14)}$	0.00	-135.49
$C_{(19)}$-$C_{(21)}$-$H_{(23)}$	120.76	120.57	$N_{(12)}$-$C_{(8)}$-$N_{(25)}$-$H_{(26)}$	-179.97	11.86
$C_{(8)}$-$N_{(25)}$-$C_{(14)}$	131.92	128.12	$H_{(11)}$-$C_{(10)}$-$N_{(12)}$-$C_{(8)}$	180.00	179.72
$C_{(8)}$-$N_{(25)}$-$H_{(26)}$	114.94	110.24	$N_{(13)}$-$C_{(10)}$-$N_{(12)}$-$C_{(8)}$	0.00	-1.46
$C_{(14)}$-$N_{(25)}$-$H_{(26)}$	113.14	114.08	$H_{(11)}$-$C_{(10)}$-$N_{(13)}$-$C_{(3)}$	-180.00	-177.46
$C_{(1)}$-$O_{(27)}$-$C_{(33)}$	118.26	118.37	$N_{(12)}$-$C_{(10)}$-$N_{(13)}$-$C_{(3)}$	0.01	3.73
$C_{(6)}$-$O_{(28)}$-$C_{(29)}$	118.66	118.38	$C_{(16)}$-$C_{(14)}$-$C_{(15)}$-$C_{(17)}$	-0.01	-0.14
$O_{(28)}$-$C_{(29)}$-$H_{(30)}$	105.76	105.65	$C_{(16)}$-$C_{(14)}$-$C_{(15)}$-$H_{(18)}$	179.99	-179.61
$O_{(28)}$-$C_{(29)}$-$H_{(31)}$	111.36	111.27	$N_{(25)}$-$C_{(14)}$-$C_{(15)}$-$C_{(17)}$	179.99	-178.25
$O_{(28)}$-$C_{(29)}$-$H_{(32)}$	111.36	111.27	$N_{(25)}$-$C_{(14)}$-$C_{(15)}$-$H_{(18)}$	-0.02	2.28
$H_{(30)}$-$C_{(29)}$-$H_{(31)}$	109.29	109.54	$C_{(15)}$-$C_{(14)}$-$C_{(16)}$-$C_{(19)}$	0.00	1.34

Dihedral angle (°)

$H_{(30)}$-$C_{(29)}$-$H_{(32)}$	109.29	109.42	$C_{(15)}$-$C_{(14)}$-$C_{(16)}$-$H_{(20)}$	-179.99	-177.95
$H_{(31)}$-$C_{(29)}$-$H_{(32)}$	109.68	109.6	$N_{(25)}$-$C_{(14)}$-$C_{(16)}$-$C_{(19)}$	-179.99	179.36
$O_{(27)}$-$C_{(33)}$-$H_{(34)}$	105.63	105.63	$N_{(25)}$-$C_{(14)}$-$C_{(16)}$-$H_{(20)}$	0.02	0.07
$O_{(27)}$-$C_{(33)}$-$H_{(35)}$	111.17	111.19	$C_{(15)}$-$C_{(14)}$-$N_{(25)}$-$C_{(8)}$	179.94	-167.44
$O_{(27)}$-$C_{(33)}$-$H_{(36)}$	111.17	111.17	$C_{(15)}$-$C_{(14)}$-$N_{(25)}$-$H_{(26)}$	-0.08	46.23
$H_{(34)}$-$C_{(33)}$-$H_{(35)}$	109.60	109.57	$C_{(16)}$-$C_{(14)}$-$N_{(25)}$-$C_{(8)}$	-0.07	14.52
$H_{(34)}$-$C_{(33)}$-$H_{(36)}$	109.60	109.6	$C_{(16)}$-$C_{(14)}$-$N_{(25)}$-$H_{(26)}$	179.91	-131.82
$H_{(35)}$-$C_{(33)}$-$H_{(36)}$	109.59	109.59	$C_{(14)}$-$C_{(15)}$-$C_{(17)}$-$C_{(21)}$	0.00	-1.05
$C_{(6)}$-$C_{(1)}$-$C_{(2)}$-$C_{(3)}$	0.00	0.68	$C_{(14)}$-$C_{(15)}$-$C_{(17)}$-$H_{(22)}$	-180.00	179.8
$C_{(6)}$-$C_{(1)}$-$C_{(2)}$-$H_{(7)}$	-180.00	-178.04	$H_{(18)}$-$C_{(15)}$-$C_{(17)}$-$C_{(21)}$	-179.99	178.41
$O_{(27)}$-$C_{(1)}$-$C_{(2)}$-$C_{(3)}$	180.00	179.77	$H_{(18)}$-$C_{(15)}$-$C_{(17)}$-$H_{(22)}$	0.00	-0.74
$O_{(27)}$-$C_{(1)}$-$C_{(2)}$-$C_{(7)}$	0.00	1.04	$C_{(14)}$-$C_{(16)}$-$C_{(19)}$-$C_{(21)}$	0.00	-1.4
$C_{(2)}$-$C_{(1)}$-$C_{(6)}$-$C_{(5)}$	0.00	-1.72	$C_{(14)}$-$C_{(16)}$-$C_{(19)}$-$Cl_{(24)}$	180.00	179.44
$C_{(2)}$-$C_{(1)}$-$C_{(6)}$-$O_{(28)}$	180.00	178.03	$H_{(20)}$-$C_{(16)}$-$C_{(19)}$-$C_{(21)}$	179.99	177.89
$O_{(27)}$-$C_{(1)}$-$C_{(6)}$-$C_{(5)}$	-180.00	179.1	$H_{(20)}$-$C_{(16)}$-$C_{(19)}$-$Cl_{(24)}$	-0.01	-1.26
$O_{(27)}$-$C_{(1)}$-$C_{(6)}$-$O_{(28)}$	0.00	-1.15	$C_{(15)}$-$C_{(17)}$-$C_{(21)}$-$C_{(19)}$	0.00	1.01
$C_{(2)}$-$C_{(1)}$-$O_{(27)}$-$C_{(33)}$	0.01	0.79	$C_{(15)}$-$C_{(17)}$-$C_{(21)}$-$H_{(23)}$	180.00	-179.16
$C_{(6)}$-$C_{(1)}$-$O_{(27)}$-$C_{(33)}$	-179.99	179.91	$H_{(22)}$-$C_{(17)}$-$C_{(21)}$-$C_{(19)}$	-180.00	-179.84
$C_{(1)}$-$C_{(2)}$-$C_{(3)}$-$C_{(4)}$	0.00	2	$H_{(22)}$-$C_{(17)}$-$C_{(21)}$-$H_{(23)}$	0.00	-0.01
$C_{(1)}$-$C_{(2)}$-$C_{(3)}$-$N_{(13)}$	-179.99	-176.02	$C_{(16)}$-$C_{(19)}$-$C_{(21)}$-$C_{(17)}$	0.00	0.23
$H_{(7)}$-$C_{(2)}$-$C_{(3)}$-$C_{(4)}$	-180.00	-179.22	$C_{(16)}$-$C_{(19)}$-$C_{(21)}$-$H_{(23)}$	180.00	-179.6
$H_{(7)}$-$C_{(2)}$-$C_{(3)}$-$N_{(13)}$	0.00	2.77	$Cl_{(24)}$-$C_{(19)}$-$C_{(21)}$-$C_{(17)}$	180.00	179.38
$C_{(2)}$-$C_{(3)}$-$C_{(4)}$-$C_{(5)}$	-0.01	-3.63	$Cl_{(24)}$-$C_{(19)}$-$C_{(21)}$-$H_{(23)}$	0.00	-0.45
$C_{(2)}$-$C_{(3)}$-$C_{(4)}$-$C_{(8)}$	180.00	178.89	$C_{(1)}$-$O_{(27)}$-$C_{(33)}$-$H_{(34)}$	179.99	179.39
$N_{(13)}$-$C_{(3)}$-$C_{(4)}$-$C_{(5)}$	179.99	174.3	$C_{(1)}$-$O_{(27)}$-$C_{(33)}$-$H_{(35)}$	-61.20	-61.83
$N_{(13)}$-$C_{(3)}$-$C_{(4)}$-$C_{(8)}$	0.00	-3.18	$C_{(1)}$-$O_{(27)}$-$C_{(33)}$-$H_{(36)}$	61.18	60.57
$C_{(2)}$-$C_{(3)}$-$N_{(13)}$-$C_{(10)}$	180.00	176.84	$C_{(6)}$-$O_{(28)}$-$C_{(29)}$-$H_{(30)}$	-179.99	-178.94
$C_{(4)}$-$C_{(3)}$-$N_{(13)}$-$C_{(10)}$	0.00	-1.11	$C_{(6)}$-$O_{(28)}$-$C_{(29)}$-$H_{(31)}$	-61.37	-60.14
$C_{(3)}$-$C_{(4)}$-$C_{(5)}$-$C_{(6)}$	0.00	2.64	$C_{(6)}$-$O_{(28)}$-$C_{(29)}$-$H_{(32)}$	61.39	62.4
$C_{(3)}$-$C_{(4)}$-$C_{(5)}$-$H_{(9)}$	-179.99	-176.65			
$C_{(8)}$-$C_{(4)}$-$C_{(5)}$-$C_{(6)}$	-180.00	179.84	**$\langle R^2 \rangle$ (a.u.)**	10395.1155	7611.6811
$C_{(8)}$-$C_{(4)}$-$C_{(5)}$-$H_{(9)}$	0.01	0.55	**μ (D)**	5.8297	3.0792
$C_{(3)}$-$C_{(4)}$-$C_{(8)}$-$N_{(12)}$	0.01	5.56	**E_h (a.u.)**	-1393.2768	-1393.2744
$C_{(3)}$-$C_{(4)}$-$C_{(8)}$-$N_{(25)}$	-179.99	-179.43	**ZPE (kcal.mol^{-1})**	173.5149	173.5958
$C_{(5)}$-$C_{(4)}$-$C_{(8)}$-$N_{(12)}$	-179.99	-171.74	**E_h + ZPE (a.u.)**	-1393.0003	-1392.9978
$C_{(5)}$-$C_{(4)}$-$C_{(8)}$-$N_{(25)}$	0.01	3.27	**HOMO-LUMO gap (eV)**	4.25	4.26
$C_{(4)}$-$C_{(5)}$-$C_{(6)}$-$C_{(1)}$	0.00	0.03	**Rot. Const. (GHz) A**	0.5882	0.3470
$C_{(4)}$-$C_{(5)}$-$C_{(6)}$-$O_{(28)}$	180.00	-179.69	**B**	0.1126	0.1855
$H_{(9)}$-$C_{(5)}$-$C_{(6)}$-$C_{(1)}$	179.99	179.31	**C**	0.0946	0.1447
$H_{(9)}$-$C_{(5)}$-$C_{(6)}$-$O_{(28)}$	-0.01	-0.41			
$C_{(1)}$-$C_{(6)}$-$O_{(28)}$-$C_{(29)}$	180.00	179.08			
$C_{(5)}$-$C_{(6)}$-$O_{(28)}$-$C_{(29)}$	0.00	-1.18			

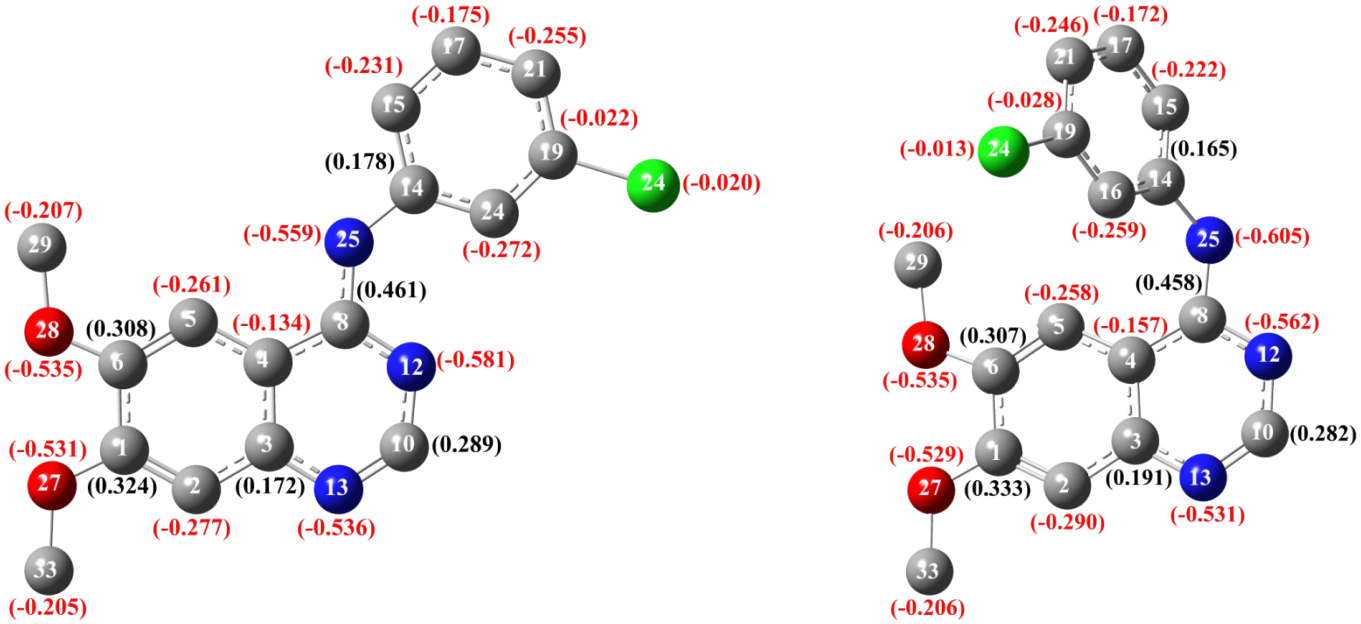

Figure S1: Atomic charge analysis of heavy atoms of AG-1478**B** and AG-1478**A** using Natural Bond Order (NBO) analysis at the B3LYP/6-311+G* level of theory.

Chapter IV

Microhydration of AG1478

Local environment and conformation of AG1478 are not the only determinant of drug-protein binding interaction. Most human proteins, if not all, contains clustered water molecules. The confined water molecules create dipolar field acting as a solvent for the drug at protein binding site [91]. In addition, water molecule can act as H-bond donor or acceptor which can impart extra stability to either the ground state or excited state of a fluorophore. Therefore water molecules at the vicinity of AG1478 were expected to alter AG1478 conformation and electronic configuration. Hence I was motivated to explore the microsolvation of AG1478 by waters contained in a moderately polar environment. In this study, AG1478 molecules in their free form are proposed to form H-bonds with water molecules. However the existence of AG1478 aggregates could be possible.

The binary mixture (acetonitrile/water) approach was employed to investigate the H-bonding interactions and conformational changes of AG1478. Analysis of fluorescence quenching using a binding model disclosed three potential sites for forming H-bonds between AG1478 and water molecules. The theoretical results were consistent with the experimental results and revealed that AG1478 might exist in equilibrium of planar and twisted structures bound to a varying numbers (3–5) of water molecules. All of the AG1478-nH_2O complexes, identified from calculations, exhibited absorption energies within the experimentally observed values (330-360 nm). In contrast to the isolated AG1478, the hydrated twisted complexes were predicted to be more energetically favoured than their planar counterparts. In this regard, AG1478 can serve as a microsolvation probe and lay the ground work for future studies of AG1478 in more complex environments such as proteins.

This chapter is presented in the form of the published paper, **Muhammad Khattab**, Feng Wang and Andrew H.A. Clayton, *Micro-Solvation of Tyrosine-Kinase Inhibitor AG1478 Explored with Fluorescence Spectroscopy and Computational Chemistry*, RSC Adv. 7 (2017), 31725-35.

RSC Advances

PAPER

View Article Online
View Journal | View Issue

Cite this: *RSC Adv.*, 2017, **7**, 31725

Micro-solvation of tyrosine-kinase inhibitor AG1478 explored with fluorescence spectroscopy and computational chemistry†

Muhammad Khattab,[a] Feng Wang*[b] and Andrew H. A. Clayton*[a]

Tyrosine kinase inhibitors (TKI) are an important class of molecules. Specific interactions of TKI with water are of interest since they appear in high resolution X-ray structures of TKI–protein complexes and are thought to be important determinants of drug efficacy. Methods for determining the specific interactions of TKI with water molecules in solution are therefore highly desirable. Recently, we revealed that the TKI, AG1478, exhibits absorbance and fluorescence spectra which are sensitive to the conformation of the molecule and the polarity of the surrounding environment. In the present work, we investigated the potential hydrogen bond binding sites of AG1478 using spectroscopic measurements of acetonitrile–water solutions. UV-Vis absorbance spectroscopy of AG1478 revealed H-bond interactions between water molecules and AG1478 in the ground state, as evidenced by changes in spectral shape and optical density with increases in water fraction. The fluorescence spectra of AG1478 in acetonitrile were also greatly influenced by water interactions, revealing fluorescence quenching (by 80%) with the addition of 2% by volume of water. The AG1478 fluorescence quantum yield decreased with increasing temperature in neat acetonitrile but revealed an unorthodox increase with increasing temperature in acetonitrile–water solution. Taken together, these changes are consistent with a specific complex or complexes formed between AG1478 and water molecules. Potential AG1478–water clusters were investigated using *ab initio* calculations. The effects of explicit hydrogen bonding on vertical excitation, topology and electronic configuration of AG1478 were examined computationally.

Received 20th April 2017
Accepted 13th June 2017

DOI: 10.1039/c7ra04435f

rsc.li/rsc-advances

1. Introduction

Several theories and models have been developed to describe the complex process of solvation of solutes in binary mixtures.[1–4] Solutes can be preferentially solvated by either solvent, nevertheless the solvent–solvent interactions can significantly influence solute–solvent interactions (solvatochromic parameters).[5] Preferential solvation occurs when a solute molecule has, at its vicinity, more of one solvent than in the bulk environment. Hence the understanding of this phenomenon plays a role in unravelling the spectroscopic, kinetic and thermodynamic behaviour of solute molecules.[6] Binary mixtures containing water as a cosolvent have been successfully deployed to quantify the number of H-bonding interactions between solute and water molecules. This is accomplished by application of various spectroscopic experiments and/or theoretical calculations using explicit water models.[7–11] Hence the organic solvents which are miscible with water are ultimately used for these kind of experiments.

Acetonitrile is characterized by good UV transparency, aqueous miscibility, low viscosity and low chemical reactivity. In addition, it has a relatively high dielectric constant and a small autoprotolysis constant.[5] Water can solubilize ionic and dipolar solutes and its colligative properties have a large bearing on vast number of biological and chemical systems through its ability to form intermolecular hydrogen bonds.[12,13] It has been reported that the structure of pure water is significantly altered upon mixing with other solvents generally and with acetonitrile specifically.[13–17] Therefore, binary mixtures of acetonitrile with water are solvents of choice in physical organic chemistry.[5,13] A number of studies have attempted to address the impact of microhydration on the geometrical and electronic properties of solute molecules by dissolving them in acetonitrile–water solutions.

For instance, the excited state H-bond dynamics of coumarin 102 were investigated in acetonitrile–water binary mixtures by Wells *et al.*[7] The experimental and simulation data revealed that two water molecules, acting as H-bond donors, can form H-bonds at the carbonyl site of coumarin 102.[7] This finding gave

[a]*Centre for Micro-Photonics, Faculty of Science, Engineering and Technology, Swinburne University of Technology, Melbourne, Victoria 3122, Australia. E-mail: aclayton@swin.edu.au*

[b]*Molecular Model Discovery Laboratory, Department of Chemistry and Biotechnology, School of Science, Faculty of Science, Engineering and Technology, Swinburne University of Technology, Melbourne, Victoria 3122, Australia. E-mail: fwang@swin.edu.au*

† Electronic supplementary information (ESI) available. See DOI: 10.1039/c7ra04435f

a more robust clue for estimating hydrogen bond strength of C 102 molecule. It was found that clustered water molecules can also turn on the bright emission of a molecule and the lifetime of the excited state was dependent on the number of water molecules in first solvation shell. Studies conducted on the adenine analogue, 2-aminopurine, have also led to similar conclusions.[18,19] Studies of Lobsiger and co-workers showed that the lifetime of 2-aminopurine increased systematically with the number of water molecules. They also found out that position of bound water molecules was important. The excited-state lifetime was much longer when one water molecule interacted with the NH_2 group of 2-aminopurine.[18]

In general, spectroscopic measurements of drugs in aqueous–organic binary mixtures provide a controllable model system to investigate the interaction of water molecules with drugs. Water molecules are highly translocated at protein binding sites and found essential for drug–protein intermolecular interactions and stability. Therefore, binding interactions between explicit water molecules and drugs affects the nature and diversity of drug chemical structures and properties. Mastering the gain in protein–drug binding affinity can be achieved by targeting or neglecting H-bonding with clustered waters.[20]

AG1478 is a tyrosine kinase inhibitor,[21–23] synthesized to mimic the purine ring of adenosine triphosphate (ATP) cofactor.[24] It possesses five H-acceptor moieties and one H-donor group, acting as a potential H-bonding target. Given that it can bind to the protein hinge region of tyrosine kinases through one to three H-bonds,[25] it is therefore important to explore the impacts of H-bonding statics and dynamics on the electronic and geometric properties of this TKI.

Our earlier experimental[26] and computational[27] studies showed that the absorbance of AG1478 was sensitive to the molecular conformation (twisted *versus* planar), while the fluorescence was influenced by the polarity and hydrogen-bonding power of the solvent.[26] We have also observed extensive fluorescence quenching of aqueous AG1478 solution compared to other non-aqueous AG1478 solutions.[26] In the last few decades, spectroscopic studies have been performed on probes in different media such as binary solvent mixtures, micelles, reverse micelles and ionic liquids.[28–31] When studies in pure water are not feasible, solvent–water binary mixtures provide a controllable environment in which to probe the influence of water against a moderately polar host solvent.[32,33] Therefore, we used the binary mixture approach to investigate the intrinsic and extrinsic H-bonding interactions of AG1478 in the ground and excited states.

In this article, the steady-state UV-Vis spectroscopy of AG1478 in acetonitrile solution containing water as a co-solvent, was investigated to reveal the spectral properties of AG1478 in the presence of water molecules. We also performed temperature-dependent fluorescence experiments to delineate the influence of dynamic *versus* static quenching between AG1478 and water molecules. In addition, time-dependant density functional theory (TD-DFT) was utilized to examine possible complexes of AG1478 with different numbers of water molecules.

2. Experimental

2.1. Materials

Spectroscopic grade acetonitrile was purchased from Thermo Fisher Scientific Inc. and was used without further purification. Deionized water (Millipore) was used to prepare the aqueous solutions. Tyrphostin AG1478 was purchased from Sapphire Bioscience Pty Ltd and used as received. A matched pair of quartz cuvettes with a path length of 1 cm was obtained from Starna Pty Ltd.

2.2. Methods

2.2.1. UV-vis spectroscopy. The absorption spectra of AG1478 were scanned using a Shimadzu Recording Spectrophotometer UV-1601. Excitation and emission measurements were performed with a Perkin Elmer LS55 Fluorescence Spectrometer. The temperature (25–70 °C) was regulated using Perkin Elmer Peltier Temperature Programmer PTP-1. The background absorbance, scatter and fluorescence were corrected using blank samples.

Solutions containing acetonitrile and water were prepared by adding a small volume of water to acetonitrile (in the range 0–16% v/v). Dilute solutions of AG1478 were prepared for spectroscopic measurements (AG1478 concentration was 10^{-5} M (absorbance) and 10^{-6} M (fluorescence)). The optical density of 300–360 nm band was adjusted to be above 0.1 for absorption experiments and was lower than 0.05 for excitation and emission measurements to minimize inner filter effect. All spectra are averages of nine scans.

2.2.2. Computational details. The geometries of ground and excited state structures were optimized by DFT and TD-DFT calculations, respectively, at the B3LYP/6-311+G* level of theory. No imaginary frequencies at the optimized structures were obtained, indicating that the corresponding geometries are true local minima. The Becke's three-parameter hybrid exchange-correlation functional (B3LYP)[34,35] with 6-311+G* basis set was employed in all calculations. Implicit solvent effect was considered in our calculations. Hence, the conductor-like polarizable continuum model (CPCM)[36] with the dielectric constant of $\varepsilon = 37$ was used (which is assumed to be the dielectric constant of acetonitrile water mixture). All calculations were performed using GAUSSIAN 09 Revision C.01 (ref. 37) on Swinburne supercomputing facilities.

First, we screened for the best possible position(s) (giving most stable complex) for binding of $n = 1$–7 water molecules to AG1478. That means an explicit water molecule(s) was included at proximity (1.7 Å) to different H-bond acceptor sites of AG1478. Secondly, we determined the most stable geometry for each complex and performed single point energy calculations in dielectric continuum with the dielectric constant of 37 using the CPCM model. We also computed the corresponding vertical excitation energy including state-specific solvation correction. Hereafter, the planar structure complexed with water molecules were referred as P-*n*w, where $n = 1$–7, and the twisted rotamer exhibiting intermolecular H-bond with water molecules were referred as T-*n*w, where $n = 1$–7. Full geometric coordinates, structural properties and energies are contained in the ESI Tables S1–S5 and Fig. S1–S4.†

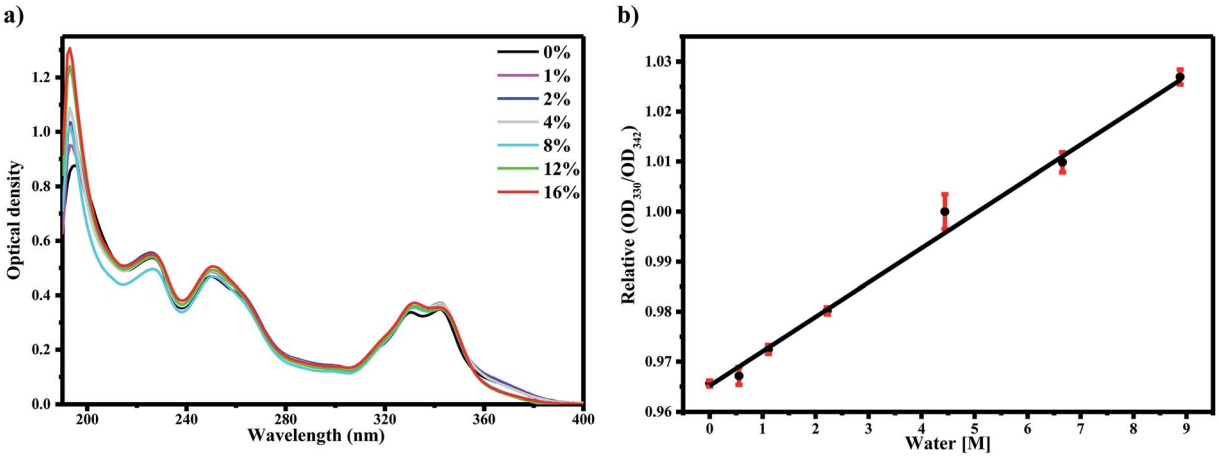

Fig. 1 Graphs of (a) absorption spectra of AG1478 (10 μM) in acetonitrile–water solutions. Legend in (a) indicates % v(water)/v(acetonitrile) of added water and (b) relative optical density of two characteristic absorption peaks as a function of water concentration. The red vertical lines indicates error bars.

3. Results and discussion

3.1. Impact of water H-bonding on AG1478 ground state

Our previous work assigned the UV-Vis absorption bands of AG1478 to transitions from their respective ground electronic states of the conformers (planar and twisted) to their electronic excited states, respectively, that is, the HOMO–LUMO of a conformer.[27] To study the impact of water on these transitions, we examined the absorption spectra of AG1478 in acetonitrile as a function of added water. As shown before,[27] the absorption spectrum of AG1478 in neat acetonitrile solution (no added water) was comprised of four major bands as shown in Fig. 1a. The lowest energy bands at 342 nm and 330 nm are assigned to S_0 to S_1 transitions in the twisted and planar conformation, respectively.[27] Consecutive addition of water (up to 0–16% v/v) to acetonitrile solution of AG1478 resulted in very small perturbations to the AG1478 absorption spectra (Fig. 1a): no significant effects on the absorption spectra but small attenuation in the regions of $\lambda < 240$ nm and near 370 nm. We stress that while these changes to the absorption spectra are very small in magnitude, and therefore should not be over-interpreted, they do provide evidence for interaction of the AG1478 with water in the ground state.

In particular we note the progressive linear increase of optical density of the 330 nm band relative to that of 342 nm peak (Fig. 1b ($R^2 = 0.99$)). We propose that the planar and twisted conformations interact with water differently (the planar conformation has an intramolecular hydrogen bond which become available to the solvent in the twisted conformation). As we will see in the next section, the fluorescence properties of AG1478 are more sensitive to water interaction.

3.2. Impact of water H-bonding on AG1478 excited state

To determine the effect of water on the AG1478 excited-state, we measured the fluorescence excitation and emission spectra of AG1478 in acetonitrile as a function of added water. The

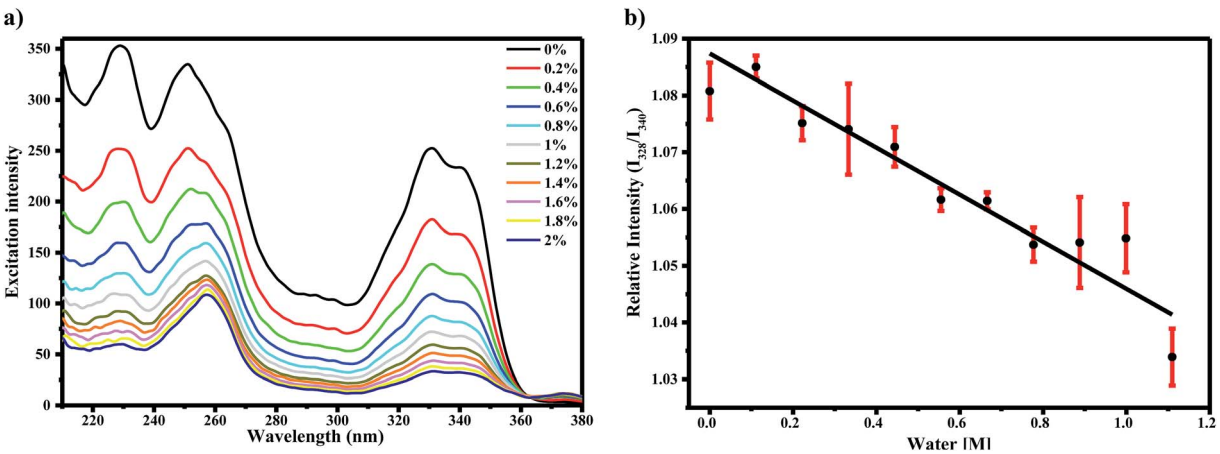

Fig. 2 (a) Excitation spectra of 1 μM AG1478 in acetonitrile/water binary solutions monitored at $\lambda_{em} = 400$ nm. Legend indicates water concentration in % v(water)/v(acetonitrile). (b) Correlation plot between relative excitation intensities of AG1478 in acetonitrile/water mixtures and molar concentration of added water. The red vertical lines indicates error bars.

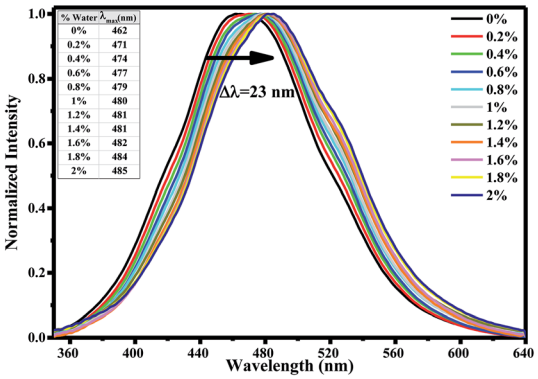

Fig. 3 Normalized emission spectra of 1 μM AG1478 in acetonitrile/water binary solutions (excitation at λ_{exc} = 330 nm). Inset shows emission maximum values and arrow indicates the red shift with increasing water percentage.

fluorescence excitation spectra of 1 μM AG1478 after subsequent addition of 2% v/v of water to acetonitrile solution revealed a noticeable attenuation of fluorescence (by 87–83%) across the range 220–350 nm as shown in Fig. 2a and the augmentation of a new band near 370 nm. The shape of the fluorescence excitation spectra was also perturbed by addition of water resulting in changes to the relative amplitudes (but not positions) of the 328 nm and 340 nm bands. Analyses showed a good (R^2 = 0.91) linear correlation between the relative intensity of 328 nm and 340 nm bands and water concentration as shown in Fig. 2b. The change in the ratio of amplitudes suggests that either the population of the planar form or the quantum yield of the planar form or both was diminished by addition of water *relative* to the twisted form of the molecule. Nevertheless, the changes in the ratio of the two bands are of the order of a few percent, in contrast to the much larger change in the amplitudes of the two bands.

In order to explore water interactions with AG1478 in the excited state, we also measured the fluorescence spectra at λ_{exc} = 330 nm of 1 μM AG1478 in binary mixtures of acetonitrile/water. By adding consecutive fractions of water in the range 0–2% v/v to the acetonitrile solution with increment of 0.2%, we observed a red shift of the emission peak and a decrease in the fluorescence quantum yield as shown in Fig. 3. A red shift of 8.5 nm was observed after addition of 0.2% v/v of water with a total bathochromic shift of 23 nm with 2% v/v of water; data are compiled in inset of Fig. 3.

The decrease in fluorescence quantum yield with increasing water concentration is shown in Fig. 4a. Again, with 2% v/v of water, the quantum yield decreased by 80%. Based on the dielectric constants of acetonitrile (ε = 36) and water (ε = 78), a 2% v/v water–acetonitrile solution would have an average dielectric constant of 37. An increase in dielectric constant from 36 to 37 cannot solely account for the changes in spectra observed. Taken together, the magnitudes of the bathochromic shifts and fluorescence quenching with water addition which are larger than expected based on bulk solvent properties alone, therefore it can be concluded that the changes in fluorescence are due to specific interactions of AG1478 with the water in the acetonitrile–water solution.

Preferential solvation studies, in which fluorophore molecules are explicitly solvated by water molecules in aqueous–organic medium, have been reported.[39–42] For instance, the tautomerism of alloxazine to isoalloxazine was triggered by water-facilitated intramolecular proton transfer owing to specific interactions between alloxazine and water molecules.[39] Acetonitrile–water mixtures covering the entire range of 0.1–90% v/v of water were used. It was found that lower water compositions upto 0.1–20% v/v can facilitate this process where water molecules were favourably bound with fluorophore through H-bonding (microsolvation). The detailed study revealed that the interaction was most likely to take place in the excited state. Beyond this concentration, the intrinsic H-bonding of water molecules would be strongly favoured forming large clusters with extensive water networks. Hence, fluorophore–water interactions is weakened in water rich media.[39]

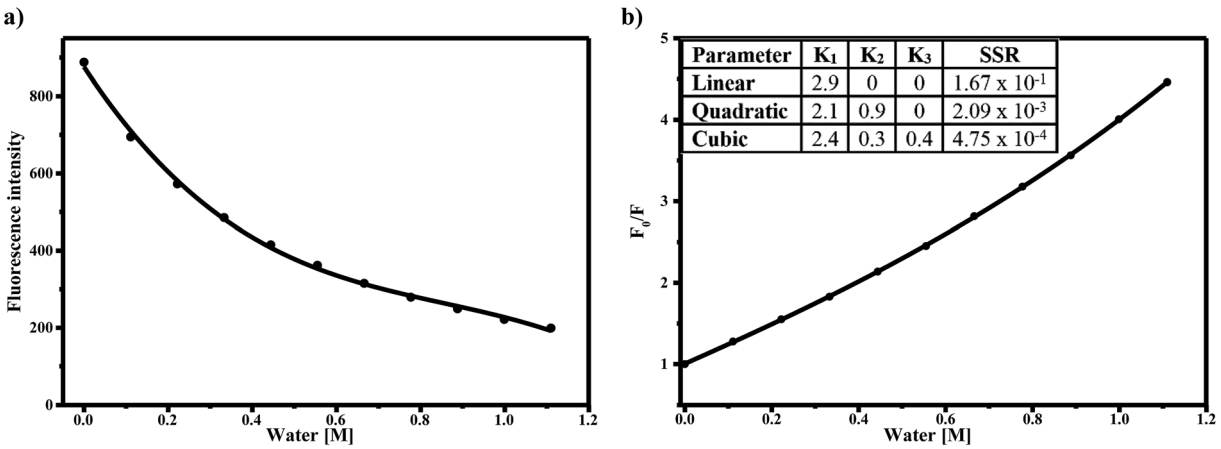

Fig. 4 (a) Intensity of emission maxima of AG1478 as a function of water added to acetonitrile solution. (b) Stern–Volmer plot of the fluorescence quenching of AG1478 in acetonitrile due to presence of increasing amounts of water. F_0/F is the emission intensity ratio of AG1478 in absence and presence of water, respectively.* See residual plot for each functional fitting in Fig. S5 in ESI.†

Barbosa *et al.* studied five standard buffers in acetonitrile–water binary mixtures.[43] It was found that the proton (solute) was preferentially solvated by water molecules evidenced by lower pH(s) than expected if hydrogen ion was solvated by acetonitrile molecules.[43] On the contrary, studies done by Wakisaka and coworkers found that phenol was preferentially solvated by water at higher mole fraction of water ≥ 0.85.[42] Preferential solvation of acetate ions was triggered by water in mixed solvents of water and acetonitrile as reported by Barbosa *et al.*[41] It was concluded that water molecules had a greater tendency to be in vicinity of acetate ions than to acetonitrile molecules reaching its maximum at water mole fraction of 0.20–0.25.[41] All these studies support our suggestion that the change in absorption and emission spectra of AG1478 upon adding minute amount of water to medium was due to preferential microsolvation of AG1478 by water molecule.

The strong decrease in fluorescence excitation and emission with added water suggests that water might be thought of as an efficient quencher of AG1478 fluorescence. Therefore, one way to understand the interaction between AG1478 and water was to quantify the water-induced fluorescence quenching by employing the Stern–Volmer equation[44]

$$\frac{F_0}{F} = 1 + K_{SV}[Q] \quad (1)$$

where F_0 and F are the fluorescence intensities in the absence and presence of quencher, K_{SV} is the quenching constant, and [Q] is the molar concentration of quencher.

A linear Stern–Volmer plot indicates the involvement of only one kind of quenching mechanism, either static or dynamic. However the deviation from linearity reveals the contribution of two mechanisms to quenching process.[45,46] The Stern–Volmer plot for AG1478 fluorescence quenching as a function of water concentration (in acetonitrile) is depicted in Fig. 4b. Of particular note is that the Stern–Volmer plot revealed departures from linearity, as revealed by poor fits to a linear function. This implies either a combination of dynamic and static quenching or possibly a complex binding process. The distinction between static/binding processes and dynamic quenching cannot be decided from the Stern–Volmer plot alone. However, measurements of fluorescence as a function of temperature can sometimes be used to distinguish between these two classes of quenching.

3.3. Temperature effect on AG1478 emission

Static and dynamic quenching mechanisms have been reportedly investigated utilizing their varying dependence on temperature, measurement of excited state lifetime or transient absorption spectrum in the presence of quencher.[47,48] To distinguish between dynamic and static/binding mechanisms of water-induced AG1478 fluorescence quenching, measurements of fluorescence as a function of temperature were carried out. Temperature-dependant emission spectra ($\lambda_{exc} = 330$ nm) were recorded in the temperature range of 25–70 °C for AG1478 in acetonitrile/water solution, as shown in Fig. 5a. A remarkable increase in AG1478 fluorescence quantum yield, in addition to a blue shift, was observed upon increasing solution temperature. A plot of fluorescence intensity as a function of varying temperature is depicted in Fig. 5b showing unorthodox behaviour.

In the context of fluorescence quenching models, an increase in fluorescence intensity with temperature is consistent with a static quenching/binding model for the AG1478–water interaction in acetonitrile–water solution. We interpret the increase in fluorescence with increasing temperature as due to a temperature-induced dissociation of water from the local vicinity of the AG1478, or alternatively a temperature induced rearrangement of the first solvation shell. In contrast, AG1478 fluorescence in neat acetonitrile (Fig. 5c and d), revealed a decrease with increasing temperature, as expected, owing to the normal increase in temperature-dependent non-radiative deactivation pathways.

Studies of Ghosh *et al.* on binding interaction between chloramphenicol (Clp) and β-lactoglobulin (βLG) disclosed fluorescence quenching of βLG with increasing concentration of Clp and the Stern–Volmer plot exhibited also an upward curvature.[49] The non-linear SV plot may arise due to either (1) simultaneous static–dynamic quenching process and/or (2) high extent of quenching (only static) at higher quencher concentration.[45,48] The lifetime measurements excluded the occurrence of dynamic quenching due to undeviating measurements upon increasing quencher concentration. Therefore it was concluded that Clp quenched the target protein fluorescence due to high extent of static quenching.

Generally, the quenching efficiency should decrease with increasing temperature owing to destabilization of fluorophore–quencher complex at ground state.[48] However an increase in the Clp–βLG binding constant with increasing temperature was observed. The rationale for this anomaly was revealed by Arrhenius plot.[50,51] Where it was concluded that the increase in binding (quenching) rate constant overweigh its decrease due to instability of complex with increasing temperature.[49] At first glance, this seems contradictory with our experiments, due to lack of time-resolved equipment and data, however it is line with our measurements and predictions. Taken into account, we have observed fluorescence quenching of AG1478 in neat solution of acetonitrile which contains traces of water (*viz.* micromolar concentration) while enhancement of emission intensity was noticed in acetonitrile/water (1% v/v = 0.55 M) solution. Given that the concentration of AG1478 was within micromolar range (1 μM), the AG1478 quenching would be due to solely static mechanism exerted by high concentration of the water quencher ($\simeq 10^6$ fold abundance). However in our case, the effect of instability of AG1478–water complex is expected to overweigh the fluorophore–quencher binding constant.

3.4. Estimation of the number of water molecules coordinated to AG1478

Because the AG1478 fluorescence quenching due to water appears to be of a static-type rather than a dynamic-type we can reinterpret the quenching in the context of a water binding model. To estimate the number of water molecules in complex

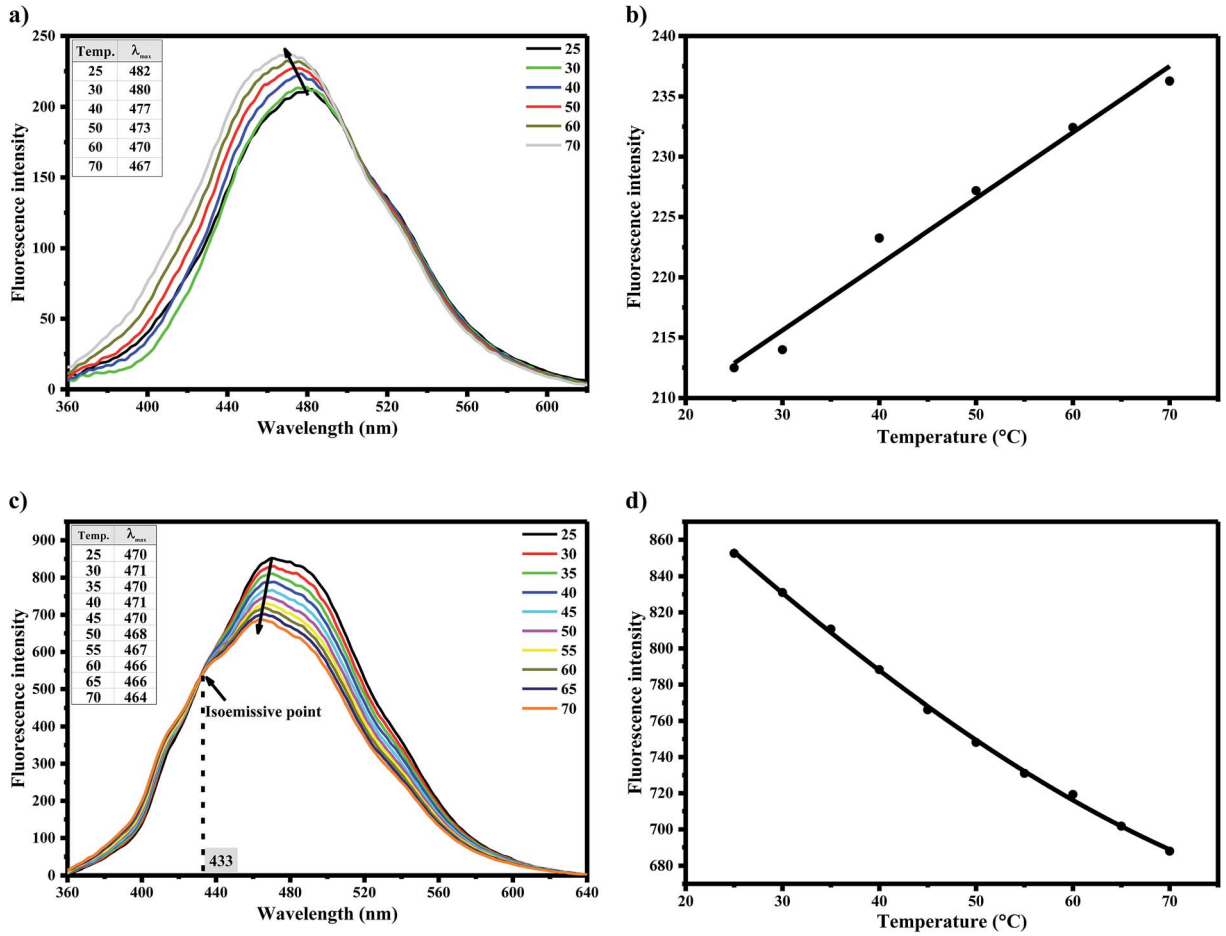

Fig. 5 (a) and (c) Temperature-dependent emission spectra (λ_{exc} = 330 nm) of 1 μM AG1478 in acetonitrile/water and acetonitrile, respectively. Inset lists solution temperature and its corresponding emission maximum. (b) and (d) Plots of fluorescence intensity of AG1478 in acetonitrile as a function of increasing solution temperature in presence and absence of water, respectively.

with the AG1478, we interpreted the Stern–Volmer plot as a purely static binding model with n water molecules bound. The form of the Stern–Volmer plot for this model is

$$F_0/F = 1 + K_1[H_2O] + K_2[H_2O]^2 + \ldots K_n[H_2O]^n \quad (2)$$

Fitting the data in Fig. 4b to this model yielded a best fit with a water coordination number of $n = 3$ (cubic function). Importantly $n = 1$ (linear function) or $n = 2$ (quadratic function) gave fits to Fig. 4b which were of poorer quality (as judged by sum of squared residuals) than $n = 3$, refer to ESI Fig. S5.† Adding higher terms to eqn (2) than $n = 3$ did not improve the fits further. Thus the quenching of the AG1478 fluorescence can be accounted for by binding of (at least) three water molecules. In other words, AG1478 is predicted to bind to target protein *via* three H-bonds and this binding interaction could be monitored by quenching of AG1478 fluorescence emission.

All these observations and conclusions were consistent with that reported by Magalhaes and coworkers for 1,8-naphthalimide derivative.[38] The 4-phenoxy-*N*-methyl-1,8-naphthalimide has almost the same spectral properties as AG1478. A negligible change in its absorption spectra upon modifying the solvent nature was observed compared to the discernible change in emission spectra. It also exhibited a broad non-structured emission spectrum with low fluorescence quantum yield. In addition, a large stokes shift was noted which was augmented by increasing solvent polarity.[38]

The experimental studies on 4-phenoxy-*N*-methyl-1,8-naphthalimide revealed the occurrence of bathochromic shift and fluorescence quenching upon adding a little amount of water to its solution in dioxane.[38] The Stern–Volmer plot showed an upward curvature indicating that the quenching process was triggered by both dynamic and static pathways. The author concluded that the non-linear fluorescence quenching could be attributed to combination of (1) non-radiative deactivation of excited state exerted by the protic (aqueous) solvent shell and (2) dynamic quenching by collision with free water molecules.[38] Since literature assured we are on track for the analyses of binding interactions between AG1478 and water molecules. We next investigate possible AG1478–water complexes using computational chemistry.

3.5. Computational study

We were the first to report the existence of AG1478 in two different geometrical conformations, twisted (t-AG1478) and

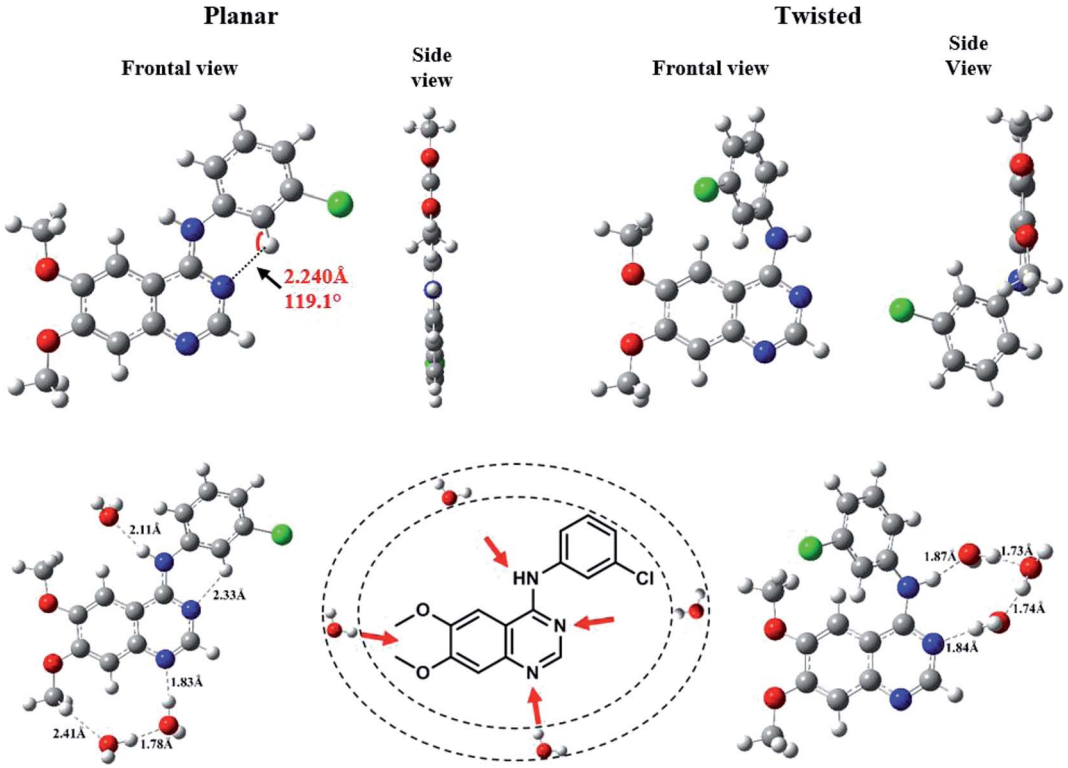

Fig. 6 Frontal and side views of the optimized geometries of conformers ground state of AG1478 at B3LYP/6-311+G* in vacuum. Strong H-bonds (<2.5 Å) are shown as dotted lines delineating bond length and angle.

planar (p-AG1478), and to link these conformers with distinct absorption bands in the AG1478 UV-vis absorption spectrum.[27] In the present study we sought to examine the effect of water on AG1478 using computational methods. We therefore generated potential AG1478·nH$_2$O complexes containing different numbers of water molecules, at different H-bond acceptor sites of AG1478, and calculated energies, geometries and spectroscopic properties of these complexes. Structures and obtained data are included in ESI Tables S1–S5 and Fig. S1–S4.† For the sake of brevity, we present here the salient results for the energy optimized complexes containing n = 1–7 water molecules in each of the twisted and planar conformers. Fig. 6 depicts the frontal and side views of the optimized planar and twisted rotamers in vacuum together with a schematic showing sites of water-docking to AG1478.

Since the N(25)–H linker group is the main acidic moiety (Lewis acid) in AG1478, it is therefore, expected that H-bonding with water molecules at the vicinity of the N(25) position will result in the stretching of bond length of N(25)–H. Hence, we calculated some geometric parameters and atomic charges of AG1478 as a function of number of water molecules in the AG1478–water complex. Fig. 7 depicts a plot of the N(25)–H bond length as a function of added water molecules (for twisted and planar AG1478 conformer). The N(25)–H bond length of the twisted AG1478 conformer system (marked in red in Fig. 7) is always longer than the planer conformer system. It is seen from this plot that as the number of water molecules increases (from 0 to 7 water molecules per AG1478), the N(25)–H bond length increased until it reached a plateau, indicting a saturation with respect to the added waters. The planar AG1478 conformer was saturated by 3 water molecules – p-AG1478·3H$_2$O – at which the plateau was reached, whereas the twisted AG1478 conformer is able to bind upto 5 water molecules, *i.e.*, t-AG1478·5H$_2$O. This may explain that the twisted conformer of AG1478 is possibly a more potent drug structure as the twist shape in space enhances binding, comparing to its planar conformer which can be less flexible in this regard.

It is known that orientation of AG1478 affects the ability to bind water molecules due to their three-dimensional

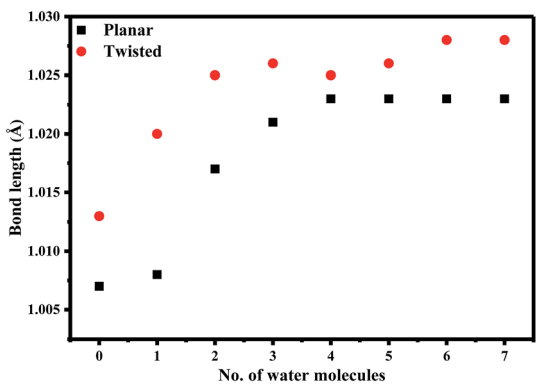

Fig. 7 Graph showing bond length of N(25)–H(26) as a function of increasing number of explicit water molecules of the optimized planar and twisted AG1478 structures in dielectric continuum of 37 at B3LYP/6-311+G*.

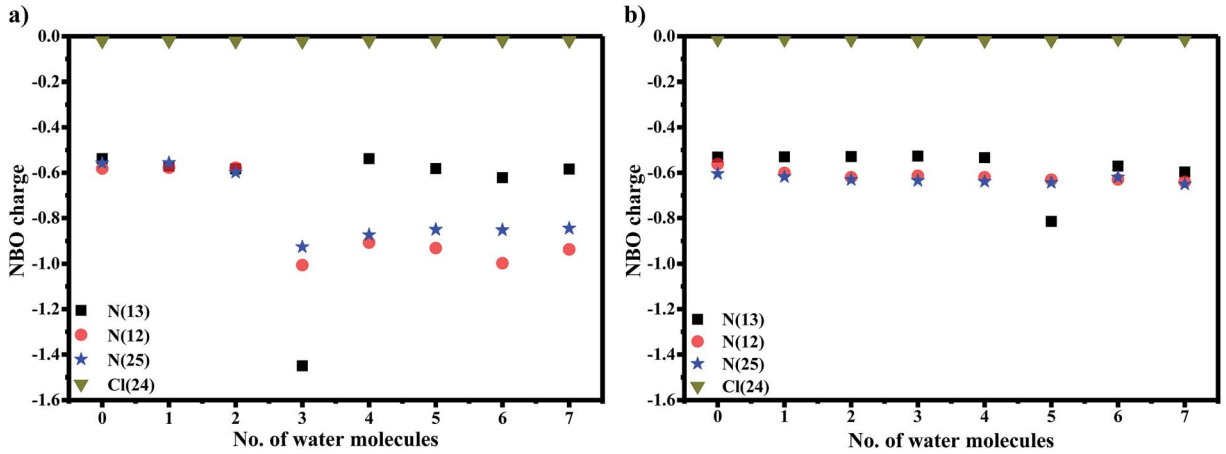

Fig. 8 Plot of NBO charge of some heterocyclic atoms (3 Ns, Cl) as a function of increasing number of explicit water molecules in the optimized (a) planar and (b) twisted structures AG1478 structures in dielectric continuum of 37 at B3LYP/6-311+G*.

structures.[52] Hydrogen bond formation requires containment of a covalently bonded hydrogen atom between two electronegative atoms. The AG1478 molecule has five electron-donating centres (three nitrogens and two oxygens). Therefore, we examined the electronic charges of some selected heteroatoms of AG1478. In Fig. 8a, NBO charges of electronegative atoms (three nitrogens and one chlorine—which serve as hydrogen bond acceptors) were plotted as a function of number of explicit water molecules in the AG1478–water complex. Charges of two oxygen atoms on the AG1478 compound were not examined because they are unlikely to form H-bond with water molecules in AG1478. Our quantum mechanical calculations indicated that the AG1478–water complexes were not formed through water molecule hydrogen bonding with the oxygen atoms of AG1478. It is seen in Fig. 8a and b that it is unlikely the chlorine atom of the AG1478 would be able to bind a water molecule as the NBO charge on Cl remained unchanged. However, the NBO charges on the nitrogen atoms indeed changed, depending on the AG1478 conformer shape and the number of water molecules in the complexes.

In the planer conformer case in Fig. 8a, the NBO charges of three nitrogen atoms in the AG1478 compound are all in the vicinity of $-0.6e$ when AG1478 forms complexes with up to 3 water molecules. A dramatic increase in negative charges of N(13) is observed when p-AG1478 form a complex with three water molecules. The NBO charge of N(13) drop from approximately $-0.6e$ to $-1.4e$ in p-AG1478·3H_2O. Interestingly, when the number of water molecules, $n \neq 3$, the NBO charges on N(13) remain almost the same (*ca.* $-0.6e$) for p-AG1478·$n$$H_2O$. It is also noted that the NBO charges on N(25) and N(12) of the p-AG1478·$n$$H_2O$ complexes are very different for $n < 3$ and $n \geq 3$ complexes.[27] However, in the t-AG1478 case, the NBO charge of N(13) shows a significant drop (more negative), from *ca.* $-0.6e$ for t-AG1478·$n$$H_2O$ ($n \neq 5$) to $-0.8e$ t-AG1478·5H_2O. That is, when forming a complex with five water molecules ($n = 5$), the charge of N(13) exhibit significant changes in t-AG1478·5H_2O, in agreement with the N(25)-H bond length change in Fig. 7.

We also estimated the binding energy between water molecules and AG1478. The graph of water binding energy as a function of number of water molecules in complex with AG1478 is shown in Fig. 9. Addition of $n = 1$–3 water molecules caused a progressive stabilization of the AG1478·$n$$H_2O$ complexes (relative to isolated constituents) as evidenced by the decreased binding energy. The figure shows that when binding with upto $n = 7$ water molecules, the complex AG1478·$n$$H_2O$ may be stable as the binding energy with respect to the AG1478 compound is negative. However, binding three water molecules ($n = 3$), AG1478·3H_2O complexes, either planar or twisted, can be the most stable complex for $n = 1$–7, as the binding energy is the most negative at $n = 3$. Further addition of more than three ($n = 4$–7) water molecules will reduce the stability of the AG1478·$n$$H_2O$ complexes. In addition, the t-AG1478·3H_2O complex is more stable than the p-AG1478·3H_2O complex as the former exhibits larger bonding energy than the latter in Fig. 9.

The computed absorbance properties (transition energy and oscillator strength) of the first excited-state of AG1478 as a function of the number of added water molecules are listed in Table 1 for the planar and twisted conformations. The

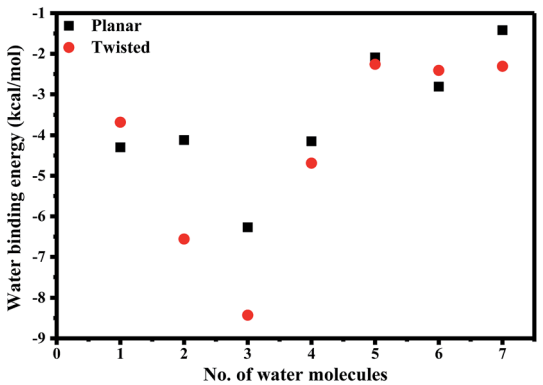

Fig. 9 Binding energy of explicit water molecules to AG1478·$n$$H_2O$ ($n = 1$–7) complexes calculated using the DFT based B3LYP/6-311+G* model.

Table 1 Ground to first excited state vertical excitation (including state-specific solvation correction) of AG1478 structures complexed with n = 1–7 explicit water molecules in dielectric continuum of 37

	P	P-1w	P-2w	P-3w	P-4w	P-5w	P-6w	P-7w
E (nm)	331	333	332	352	340	341	342	341
Osc. str.	0.5229	0.5475	0.4748	**0.4206**	0.4281	0.4492	0.4559	0.4601
	T	T-1w	T-2w	T-3w	T-4w	T-5w	T-6w	T-7w
E (nm)	342	340	346	366	369	354	334	328
Osc. str.	0.2476	0.2511	0.2515	0.2278	**0.2269**	0.2386	0.2329	0.2349

calculated S_0 to S_1 transition wavelength of free planar structure was 331 nm. Addition of one water molecule, caused a red-shift from 331 nm to 333 nm (by 2 nm) and a slight increase in oscillator strength. However, a very large red-shift by 21 nm to 352 nm was observed when three molecules of water were complexed with AG1478. Further additions of water (4–7 water molecules) caused a blue shift (from 352 nm) back to 340–342 nm. It was also notable that P-3w structure exhibited the lowest oscillator strength among other hydrated isomers Since AG1478·3H_2O exhibited the lowest energy absorption transition among other hydrated complexes, therefore it has the smallest HOMO–LUMO energy gap. Hence it was again concluded that the trihydrated complex is the most stable structures of AG1478. The low oscillator strength of absorption transition of AG1478·3H_2O might in part contribute to the observed fluorescence quenching.

The AG148 in the twisted configuration showed a different trend, where the excitation energy of free AG1478 was computed at 342 nm. By adding one water molecule, there was a blue-shift by 2 nm followed by 6 nm red-shift with 2 water molecules. As for the planar configuration, addition of 3–5 waters produced complexes with red-shifted absorption bands, calculated at 366 nm, 369 nm and 354 nm, respectively. Further additions of water caused a blue shift in the calculated absorbance bands to 334 nm (6 waters) and 328 nm (7 waters). It may be coincidence, but it appeared that the planar and twisted absorbance bands underwent an inversion, particularly at high water hydration.

Moreover, while we do not expect exact agreement in the prediction of relative absorbance of the 330 nm and 340 nm bands by theory, the prediction of an inversion of the twisted and planar absorbance bands at high hydration might be related to the inversion of the relative amplitudes of the 330 nm and 340 nm bands seen in the experimental absorbance spectra. The prediction from the computation studies of a red-shifted absorption band may also have some relevance to the experimental absorbance and excitation spectra, both showing a shoulder or extra band near 370 nm over a limited range of water concentrations. The shoulder at 370 nm has higher optical density due to promotion of absorption from T-3w and T-4w structures at 366 nm and 369 nm, respectively at lower water concentration (till 4% v/v of added water). While at higher water concentration (≥8% v/v), the higher water complexes of both planar and twisted structures showed absorbance in the range of 328–354 nm (refer to Table 1) resulting in reduction in amplitude of the 370 nm shoulder, as observed experimentally.

To summarize, the geometric properties, heteroatom charges, energetics of stabilization and computed absorbance spectra as a function of added water pointed to 3–4 molecules as having largest effect on AG1478 properties. These results are in good agreement with the spectroscopic results showing that about 3 water molecules have the largest influence on fluorescence quenching. It is important to stress that we are not suggesting that only three water molecules make up the solvation shell of AG1478 but rather hydrogen bonds between the water and AG1478 are important determinants of the spectroscopy of this molecule. In an ensemble of AG1478 in solution, we would expect a distribution of micro-solvation states containing zero, one, two, three or more water molecules and acetonitrile molecules as well. The distribution will be dictated in part by the water fraction and by the relative energetics of the relevant solute–solvent and solvent–solvent interactions. In our work we have attempted to simplify the system theoretically by treating the acetonitrile as a dielectric continuum and the water explicitly. This is clearly an approximation.

It is important to address some important differences between the theory and experiment. The theoretical calculations do not address temperature or configurational averaging which are also important. On the other hand, the spectroscopic experiments are ensemble averages which occur in equilibrium at room temperature. To relate the two studies more precisely would require knowledge of the precise configurations and their population distributions. Nevertheless, the computational study here has allowed us to identify specific sites of H-bonding from water that are important determinants of AG1478 spectroscopy.

Literature studies have emphasized that enzyme activity constitutes an intricate function of clustered water molecules in organic solvents. The conformational flexibility and enzymatic activity relies on the water content of the protein.[53–55] Taken into account that preferential solvation is a well-established explicit model that can describe qualitatively and quantitatively the protein surface occupancy by water (hydration/solvation) and cosolvent (solvation) molecules.[56,57] Our experiments and theory are of great relevance to understanding micro-solvation and H-bonding interactions in the quinazoline class of TKI. In structures of TKI complexed with proteins, H-bonding to water in the

protein binding site and to amino acids inside the protein are typically observed.[58,59] Given the high sensitivity of AG1478 fluorescence to hydration (as observed here from the acetonitrile–water mixtures), we would predict that fluorescence will be a useful probe of water–TKI interactions in protein binding sites. More detailed study of micro-solvation of AG1478 can be revealed using molecular dynamics (MD) which is out of the scope of this study.

4. Conclusion

Spectroscopic analysis of AG1478 in acetonitrile–water binary mixtures was a successful strategy to quantify sites available for H-bonding of AG1478. Analysis of fluorescence quenching using a binding model disclosed three potential sites for forming H-bonds between AG1478 and water molecules. The theoretical study was consistent with experimental results and revealed that AG1478 might exist in equilibrium of planar and twisted structures bound to varying number (1–7) of water molecules. All of the AG1478 : water complexes exhibited calculated excitation energies within the experimentally observed values. The hydrated twisted structures were predicted to be more energetically favoured than hydrated planar counterparts, in contrast to dehydrated AG1478. In this regard, we predict that the extend of hydration of the drug binding site in the protein may be an important determinant of whether planar or twisted drug conformation is populated in the drug–protein complex. The studies conducted here show that AG1478 can be used as a micro-solvation probe and lay the ground work for future studies of AG1478 in more complex environments such as proteins.

Acknowledgements

M. Khattab acknowledges Swinburne University Postgraduate Research Award (SUPRA). FW acknowledges supercomputer support from Swinburne University of Technology.

References

1 M. Jabbari, N. Khosravi, M. Feizabadi and D. Ajloo, *RSC Adv.*, 2017, **7**, 14776–14789.
2 V. T. B. Pham, H. M. Hoang, G. Grampp and D. R. Kattnig, *J. Phys. Chem. B*, 2017, **121**, 2677–2683.
3 M. Daneri and C. J. Abelt, *J. Photochem. Photobiol., A*, 2015, **310**, 106–112.
4 A. Duereh, Y. Sato, R. L. Smith and H. Inomata, *J. Phys. Chem. B*, 2015, **119**, 14738–14749.
5 S. Sanli, *J. Solution Chem.*, 2013, **42**, 967–978.
6 D. C. da Silva, I. Ricken, M. A. D. Silva and V. G. Machado, *J. Phys. Org. Chem.*, 2002, **15**, 420–427.
7 N. P. Wells, M. J. McGrath, J. I. Siepmann, D. F. Underwood and D. A. Blank, *J. Phys. Chem. A*, 2008, **112**, 2511–2514.
8 K. Bhaskaran-Nair, M. Valiev, S. H. M. Deng, W. A. Shelton, K. Kowalski and X. B. Wang, *J. Chem. Phys.*, 2015, **143**, 224301.
9 D. Ghosh, O. Isayev, L. V. Slipchenko and A. I. Krylov, *J. Phys. Chem. A*, 2011, **115**, 6028–6038.
10 J. W. Ho, H. C. Yen, H. Q. Shi, L. H. Cheng, C. N. Weng, W. K. Chou, C. C. Chiu and P. Y. Cheng, *Angew. Chem., Int. Ed.*, 2015, **54**, 14772–14776.
11 V. B. Pacheco and P. Chaudhuri, *J. Phys. Chem. A*, 2013, **117**, 5675–5684.
12 D. S. Venables and C. A. Schmuttenmaer, *J. Chem. Phys.*, 2000, **113**, 11222–11236.
13 J. Catalan, C. Diaz and F. Garcia-Blanco, *Org. Biomol. Chem.*, 2003, **1**, 575–580.
14 P. Petong, R. Pottel and U. Kaatze, *J. Phys. Chem. A*, 2000, **104**, 7420–7428.
15 D. B. Wong, K. P. Sokolowsky, M. I. El-Barghouthi, E. E. Fenn, C. H. Giammanco, A. L. Sturlaugson and M. D. Fayer, *J. Phys. Chem. B*, 2012, **116**, 5479–5490.
16 H. Tanaka, J. Walsh and K. E. Gubbins, *Mol. Phys.*, 1992, **76**, 1221–1233.
17 G. Matisz, A. M. Kelterer, W. M. F. Fabian and S. Kunsagi-Mate, *Phys. Chem. Chem. Phys.*, 2015, **17**, 8467–8479.
18 S. Lobsiger, S. Blaser, R. K. Sinha, H. M. Frey and S. Leutwyler, *Nat. Chem.*, 2014, **6**, 989–993.
19 M. Barbatti and H. Lischka, *Phys. Chem. Chem. Phys.*, 2015, **17**, 15452–15459.
20 A. T. Garcia-Sosa, *J. Chem. Inf. Model.*, 2013, **53**, 1388–1405.
21 A. Gazit, J. Chen, H. App, G. McMahon, P. Hirth, I. Chen and A. Levitzki, *Bioorg. Med. Chem.*, 1996, **4**, 1203–1207.
22 Z. Shi, A. K. Tiwari, S. Shukla, R. W. Robey, I. W. Kim, S. Parmar, S. E. Bates, Q. S. Si, C. S. Goldblatt, I. Abraham, L. W. Fu, S. V. Ambudkar and Z. S. Chen, *Biochem. Pharmacol.*, 2009, **77**, 781–793.
23 L. Caja, P. Sancho, E. Bertran, C. Ortiz, J. S. Campbell, N. Fausto and I. Fabregat, *Biochem. Pharmacol.*, 2011, **82**, 1583–1592.
24 F. A. Al-Obeidi and K. S. Lam, *Oncogene*, 2000, **19**, 5690–5701.
25 Y. Liu and N. S. Gray, *Nat. Chem. Biol.*, 2006, **2**, 358–364.
26 M. Khattab, F. Wang and A. H. Clayton, *Spectrochim. Acta, Part A*, 2016, **164**, 128–132.
27 M. Khattab, S. Chatterjee, A. H. A. Clayton and F. Wang, *New J. Chem.*, 2016, **40**, 8296–8304.
28 D. Banerjee and S. K. Pal, *J. Phys. Chem. A*, 2008, **112**, 7314–7320.
29 F. Gao, X. J. Ye, H. R. Li, X. L. Zhong and Q. Wang, *ChemPhysChem*, 2012, **13**, 1313–1324.
30 M. K. Nayak, *J. Photochem. Photobiol., A*, 2012, **241**, 26–37.
31 K. Suda, M. Terazima and Y. Kimura, *Chem. Phys. Lett.*, 2012, **531**, 70–74.
32 T. S. Choi, J. W. Lee, K. S. Jin and H. I. Kim, *Biophys. J.*, 2014, **107**, 1939–1949.
33 M. T. Sonoda, N. H. Moreira, L. Martinez, F. W. Favero, S. M. Vechi, L. R. Martins and M. S. Skaf, *Braz. J. Phys.*, 2004, **34**, 3–16.
34 A. D. Becke, *J. Chem. Phys.*, 1993, **98**, 1372–1377.
35 A. D. Becke, *J. Chem. Phys.*, 1993, **98**, 5648–5652.
36 M. Cossi, N. Rega, G. Scalmani and V. Barone, *J. Comput. Chem.*, 2003, **24**, 669–681.

37 G. W. T. M. J. Frisch, H. B. Schlegel, G. E. Scuseria, M. A. Robb, J. R. Cheeseman, G. Scalmani, V. Barone, B. Mennucci, G. A. Petersson, H. Nakatsuji, M. Caricato, X. Li, H. P. Hratchian, A. F. Izmaylov, J. Bloino, G. Zheng, J. L. Sonnenberg, M. Hada, M. Ehara, K. Toyota, R. Fukuda, J. Hasegawa, M. Ishida, T. Nakajima, Y. Honda, O. Kitao, H. Nakai, T. Vreven, J. A. Montgomery Jr, J. E. Peralta, F. Ogliaro, M. Bearpark, J. J. Heyd, E. Brothers, K. N. Kudin, V. N. Staroverov, R. Kobayashi, J. Normand, K. Raghavachari, A. Rendell, J. C. Burant, S. S. Iyengar, J. Tomasi, M. Cossi, N. Rega, J. M. Millam, M. Klene, J. E. Knox, J. B. Cross, V. Bakken, C. Adamo, J. Jaramillo, R. Gomperts, R. E. Stratmann, O. Yazyev, A. J. Austin, R. Cammi, C. Pomelli, J. W. Ochterski, R. L. Martin, K. Morokuma, V. G. Zakrzewski, G. A. Voth, P. Salvador, J. J. Dannenberg, S. Dapprich, A. D. Daniels, Ö. Farkas, J. B. Foresman, J. V. Ortiz, J. Cioslowski, and D. J. Fox, *Gaussian 09, Revision C.01*, Gaussian, Inc., Wallingford CT, 2009.

38 J. L. Magalhaes, R. V. Pereira, E. R. Triboni, P. Berci, M. H. Gehlen and F. C. Nart, *J. Photochem. Photobiol., A*, 2006, **183**, 165–170.

39 S. D. Choudhury and H. Pal, *J. Phys. Chem. B*, 2016, **120**, 11970–11977.

40 V. A. Sirotkin and A. A. Kuchierskaya, *J. Phys. Chem. B*, 2017, **121**, 4422–4430.

41 J. Barbosa, D. Barron, R. Berges, V. SanzNebot and I. Toro, *J. Chem. Soc., Faraday Trans.*, 1997, **93**, 1915–1920.

42 A. Wakisaka, S. Takahashi and N. Nishi, *J. Chem. Soc., Faraday Trans.*, 1995, **91**, 4063–4069.

43 J. Barbosa and V. Sanznebot, *J. Chem. Soc., Faraday Trans.*, 1994, **90**, 3287–3292.

44 H. Boaz and G. K. Rollefson, *J. Am. Chem. Soc.*, 1950, **72**, 3435–3443.

45 B. K. Paul, N. Ghosh and S. Mukherjee, *Langmuir*, 2014, **30**, 5921–5929.

46 B. K. Paul, D. Ray and N. Guchhait, *Phys. Chem. Chem. Phys.*, 2013, **15**, 1275–1287.

47 I. Y. S. Lee and H. Suzuki, *J. Photochem. Photobiol., A*, 2008, **195**, 254–260.

48 J. R. Lakowicz, *Principles of fluorescence spectroscopy*, Springer Science & Business Media, 2013.

49 N. Ghosh, R. Mondal and S. Mukherjee, *Langmuir*, 2015, **31**, 8074–8080.

50 F. F. Tian, F. L. Jiang, X. L. Han, C. Xiang, Y. S. Ge, J. H. Li, Y. Zhang, R. Li, X. L. Ding and Y. Liu, *J. Phys. Chem. B*, 2010, **114**, 14842–14853.

51 J. Q. Tong, F. F. Tian, Q. Li, L. L. Li, C. Xiang, Y. Liu, J. Dai and F. L. Jiang, *Photochem. Photobiol. Sci.*, 2012, **11**, 1868–1879.

52 A. Ganesan, J. Dreyer, F. Wang, J. Akola and J. Larrucea, *J. Mol. Graphics Modell.*, 2013, **45**, 180–191.

53 T. Kijima, S. Yamamoto and H. Kise, *Enzyme Microb. Technol.*, 1996, **18**, 2–6.

54 K. Griebenow and A. M. Klibanov, *J. Am. Chem. Soc.*, 1996, **118**, 11695–11700.

55 Y. L. Khmelnitsky, V. V. Mozhaev, A. B. Belova, M. V. Sergeeva and K. Martinek, *Eur. J. Biochem.*, 1991, **198**, 31–41.

56 S. N. Timasheff, *Proc. Natl. Acad. Sci. U. S. A.*, 2002, **99**, 9721–9726.

57 T. Arakawa, Y. Kita and S. N. Timasheff, *Biophys. Chem.*, 2007, **131**, 62–70.

58 N. M. Levinson and S. G. Boxer, *Nat. Chem. Biol.*, 2014, **10**, 127–132.

59 E. De Moliner, N. R. Brown and L. N. Johnson, *Eur. J. Biochem.*, 2003, **270**, 3174–3181.

Supporting Information

Cartesian Coordinates (Å) of optimized ground state of the planar and twisted structures and their corresponding water complexes, where B3LYP/6-311+G* functional and CPCM model (ε= 37.219) were used for optimization.

Planar

C	-4.00873000	-0.23163400	0.00029000
C	-3.35364500	-1.44274300	0.00005100
C	-1.93981500	-1.50696800	-0.00016500
C	-1.18791700	-0.30630800	-0.00011500
C	-1.87350400	0.93650700	0.00010200
C	-3.24947200	0.98784400	0.00029900
H	-3.89574700	-2.37873800	0.00001400
C	0.24344800	-0.46879800	-0.00027300
H	-1.32783200	1.87012800	0.00009400
C	-0.03100900	-2.74112700	-0.00060700
H	0.46199600	-3.71025100	-0.00084000
N	0.79718800	-1.67593100	-0.00053300
N	-1.34262500	-2.74124600	-0.00041900
C	2.44127900	0.79541100	-0.00026100
C	2.92876700	2.11557300	-0.00061100
C	3.35560700	-0.26857400	0.00003200
C	4.29344600	2.36529100	-0.00066000
H	2.23155100	2.94771800	-0.00084100
C	4.71627500	0.02138700	-0.00003800
H	3.00312100	-1.28656300	0.00028100
C	5.21550200	1.31675000	-0.00037800
H	4.64846800	3.39000700	-0.00093300
H	6.28155100	1.50554500	-0.00043000
Cl	5.85338400	-1.33298600	0.00034400
N	1.04431400	0.64485000	-0.00014400
H	0.55372400	1.52463300	0.00002200
O	-5.35014400	-0.07388600	0.00051300
O	-3.98770600	2.12368100	0.00050900
C	-3.30832400	3.38083300	0.00055400
H	-4.09022100	4.13643800	0.00075600
H	-2.69078200	3.49336500	0.89554100
H	-2.69104700	3.49357200	-0.89459000
C	-6.17371300	-1.24422200	0.00057900
H	-7.19833800	-0.88064000	0.00081600
H	-5.99642800	-1.84585800	-0.89405800
H	-5.99606700	-1.84601000	0.89504200

P-1w

C	3.83950400	-0.36301900	-0.00273500
C	3.28032200	0.89583000	-0.00704900
C	1.87654200	1.06642000	-0.00690800
C	1.03299200	-0.07072300	-0.00251000
C	1.62073000	-1.36210300	0.00158300
C	2.98848800	-1.52034000	0.00118500
H	3.89614600	1.78477000	-0.00988900
C	-0.38215700	0.20035900	-0.00325100
H	1.00445100	-2.25018900	0.00451200
C	0.05793200	2.44510600	-0.01373300
H	-0.35510800	3.45038100	-0.01927200
N	-0.84394900	1.44762500	-0.00888000
N	1.36740500	2.34096500	-0.01255500
C	-2.67086300	-0.88837900	0.00218700

C	-3.25548100	-2.16785700	0.00702700
C	-3.50099600	0.24191100	-0.00147500
C	-4.63512800	-2.31402700	0.00815500
H	-2.62178900	-3.04917700	0.00992900
C	-4.87974200	0.05573400	-0.00030300
H	-3.07269600	1.23026500	-0.00526800
C	-5.47489000	-1.19859200	0.00448400
H	-5.06665100	-3.30883500	0.01191300
H	-6.55220900	-1.30621800	0.00530000
Cl	-5.91104600	1.49167200	-0.00500200
N	-1.26512100	-0.84595500	0.00164000
H	-0.84569700	-1.76205400	0.00584800
O	5.16308900	-0.62362400	-0.00231300
O	3.63595300	-2.70917800	0.00457100
C	2.86142100	-3.91072700	0.00927800
H	3.58309600	-4.72394300	0.01158800
H	2.23797000	-3.97228700	0.90512800
H	2.23674000	-3.97853400	-0.88525800
C	6.07720400	0.47818700	-0.00710500
H	7.06940700	0.03392500	-0.00606100
H	5.94765700	1.08829300	-0.90404200
H	5.94888000	1.09513200	0.88532700
O	2.96919600	4.71199900	-0.05042000
H	2.41284400	3.89985500	-0.03365900
H	2.69521600	5.25148300	0.69982600

P-2w

C	-3.85928900	0.17122800	-0.16411700
C	-3.29303300	-1.07210400	0.00905700
C	-1.89294500	-1.21811600	0.14304000
C	-1.06174200	-0.07132100	0.10031000
C	-1.65499900	1.20623500	-0.07962700
C	-3.02056800	1.33553500	-0.21007800
H	-3.89918600	-1.96696600	0.04505500
C	0.35177300	-0.31752200	0.23761300
H	-1.03789900	2.09359400	-0.11605800
C	-0.07046500	-2.56228600	0.41462800
H	0.34833400	-3.55731700	0.54398000
N	0.81839000	-1.55721800	0.38955100
N	-1.37823500	-2.48008700	0.30475900
C	2.65323200	0.64860000	0.27499700
C	3.33868100	1.69230200	0.91422600
C	3.38617400	-0.37573100	-0.34115600
C	4.72913100	1.70768900	0.94375600
H	2.77599900	2.49055700	1.38286500
C	4.77330700	-0.33623500	-0.28443900
H	2.88230600	-1.18301800	-0.84856500
C	5.46998100	0.68676300	0.34954900
H	5.24485300	2.52036500	1.44369300
H	6.55240600	0.68766800	0.37895600
Cl	5.68335800	-1.63845300	-1.06169400
N	1.24330500	0.71959600	0.22373300
H	0.88092500	1.66869300	0.27024500
O	-5.18202500	0.40680100	-0.30314600
O	-3.68106900	2.50606400	-0.38830700
C	-2.92077900	3.71428300	-0.44856100
H	-3.64733900	4.51043900	-0.59381600
H	-2.37237600	3.87964900	0.48155200
H	-2.22090700	3.69615200	-1.28750700
C	-6.08085000	-0.70620200	-0.27220000

H	-7.07392400	-0.28341800	-0.40335300
H	-5.86753400	-1.40345000	-1.08596200
H	-6.02645900	-1.22621400	0.68727300
O	-2.91995800	-4.87762200	0.41008600
H	-2.39300300	-4.04514700	0.38194600
H	-2.83695200	-5.22859300	1.30391000
O	0.60890900	3.60353300	0.17195000
H	0.56242300	4.19787700	0.93022400
H	1.03452600	4.09787400	-0.53859200

P-3w

C	4.13919100	-0.47473200	-0.34781900
C	3.49174600	-1.54626300	0.22823100
C	2.08768900	-1.53713900	0.39859700
C	1.34578300	-0.40252900	-0.01661800
C	2.01772500	0.68681300	-0.62670400
C	3.38301300	0.66437000	-0.79386600
H	4.03236000	-2.42291200	0.55856600
C	-0.06981400	-0.46637500	0.19276200
H	1.45023600	1.53852000	-0.97181400
C	0.17790600	-2.57605200	1.06795100
H	-0.32223300	-3.43759500	1.50260900
N	-0.63283500	-1.54591600	0.73478300
N	1.48131400	-2.63867800	0.94417700
C	-2.24526400	0.61251500	-0.38411500
C	-2.93595500	1.82660400	-0.23664200
C	-2.94363600	-0.51872000	-0.83425400
C	-4.29345200	1.90383300	-0.52520300
H	-2.40044800	2.70533100	0.10340900
C	-4.30072400	-0.40742500	-1.10645800
H	-2.43888200	-1.46353700	-0.96793900
C	-5.00253600	0.78403100	-0.96030700
H	-4.81146000	2.84925800	-0.40496900
H	-6.06158600	0.83794600	-1.17869900
Cl	-5.16273100	-1.84528100	-1.67022600
N	-0.85979500	0.60602400	-0.15561500
H	-0.45373800	1.52530100	0.02615900
O	5.47037900	-0.39342500	-0.55374900
O	4.11547600	1.64900200	-1.36766800
C	3.43452400	2.81013700	-1.84836400
H	4.20788800	3.45435500	-2.25980200
H	2.71976200	2.54824600	-2.63290700
H	2.91986500	3.32775000	-1.03485600
C	6.29386800	-1.49104500	-0.14670600
H	7.31037700	-1.20502500	-0.40532800
H	6.22044400	-1.65544300	0.93092300
H	6.02058900	-2.40341700	-0.68215600
O	-2.28695900	-0.60244900	2.88928700
H	-3.24096100	-0.60061400	2.74961800
H	-1.88043300	-1.02124900	2.09992400
O	-1.13532800	1.83595300	3.44888800
H	-1.55549700	0.96447800	3.26899800
H	-0.61333700	1.74041100	4.25317400
O	0.05068900	2.93719500	1.23082300
H	-0.09022500	3.88766000	1.16181700
H	-0.36153400	2.63195500	2.07015000

P-4w

C	4.19853400	-0.72841500	-0.20374000
C	3.51129600	-1.63165100	0.57772500

C	2.10457500	-1.55981300	0.70353100
C	1.39686800	-0.54069800	0.01747900
C	2.11126400	0.37912600	-0.79179000
C	3.48045100	0.29845000	-0.90659100
H	4.02255600	-2.41911300	1.11457900
C	-0.02950100	-0.54310700	0.18537800
H	1.58182700	1.16926300	-1.30280100
C	0.16573900	-2.37584800	1.56385400
H	-0.35944900	-3.09373900	2.18880700
N	-0.61820200	-1.45025900	0.96815300
N	1.46801600	-2.49259300	1.48195700
C	-2.19912600	0.34058600	-0.65802400
C	-2.90323000	1.55067400	-0.74733600
C	-2.88529500	-0.86639600	-0.86030700
C	-4.26614500	1.55234500	-1.02449700
H	-2.37593100	2.48527800	-0.59900400
C	-4.24795600	-0.83009800	-1.12373200
H	-2.36540800	-1.81175100	-0.81459900
C	-4.96383800	0.35934900	-1.21048700
H	-4.79692500	2.49607400	-1.08862700
H	-6.02676900	0.35557900	-1.41655400
Cl	-5.09663400	-2.36134800	-1.37185500
N	-0.80666900	0.38926400	-0.45128400
H	-0.37506000	1.28806500	-0.67867700
O	5.53720200	-0.71861800	-0.38029900
O	4.24915200	1.13157300	-1.64998400
C	3.60127900	2.16799300	-2.39204500
H	4.39885400	2.71265100	-2.89192300
H	2.92133900	1.74678700	-3.13764800
H	3.05064100	2.84068700	-1.73057900
C	6.32243200	-1.70666800	0.29438700
H	7.35295100	-1.50177200	0.01484400
H	6.21074000	-1.62061300	1.37788200
H	6.04652800	-2.71314500	-0.02928100
O	-0.09198300	3.71715400	1.92455300
H	-0.70724200	3.13499000	2.42695600
H	0.71385900	3.79909700	2.44630500
O	-2.58584000	-0.40118600	2.73481700
H	-3.49777900	-0.50000800	2.43798400
H	-2.01399600	-0.83282200	2.05896200
O	-1.85019000	2.16609100	3.32721000
H	-2.10803500	1.24085100	3.10850800
H	-1.81138000	2.23368800	4.28741700
O	0.24419500	3.06381500	-0.69776300
H	-0.05870300	3.76579800	-1.28374400
H	0.13377900	3.37658000	0.22983900

P-5w

C	-4.07808500	0.03384700	-0.54631500
C	-3.49711600	1.18514300	-0.05878500
C	-2.09637800	1.27391400	0.10454400
C	-1.28232500	0.16350400	-0.23014100
C	-1.88821200	-1.01264400	-0.73950500
C	-3.25332400	-1.08841200	-0.89839300
H	-4.09337800	2.04713900	0.20750600
C	0.13202700	0.33828300	-0.04801700
H	-1.27793900	-1.86960500	-0.98173500
C	-0.25326600	2.47517300	0.71093000
H	0.18419500	3.39090700	1.09935400
N	0.61859000	1.48678200	0.43348400

N	-1.55820800	2.44557800	0.57664000
C	2.39766400	-0.56566700	-0.53895600
C	3.19276700	-1.68035400	-0.23587200
C	2.99917000	0.57712400	-1.08635900
C	4.56386600	-1.64879900	-0.46767000
H	2.73005100	-2.56718900	0.17982600
C	4.37188600	0.58037000	-1.29450400
H	2.40781500	1.44219400	-1.34710600
C	5.17768900	-0.51314300	-0.99469300
H	5.16661400	-2.51773300	-0.22680800
H	6.24608400	-0.48087200	-1.16728300
Cl	5.11439700	2.03001900	-1.98147300
N	1.00297200	-0.66897700	-0.36000400
H	0.65052000	-1.62868600	-0.32154700
O	-5.40189600	-0.14422500	-0.73469900
O	-3.92189300	-2.16551300	-1.37578600
C	-3.16392300	-3.31191200	-1.77226600
H	-3.89457400	-4.04339800	-2.10926800
H	-2.48580500	-3.06458000	-2.59350400
H	-2.59375300	-3.71630900	-0.93293500
C	-6.29203300	0.92673400	-0.40245400
H	-7.28929300	0.55771200	-0.62873000
H	-6.22350000	1.17552100	0.65916200
H	-6.08105100	1.81171900	-1.00735200
O	-3.08802800	4.76060400	1.28292300
H	-2.55889100	3.96729000	1.03897500
H	-2.75868600	5.48952000	0.74515200
O	0.32004500	-3.11284100	2.89280000
H	0.90462900	-2.38499500	3.20638200
H	-0.52224600	-3.02056400	3.35151400
O	2.59917300	1.17363400	2.46885100
H	3.51050800	1.22788500	2.15859200
H	2.02133800	1.33955600	1.69018200
O	2.00267200	-1.15518600	3.78180600
H	2.21000600	-0.31530400	3.31127800
H	1.99107700	-0.96158000	4.72540000
O	0.16534600	-3.36714800	0.18682900
H	0.56457300	-4.18657500	-0.12459200
H	0.21769100	-3.35962800	1.17068900

P-6w

C	-3.75981100	-0.84635400	-0.58348300
C	-3.38401800	0.39983200	-0.12852800
C	-2.02008500	0.72067500	0.05308000
C	-1.02945500	-0.25085700	-0.23457900
C	-1.42582900	-1.52823500	-0.70478000
C	-2.75698500	-1.83214700	-0.87684800
H	-4.11953600	1.16099100	0.09307200
C	0.33458300	0.16301100	-0.05568600
H	-0.67918100	-2.28154300	-0.90641000
C	-0.40623100	2.22729200	0.63647500
H	-0.13073300	3.21267700	1.00236500
N	0.61925200	1.39070100	0.39188600
N	-1.68710400	1.97856300	0.49280400
C	2.72022400	-0.35707100	-0.53351400
C	3.69588400	-1.30997000	-0.20699800
C	3.11488500	0.85532900	-1.11826100
C	5.04040100	-1.05032600	-0.45138300
H	3.39439500	-2.25125600	0.23608500
C	4.46580100	1.08762500	-1.33864400

H	2.38338000	1.59939900	-1.39669300
C	5.44855500	0.15793000	-1.01496600
H	5.78404200	-1.79591500	-0.19178400
H	6.49496800	0.36832200	-1.19713000
Cl	4.94541500	2.62225200	-2.07319300
N	1.36407900	-0.69118200	-0.33931000
H	1.17974000	-1.69522100	-0.26910300
O	-5.03156900	-1.24269100	-0.79224000
O	-3.23316700	-3.02062800	-1.31807400
C	-2.29270400	-4.04205800	-1.66200300
H	-2.88933200	-4.89486000	-1.97698300
H	-1.65086600	-3.71831900	-2.48581700
H	-1.67815400	-4.31704700	-0.80190600
C	-6.09050400	-0.31394900	-0.53493000
H	-7.00830900	-0.84410800	-0.77668800
H	-6.10256800	-0.01747100	0.51646000
H	-5.99664800	0.56948600	-1.17049600
O	-3.51421400	4.01359800	1.19289800
H	-2.87459900	3.30301700	0.93799500
H	-3.05205100	4.85595900	1.11914100
O	1.31109200	-3.15900600	2.99430700
H	1.73099600	-2.31338500	3.27431000
H	0.52049300	-3.27765400	3.53202000
O	2.62884000	1.50590700	2.41476400
H	3.50594400	1.75594400	2.10204600
H	2.02759600	1.53442800	1.63634000
O	2.54755400	-0.85883800	3.79034400
H	2.56926800	-0.00872600	3.29363600
H	2.50998800	-0.64329100	4.72847400
O	1.00855800	-3.47048300	0.30675000
H	1.50634400	-4.22630600	-0.02312000
H	1.12473000	-3.43599700	1.28451600
O	-6.06817900	3.96952200	0.16100500
H	-5.15952300	3.97407100	0.53137800
H	-6.65559600	3.67852800	0.86719500

P-7w

C	-3.57194600	-0.15377800	-0.28739500
C	-3.00530000	1.04922800	0.07606400
C	-1.60070000	1.18235500	0.16045600
C	-0.77257400	0.06807600	-0.12534000
C	-1.36733300	-1.15957800	-0.51088200
C	-2.73464400	-1.27679000	-0.59181400
H	-3.62107500	1.91303500	0.28945900
C	0.64421900	0.28667500	-0.02409700
H	-0.74669800	-2.01920200	-0.71506800
C	0.24073300	2.46819100	0.57972900
H	0.67164000	3.42201900	0.87169700
N	1.12320300	1.47990300	0.34369100
N	-1.06817900	2.40021400	0.50875700
C	2.90974900	-0.60211000	-0.53535600
C	3.74620700	-1.66277500	-0.16019800
C	3.45786300	0.50043100	-1.20664300
C	5.10735000	-1.61675500	-0.44335400
H	3.32439900	-2.51850900	0.35275100
C	4.82219200	0.52113300	-1.46304500
H	2.83227600	1.32152900	-1.52390600
C	5.66911700	-0.51873200	-1.09343500
H	5.74340100	-2.44336300	-0.14594900
H	6.72977700	-0.47437800	-1.30651800

Cl	5.49846200	1.92019400	-2.30520900
N	1.52444700	-0.72222600	-0.29648600
H	1.19694500	-1.68400900	-0.17380000
O	-4.89775500	-0.38525500	-0.39425000
O	-3.39931500	-2.40814300	-0.94524000
C	-2.63426100	-3.57013800	-1.29119300
H	-3.36373900	-4.34312600	-1.51948900
H	-2.01546600	-3.37527500	-2.17037400
H	-2.00572400	-3.88493500	-0.45614100
C	-5.80679500	0.65382000	-0.00009500
H	-6.80185000	0.25551300	-0.18209400
H	-5.68658600	0.87772900	1.06239700
H	-5.65164600	1.56147800	-0.58424000
O	-2.59203600	4.72760900	0.93625400
H	-2.03045600	3.92380000	0.79765800
H	-2.12815200	5.47382900	0.54030900
O	1.06355700	-2.96585700	3.13566400
H	1.64313500	-2.20487700	3.36989900
H	0.24145500	-2.85971300	3.62684700
O	3.17829300	1.35598200	2.33215200
H	4.07941000	1.43983900	1.99949200
H	2.57708100	1.45535200	1.56051600
O	2.72790400	-0.90737800	3.80700100
H	2.88057600	-0.09416900	3.27324700
H	2.75135900	-0.65064100	4.73519300
O	0.77630900	-3.39504100	0.46287400
H	1.19307500	-4.21577800	0.17897400
H	0.88060000	-3.32478500	1.44023500
O	-5.09447000	4.13388100	-0.03927600
H	-4.22767400	4.41679600	0.32461500
H	-5.76552300	4.38860300	0.60372800
H	-5.40244700	-2.55199900	-1.17255200
H	-6.92516600	-2.41239400	-1.41916400
O	-6.20327900	-3.05035100	-1.40284200

Twisted

C	2.89761800	-0.90609000	-0.01708300
C	3.14745400	0.35652100	0.47019600
C	2.18000800	1.38452800	0.35455700
C	0.91855000	1.09067100	-0.23038600
C	0.68735000	-0.20552100	-0.76322500
C	1.64490000	-1.18726800	-0.66829000
H	4.09210100	0.60802600	0.93282600
C	-0.00485100	2.18104400	-0.28082500
H	-0.24615100	-0.41580600	-1.26214300
C	1.60078900	3.57219600	0.57548700
H	1.86348000	4.58850300	0.85788300
N	0.35813000	3.41000200	0.08246900
N	2.51082000	2.64346900	0.77170900
C	-2.24877400	1.06678100	-0.54046900
C	-3.32257300	0.94054200	-1.43141900
C	-2.18253300	0.23441800	0.58357400
C	-4.31089100	-0.01071600	-1.20322400
H	-3.37378100	1.58599300	-2.30143100
C	-3.17203800	-0.72335400	0.77138100
H	-1.38177800	0.33731900	1.30400600
C	-4.24419100	-0.86523800	-0.10226600
H	-5.13898700	-0.10009600	-1.89769000
H	-5.00413300	-1.61699200	0.06997400
Cl	-3.06934200	-1.77547400	2.18536100

N	-1.28952900	2.07766400	-0.78514300
H	-1.68463600	2.98748300	-0.98924900
O	3.75742900	-1.94427800	0.04089100
O	1.52399300	-2.44629400	-1.15332100
C	0.31581100	-2.80217300	-1.82890500
H	0.43950100	-3.84176000	-2.12279500
H	-0.54729000	-2.70883100	-1.16495200
H	0.16842500	-2.18492900	-2.71895800
C	5.03059900	-1.74394400	0.66320200
H	5.54066300	-2.70195400	0.59975100
H	5.60859300	-0.98334700	0.13288600
H	4.91210900	-1.45831500	1.71112800

T-1w

C	3.13934400	-0.69125800	-0.07109600
C	3.19732300	0.56980000	0.47830900
C	2.07770500	1.43475900	0.43274300
C	0.86347100	0.97335500	-0.14374500
C	0.82852100	-0.31459700	-0.74102500
C	1.93208000	-1.13437200	-0.71652400
H	4.10075200	0.94565600	0.93895700
C	-0.22646900	1.90090900	-0.12201300
H	-0.07165300	-0.64859500	-1.23320800
C	1.17457700	3.49156100	0.77902400
H	1.27878000	4.52217200	1.10741900
N	-0.03923800	3.15672600	0.29950600
N	2.22001000	2.70891200	0.91058400
C	-2.24819700	0.43960000	-0.42454400
C	-3.28174200	0.17692700	-1.33289300
C	-2.03734400	-0.43088400	0.65211900
C	-4.08680900	-0.94547000	-1.16965700
H	-3.44444700	0.85233800	-2.16546700
C	-2.84223000	-1.55684700	0.77533600
H	-1.26750900	-0.22869800	1.38510400
C	-3.87146000	-1.83567200	-0.11728600
H	-4.88488000	-1.14019600	-1.87761900
H	-4.48649000	-2.71846200	0.00413000
Cl	-2.55708600	-2.65392500	2.12913000
N	-1.49122000	1.62222100	-0.59551800
H	-2.05101900	2.46202700	-0.74214800
O	4.15363300	-1.58029700	-0.07972400
O	1.99885300	-2.36928900	-1.26844100
C	0.84286900	-2.87767400	-1.93815000
H	1.12131300	-3.86689300	-2.29352800
H	-0.00373100	-2.95892300	-1.25168300
H	0.57273100	-2.24557700	-2.78812300
C	5.38879700	-1.21353100	0.54391700
H	6.04084800	-2.07592800	0.42999600
H	5.83396200	-0.34751400	0.04843600
H	5.24072400	-1.00041700	1.60516400
O	-2.46033200	4.42779600	-0.38351100
H	-1.54515300	4.29620000	-0.05365700
H	-2.43047000	5.10919800	-1.06467500

T-2w

C	3.40734200	0.07485200	-0.11702500
C	3.10035700	1.29507600	0.44174600
C	1.77534000	1.79185100	0.41794400
C	0.74119500	0.99843100	-0.14574700
C	1.07860200	-0.23847800	-0.75646900

C	2.37404400	-0.69913300	-0.75189800
H	3.85990600	1.91827100	0.89379700
C	-0.57744800	1.55935600	-0.10169900
H	0.30990500	-0.81856600	-1.24249800
C	0.31234900	3.48771500	0.79503800
H	0.11499700	4.50171600	1.13322900
N	-0.76094000	2.81265800	0.33219700
N	1.54355800	3.04993500	0.90356800
C	-2.04160000	-0.45127300	-0.37309700
C	-2.92657600	-1.04619400	-1.28260400
C	-1.58249400	-1.19090700	0.72507900
C	-3.33420400	-2.36374700	-1.10118400
H	-3.28577000	-0.47240900	-2.12934000
C	-1.98907000	-2.51160600	0.86642300
H	-0.92805200	-0.74103500	1.46031000
C	-2.86263900	-3.12054600	-0.02828100
H	-4.01850900	-2.81509700	-1.81128900
H	-3.16650100	-4.15090000	0.10730400
Cl	-1.38974600	-3.43557700	2.24726900
N	-1.69768600	0.90535000	-0.55892400
H	-2.49759500	1.50376600	-0.79041300
O	4.63749200	-0.47745200	-0.14561000
O	2.79211500	-1.85796700	-1.31507500
C	1.82794100	-2.67999000	-1.97687300
H	2.37964300	-3.54349100	-2.34073300
H	1.04941600	-3.00748400	-1.28318900
H	1.37576100	-2.15228600	-2.82071000
C	5.72035700	0.23243800	0.46489400
H	6.59442300	-0.40087000	0.33525100
H	5.88519500	1.19276600	-0.02932100
H	5.53264000	0.38855500	1.52978000
O	-3.19632200	4.26136700	0.50850400
H	-2.32273500	3.79995100	0.49096800
H	-3.04684500	5.17621700	0.24447700
O	-4.10864800	2.40786300	-1.23548600
H	-4.94196100	1.97716300	-1.01406600
H	-4.00081500	3.17537300	-0.63117500

T-3w

C	-3.54574500	-0.93880500	-0.14232700
C	-2.90403500	-2.01367700	0.43073400
C	-1.49170500	-2.10390100	0.42081900
C	-0.72796100	-1.04773000	-0.14372000
C	-1.40231300	0.03389600	-0.76898300
C	-2.77545300	0.09762300	-0.77877600
H	-3.45480400	-2.82732700	0.88269100
C	0.69413700	-1.20214900	-0.09230400
H	-0.82681200	0.80662200	-1.25476300
C	0.40126000	-3.29344000	0.82799000
H	0.88460100	-4.19919000	1.18435300
N	1.23452500	-2.33548300	0.36658100
N	-0.90585500	-3.23565700	0.91750400
C	1.56004600	1.12800300	-0.34691700
C	2.30052300	1.95884000	-1.20255600
C	0.87963800	1.69700600	0.73981500
C	2.34252100	3.33062200	-0.98154300
H	2.84268900	1.51680200	-2.03016000
C	0.92578800	3.07354100	0.92053800
H	0.33297500	1.07724000	1.43842100
C	1.64643200	3.91317800	0.07910500

H	2.91803700	3.96182800	-1.65012900
H	1.66789900	4.98281100	0.24550400
Cl	0.05155000	3.77170900	2.28890900
N	1.57779200	-0.25849900	-0.57376400
H	2.45629400	-0.62679500	-0.95554300
O	-4.88240100	-0.76713200	-0.18589800
O	-3.50704200	1.07716700	-1.36067100
C	-2.81674800	2.13103200	-2.03666100
H	-3.59194600	2.78871400	-2.42243200
H	-2.17472800	2.68519700	-1.34737500
H	-2.22142600	1.73970300	-2.86569600
C	-5.71974500	-1.75777000	0.42014200
H	-6.73841100	-1.40657300	0.27588200
H	-5.59175700	-2.72705400	-0.06729900
H	-5.50780800	-1.84646800	1.48822300
O	3.82371300	-2.86732200	1.39447300
H	2.95243400	-2.62324600	0.99843500
H	3.84755000	-2.50133100	2.28556700
O	3.99205800	-0.97422300	-1.96317100
H	4.70206500	-1.45830200	-1.48280700
H	3.85819700	-1.42302800	-2.80539700
O	5.76848500	-2.33005400	-0.40585600
H	5.15401500	-2.53986000	0.33625600
H	6.51101500	-1.83641300	-0.04057700

T-4w

C	-3.85477800	-0.88187600	0.02618000
C	-3.18881000	-1.99534500	0.48707500
C	-1.78632500	-2.11436800	0.34074400
C	-1.05112000	-1.04899800	-0.24288900
C	-1.75463000	0.07530400	-0.75039600
C	-3.12092500	0.16854000	-0.62797800
H	-3.71503800	-2.81888800	0.95024200
C	0.36818900	-1.23429100	-0.32952700
H	-1.21066500	0.85956500	-1.25310900
C	0.09920100	-3.36970700	0.50127000
H	0.58652000	-4.30672100	0.75808500
N	0.91172100	-2.41225700	0.00498100
N	-1.18875500	-3.28305300	0.72812700
C	1.21544500	1.10509500	-0.55325400
C	1.83671700	1.96553100	-1.46898700
C	0.66466500	1.63307600	0.62253000
C	1.89503400	3.33200800	-1.21544700
H	2.26818600	1.55628400	-2.37518800
C	0.71747200	3.00452200	0.83575000
H	0.21152300	0.98465800	1.36108000
C	1.32613800	3.87426500	-0.06273200
H	2.37800900	3.98911900	-1.93042900
H	1.35694400	4.93928600	0.13011700
Cl	0.00458900	3.65610800	2.31486100
N	1.23017700	-0.28125700	-0.81667500
H	2.13795100	-0.62596600	-1.15676000
O	-5.18599400	-0.68391900	0.11221600
O	-3.87749800	1.19300800	-1.08920100
C	-3.22453700	2.26972100	-1.76608700
H	-4.01403300	2.96586000	-2.03896400
H	-2.50645500	2.76793900	-1.10984600
H	-2.71983100	1.91598200	-2.66882900
C	-5.98807900	-1.69097900	0.73827400
H	-7.00819700	-1.31714400	0.69998100

H	-5.92128900	-2.63592200	0.19407000
H	-5.68787800	-1.83767900	1.77841800
O	3.58798900	-3.22368300	-0.14381100
H	2.63218900	-2.96531700	-0.06135000
H	3.62895700	-4.17163100	-0.31319000
O	3.85335200	-0.98960400	-1.80629600
H	4.50899800	-0.45197900	-1.31476100
H	3.94159900	-1.89127200	-1.44804000
O	5.73801300	0.19303600	-0.12534200
O	5.31604100	-1.91757200	1.55975400
H	5.67007000	-0.49179300	0.57767700
H	5.56863500	1.04828800	0.28527900
H	4.72179700	-2.49122900	1.02898700
H	6.04483600	-2.46439700	1.87314000

T-5w

C	-3.77814900	-1.42747800	-0.12862000
C	-2.94792200	-2.36836500	0.43896400
C	-1.54328200	-2.20555800	0.41159800
C	-0.98542700	-1.03316900	-0.16458800
C	-1.84950400	-0.09079100	-0.78188400
C	-3.21215600	-0.27266700	-0.77497800
H	-3.33905500	-3.26550600	0.89913100
C	0.44216400	-0.93306700	-0.13011000
H	-1.42931100	0.77140200	-1.27578900
C	0.53270800	-3.04444100	0.79645100
H	1.17216000	-3.85029500	1.14694700
N	1.18247200	-1.95594300	0.32029100
N	-0.76083400	-3.21437200	0.90516600
C	0.83099100	1.52004900	-0.39271400
C	1.31004700	2.47200000	-1.30272500
C	0.11581400	1.94433500	0.73537200
C	1.06820400	3.82514800	-1.08945700
H	1.86684000	2.14580500	-2.17298300
C	-0.13061900	3.30033900	0.90764700
H	-0.23349700	1.23032100	1.46982300
C	0.33479100	4.25968100	0.01487600
H	1.44387100	4.55402800	-1.79926900
H	0.13317900	5.31133800	0.17535300
Cl	-1.04716400	3.81705000	2.32602300
N	1.13436900	0.15807100	-0.60676300
H	2.08568200	-0.02133300	-0.93238500
O	-5.12336400	-1.49745700	-0.15749700
O	-4.11283800	0.56038700	-1.34635700
C	-3.62970600	1.72094400	-2.02791500
H	-4.51461800	2.23082000	-2.40099800
H	-3.08707100	2.37915900	-1.34485500
H	-2.98597100	1.44223300	-2.86611100
C	-5.76426200	-2.62031000	0.45845400
H	-6.83056500	-2.45731000	0.32376700
H	-5.46942400	-3.55236200	-0.02907400
H	-5.52951400	-2.66594800	1.52436300
O	3.34241400	-1.28227800	2.24399800
H	2.63540600	-1.47516800	1.59620400
H	3.08289400	-1.69737500	3.07459100
O	3.78426800	-0.07572000	-1.95350600
H	4.61734200	0.21682100	-1.50884900
H	3.80119400	0.25328000	-2.85926400
O	6.05689100	0.34106700	-0.55363700
O	5.57026800	-1.98497300	0.75223600

H	5.99435600	-0.47217900	0.00771100
H	6.14471100	1.09900800	0.03492600
H	4.90183400	-1.75121100	1.42883300
H	5.04926100	-2.42130000	0.04509800
H	3.77610700	-1.88875600	-1.68048000
H	2.90455800	-2.69276400	-0.70111300
O	3.72701500	-2.74937000	-1.21661900

T-6w

C	-3.55803300	-1.31548500	-0.14128800
C	-2.59120100	-2.29652400	-0.11654900
C	-1.26218000	-2.01314000	-0.50688100
C	-0.90546000	-0.68707600	-0.86630300
C	-1.91957700	0.30456600	-0.92665800
C	-3.21852500	0.00931900	-0.58449500
H	-2.82334100	-3.31299300	0.17116800
C	0.48001900	-0.47097500	-1.17623400
H	-1.67258300	1.29885100	-1.26456200
C	0.82404400	-2.74580500	-1.03490700
H	1.52765400	-3.56471500	-1.16052800
N	1.29697700	-1.52426600	-1.33822900
N	-0.36406300	-3.04768400	-0.56489200
C	0.70590500	1.97796000	-0.72816700
C	0.90045000	3.17431000	-1.42611600
C	0.26564000	2.01314800	0.60050300
C	0.64557500	4.39365400	-0.80436900
H	1.24527200	3.14213100	-2.45323800
C	-0.00388000	3.24286800	1.18753400
H	0.14124700	1.09896800	1.16621600
C	0.17962400	4.44342200	0.50873900
H	0.79818000	5.31756200	-1.35121700
H	-0.03360100	5.38936200	0.99085400
Cl	-0.57753100	3.27659800	2.85658000
N	1.04588800	0.75747800	-1.37130500
H	2.02305800	0.74078900	-1.68879000
O	-4.84997500	-1.49136300	0.20164000
O	-4.25479100	0.88071400	-0.62867000
C	-4.00295300	2.21472800	-1.07641600
H	-4.96205000	2.72507700	-1.03082400
H	-3.28718500	2.71960700	-0.42273500
H	-3.63390900	2.21928500	-2.10535300
C	-5.26993800	-2.78481600	0.64959600
H	-6.32803900	-2.68493400	0.87824200
H	-5.13184700	-3.53262700	-0.13475100
H	-4.72475700	-3.08144100	1.54859100
O	4.02000400	-1.72884800	-1.89318600
H	3.03256300	-1.68197100	-1.81050800
H	4.24358000	-2.38396100	-2.56375800
O	3.90570300	1.03671300	-1.83566400
H	4.19792000	1.20619000	-0.92219700
H	4.18299000	0.12266200	-2.03212200
O	4.60755100	-1.73026600	0.84171900
H	4.62280800	-0.76679600	0.98406100
H	4.49717800	-1.85567700	-0.12158300
O	2.94713300	-3.20890600	2.43297700
H	3.52648200	-3.69040000	3.03363000
H	3.52697900	-2.66981400	1.84541000
O	4.64544900	1.13886100	0.94185400
H	5.49292900	1.53113200	1.18713600
H	3.97798800	1.55125500	1.50490000

O	0.53314100	-4.56451400	1.89331300
H	1.36366400	-4.06775800	2.03041300
H	0.11244400	-4.19068300	1.10086500

T-7w

C	3.25755100	-1.64035000	-0.32486700
C	3.34998400	-0.26679400	-0.27290100
C	2.22301700	0.54552500	-0.53249900
C	0.96786900	-0.05662300	-0.80621500
C	0.89704200	-1.47246600	-0.89205600
C	2.00475000	-2.25545000	-0.66334500
H	4.28730500	0.22500500	-0.05164000
C	-0.13141700	0.84268600	-1.03594100
H	-0.03605900	-1.94466600	-1.15351500
C	1.33169600	2.61989800	-0.85795700
H	1.46057100	3.69754200	-0.91220000
N	0.08764500	2.16812300	-1.08910500
N	2.39098300	1.90710200	-0.55382000
C	-2.08094900	-0.69666500	-0.75042900
C	-2.88150800	-1.46854500	-1.59662600
C	-2.00593100	-0.99573400	0.61519100
C	-3.59173800	-2.55122300	-1.08288400
H	-2.93500300	-1.22343900	-2.65119000
C	-2.70694900	-2.09585700	1.09320700
H	-1.44339500	-0.35876200	1.28823600
C	-3.50274300	-2.88485400	0.26767200
H	-4.21064000	-3.15111500	-1.74091200
H	-4.04222800	-3.73396600	0.66882900
Cl	-2.60274500	-2.48869300	2.81221300
N	-1.41184800	0.44238800	-1.28131900
H	-2.05231400	1.16411000	-1.63453400
O	4.27560400	-2.49396200	-0.09757600
O	2.03149200	-3.60827200	-0.73352100
C	0.83029100	-4.29446100	-1.09345000
H	1.08478300	-5.35163500	-1.09107700
H	0.03714700	-4.10626600	-0.36549700
H	0.49598900	-4.00014600	-2.09165500
C	5.55883500	-1.95561600	0.24046800
H	6.20573800	-2.81636400	0.39016100
H	5.94886700	-1.33890600	-0.57260200
H	5.50524300	-1.36996500	1.16105900
O	-1.88900600	4.14339700	-0.93097000
H	-1.13453200	3.50786100	-1.03573500
H	-1.57830100	5.02898700	-1.14951400
O	-3.53986800	2.25436800	-2.09007000
H	-4.22943200	2.08746400	-1.42326300
H	-3.13227500	3.10610100	-1.84582000
O	-3.12572200	3.31764300	1.44330900
H	-3.90732800	2.84912900	1.10000600
H	-2.68661300	3.71757500	0.66666100
O	-1.39189300	1.55313300	2.68190200
H	-0.77832800	2.04984800	3.23453200
H	-1.99915800	2.20691900	2.26923000
O	-5.29394400	1.94158300	0.15597700
H	-6.14379600	2.39924200	0.14070800
H	-5.46984500	1.04213600	0.45983400
O	6.08292900	2.86909500	2.35017800
H	5.98027700	3.67208200	2.87275300
H	5.61753000	3.02256600	1.49994500
O	4.79163600	3.27642600	-0.04566600

H	5.32764100	3.25850500	-0.84626200
H	3.95873900	2.77654400	-0.23714000

Table S1. Selected spatial parameters and energies of ground state of four structures of AG1478 rotamers complexed with one water molecule (P-1w) in the gas phase (optimized at B3LYP/6-311+G*).

		P-1w			
Parameter		**(1)**	**(2)**	**(3)**	**(4)**
<R2> (a.u.)		11540.3537	10967.7902	10797.8090	12233.6722
μ (D)		5.1725	7.6347	6.8047	**3.6749**
E_h (a.u.)		-1469.735099	-1469.729833	-1469.731679	-1469.730528
ZPE (kcal/mol)		188.783040	188.576890	188.857020	188.292300
E_h + ZPE (a.u.)		**-1469.434254**	-1469.429317	-1469.430716	-1469.430466
Rotational Const. (GHz)	**A**	0.4173	0.4680	0.4697	0.5160
	B	0.1073	0.1074	0.1116	0.0953
	C	0.0855	0.0930	0.0923	0.0805
HOMO-LUMO gap (eV)		**3.6791**	4.2993	4.2580	4.2942
HOMO (Ha)		-0.20141	-0.2266	-0.2117	-0.2351
LUMO (Ha)		-0.06620	-0.0686	-0.0552	-0.0773
ΔE_{Tot} (kcal/mol)		0.00	3.10	2.22	2.38
		T-1w			
		(1)	**(2)**	**(3)**	**(4)**
<R2> (a.u.)[a]		8841.5171	8532.2868	8230.0944	8864.7514
μ (D)[b]		4.1200	3.0395	**2.0863**	3.5443
E_h (a.u.)[c]		-1469.732375	-1469.734892	-1469.725746	-1469.728043
ZPE (kcal/mol)[d]		189.008020	189.277610	188.681290	188.339290
E_h + ZPE (a.u.)		-1469.431171	**-1469.433259**	-1469.425063	-1469.427905
Rotational Const. (GHz)	**A**	0.3190	0.2687	0.2841	0.2840
	B	0.1548	0.1830	0.1653	0.1659
	C	0.1246	0.1283	0.1463	0.1230
HOMO-LUMO gap (eV)[e]		4.2838	**4.2253**	4.4403	4.3282
HOMO (Ha)		-0.2261	-0.2209	-0.2309	-0.2290
LUMO (Ha)		-0.0687	-0.0657	-0.0677	-0.0699
ΔE_{Tot} (kcal/mol)[f]		1.31	0.00	5.14	3.36

[a] Electronic spatial extent in hatree
[b] Dipole moment in debye
[c] Total molecular energy in hatree
[d] Zero-point energy in kcal/mol
[e] Energy gap between highest occupied molecular orbital and lowest unoccupied molecular orbital in eV
[f] Energy destabilization relative to the most stable isomer in kcal/mol

Table S2. Selected spatial parameters and energies of ground state of six structures of AG1478 rotamers bound to two water molecule (P-2w) in the gas phase (optimized at B3LYP/6-311+G*).

	P-2w					
Parameter	**(1)**	**(2)**	**(3)**	**(4)**	**(5)**	**(6)**
<R2> (a.u.)	12117.2735	12059.9573	13349.7041	11413.1724	12948.6809	12683.1339
μ (D)	6.9528	7.9356	**2.5857**	9.7131	5.2900	5.3348
E_h (a.u.)	-1546.188112	-1546.190484	-1546.188902	-1546.186428	-1546.183234	-1546.186196
ZPE (kcal/mol)	204.034340	204.278200	203.759310	203.966190	203.387380	203.751800
E_h + ZPE (a.u.)	-1545.862963	**-1545.864946**	-1545.864191	-1545.861387	-1545.859116	-1545.861497
Rot. Const. (GHz) A	0.3557	0.3397	0.3604	0.3751	0.4251	0.4228
B	0.1027	0.1068	0.0929	0.1069	0.0906	0.0945
C	0.0838	0.0827	0.0739	0.0908	0.0782	0.0783
HOMO-LUMO gap (eV)	4.3102	4.2993	**4.2672**	4.3021	4.3080	4.2980
HOMO (Ha)	-0.2299	-0.2145	-0.2267	-0.2175	-0.2309	-0.2148
LUMO (Ha)	-0.0715	-0.0565	-0.0698	-0.0594	-0.07258	-0.0568
ΔE_{Tot} (kcal/mol)	1.24	0.00	0.47	2.23	3.66	2.16
	T-2w					
	(1)	**(2)**	**(3)**	**(4)**	**(5)**	**(6)**
<R2> (a.u.)	9783.5510	9782.9577	10014.4313	9663.9626	9825.5268	9476.0802
μ (D)	2.5945	2.5706	2.8414	2.1291	3.1990	**2.0927**
E_h (a.u.)	-1546.192652	-1546.192652	-1546.186083	-1546.199183	-1546.188237	-1546.178980
ZPE (kcal/mol)	204.622710	204.614520	203.800130	205.393300	203.948760	203.389040
E_h + ZPE (a.u.)	-1545.866565	-1545.866578	-1545.861307	**-1545.871868**	-1545.863224	-1545.854859
Rotat. Const. (GHz) A	0.2495	0.2495	0.2420	0.2213	0.2326	0.2403
B	0.1537	0.1537	0.1500	0.1716	0.1600	0.1480
C	0.1118	0.1118	0.1092	0.1128	0.1112	0.1254
HOMO-LUMO gap (eV)	4.2068	4.2065	4.3004	**4.2000**	4.2316	4.4806
HOMO (Ha)	-0.22445	-0.22441	-0.23116	-0.2200	-0.22595	-0.2375
LUMO (Ha)	-0.06985	-0.06982	-0.07312	-0.0656	-0.07044	-0.0728
ΔE_{Tot} (kcal/mol)	3.33	3.32	6.63	0.00	5.42	10.67

[a] Electronic spatial extent in hatree
[b] Dipole moment in debye
[c] Total molecular energy in hatree
[d] Zero-point energy in kcal/mol
[e] Energy gap between highest occupied molecular orbital and lowest unoccupied molecular orbital in eV
[f] Energy destabilization (relative energy difference) relative to the most stable isomer in kcal/mol

Table S3. Selected values of dipole moment (debye) and energies of ground state of four structures of AG1478 rotamers bound to three water molecules (P-3w) in the gas phase (optimized at B3LYP/6-311+G*).

	P-3w			
Parameter	**(1)**	**(2)**	**(3)**	**(4)**
μ **(D)**	6.6372	6.6376	7.6747	**4.3679**
HOMO-LUMO gap (eV)	4.2683	4.2683	4.2870	**4.1809**
E_h **+ ZPE (a.u.)**	-1622.302610	-1622.302604	-1622.302645	**-1622.310945**
ΔE_{Tot} **(kcal/mol)**	5.230	5.234	5.208	**0.000**
	T-3w			
	(1)	**(2)**	**(3)**	**(4)**
μ **(D)**	2.8020	1.3456	3.5662	**1.3473**
HOMO-LUMO gap (eV)	4.1918	**4.0672**	4.1382	4.0675
E_h **+ ZPE (a.u.)**	-1622.298358	-1622.309341	-1622.293538	**-1622.309343**
ΔE_{Tot} **(kcal/mol)**	6.893	0.001	9.918	**0.000**

Table S4. Selected values of dipole moment (debye) and energies of ground state of four structures of AG1478 rotamers bound to four water molecules (P-4w) in the gas phase (optimized at B3LYP/6-311+G*).

	P-4w			
Parameter	**(1)**	**(2)**	**(3)**	**(4)**
μ **(D)**	8.8133	4.8159	5.0003	**3.8824**
HOMO-LUMO gap (eV)	4.2484	4.2846	4.2353	**4.2111**
E_h **+ ZPE (a.u.)**	-1698.73301	-1698.733285	-1698.739464	**-1698.750851**
ΔE_{Tot} **(kcal/mol)**	11.195	11.023	7.145	**0.000**
	T-4w			
	(1)	**(2)**	**(3)**	**(4)**
μ **(D)**	2.6920	**1.3674**	2.3107	1.6350
HOMO-LUMO gap (eV)	4.2294	4.1872	4.2772	**4.0759**
E_h **+ ZPE (a.u.)**	-1698.731925	-1698.732469	-1698.739131	**-1698.746396**
ΔE_{Tot} **(kcal/mol)**	9.081	8.739	4.559	**0.000**

Table S5. Selected values of dipole moment (debye) and energies of ground state of four structures of AG1478 rotamers bound to five water molecules (P-5w) in the gas phase (optimized at B3LYP/6-311+G*).

	P-5w			
Parameter	**(1)**	**(2)**	**(3)**	**(4)**
μ **(D)**	4.6015	4.0680	**3.4410**	4.3375
HOMO-LUMO gap (eV)	4.2702	4.2887	**4.1888**	4.2503
E_h **+ ZPE (a.u.)**	-1775.170932	-1775.162351	**-1775.184644**	-1775.164725
ΔE_{Tot} **(kcal/mol)**	8.604	13.989	**0.000**	12.499
	T-5w			
	(1)	**(2)**	**(3)**	**(4)**
μ **(D)**	4.2740	**2.4043**	6.3786	6.3779
HOMO-LUMO gap (eV)	4.2702	4.2909	4.2332	**4.1192**
E_h **+ ZPE (a.u.)**	-1775.172324	-1775.174615	-1775.172291	**-1775.179012**
ΔE_{Tot} **(kcal/mol)**	4.197	2.759	4.217	**0.000**

Figure S1. Structural configuration of the most stable planar conformers complexed with n=1-7 water molecules in gas phase at B3LYP/6-311+G*.

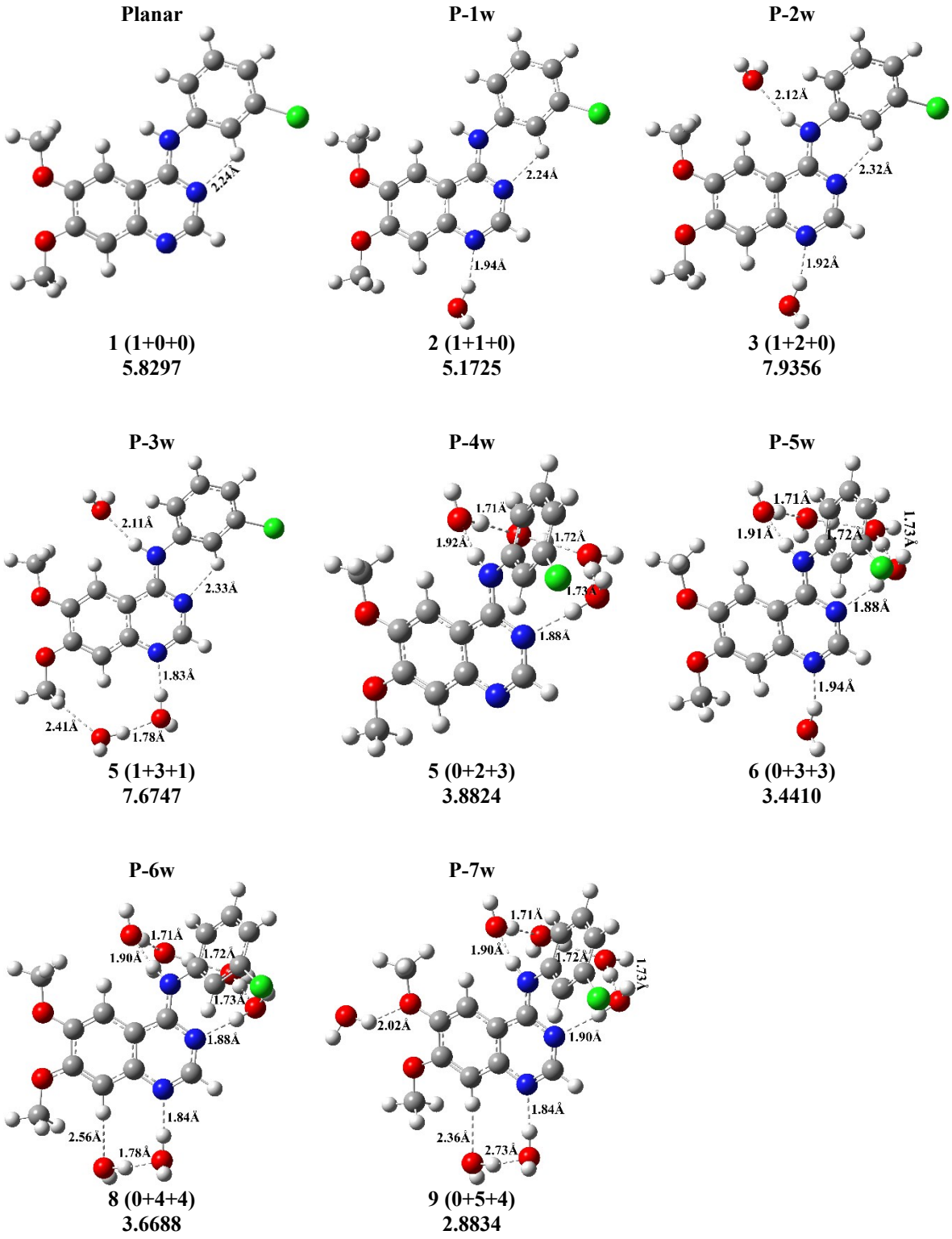

[1] Total number of H-bonds (Intramolecular H-bond + Intermolecular H-bonds between AG1478 and water + Intermolecular H-bonds between two water molecules)
[2] Dipole moment (Debye)

Figure S2. Structural configuration of the most stable twisted conformers complexed with n=1-7 water molecules in gas phase at B3LYP/6-311+G*.

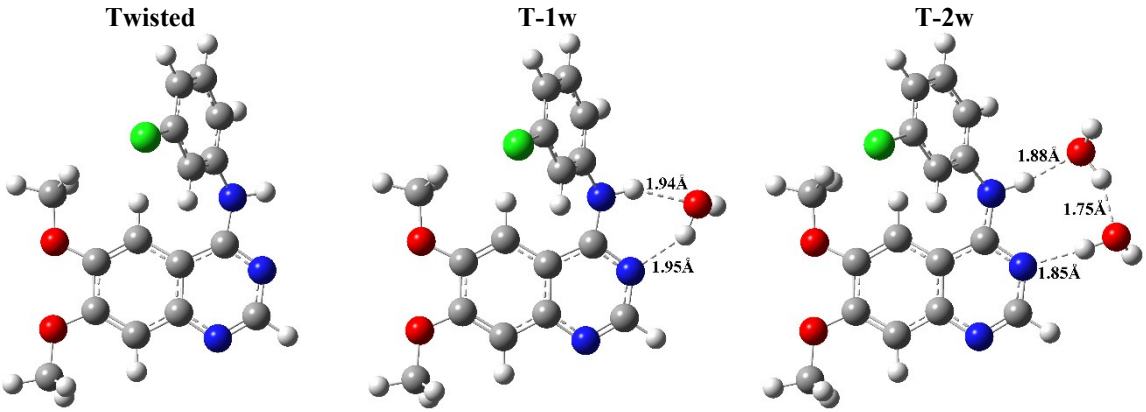

	Twisted	T-1w	T-2w
H-bond[1]	0	2 (2+0)	3 (2+1)
DM[2]	3.0792	3.0395	2.1291

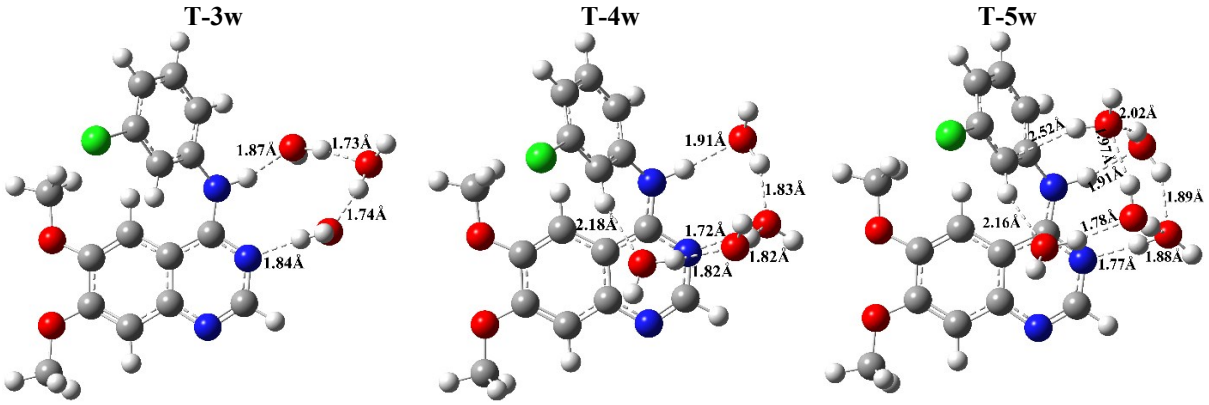

	T-3w	T-4w	T-5w
H-bond[1]	4 (2+2)	6 (3+3)	9 (4+5)
DM[2]	1.3473	2.3107	2.4043

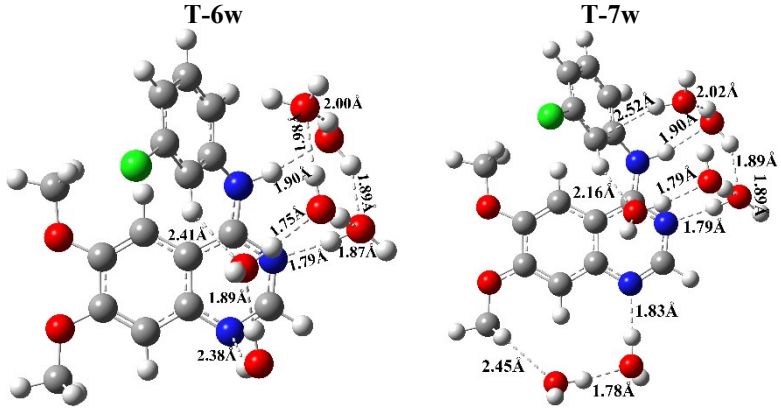

	T-6w	T-7w
H-bond[1]	10 (4+6)	11 (5+6)
DM[2]	6.6983	4.1771

[1] Total number of H-bonds (Intramolecular H-bond + Intermolecular H-bonds between AG1478 and water + Intermolecular H-bonds between two water molecules)
[2] Dipole moment (Debye)

Figure S3. Structural configuration of the most stable planar conformers complexed with n=1-7 water molecules in DMF at B3LYP/6-311+G*.

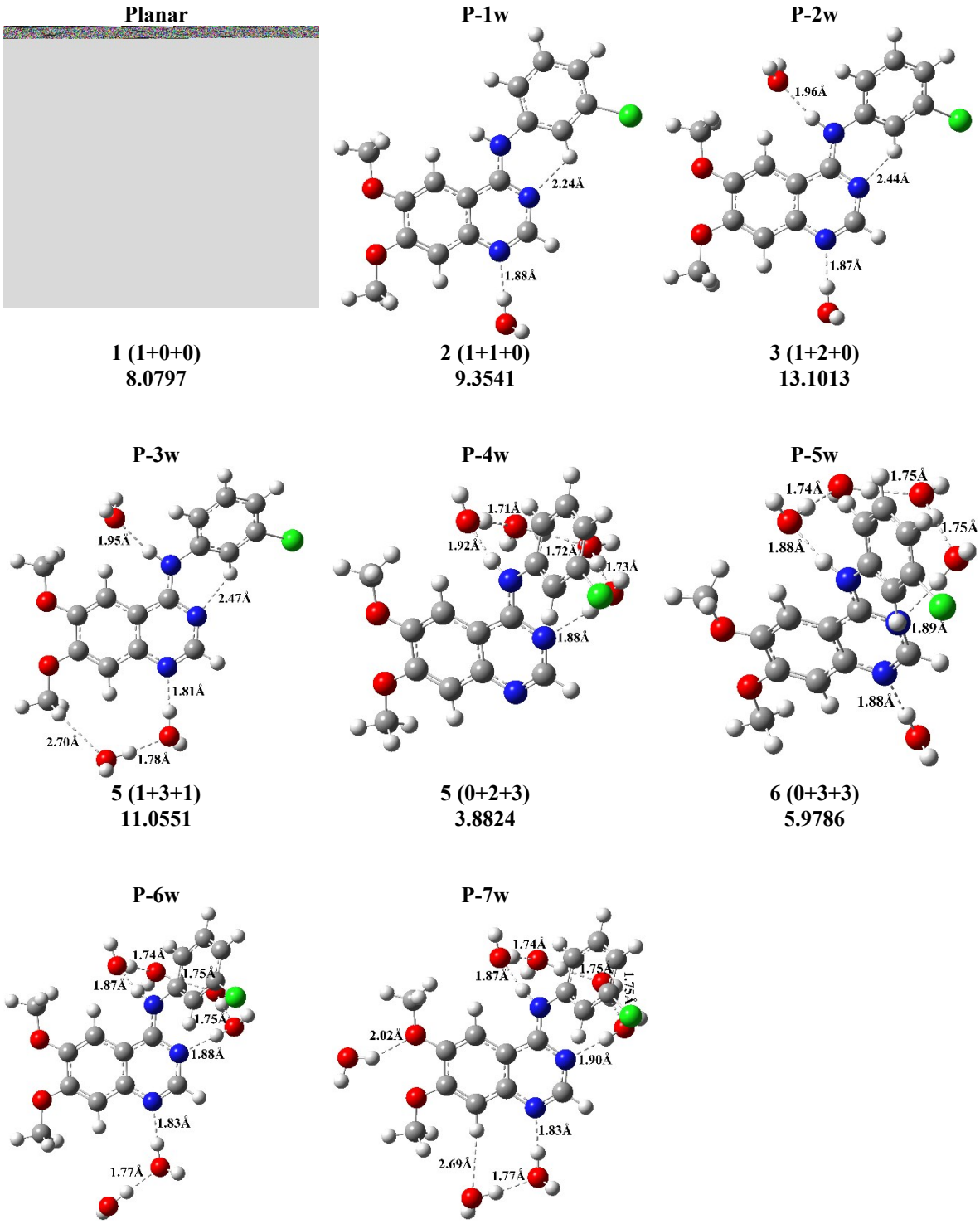

[1] Total number of H-bonds (Intramolecular H-bond + Intermolecular H-bonds between AG1478 and water + Intermolecular H-bonds between two water molecules)
[2] Dipole moment (Debye)

Figure S4. Structural configuration of the most stable twisted conformers complexed with n=1-7 water molecules in DMF at B3LYP/6-311+G*.

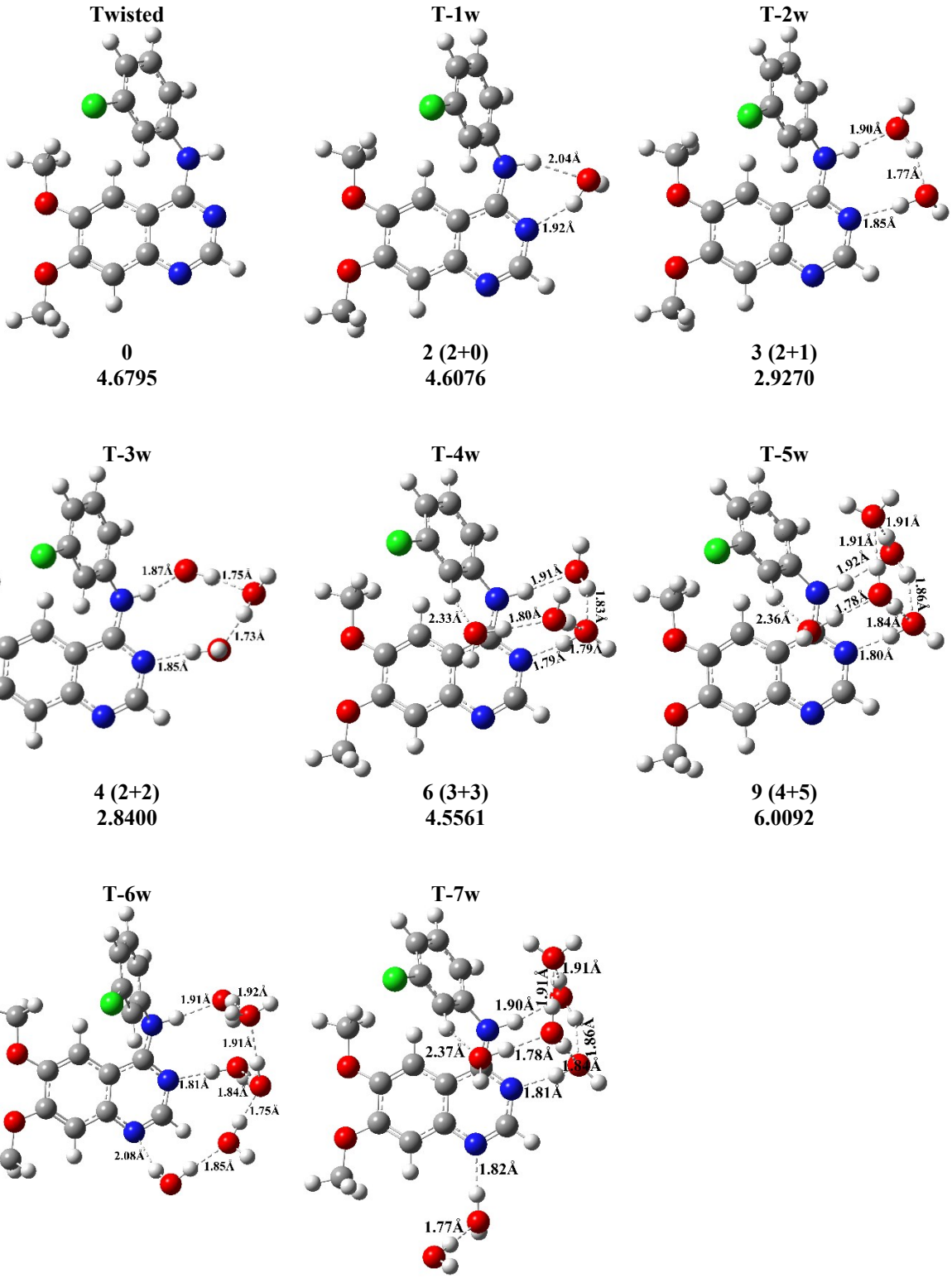

H-bond[1]	**0**	**2 (2+0)**	**3 (2+1)**
DM[2]	**4.6795**	**4.6076**	**2.9270**
H-bond[1]	**4 (2+2)**	**6 (3+3)**	**9 (4+5)**
DM[2]	**2.8400**	**4.5561**	**6.0092**
H-bond[1]	**8 (3+5)**	**10 (4+6)**	
DM[2]	**10.1874**	**10.2738**	

[1] Total number of H-bonds (Intramolecular H-bond + Intermolecular H-bonds between AG1478 and water + Intermolecular H-bonds between two water molecules)
[2] Dipole moment (Debye)

Figure S5. Residual plot for a) linear fitting, b) Quadratic fitting and c) Cubic fitting of Stern-Volmer plot

a)

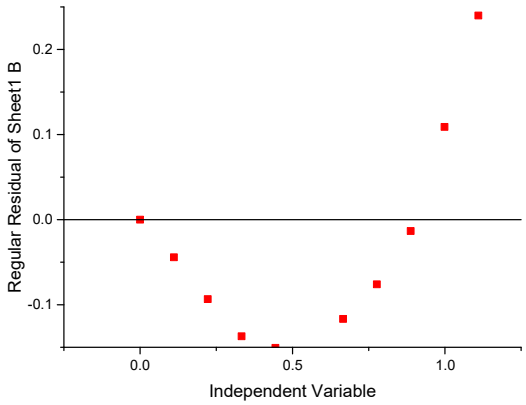

b)

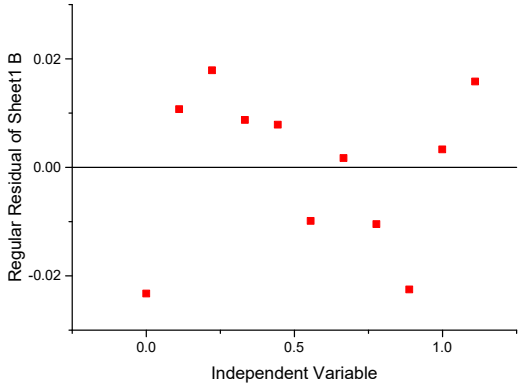

c)

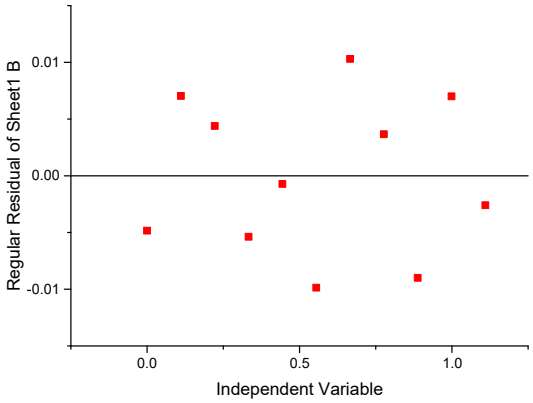

Chapter V

Prototropic States of AG1478

For cancer cells diagnosis and targeting, various fluorescence-labelling probes [166-169] and functionalized nanoparticles [170, 171] have been developed. However the synthesis of such probes and nanoparticles is quite complicated and expensive. Their usage has several disadvantages such as system instability, non-ignorable background signal and photobleaching [172]. Thus it is a great advantage if an anticancer ligand can be a self pH-reporter of its microenvironment. This would help in monitoring drug distribution in cells and organs and predicting the binding interactions with the target macromolecule. In addition, it helps in studying drug cellular metabolisms and gaining insights into the pH-dependent physiological and pathological processes [173-175].

The pH of physiological fluids varies greatly from acidic to weak basic 1.5-8.5 in human body. Moreover, the pH differs intracellularly in a typical mammalian cell from 4.7 in lysosome to 8.0 in mitochondria [176, 177]. It was found that cancer cells are characterized by abnormal intracellular acidic pH values [171, 178]. During transit of AG1478 to its cognate kinase, it will encounter different pH environments that could have a major influence on the structural and electronic configurations. To address this, we report the UV-Vis spectroscopic and computational studies on AG1478 as a function of solution pH.

Absorption spectrum of AG1478 was found sensitive to solution pH. Optical density and absorption maximum of AG1478 varied significantly with the change in pH as can be seen in **figure 5.1**. The acid dissociation constant (pKa) of AG1478 was estimated, for the first time, at 5.58 ± 0.01. On the basis of computational spectra and transition energies, the experimental spectra of AG1478 in acidic solution were assigned to a two twisted conformers protonated at N(1) and N(3) of the quinazoline moiety. At pH 7–12, only the neutral planar conformer contributed to the observed spectra. The absorption spectra at pH> 12 were fitted to a mixture of two neutral and two deprotonated conformers of AG1478. Hence, our study revealed a pH-induced changes in the conformational and electronic configurations of AG1478.

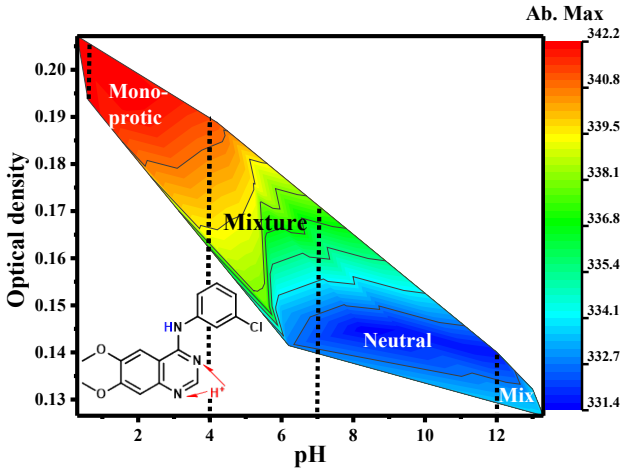

Figure 5.1. The 2D contour plot of AG1478 optical density and absorption maximum as a function of solution pH. The arrows on 2D structure of AG1478 refers to the protonation sites while the inserted labels denotes the prototropic state of AG1478 within a specified pH range.

This chapter is presented in the form of the published paper, **Muhammad Khattab**, Feng Wang and Andrew H.A. Clayton, *A pH-induced conformational switch in a tyrosine kinase inhibitor identified by electronic spectroscopy and quantum chemical calculations, Sci. Rep.* 7 (2017), 16271.

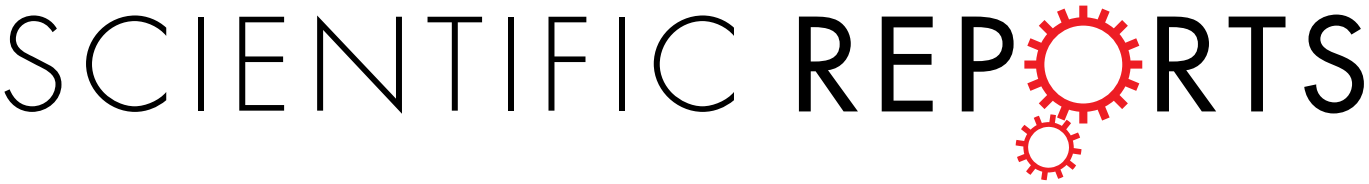

OPEN

Received: 13 September 2017
Accepted: 14 November 2017
Published online: 24 November 2017

A pH-induced conformational switch in a tyrosine kinase inhibitor identified by electronic spectroscopy and quantum chemical calculations

Muhammad Khattab[1], Feng Wang[2,3,4] & Andrew H. A. Clayton[1]

Tyrosine kinase inhibitors (TKIs) are a major class of drug utilised in the clinic. During transit to their cognate kinases, TKIs will encounter different pH environments that could have a major influence on TKI structure. To address this, we report UV-Vis spectroscopic and computational studies of the TKI, AG1478, as a function of pH. The electronic absorption spectrum of AG1478 shifted by 10 nm (from 342 nm to 332 nm) from acid to neutral pH and split into two peaks (at 334 nm and 345 nm) in highly alkaline conditions. From these transitions, the pKa value was calculated as 5.58 ± 0.01. To compute structures and spectra, time-dependent density functional theory (TD-DFT) calculations were performed along with conductor-like polarizable continuum model (CPCM) to account for implicit solvent effect. On the basis of the theoretical spectra, we could assign the AG1478 experimental spectrum at acidic pH to a mixture of two twisted conformers (71% AG1478 protonated at quinazolyl nitrogen N(1) and 29% AG1478 protonated at quinazolyl nitrogen N(3)) and at neutral pH to the neutral planar conformer. The AG1478 absorption spectrum (pH 13.3) was fitted to a mixture of neutral (70%) and NH-deprotonated species (30%). These studies reveal a pH-induced conformational transition in a TKI.

Determination of acid dissociation constant (pKa) of drugs gains paramount significance from the perspective of dosage form formulation, pharmaceutical analysis, and studying drug pharmacokinetics[1,2]. Drug solubility, lipophilicity, protein binding and membrane permeability are also influenced by its pKa value[3]. For instance, basic drugs with pKa > 7.4 (blood pH) are ionized displaying slower diffusion rates across cellular membranes[2]. Hence the drug ionization constant is one of its very important physicochemical properties.

Several techniques[4] have been used for pKa determinations such as potentiometric titration[5,6], UV-Vis spectroscopy[7,8], reverse-phase high performance liquid chromatography[9], and capillary electrophoresis[10]. UV-Vis spectroscopy takes advantage over other techniques since it is accurate, precise, reproducible and cost-effective using only micromolar concentrations of samples. It has been used for exploring electronic properties of the ground and excited states of fluorophores[11,12]. It has helped in studying physicochemical phenomena like FRET[13], proton transfer[14,15] and solvatochromism[16,17]. The two prerequisites for successful determination of pKa by UV-Vis spectrophotometry are a) presence of chromophore near to ionization centre and b) change in absorbance spectrum as a function of compound ionization[2]. For this reason, optical pH probes have gained a wide range of applications in analytical and biomedicinal chemistry[18]. These probes have been used for measuring intracellular pH[19,20] and monitoring blood pH[21]. Such probes are cornerstone for the development of chemical sensors used in cell biology, biomedical diagnostics and environmental monitoring[22,23].

[1]Centre for Micro-Photonics, Faculty of Science, Engineering and Technology, Swinburne University of Technology, Melbourne, Victoria, 3122, Australia. [2]Molecular Model Discovery Laboratory, Department of Chemistry and Biotechnology, Faculty of Science, Engineering and Technology, Swinburne University of Technology, Melbourne, Victoria, 3122, Australia. [3]School of Chemistry (Bio21 Institute), University of Melbourne, Parkville, Victoria, 3052, Australia. [4]School of Physics, University of Melbourne, Parkville, Victoria, 3052, Australia. Correspondence and requests for materials should be addressed to F.W. (email: fwang@swin.edu.au) or A.H.A.C. (email: aclayton@swin.edu.au)

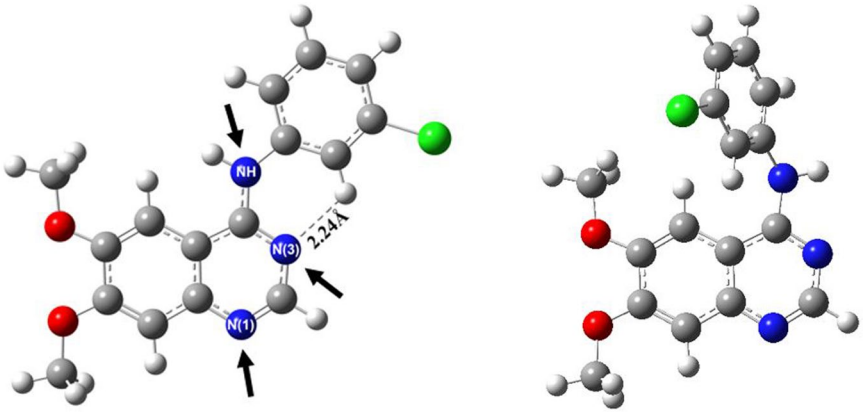

Figure 1. Molecular structure of AG1478 in its planar and twisted conformations[55]. White, grey, blue, red and green colors of atoms denotes to hydrogen, carbon, nitrogen, oxygen and chlorine atoms respectively. Dashed line and label refers to the intramolecular hydrogen bond and its length.

Numerous studies reported that the protonation pattern of a chromophore can affect its UV-Vis absorption and fluorescence spectrum[7,8,24]. Protonation in some cases causes a bathochromic shift of absorption maxima with varying optical densities of absorbance bands[25–27]. Accordingly, the acid-base properties of a chromophore can be evaluated by means of absorption/fluorescence spectroscopy[24]. A number of theoretical studies have also been performed to investigate the protonation processes[28,29], the electronic and geometric structures of the excited prototropic states[30–32] and protonation microequilibria[33,34].

Tyrosine Kinase Inhibitors (TKIs) are organic compounds showing anti-proliferative activity against cancer cells[35]. In the last two decades, extensive research has been conducted to develop new generations of selective TKIs with higher potency and resistance to tyrosine kinase mutations[36–38]. 4-anilinoquinazoline-based TKIs have been intensively studied, leading to a number of FDA-approved drugs such as Afatinib[39], Erlotinib[40], Gefitinib[41], Lapatinib[42], and Vandetanib[43].

AG1478 is one of the tyrosine kinase inhibitors[44,45] besides being a potential DNA intercalating agent[46]. It inhibits cell growth through binding to epidermal growth factor receptor. Preclinical and clinical studies showed its selectivity and efficacy to inhibit hepatocellular carcinoma[45], autocrine growth in human lung and prostate cancer cell lines[47], cisplatin-resistant human lung adenocarcinoma[48], and proliferation of nasopharyngeal carcinoma CNE2 cells[49]. Studies on active pharmaceuticals which bind to cell DNA emphasised that the cationic form of a drug intercalates with DNA bases more strongly than neutral species, while the anionic form of a chromophore is a poor intercalating agent due to the columbic repulsion between negatively charged DNA backbone and drug[50–52].

Our own studies on AG1478 have revealed that the spectroscopic properties are sensitive to both environment[53,54] and AG1478 conformational state[55]. For example, two conformers- one planar and the other twisted- were identified based on quantum chemical calculations and experimental absorption spectra[55]. Structures of AG1478 in its planar and twisted conformations are depicted in Fig. 1. Two nitrogens on the quinazoline ring are denoted N1 and N3, respectively, while the aniline ring amino moiety is denoted by NH linker.

However, the detailed optical properties and electronic structure of prototropic forms of AG1478 have not been reported so far. In this article, we probe the UV-Vis spectral properties of AG1478 as a function of solution pH. A theoretical investigation of protonated, neutral and deprotonated forms of AG1478 is also performed. Based on our theoretical calculations, we assign the observed AG1478 spectra gaining insights into the geometry and electronic excitations of the prototropic forms of AG1478. We discuss the implications of our findings to drug pharmacodynamics.

Results

Absorption spectroscopy study. Absorption spectra of AG1478 in different pH-buffered solutions (pH 0.3 to 13.3) were measured. Figure 2 depicts selected absorption spectra for AG1478 at pH 2, 8.3 and 13.3. The recorded absorption spectra in strongly acidic conditions at pH 0.3–2.3 (0.3, 0.6, 0.9, 1.2, 1.6 and 2) exhibited a prominent peak in the 300–400 nm region with λ_{max} at 342 nm. Spectra of AG1478 in alkaline solutions at pH 7.3–12 had relatively reduced optical densities in the 300–400 nm region compared to acidic conditions and were shifted to the blue with a λ_{max} at 332 nm. The highly alkaline solutions of AG1478 (pH 13.3) displayed two overlapping peaks at 334 nm and 345 nm with enhanced absorbance in 380–400 nm region with respect to AG1478 spectrum at pH 8.3, as indicated in Fig. 2.

A plot of the longest wavelength absorption peak of AG1478 in all studied buffer solutions is depicted in Fig. 3. The absorbance maximum of AG1478 was *ca*. 342 nm in pH 0.3–2.3 buffered solutions. A hypsochromic shift of 0.0 ± 0.4 nm, 0.3 ± 0.3 nm and 1.6 ± 0.4 nm was observed by changing pH 2.3 to 3.2, 3.2 to 4.2 and 4.2 to 5.2, respectively. This systematic blue shift continued reaching its maximum at pH 7.3 (10.0 ± 0.4 nm, relative to pH 2.3), refer to Fig. 3. The absorption maximum was then constant at *ca*. 332 nm over the pH range of 7.3–12. The broad absorption band of AG1478 at pH 13 and 13.3 showed two absorption maxima at *ca*. 334 nm and 345 nm.

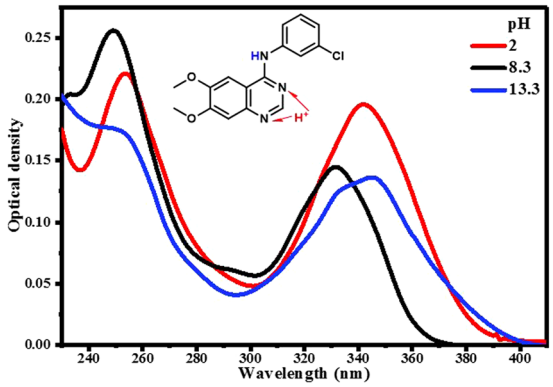

Figure 2. Representative absorption spectra of AG1478 in aqueous buffered solutions at pH 2, 8.3 and 13.3.

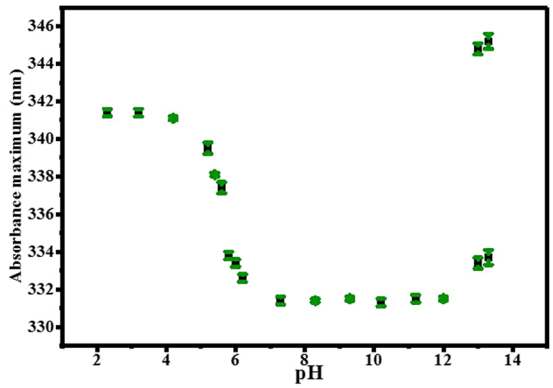

Figure 3. Wavelength absorption maxima in 300–400 nm region of AG1478 in aqueous buffered solutions at pH ranging from 2.3 to 13.3. Values were determined from the average of five scans. Error bars indicate 95% confidence interval widths.

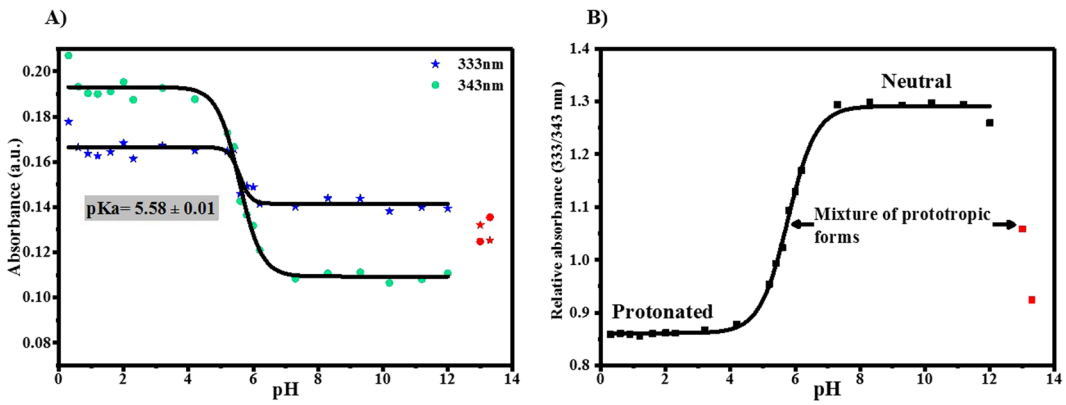

Figure 4. (**A**) Plot of influence of solution pH on the optical density of AG1478 at 333 nm and 343 nm and (**b**) Plot of 333/343 nm absorbance ratio as a function of solution pH. Data points (marked red) at pH 13 and 13.3 were excluded from Boltzmann function fit.

A plot of the optical density of AG1478 at 333 nm and at 343 nm as a function of solution pH is illustrated in Fig. 4a. The 333 nm and 343 nm wavelengths were selected as a measure for the absorbance due to the planar and twisted conformers, respectively. At both wavelengths, the optical densities remained relatively constant in the pH range 1–4, decreased in the pH range 4–7 and then plateaued from pH 7–12. These features are consistent with an equilibrium transition from one protonation form to another. Using a Boltzmann function to fit the data in the pH range 1–12, we extracted a pKa of 5.58 ± 0.01 for the AG1478 molecule. Further changes to AG1478 optical density at the very end and beyond the practical pH scale *viz.* $pH \geq 12$ and $pH \leq 0.6$ can be seen in Fig. 4a, but these values were not analysed further. We also plotted the change in ratio of AG1478 absorbance at 333 nm

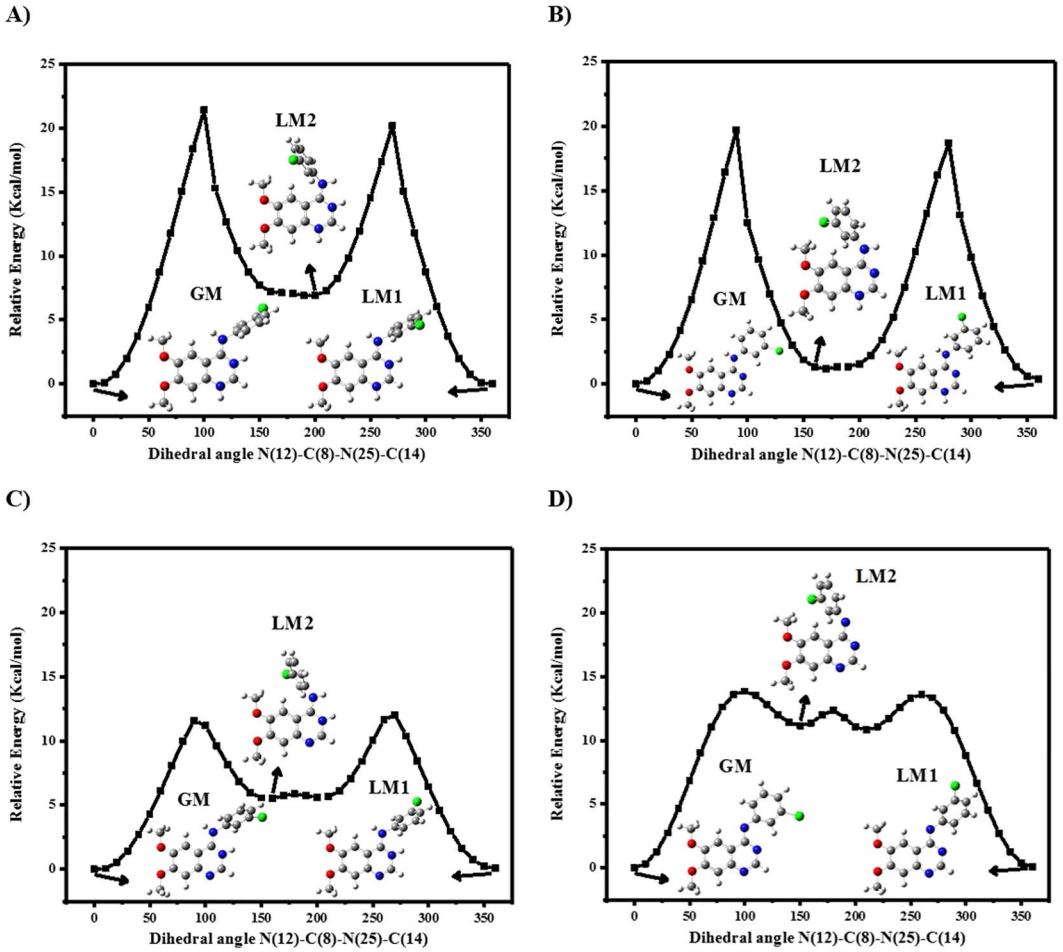

Figure 5. Potential energy surface scan of (**a**) $^{+}$N(1)H^{+}N(3)H, (**b**) $^{+}$N(1)H, (**c**) $^{+}$N(3)H and (**d**) deprotonated structures of AG1478 at B3LYP/6-31 G in vacuum. Arrows refers to the 3D structure of AG1478 at a corresponding point on PES surface. White, grey, blue, red and green colors of atoms denotes to hydrogen, carbon, nitrogen, oxygen and chlorine atoms respectively.

to 343 nm as a function of pH, Fig. 4b. The transition at acid pH is very clearly visible from this plot as well as a second transition at pH > 12. The pKa values extracted from Fig. 4b (pKa AG1478 = 5.7) agreed well with the values obtained from Fig. 4a (pKa AG1478 = 5.6).

To summarize, it is clear that the protonation state of AG1478 influences significantly its spectroscopic properties. However based on the experiments alone it is not possible to assign the spectra to specific species. The changes in AG1478 spectral properties upon changing solution pH could be attributed to a proton-induced change in AG1478 conformation and/or a change in AG1478 electronic configuration. Therefore, we aim to computationally explore the geometrical structures and vertical excitation energies of neutral and various ionic species of AG1478 in the next section.

Computational study. In our theoretical study, we considered five prototropic structures of AG1478. We performed potential energy surface (PES) scan for four AG1478 structures in gas phase, diprotonated at N(1) N(3), monoprotonated at each N(1) and N(3) and deprotonated at NH linker as shown in Fig. 5a,b,c and d. PES scan of neutral form of AG1478 was published earlier by Khattab *et al.*[55] All PES scan plots are depicted in Fig. 5 together with 3D structures of the global minimum and local minima.

PES of diprotonated AG1478 (Fig. 5a) showed one global minimum with calculated energy difference of ≈7 kcal/mole with the second local minimum. All diprotonated structures had anilino group twisted relative to quinazolyl moiety.

The PES of the protonated AG1478 at N(1) exhibited a global minimum and two local minima with a very small energy difference (≈2 kcal/mole), as shown in Fig. 5b. Unlike the diprotonated species, the global minimum structure of protonated AG1478 at N(1) had the quinazoline and aniline rings in a planar conformation. Similar to the diprotonated form, the aniline group was twisted relative to quinazoline ring in the highest energy local minimum.

The PES of AG1478 monoprotonated at N(3) had a global minimum and two local minima with a nearly similar energy difference to the PES di-protonated at N(1)N(3) (≈6 kcal/mole). The two local minima at step 17

Structure	GM	LM1	LM2
$^{+}$N(1)H^{+}N(3)H	−315.99	−315.77	−311.54
$^{+}$N(1)H	−168.67	−168.47	−165.79
$^{+}$N(3)H	−164.99	−164.99	−161.07
Deprotonated	292.20	292.22	297.26

Table 1. The proton binding energy values (kcal/mole) of ionic forms of AG1478 in water at B3LYP/6-311+G*. *GM, global minimum; LM, local minimum.

and 21 were almost identical and therefore we attributed these to one structural form of AG1478. All protonated structures at N(3) were identified as twisted conformers similar to N(1)N(3) protonated structures as indicated in Fig. 5c.

In case of deprotonated structure of AG1478, PES scan showed two higher energy local minima than the global minimum (>10 kcal/mole) as can be seen in Fig. 5d. Minima at step 16 and 22 are almost structurally similar, therefore one of them was considered. Deprotonated AG1478 were identified as planar, pseudo-planar and twisted structures as calculated for monoprotonated N(1) structures.

The global minimum and the first local minimum structures in Fig. 5b and d were planar and pseudo-planar conformers respectively. Generally, planar conformations of AG1478 is energetically favoured when a proton at N(1) site is added or abstracted. However, addition of proton to N(3) site results in breakage of intramolecular H-bond responsible for maintaining structural coplanarity and extra stability of planar conformation over the twisted one. Therefore, N(3) protonated structures adopted only twisted configurations.

Global minima (GM) and local minima (LM) geometries were re-optimised using B3LYP/6-311+G* model and dielectric constant of water. A list of molecular coordinates of all studied structures is in Supplementary Materials Table S1. We calculated the binding energy for formation of prototropic states of AG1478 which are listed in Table 1. The proton binding energy was calculated by subtracting summation of total molecular energy (incl. zero point energy correction) of global minimum structure of neutral AG1478 and no/one/two proton(s) from total molecular energy of deprotonated/monoprotonated/diprotonated structures respectively.

Formation of diprotonated structure was theoretically calculated as the most favourable prototropic structure of AG1478. The maximum energy difference between minima structures was estimated <5 kcal/mole. Binding energy values exhibited small energy difference between monoprotonated AG1478 structures with energetic preference to N(1) protonation. A small energy gap (<4 kcal/mole) between different minima was revealed suggesting easy interconversion between conformers of same protonated structures. Also, the energy difference between different minima of $^{+}$N(1)H and $^{+}$N(3)H structures was less than 8 kcal/mole. In contrary, deprotonation of NH linker required spending energy (endothermic process). The order of structural stability based on binding energy calculations is as follows $^{+}$N(1)H^{+}N(3)H > $^{+}$N(1)H > $^{+}$N(3)H > deprotonated.

An earlier study on quinazoline moiety is in line with our results. Sawunyama and coworkers calculated the proton binding affinity to each nitrogen of quinazoline[56]. Results revealed that protonation proceeds at any of quinazolyl nitrogens with binding affinity difference by 0.1–1.3 kcal/mole depending on applied model. Diprotonation at two nitrogens had a greater binding energy than one bound proton. It was concluded that quinazoline protonation proceeds as follows dication ≫ N3 monocation > N1 monocation. In contrary to our results, N3 monocation is slightly energetically favoured than N1 counterpart[56]. It might be due to the lack of 4-substituent group which would alter electron density of quinazoline ring.

Absorption spectra of protonated AG1478 were calculated deploying TD-DFT and the dielectric constant of water ($\varepsilon = 78.35$) in CPCM model. Complete spectra of various prototropic forms of AG1478 are depicted in Supplementary Materials Fig. S2. The lowest excitation energy transitions along with the corresponding oscillator strength and molecular orbital (MO) transitions are listed in Table 2. The maximum wavelength of the lowest lying electronic transitions of AG1478 ranged from 322 to 386 nm, depending on protonation state and conformation, however the number of transitions and MO contribution also varied to some extent. In contrary to all other studied structures, the diprotonated form exhibited two transitions in 300–400 nm region where HOMO → LUMO contributed to the lowest energy transition ($S_0 \rightarrow S_1$) at 355–364 nm and HOMO → LUMO+1 and HOMO-2 → LUMO contributed to the higher energy transition ($S_0 \rightarrow S_2$) at 321–327 nm. For the monoprotonated, neutral and deprotonated structures, HOMO → LUMO transition was the main contributing transition for only one electronic transition as indicated in Table 2.

To assign the experimental spectra, we exploited solver tool in excel to find the minimal value of sum of squared residuals between observed spectrum and theoretically fitted spectrum within the 300–400 nm region. In Fig. 6, the normalised experimental spectrum of AG1478 in acidic (pH 3.2), alkaline (pH 9.3) and strong alkaline (pH 13.3) solutions are depicted along with the best fit to the sum of theoretical spectra within region of 300–400 nm. To fit theoretical spectra to experiment at pH 3.2, the neutral and deprotonated forms of AG1478 were excluded since they cannot experimentally exist at low pH (AG1478 pKa = 5.6). The diprotic structures were excluded from the fit because the calculated diprotonated structures exhibited two transitions at *ca*. 360 nm and 324 nm while the experiment showed only one absorption maximum at 342 nm. Thus, monoprotic forms of AG1478 were only used to fit the experimental spectrum. We found that the combination of 71% of monoprotonated AG1478 (N1-LM2) and 29% of monoprotonated AG1478 (N3-LM1) accounted for the AG1478 spectrum at pH 3.2. The two structures adopted twisted conformations as can be seen in Fig. 6a.

The absorption maximum of AG1478 at pH 9.3 was observed at 332 nm while the lowest energy transitions of the deprotonated structures were calculated at 371 nm, 368 nm and 386 nm. We therefore excluded the anionic

Structure	Exc. E (nm)	Osc. str.	No. of transitions	Transition contribution
N1N3-GM	355 321	0.3279	2	H→L (91%)
		0.1346		H→L+1 (79%), H-2→L (16%)
N1N3-LM1	356 322	0.3335	2	H→L (92%)
		0.1373		H→L+1 (81%), H-2→L (15%)
N1N3-LM2	364 327	0.2010	2	H→L (89%)
		0.1435		H→L+1 (76%), H-2→L (15%)
N1-GM	363	0.7613	1	H→L (98%)
N1-LM1	356	0.6740	1	H→L (98%)
N1-LM2	347	0.3198	1	H→L (96%)
N3-GM	322	0.2761	1	H→L (91%)
N3-LM1	326	0.3103	1	H→L (92%)
N3-LM2	347	0.2828	1	H→L (95%)
Neut-GM	331	0.6556	1	H→L (97%)
Neut-LM	337	0.3158	1	H→L (96%)
De-GM	371	0.7830	1	H→L (98%)
De-LM1	368	0.6127	1	H→L (98%)
De-LM2	386	0.2769	1	H→L (97%)

Table 2. Wavelength, oscillator strength and molecular orbital transition contribution of the longest wavelength excitation bands in the 300–400 nm region for AG1478 in water using B3LYP/6-311+G* model. Only transition contribution > 10% is considered significant and listed in the table. *GM, global minimum; LM, local minimum; H, HOMO; L, LUMO; Neut, Neutral.

forms of AG1478, especially the plateaued AG1478 absorbance at pH 7.2–12 (Fig. 4a) indicated presence of only one prototropic state. The absorption maximum of GM and LM structures of neutral AG1478 were computed at 331 nm and 337 nm respectively. However, only the neutral planar (GM) conformer was reasonably fit to the experimental spectrum at pH 9.3 as shown in Fig. 6b.

The observed spectrum of AG1478 at pH 13.3 exhibited two absorption maxima at 334 and 345 nm. From the pH titration plot in Fig. 4b, we have a mixture of species at pH 13 (transition region). The calculated absorption maxima lie within 331–337 nm and the 368–386 nm for neutral and deprotonated structures respectively. Therefore, the experimental spectrum was fit to a mixture of neutral and deprotonated species. A mixture of neutral (GM), neutral (LM), deprotonated (GM) and deprotonated (LM2) forms contributed collectively by 28%, 42%, 26% and 4% respectively to the measured spectrum as indicated in Fig. 6c. Note that the deprotonated LM1 form was considered in the fitting to the spectrum but had a negligible contribution (<0.1%). It is noteworthy that the twisted neutral conformation (Neut-LM) was 1.5 fold more populated than the planar configuration (Neut-GM). However, the planar structure of deprotonated AG1478 contributed by more than 6-fold compared to its twisted counterpart.

Discussion

By studying the pH-dependent spectral properties of the tyrosine kinase inhibitor AG1478 and combining these observations with theoretical calculations, we obtained new insights into acid/base interactions and geometrical/electronic configurations of the drug. Based on theoretical calculations, we identified the protonation sequence of AG1478 nitrogens and how it is correlated to experiments. The acid dissociation constant of the AG1478 molecule was determined from the experimental pH-titration curve. Combined experimental and theoretical studies enabled us to assign each experimental spectrum to the relevant contribution of AG1478 structures. We also identified structural conformations of AG1478, whether the aniline and quinazoline moieties are coplanar or twisted, at different pH values which has not been reported so far.

AG1478 contains three potential protonation sites at two quinazolyl nitrogens and amino moiety. At pH 0.3–3.2, the absorption maximum of AG1478 in 300–400 nm region was observed at 342 nm. The observed spectrum at pH 3.2 was assigned to two monoprotonated structures of AG1478 adopting twisted configurations. One structure is protonated at N(1) and the other one is protonated at N(3) and both contributed by 71% and 29% respectively. The absorption spectra of AG1478 exhibited a systematic dependence on solution acidity at pH 3.2–7.3. Starting from pH 7.3 to 12, the absorption peak was observed at 332 nm. The spectrum obtained at pH 9.3 was solely assigned to neutral planar conformer of AG1478. At pH 13 and 13.3, emergence of two overlapping bands were observed at 334 nm and 345 nm. The measured spectrum at pH 13.3 was assigned to the sum of neutral (planar (28%) and twisted (42%)) and deprotonated (planar (26%) and pseudo-planar (4%)) forms of AG1478. These results indicated that the coplanarity of aniline and quinazoline rings are favoured for neutral and deprotonated forms of AG1478 in alkaline solutions, while AG1478 adopts twisted configurations in acidic solutions.

The results of our study both complement and extend earlier studies on related molecules. Gefitinib, a 4-anilinoquinazoline-based tyrosine kinase inhibitor[57,58], has the same chromophore and biological function as AG1478. The UV-Vis absorption measurements revealed that the diprotonated form (protonation at *only one* quinazolyl nitrogen) of Gefitinib prevails in acidic solutions of pH ≤ 3, giving rise to an absorption band at 340 nm. The neutral form of Gefitinib predominates in alkaline solutions at pH > 7.2 showing a blue-shifted

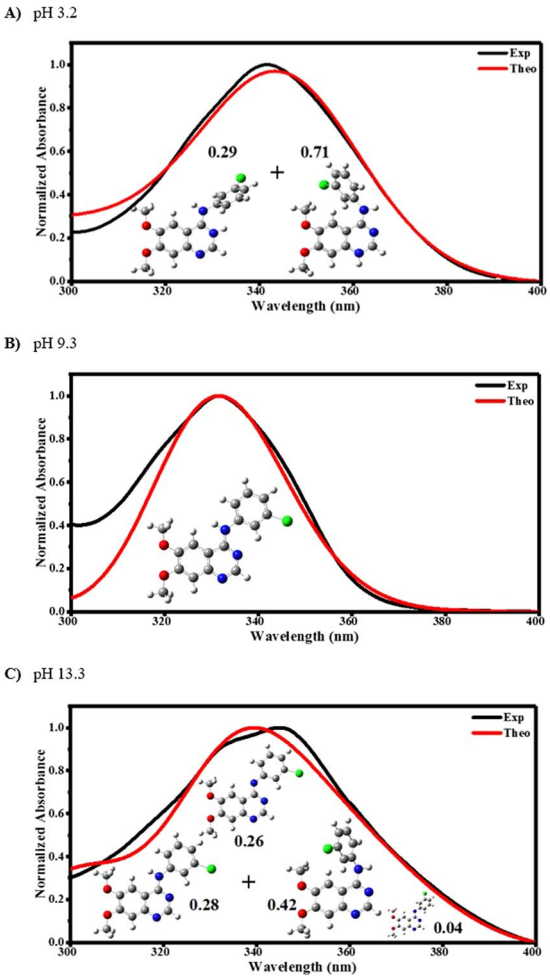

Figure 6. Fits of theoretical spectra to experimental spectra of AG1478 in (**a**) acidic (pH 3.2), (**b**) alkaline (pH 9.3) and (**c**) alkaline (pH 13.3) solution. White, grey, blue, red and green spheres denotes hydrogen, carbon, nitrogen, oxygen and chlorine atoms respectively.

absorption peak at 331 nm[59]. These results are in a good agreement (±2 nm) with our experiments. The absorption maxima of AG1478 in the acidic (pH 0.3–3.2) and alkaline (pH 7.2–12) solutions were 342 nm and 332 nm respectively. In addition, the acid dissociation constant of AG1478 (pKa = 5.6) was very close to that of Gefitinib (pKa = 5.4)[59].

Our spectral assignments agree well with conclusions based on experimental and theoretical studies of quinazoline. In acidic conditions quinazoline consists of a mixture of monocations protonated at N1 or N3 and this has been rationalised theoretically by the similar protonation affinities at N1 and N3[56]. According to our experiments and theory N1 and N3 are both significantly populated at acid pH and have similar protonation affinities. Our assignment of neutral AG1478 at neutral to slightly alkaline pH agrees well with experimental studies on quinazoline[56]. The lack of di-protonated AG1478 or mono-protonated ($^{+}NH_2$ linker) AG1478 populations in our spectral assignments is consistent with the very low pKa for formation of these protonation states in the parent chromophores (pKa (di-protonated quinazoline) $= -5.5$[60–63], pKa($^{+}NH_2$ aniline) < 0)[64].

Our results have potential implications for the pharmacodynamics of quinazoline-based drugs. Iressa®, Tarceva®, Tykerb®, Tyverb®, Gilotrif® and Caprelsa® are oral dosage forms of 4-aminoquinazoline-based tyrosine kinase inhibitors. Our results point to the prototropic and geometric forms of AG1478 during its journey in the gastrointestinal tract. According to our analysis, the *monocationic twisted* structure of AG1478 would be mainly populated in the gastric juice (pH = 2) of the stomach and duodenum (pH = 4.6). The *neutral planar* form of AG1478 would be the dominant (uncomplexed) drug species in the blood plasma and intestinal fluids (pH 7.4–7.6).

The cellular and sub-cellular environments of cancer cells can also vary in pH and this may influence AG1478 conformations, drug-cell interactions and cellular dynamics. In this context, the changes in pH of the microenvironment as the molecule transits from the vicinity of a cancerous cell (acidic) in the outer membrane to the nuclear interior (slightly basic) also gains relevance. For example, cancer cell membranes tend to be negatively charged, and so would be expected to preferentially bind the positively-charged AG1478 as opposed to the neutral AG1478. The twisted versus planar conformer of AG1478 might also confer different membrane binding,

membrane translocation and intracellular trafficking properties. These speculations await further experimental enquiry. Overall, our study paves the way for understanding the conformation of anticancer drugs in different environments.

Conclusion

By combining theory with experiment we have identified the conformations and protropic forms of AG1478 across the pH range 2.3–13.3 for the first time. The electronic absorbance spectrum of AG1478 was found to be an excellent reporter of the pH of its microenvironment and undergoes significant pH-induced transitions in amplitude and spectral position. Our calculations reveal that the structure of AG1478 undergoes a transformation from planar to twisted upon solution acidification. Overall, our results have ramifications for drug formulation and for understanding pharmacokinetics in the different pH environments encountered in the body and in cells.

Materials and Methods

Materials. *N*,*N*-Dimethylsulfoxide, phosphoric acid, boric acid, acetic acid and sodium hydroxide were purchased from Sigma Aldrich Pty Ltd. AG1478 was obtained from AdooQ Bioscience company. Millipore deionized water was used in preparation of universal buffer solutions ranging from pH 2.3–12. Universal buffer was prepared by adding equal volumes of 0.04 M phosphoric acid, 0.04 M boric acid and 0.04 M acetic acid and titrating the solution with 0.2 M NaOH to the required pH. The strong acidic ($pH \leq 2$) and alkaline ($pH \geq 12$) solutions were prepared by using 1 M HCl and 1 M NaOH, respectively. pH was measured using Mettler Toledo SevenEasy S20 pH meter to ± 0.01 pH resolution. A pair of matched quartz cuvettes of 1 cm path length was deployed in all experiments.

Methods

UV-Vis spectroscopy. Absorption measurements were conducted as described earlier[53]. Equal volume of buffer solution was added to both sample and reference cuvette. Since AG1478 is partially soluble in water, it was preferred to use another vehicle to deliver AG1478 into buffer solution and without affecting the characteristics of bulk aqueous environment. Therefore, we added 10 μL of 2 mM AG1478 in DMSO to the sample cuvette and 10 μL of pure DMSO to the reference cuvette. The final solution contained 10 μM AG1478 in 99.5% (aqueous buffer): 0.5% DMSO (v/v). Solutions were shaken and left 10 minutes for equilibrium. Absorption maxima were obtained using originlab software. Values of mean, standard deviation and confidence interval were determined using Excel. Regression analysis of experimental spectrum was done using solver function in Excel. The observed absorption maxima were calculated at 95% confidence interval.

Computational details. Relaxed potential energy surface scan was performed for four prototropic structures of AG1478 in vacuum using B3LYP/6–31 G model, the same model employed in our previous study[55]. The potential energy surface was built by varying N(12)-C(8)-N(25)-C(14) dihedral angle from 0° to 360° in 10° stepwise rotation. Density functional theory (DFT) and time-dependent DFT were deployed for geometry optimization of the ground state and for excitation energy calculations of excited state structures, respectively. Becke three-parameters Lee-Yang-Parr hybrid functional (B3LYP)[65,66] in combination with 6–311 + G(d) basis set was employed in all other calculations. The calculated vibrational frequencies showed that all re-optimized structures are true local minima. The conductor-like polarizable continuum model (CPCM)[67] with $\varepsilon = 78.35$ was used to approximately describe the polarity of bulk environment. The UV-Vis absorption spectra of different ionized AG1478 states in water were then calculated for the singlet–singlet transitions of the lowest 45 excited states. All simulations were performed using GAUSSIAN 09 Revision C.01[68] on swinburne supercomputing facilities.

References

1. Pandey, M. M., Jaipal, A., Kumar, A., Malik, R. & Charde, S. Y. Determination of pK(a) of felodipine using UV-Visible spectroscopy. *Spectrochim. Acta. A Mol. Biomol. Spectrosc.* **115**, 887–890 (2013).
2. Martinez, C. H. R. & Dardonville, C. Rapid Determination of Ionization Constants (pK(a)) by UV Spectroscopy Using 96-Well Microtiter Plates. *ACS Med. Chem. Lett.* **4**, 142–145 (2013).
3. Manallack, D. T. The pK(a) Distribution of Drugs: Application to Drug Discovery. *Perspect. Medicin. Chem.* **1**, 25–38 (2007).
4. Reijenga, J., van Hoof, A., vanLoon, A. & Teunissen, B. Development of Methods for the Determination of pKa Values. *Anal. Chem. Insights* **8**, 53–71 (2013).
5. Ke, J. *et al.* Determination of pKa values of alendronate sodium in aqueous solution by piecewise linear regression based on acid-base potentiometric titration. *J. Pharm. Anal.* **6**, 404–409 (2016).
6. Volgyi, G. *et al.* Potentiometric and spectrophotometric pK(a) determination of water-insoluble compounds: Validation study in a new cosolvent system. *Anal. Chim. Acta* **583**, 418–428 (2007).
7. Hranjec, M. *et al.* Fluorescent benzimidazo[1,2-a]quinolines: synthesis, spectroscopic and computational studies of protonation equilibria and metal ion sensitivity. *New J. Chem.* **41**, 358–371 (2017).
8. Ryazanova, O. A., Voloshin, I. M., Makitruk, V. L., Zozulya, V. N. & Karachevtsev, V. A. pH-Induced changes in electronic absorption and fluorescence spectra of phenazine derivatives. *Spectrochim. Acta. A Mol. Biomol. Spectrosc.* **66**, 849–859 (2007).
9. Wiczling, P., Markuszewski, M. J. & Kaliszan, R. Determination of pK(a) by pH gradient reversed-phase HPLC. *Anal. Chem.* **76**, 3069–3077 (2004).
10. Marvanova, P. *et al.* Synthesis and Determination of Physicochemical Properties of New 3-(4-Arylpiperazin-1-yl)-2-hydroxypropyl 4-Alkoxyethoxybenzoates. *Molecules* **21** (2016).
11. Deria, P., Yu, J. R., Smith, T. & Balaraman, R. P. Ground-State versus Excited-State Interchromophoric Interaction: Topology Dependent Excimer Contribution in Metal-Organic Framework Photophysics. *J. Am. Chem. Soc.* **139**, 5973–5983 (2017).
12. Ma, J. *et al.* A Stable Saddle-Shaped Polycyclic Hydrocarbon with an Open-Shell Singlet Ground State. *Angew. Chem. Int. Ed.* **56**, 3280–3284 (2017).
13. An, N. Q. *et al.* A new FRET-based ratiometric probe for fluorescence and colorimetric analyses of adenosine 5′-triphosphate. *Polym. Chem.* **8**, 1138–1145 (2017).
14. Dommett, M. & Crespo-Otero, R. Excited state proton transfer in 2′-hydroxychalcone derivatives. *Phys. Chem. Chem. Phys.* **19**, 2409–2416 (2017).

15. Fujii, K. *et al*. Excited-State Proton Transfer of Cyanonaphthols in Protic Ionic Liquids: Appearance of a New Fluorescent Species. *J. Phys. Chem. B* **121**, 6042–6049 (2017).
16. Matsui, M. *et al*. UV-vis absorption and fluorescence spectra, solvatochromism, and application to pH sensors of novel xanthene dyes having thienyl and thieno[3,2-b]thienyl rings as auxochrome. *Dyes Pigm.* **139**, 533–540 (2017).
17. Koeppe, B., Guo, J., Tolstoy, P. M., Denisov, G. S. & Limbach, H. H. Solvent and H/D Isotope Effects on the Proton Transfer Pathways in Heteroconjugated Hydrogen-Bonded Phenol-Carboxylic Acid Anions Observed by Combined UV-vis and NMR Spectroscopy. *J. Am. Chem. Soc.* **135**, 7553–7566 (2013).
18. Wencel, D., Abel, T. & McDonagh, C. Optical Chemical pH Sensors. *Anal. Chem.* **86**, 15–29 (2014).
19. Han, J. Y. & Burgess, K. Fluorescent Indicators for Intracellular pH. *Chem. Rev.* **110**, 2709–2728 (2010).
20. Wang, R., Yu, C. W., Yu, F. B. A. & Chen, L. X. Molecular fluorescent probes for monitoring pH changes in living cells. *TrAC, Trends Anal. Chem.* **29**, 1004–1013 (2010).
21. Stich, M. I., Fischer, L. H. & Wolfbeis, O. S. Multiple fluorescent chemical sensing and imaging. *Chem. Soc. Rev.* **39**, 3102–3114 (2010).
22. Shi, W., Li, X. H. & Ma, H. M. Fluorescent probes and nanoparticles for intracellular sensing of pH values. *Methods Appl. Fluoresc.* **2** (2014).
23. Schaferling, M. The Art of Fluorescence Imaging with Chemical Sensors. *Angew. Chem. Int. Ed.* **51**, 3532–3554 (2012).
24. Grante, I., Actins, A. & Orola, L. Protonation effects on the UV/Vis absorption spectra of imatinib: A theoretical and experimental study. *Spectrochim. Acta. A Mol. Biomol. Spectrosc.* **129**, 326–332 (2014).
25. Nakhmanovich, G. *et al*. Protonation-deprotonation effects on the electrooptics of bipyridine containing PPV derivatives. *Synth. Met.* **101**, 269–270 (1999).
26. Alata, I., Broquier, M., Dedonder, C., Jouvet, C. & Marceca, E. Electronic excited states of protonated aromatic molecules: Protonated Fluorene. *Chem. Phys.* **393**, 25–31 (2012).
27. Ginocchietti, G., Mazzucato, U. & Spalletti, A. Protonation effect on the excited state behaviour of some aza-analogues of EE-distyrylbenzene. *Int. J. Photoenergy* **6**, 241–250 (2004).
28. Sukker, G. M., Elroby, S. A. & Hilal, R. Gas-phase acidity and dynamics of the protonation processes of carbidopa and levodopa. A QM/QD study. *J. Biomol. Struct. Dyn.* **34**, 2268–2280 (2016).
29. Bahrle, C., Nick, T. U., Bennati, M., Jeschke, G. & Vogel, F. High-Field Electron Paramagnetic Resonance and Density Functional Theory Study of Stable Organic Radicals in Lignin: Influence of the Extraction Process, Botanical Origin, and Protonation Reactions on the Radical g Tensor. *J. Phys. Chem. A* **119**, 6475–6482 (2015).
30. Pan, Z. H., Zhou, J. W. & Luo, G. G. Experimental and theoretical study of enol-keto prototropic tautomerism and photophysics of azomethine-BODIPY dyads. *Phys. Chem. Chem. Phys.* **16**, 16290–16301 (2014).
31. Goller, A. H., Strehlow, D. & Hermann, G. The excited-state chemistry of phycocyanobilin: A semiempirical study. *Chemphyschem* **6**, 1259–1268 (2005).
32. Mason, B. D., Schoneich, C. & Kerwin, B. A. Effect of pH and light on aggregation and conformation of an IgG1 mAb. *Mol. Pharm.* **9**, 774–790 (2012).
33. Salehzadeh, S., Gholiee, Y. & Bayat, M. Prediction of Microscopic Protonation Constants of Polybasic Molecules Via Computational Methods: A Complete Microequilibrium Analysis of Spermine. *Int. J. Quantum Chem.* **111**, 3608–3615 (2011).
34. Salehzadeh, S., Yaghoobi, F. & Bayat, M. Illustration of all species and all microspecies involved in full protonation steps of spermine and determination of corresponding most abundant and most stable conformers, a gas phase theoretical study. *Chem. Phys.* **361**, 18–26 (2009).
35. Hojjat-Farsangi, M. Small-molecule inhibitors of the receptor tyrosine kinases: promising tools for targeted cancer therapies. *Int. J. Mol. Sci.* **15**, 13768–13801 (2014).
36. Fabbro, D., Cowan-Jacob, S. W., Mobitz, H. & Martiny-Baron, G. Targeting cancer with small-molecular-weight kinase inhibitors. *Methods Mol. Biol.* **795**, 1–34 (2012).
37. Zhang, J., Yang, P. L. & Gray, N. S. Targeting cancer with small molecule kinase inhibitors. *Nat. Rev. Cancer* **9**, 28–39 (2009).
38. Janne, P. A., Gray, N. & Settleman, J. Factors underlying sensitivity of cancers to small-molecule kinase inhibitors. *Nat. Rev. Drug Discov.* **8**, 709–723 (2009).
39. Sequist, L. V. *et al*. Phase III Study of Afatinib or Cisplatin Plus Pemetrexed in Patients With Metastatic Lung Adenocarcinoma With EGFR Mutations. *J. Clin. Oncol.* **31**, 3327 (2013).
40. Dowell, J., Minna, J. D. & Kirkpatrick, P. Erlotinib hydrochloride. *Nat. Rev. Drug Discov.* **4**, 13–14 (2005).
41. Cohen, M. H., Williams, G. A., Sridhara, R., Chen, G. & Pazdur, R. FDA drug approval summary: Gefitinib (ZD1839) (Iressa (R)) tablets. *Oncologist* **8**, 303–306 (2003).
42. Wood, E. R. *et al*. A unique structure for epidermal growth factor receptor bound to GW572016 (Lapatinib): Relationships among protein conformation, inhibitor off-rate, and receptor activity in tumor cells. *Cancer Res.* **64**, 6652–6659 (2004).
43. Morabito, A. *et al*. Vandetanib (ZD6474), a Dual Inhibitor of Vascular Endothelial Growth Factor Receptor (VEGFR) and Epidermal Growth Factor Receptor (EGFR) Tyrosine Kinases: Current Status and Future Directions. *Oncologist* **14**, 378–390 (2009).
44. Shi, Z. *et al*. Inhibiting the function of ABCB1 and ABCG2 by the EGFR tyrosine kinase inhibitor AG1478. *Biochem. Pharmacol.* **77**, 781–793 (2009).
45. Caja, L. *et al*. The tyrphostin AG1478 inhibits proliferation and induces death of liver tumor cells through EGF receptor-dependent and independent mechanisms. *Biochem. Pharmacol.* **82**, 1583–1592 (2011).
46. Garofalo, A. *et al*. Design, Synthesis, and DNA-Binding of N-Alkyl(anilino)quinazoline Derivatives. *J. Med. Chem.* **53**, 8089–8103 (2010).
47. Bojko, A. *et al*. The effect of tyrphostins AG494 and AG1478 on the autocrine growth regulation of A549 and DU145 cells. *Folia Histochem. Cytobiol.* **50**, 186–195 (2012).
48. Ma, L., Yan, H. Q. & Zhou, Q. H. AG1478 inhibits the migration and invasion of cisplatin-resistant human lung adenocarcinoma cells via the cell cycle regulation by matrix metalloproteinase-9. *Oncol. Lett.* **8**, 921–927 (2014).
49. Zhu, X. F. *et al*. EGFR tyrosine kinase inhibitor AG1478 inhibits cell proliferation and arrests cell cycle in nasopharyngeal carcinoma cells. *Cancer Lett.* **169**, 27–32 (2001).
50. Herbert, H. E., Halls, M. D., Hratchian, H. P. & Raghavachari, K. Hydrogen-bonding interactions in peptide nucleic acid and deoxyribonucleic acid: A comparative study. *J. Phys. Chem. B* **110**, 3336–3343 (2006).
51. Tan, Z. J. & Chen, S. J. Electrostatic free energy landscapes for DNA helix bending. *Biophys. J.* **94**, 3137–3149 (2008).
52. Maffeo, C. *et al*. Close encounters with DNA. *J. Phys. Condens. Matter* **26** (2014).
53. Khattab, M., Wang, F. & Clayton, A. H. UV–Vis spectroscopy and solvatochromism of the tyrosine kinase inhibitor AG-1478. *Spectrochim. Acta. A Mol. Biomol. Spectrosc.* **164**, 128–132 (2016).
54. Khattab, M., Wang, F. & Clayton, A. H. Micro-solvation of tyrosine-kinase inhibitor AG1478 explored with fluorescence spectroscopy and computational chemistry. *RSC Adv.* **7**, 31725–31735 (2017).
55. Khattab, M., Chatterjee, S., Clayton, A. H. A. & Wang, F. Two conformers of a tyrosine kinase inhibitor (AG-1478) disclosed using simulated UV-Vis absorption spectroscopy. *New J. Chem.* **40**, 8296–8304 (2016).
56. Sawunyama, P. & Bailey, G. W. Quantum mechanical study of the competitive hydration between protonated quinazoline and Li+, Na+, and Ca2+ ions. *J. Phys. Chem. A* **105**, 9717–9724 (2001).

57. Kitazaki, T. *et al.* Gefitinib, an EGFR tyrosine kinase inhibitor, directly inhibits the function of P-glycoprotein in multidrug resistant cancer cells. *Lung Cancer* **49**, 337–343 (2005).
58. Russo, A. *et al.* A decade of EGFR inhibition in EGFR-mutated non small cell lung cancer (NSCLC): Old successes and future perspectives. *Oncotarget* **6**, 26814–26825 (2015).
59. Huang, Y. *et al.* Cucurbit[7,8]urils binding to gefitinib and the effect of complex formation on the solubility and dissolution rate of the drug. *RSC Adv.* **4**, 3348–3354 (2014).
60. Albert, A., Spinner, E. & Armarego, W. L. Quinazolines .1. Cations of Quinazoline. *J. Chem. Soc.*, 2689 (1961).
61. Albert, A. & Armarego, W. L. Covalent hydration in nitrogen-containing heteroaromatic compounds. I. Qualitative aspects. *Adv. Heterocycl. Chem.* **4**, 1–42 (1965).
62. Perrin, D. D. Covalent hydration in nitrogen heteroaromatic compounds. II. Quantitative aspects. *Adv. Heterocycl. Chem.* **4**, 43–73 (1965).
63. Bunting, J. W. & Perrin, D. D. Kinetics of Reversible Addition of Water to Substituted Quinazolines and Some Triazanaphthalenes. *J. Chem. Soc. B-Phys. Org.*, 950 (1967).
64. Song, Y. *et al.* Acid-Base Interactions of Polystyrene Sulfonic Acid in Amorphous Solid Dispersions Using a Combined UV/FTIR/XPS/ssNMR Study. *Mol. Pharm.* **13**, 483–492 (2016).
65. Becke, A. D. A New Mixing of Hartree-Fock and Local Density-Functional Theories. *J. Chem. Phys.* **98**, 1372–1377 (1993).
66. Becke, A. D. Density-Functional Thermochemistry .3. The Role of Exact Exchange. *J. Chem. Phys.* **98**, 5648–5652 (1993).
67. Cossi, M., Rega, N., Scalmani, G. & Barone, V. Energies, structures, and electronic properties of molecules in solution with the C-PCM solvation model. *J. Comput. Chem.* **24**, 669–681 (2003).
68. Gaussian 09, Revision C.01 (Gaussian, Inc., Wallingford CT, 2009).

Acknowledgements

MK acknowledges the Swinburne University Postgraduate Research Award (SUPRA). Swinburne University supercomputing (Green/gSTAR) is thanked for computing facilities. FW acknowledges Swinburne University of Technology for financial support of her Academic Sabbatical Award, School of Chemistry (Bio21 Institute) and School of Physics, the University of Melbourne for administrative support of her Academic Sabbatical in 2017. AHAC acknowledges the ARC for on-going grant support.

Author Contributions

A.H.A.C. and F.W. supervised the research. M.K. conducted the experiments and carried out the calculations. All authors were involved in analysis, writing and editing the manuscript.

Additional Information

Supplementary information accompanies this paper at https://doi.org/10.1038/s41598-017-16583-z.

Competing Interests: The authors declare that they have no competing interests.

Publisher's note: Springer Nature remains neutral with regard to jurisdictional claims in published maps and institutional affiliations.

A pH-induced conformational switch in a tyrosine kinase inhibitor identified by electronic spectroscopy and quantum chemical calculations

Muhammad Khattab[a], Feng Wang[b,c,d*] and Andrew H. A. Clayton[a*]

[a] *Centre for Micro-Photonics, Faculty of Science, Engineering and Technology, Swinburne University of Technology, Melbourne, Victoria, 3122, Australia*

[b] *Molecular Model Discovery Laboratory, Department of Chemistry and Biotechnology, Engineering and Technology, Swinburne University of Technology, Melbourne, Victoria, 3122, Australia*

[c] *School of Chemistry (Bio21 Institute), University of Melbourne, Parkville, Victoria 3052, Australia*

[d] *School of Physics, University of Melbourne, Parkville, Victoria 3052, Australia*

*Corresponding authors: aclayton@swin.edu.au

fwang@swin.edu.au

Supplementary Information

Table S1. Molecular coordinates of optimised protonated structures of AG1478 using B3LYP/6-311+G* model

N(1)N(3)-GM

C	-0.00401400	-0.00456400	0.02425200
C	0.09236100	0.34471200	1.36471800
C	1.34382400	0.39703300	1.97091400
C	2.52735100	0.10507000	1.25489300
C	2.42057200	-0.24104000	-0.10884800
C	1.18842200	-0.30103000	-0.72778600
H	-0.79244900	0.57387100	1.94178800
C	3.77245300	0.16538900	1.95582700
H	3.30474500	-0.46147900	-0.68834200
C	2.60184400	0.80397600	3.93765000
H	2.65029100	1.07686300	4.98146300
N	3.73214100	0.52594200	3.28369000
N	1.45287900	0.74190600	3.31685200
C	6.21802200	-0.05618900	2.12396100
C	6.87929100	1.16229700	2.26382000
C	6.75847000	-1.24669400	2.60964100
C	8.10920200	1.18582300	2.91884600
H	6.44502800	2.06948500	1.86128700
C	7.98960900	-1.19138400	3.25374200
H	6.23062600	-2.18369400	2.48582700
C	8.67133800	0.01248100	3.41561700
H	8.63745800	2.12439700	3.03688400
H	9.62895800	0.03243700	3.92093100
Cl	8.69315000	-2.67472100	3.87461600
N	4.95377300	-0.10757100	1.42571100
H	4.97941900	-0.40221000	0.45813400
O	-1.13905100	-0.09371900	-0.65566600
O	0.98085200	-0.62012000	-2.00788000
C	2.10469900	-0.94313100	-2.84355900
H	1.68134900	-1.16751200	-3.81830500
H	2.78314300	-0.09150200	-2.92216200
H	2.63141100	-1.81842600	-2.45845100
C	-2.39133700	0.16957200	0.00692600
H	-3.15114200	0.02595100	-0.75531900

H	-2.54525500	-0.53624900	0.82452400
H	-2.41962000	1.19693700	0.37279600
H	4.60321100	0.57753000	3.80573400
H	0.61328600	0.95275900	3.84859000

N(1)N(3)-LM1

C	0.00000000	0.00000000	0.00000000
C	0.00000000	0.00000000	1.38866019
C	1.21124281	0.00000000	2.07339637
C	2.44919629	0.00072084	1.39112924
C	2.43991939	0.00204104	-0.01957566
C	1.24932181	-0.00303133	-0.71765038
H	-0.92861078	-0.00165814	1.94203293
C	3.64844415	0.00945681	2.16930853
H	3.36710830	0.01287501	-0.57295097
C	2.33125301	0.00097185	4.16279177
H	2.30496536	-0.00172813	5.24249757
N	3.51188594	0.00616905	3.53890540
N	1.22402641	0.00108025	3.46679486
C	6.09652001	0.06606742	2.43854272
C	6.83877519	-1.09982145	2.61443678
C	6.52301484	1.29304365	2.94707903
C	8.03509365	-1.03136597	3.32455961
H	6.48563839	-2.03783088	2.20360053
C	7.71745485	1.32726104	3.65993434
H	5.94508254	2.19354297	2.78180300
C	8.48020699	0.17895224	3.85287282
H	8.62576402	-1.92788650	3.47095507
H	9.40935137	0.22876759	4.40694982
Cl	8.27316428	2.85811476	4.31410576
N	4.87408212	0.01649488	1.67018082
H	4.97270045	-0.03578095	0.66449459
O	-1.08828460	0.00368196	-0.75764540
O	1.13375121	-0.00778572	-2.04805413
C	2.32190114	-0.02662090	-2.85677498
H	1.96884987	-0.04120089	-3.88380405
H	2.91983278	0.87029027	-2.68406861
H	2.90979735	-0.92399485	-2.65444712
C	-2.39024812	0.01580006	-0.13953396
H	-3.09579774	0.01841516	-0.96480527
H	-2.53165370	-0.87867502	0.46865563
H	-2.51738095	0.91678813	0.46228068
H	4.35021918	0.00061827	4.11379495
H	0.34296072	0.00346484	3.97191490

N(1)N(3)-LM2

C	0.85644300	0.13940000	-0.17661300
C	0.33598600	0.69492800	0.98467300
C	1.13308000	0.79257100	2.11882900
C	2.48199600	0.34770100	2.13234100
C	2.99010200	-0.23248100	0.94631300
C	2.21176900	-0.34123600	-0.18753400
H	-0.68537800	1.04760600	1.01987400
C	3.22184000	0.48503900	3.35126200
H	3.99875300	-0.60579000	0.92569100
C	1.26929500	1.41855800	4.39491400
H	0.81675900	1.82716100	5.28646800
N	2.53846300	1.01501000	4.43368500
N	0.58834700	1.32404000	3.28409900
C	5.53472800	-0.21728000	2.68237900
C	5.98643400	-1.53390000	2.67213000
C	6.13351700	0.77175400	1.90329500
C	7.05228300	-1.87092400	1.84029700
H	5.50882200	-2.27811400	3.29773600
C	7.18949300	0.40288500	1.07687300
H	5.78672600	1.79646500	1.94429800
C	7.65750700	-0.90796600	1.03546200
H	7.41387900	-2.89205200	1.81598700
H	8.48398200	-1.17159100	0.38724800
Cl	7.95162700	1.62634100	0.07387300
N	4.48478200	0.15823500	3.59925300
H	4.79153800	0.22133700	4.56462500
O	0.19176800	-0.00038900	-1.31418900
O	2.60650200	-0.87509400	-1.34815800
C	3.94590000	-1.37994900	-1.47083700

H	4.02019400	-1.74951800	-2.48959400
H	4.67300100	-0.58149500	-1.31279800
H	4.11541900	-2.19741200	-0.76766300
C	-1.17575000	0.44672800	-1.40510800
H	-1.47749900	0.22965600	-2.42526100
H	-1.80355000	-0.10620500	-0.70509900
H	-1.23903300	1.51952200	-1.21789300
H	3.02323100	1.13816300	5.31747700
H	-0.37664300	1.64149100	3.28498600

N(1)-GM

C	0.00252200	0.00019600	0.00061400
C	-0.00083500	0.00016900	1.38336400
C	1.21473200	-0.00002700	2.07898100
C	2.45304500	-0.00020700	1.40586900
C	2.43873500	-0.00014600	-0.00969200
C	1.25234800	0.00004600	-0.71041900
H	-0.92947600	0.00030600	1.93779100
C	3.64014600	-0.00043000	2.22805100
H	3.36265100	-0.00022400	-0.56958000
C	2.38149600	-0.00016200	4.13920100
H	2.30821000	-0.00011000	5.21980900
N	3.56356300	-0.00035800	3.57424900
N	1.23128500	-0.00002900	3.46089500
C	6.16909100	-0.00085500	2.18624300
C	7.21108500	-0.00104300	1.24529400
C	6.47045800	-0.00080800	3.55386800
C	8.53420600	-0.00118000	1.66453400
H	6.98567700	-0.00107900	0.18389300
C	7.80771500	-0.00094400	3.93710900
H	5.68599600	-0.00067000	4.29140600
C	8.85313200	-0.00113000	3.02240600
H	9.32845000	-0.00132400	0.92680600
H	9.88330600	-0.00123400	3.35535100
Cl	8.17828300	-0.00088000	5.66197000
N	4.85818200	-0.00072700	1.65038100
H	4.85527400	-0.00088300	0.64142200
O	-1.09137100	0.00037000	-0.76858900
O	1.14202400	0.00011800	-2.05118600
C	2.33631800	-0.00002000	-2.84315300
H	1.99918000	0.00006600	-3.87623700
H	2.93052700	0.89605800	-2.64989800
H	2.93027300	-0.89628100	-2.64996400
C	-2.38542600	0.00055500	-0.14567000
H	-3.09904700	0.00064000	-0.96485300
H	-2.52065500	-0.89581500	0.46268600
H	-2.52041100	0.89697900	0.46266000
H	0.35673800	0.00009900	3.97261800

N(1)-LM1

C	-0.06622000	-0.60845900	0.39563300
C	0.07770400	0.62555200	1.00337800
C	1.34750800	1.05126600	1.41340600
C	2.49182100	0.25154300	1.22251200
C	2.32715700	-1.01146100	0.60436000
C	1.08594400	-1.44511400	0.19266000
H	-0.77677000	1.26780200	1.16819100
C	3.74639600	0.79083600	1.68508900
H	3.17605000	-1.66239700	0.45350100
C	2.72058900	2.69479000	2.42528600
H	2.76507700	3.67107200	2.89262000
N	3.82093400	2.00023600	2.27802300
N	1.51495800	2.27884000	2.02528000
C	6.20842800	0.41874600	1.93563900
C	6.49449800	1.08487000	3.13099700
C	7.24915800	-0.02481600	1.11122900
C	7.82179100	1.31802200	3.48009300
H	5.69645400	1.41299200	3.77960600
C	8.56254400	0.21605100	1.49233500
H	7.03520400	-0.54514500	0.18523000
C	8.87153000	0.89028300	2.66864100
H	8.04355700	1.83429100	4.40736700
H	9.90200400	1.07087800	2.94794600
Cl	9.86567600	-0.34499700	0.44737600
N	4.88792900	0.09300200	1.52394000

H	4.82527000	-0.74429300	0.96453300
O	-1.22485000	-1.11857000	-0.03534000
O	0.83195900	-2.62529400	-0.40165600
C	1.92034600	-3.52510900	-0.64471500
H	1.47724400	-4.39269600	-1.12629200
H	2.65851300	-3.07164100	-1.31032200
H	2.39273500	-3.82649100	0.29307100
C	-2.43023000	-0.35593700	0.13140100
H	-3.22036600	-0.97048700	-0.29086600
H	-2.62795300	-0.17499300	1.18970500
H	-2.36690600	0.58940400	-0.41099900
H	0.71173900	2.87645900	2.17937200

N(1)-LM2

C	0.63714600	-0.42927400	0.33921600
C	0.25239100	0.10380800	1.55606900
C	1.21034800	0.69510100	2.38838300
C	2.57940700	0.72514700	2.03724100
C	2.94931200	0.20328900	0.77149200
C	2.01383300	-0.35591600	-0.06925800
H	-0.78327500	0.08953300	1.86682500
C	3.47120300	1.33312900	2.98824100
H	3.97700600	0.26251600	0.45366900
C	1.71436900	1.96162600	4.32395800
H	1.32454400	2.47423700	5.19489600
N	2.99619200	1.99438400	4.07491400
N	0.82714600	1.30729000	3.56484500
C	5.71443500	0.51807900	2.17762500
C	6.72322800	1.10073000	1.41025600
C	5.62873300	-0.87040600	2.30833300
C	7.64477600	0.28510600	0.75759600
H	6.77926000	2.17946800	1.32311300
C	6.55003400	-1.66001100	1.63103600
H	4.86550100	-1.32128300	2.92979300
C	7.56281800	-1.10258900	0.85552900
H	8.43001000	0.73250200	0.15913800
H	8.27342800	-1.73796400	0.34167800
Cl	6.44002700	-3.41072700	1.77891500
N	4.81603500	1.36166700	2.90025100
H	5.24032000	1.96417900	3.59693000
O	-0.18946800	-1.01208900	-0.53474700
O	2.26936400	-0.86106400	-1.29181200
C	3.61175000	-0.81229800	-1.78954700
H	3.57192800	-1.26522300	-2.77672700
H	3.95821000	0.22046500	-1.87238600
H	4.28547800	-1.38512500	-1.14848300
C	-1.58502900	-1.12335200	-0.21313700
H	-2.03585800	-1.63174400	-1.06080700
H	-1.72589100	-1.71662600	0.69245500
H	-2.03264400	-0.13486700	-0.09374400
H	-0.14864100	1.30733400	3.83648000

N(3)-GM

C	0.00938700	0.00900900	0.02842700
C	0.10438000	0.31296800	1.37343400
C	1.35391900	0.36233800	2.01443000
C	2.53004100	0.09430700	1.26853000
C	2.43030100	-0.21413500	-0.10912900
C	1.20138800	-0.25851300	-0.73061600
H	-0.77346700	0.51999100	1.96921900
C	3.77252900	0.15201700	1.97219800
H	3.31593800	-0.42099100	-0.69303500
C	2.52710300	0.71512200	3.93626000
H	2.62028100	0.95462500	4.98832900
N	3.71392100	0.46710600	3.28872800
N	1.37820800	0.67261100	3.36045900
C	6.23006600	-0.02310500	2.09615700
C	7.05393500	1.08767400	1.91964500
C	6.62198500	-1.09458800	2.90011500
C	8.29041900	1.12373900	2.55998100
H	6.72871600	1.90680400	1.28942600
C	7.85689100	-1.02610000	3.53728900
H	5.98262300	-1.96090600	3.01483300
C	8.69898500	0.07008700	3.37574800
H	8.94104300	1.98035000	2.42816200

H	9.65832200	0.10061900	3.87735900
Cl	8.36483200	-2.36544700	4.55636300
N	4.96490700	-0.08291200	1.41332800
H	4.98994100	-0.26098900	0.41984800
O	-1.13471100	-0.06394700	-0.66425500
O	0.99756400	-0.54066400	-2.03095300
C	2.12959400	-0.81853200	-2.86398200
H	1.72215600	-1.00761100	-3.85361000
H	2.80458800	0.03964200	-2.90233800
H	2.66434200	-1.70363900	-2.51152100
C	-2.37587900	0.17777200	0.01572000
H	-3.14684900	0.05919300	-0.74070700
H	-2.52593400	-0.55055300	0.81517500
H	-2.40477800	1.19221300	0.41816600
H	4.57463900	0.53266000	3.82107600

N(3)-LM1

C	-0.07398200	-0.49433300	0.42345100
C	0.13891400	0.61849200	1.21529300
C	1.43495500	0.97254100	1.62720000
C	2.53558600	0.17256500	1.22628600
C	2.31556200	-0.96082600	0.40816500
C	1.04201800	-1.30065000	0.00736900
H	-0.67901900	1.24725800	1.53814700
C	3.82915000	0.57080600	1.68364000
H	3.14451300	-1.57061500	0.07865800
C	2.76999000	2.41433200	2.78155100
H	2.95674900	3.28700800	3.39515400
N	3.88839400	1.68829000	2.44752500
N	1.57927500	2.10128400	2.41030800
C	6.27736500	0.29955400	1.82755500
C	6.90201400	1.39908200	1.23896000
C	6.92041400	-0.45767700	2.80776900
C	8.18603700	1.75089200	1.65092700
H	6.39807600	1.96148000	0.46159400
C	8.20689800	-0.09263400	3.18779400
H	6.42355500	-1.30792100	3.25780600
C	8.84881500	1.00724700	2.62467700
H	8.68071400	2.60332000	1.20026300
H	9.84988800	1.27593300	2.93857600
Cl	9.03393900	-1.04108200	4.41544800
N	4.95963700	-0.09106700	1.40817500
H	4.87832900	-0.97296800	0.92310400
O	-1.26993300	-0.90842300	-0.01476300
O	0.72674100	-2.35394900	-0.76938000
C	1.77825300	-3.20997200	-1.23258400
H	1.28799300	-3.97590700	-1.82763000
H	2.48464200	-2.65662600	-1.85579100
H	2.30007400	-3.67464300	-0.39276000
C	-2.44180600	-0.16648800	0.35590900
H	-3.27303900	-0.68926300	-0.10925700
H	-2.56768900	-0.16099900	1.44037300
H	-2.38798700	0.85565800	-0.02390400
H	4.78628900	1.99852100	2.80265100

N(3)-LM2

C	0.63530100	-0.39620800	0.33994700
C	0.27330100	0.24918100	1.50692100
C	1.23892900	0.85782600	2.32547200
C	2.61648800	0.77850000	1.96739100
C	2.97447700	0.14522300	0.75017100
C	2.01802800	-0.42984800	-0.05506600
H	-0.76019800	0.32229900	1.81519800
C	3.54806400	1.40678100	2.84689500
H	4.00582600	0.12653600	0.43953500
C	1.67293000	2.14668300	4.15076100
H	1.39018700	2.72730900	5.02019100
N	3.01863500	2.08988700	3.89797100
N	0.78984800	1.54841400	3.43059900
C	5.75565100	0.48412400	2.10583900
C	6.76183300	0.94595600	1.25826400
C	5.63547900	-0.87454200	2.40442800
C	7.65003400	0.03349100	0.69384300
H	6.84230600	2.00455800	1.04067300
C	6.52246000	-1.76404200	1.80958400

H	4.87330400	-1.22748500	3.08751600
C	7.53394400	-1.32998900	0.95731600
H	8.43461800	0.38499300	0.03384700
H	8.21780200	-2.04112300	0.51091700
Cl	6.36974100	-3.48043200	2.16557000
N	4.89090100	1.43689100	2.73457700
H	5.37213400	2.13130000	3.29305400
O	-0.21351700	-1.00007900	-0.49924400
O	2.25829400	-1.04338200	-1.22921600
C	3.60682300	-1.11335700	-1.70848200
H	3.55079600	-1.64400900	-2.65532700
H	4.01378900	-0.11280700	-1.87124300
H	4.23913300	-1.66867800	-1.01215200
C	-1.61484400	-1.01295000	-0.18409100
H	-2.08696500	-1.56224800	-0.99392900
H	-1.79203900	-1.52418000	0.76402500
H	-2.01050500	0.00368800	-0.14563500
H	3.63833800	2.53993500	4.56213600

Neut-GM

C	-4.00873800	-0.23157100	0.00029000
C	-3.35370600	-1.44275400	0.00005000
C	-1.93990300	-1.50699200	-0.00016800
C	-1.18796600	-0.30634800	-0.00011900
C	-1.87345300	0.93648000	0.00009900
C	-3.24942700	0.98787000	0.00029800
H	-3.89599800	-2.37864300	0.00001300
C	0.24344500	-0.46875300	-0.00027900
H	-1.32775200	1.87006000	0.00009100
C	-0.03097400	-2.74116400	-0.00061300
H	0.46204200	-3.71029700	-0.00084600
N	0.79720600	-1.67599500	-0.00054000
N	-1.34262000	-2.74132900	-0.00042400
C	2.44118000	0.79538500	-0.00026400
C	2.92864900	2.11557200	-0.00061500
C	3.35556100	-0.26858200	0.00003400
C	4.29332200	2.36529700	-0.00066100
H	2.23143200	2.94768700	-0.00084800
C	4.71621700	0.02145500	-0.00003300
H	3.00314200	-1.28658900	0.00028500
C	5.21546400	1.31678000	-0.00037500
H	4.64830400	3.39001700	-0.00093600
H	6.28149400	1.50568000	-0.00042500
Cl	5.85338200	-1.33307300	0.00035600
N	1.04422700	0.64481000	-0.00014900
H	0.55366800	1.52464200	0.00001400
O	-5.35015400	-0.07383800	0.00051500
O	-3.98751900	2.12377200	0.00050900
C	-3.30786300	3.38100400	0.00055500
H	-4.08968400	4.13667200	0.00075800
H	-2.69033900	3.49334200	0.89552900
H	-2.69060700	3.49355100	-0.89457800
C	-6.17385600	-1.24424000	0.00058200
H	-7.19845100	-0.88060700	0.00082100
H	-5.99656400	-1.84581600	-0.89406600
H	-5.99620000	-1.84596800	0.89505500

Neut-LM

C	2.89681300	-0.90709200	-0.01690100
C	3.14737300	0.35549700	0.47015100
C	2.18046400	1.38396600	0.35441200
C	0.91875900	1.09067500	-0.23025700
C	0.68685200	-0.20545300	-0.76290700
C	1.64392100	-1.18768400	-0.66798100
H	4.09226700	0.60644000	0.93258800
C	-0.00422700	2.18149900	-0.28078000
H	-0.24675400	-0.41535200	-1.26177200
C	1.60246500	3.57210800	0.57470500
H	1.86580000	4.58838000	0.85666600
N	0.35965500	3.41046700	0.08199400
N	2.51203200	2.64293600	0.77117000
C	-2.24809600	1.06724000	-0.54041000
C	-3.32065400	0.93986000	-1.43262800
C	-2.18278700	0.23580000	0.58436100
C	-4.30875300	-0.01178700	-1.20498900

H	-3.37113400	1.58467700	-2.30313600
C	-3.17200600	-0.72236300	0.77157000
H	-1.38297100	0.33971700	1.30570100
C	-4.24297600	-0.86547400	-0.10331900
H	-5.13590100	-0.10215400	-1.90044100
H	-5.00273000	-1.61753200	0.06842000
Cl	-3.07054000	-1.77343400	2.18654900
N	-1.28901900	2.07857600	-0.78430100
H	-1.68418300	2.98830000	-0.98873100
O	3.75612400	-1.94568400	0.04117600
O	1.52230000	-2.44668600	-1.15295400
C	0.31403000	-2.80178900	-1.82910200
H	0.43721300	-3.84140100	-2.12307600
H	-0.54920500	-2.70800300	-1.16542600
H	0.16742100	-2.18430800	-2.71908200
C	5.02963100	-1.74589300	0.66329900
H	5.53917900	-2.70416700	0.59989300
H	5.60785600	-0.98568700	0.13272500
H	4.91140300	-1.46007300	1.71117700

De-GM

C	0.02460200	-0.01407100	0.00715300
C	0.00997200	0.01329500	1.38701300
C	1.21573600	0.03175100	2.13100100
C	2.44807000	0.02062200	1.44537400
C	2.45089200	-0.00818600	0.03223800
C	1.27430000	-0.02486000	-0.68656800
H	-0.92116400	0.02213500	1.93889800
C	3.67980800	0.04025200	2.23913200
H	3.40987300	-0.01649800	-0.46581000
C	2.31480700	0.07800600	4.12007100
H	2.27707100	0.10240400	5.21018600
N	3.55017600	0.06917200	3.59848400
N	1.14590500	0.06077900	3.50790100
C	6.09347900	0.03138900	2.13281900
C	7.17360600	0.09980700	1.21101000
C	6.44382800	-0.04810500	3.50943900
C	8.49759500	0.09248600	1.62119300
H	6.93218800	0.15868500	0.15459100
C	7.78143000	-0.05599100	3.88197000
H	5.66278700	-0.09846800	4.25039900
C	8.83391100	0.01377700	2.97846300
H	9.29012100	0.14761800	0.88090800
H	9.86499300	0.00735600	3.30938800
Cl	8.16559900	-0.16046800	5.62063100
N	4.83155500	0.03627700	1.57591800
O	-1.08341000	-0.03210600	-0.78283600
O	1.18766400	-0.05122100	-2.04970300
C	2.40245600	-0.05741600	-2.79545700
H	2.10770900	-0.07662300	-3.84272100
H	2.99252900	0.84237500	-2.59857700
H	3.00222600	-0.94361300	-2.56865300
C	-2.36334900	-0.02068400	-0.15165000
H	-3.09142700	-0.03727100	-0.95979600
H	-2.49934000	-0.90194900	0.48107700
H	-2.50078000	0.88480300	0.44567500

De-LM1

C	0.08054700	-0.60886900	0.03848700
C	0.03488200	0.23566300	1.12955700
C	1.22275800	0.68658900	1.75714000
C	2.46768000	0.26030000	1.25106200
C	2.50411700	-0.60203000	0.13233300
C	1.34444900	-1.03717200	-0.47404900
H	-0.90867900	0.57578900	1.53641700
C	3.67951800	0.72703000	1.92584300
H	3.47422200	-0.90931700	-0.23251900
C	2.28299200	1.89006900	3.36906300
H	2.22151300	2.56173000	4.22693900
N	3.52579300	1.55549300	3.00260200
N	1.12418500	1.52709200	2.84543600
C	6.05228700	0.58087300	2.08944800
C	6.26910300	0.39102500	3.47654800
C	7.18378200	0.90186100	1.30158100
C	7.53737500	0.51691300	4.03031700

H	5.42909300	0.13685400	4.10979900
C	8.43435100	1.03095800	1.88673300
H	7.05716500	1.04104000	0.23419200
C	8.64984200	0.84538900	3.24801100
H	7.67268200	0.35638200	5.09598100
H	9.63759900	0.94574500	3.68045900
Cl	9.81869800	1.44520200	0.84981000
N	4.85468300	0.36354700	1.43494600
O	-1.01109900	-1.08884900	-0.61798500
O	1.28851700	-1.86912700	-1.55681600
C	2.51971100	-2.32891500	-2.10837800
H	2.24943000	-2.96707400	-2.94725400
H	3.12993100	-1.49447500	-2.46617200
H	3.08949600	-2.90937400	-1.37689100
C	-2.30352100	-0.70289300	-0.15175800
H	-3.01474500	-1.19566700	-0.81117000
H	-2.46726600	-1.03558700	0.87686500
H	-2.43826900	0.38046000	-0.21291700

De-LM2

C	0.67556900	-0.33356600	0.34881700
C	0.28272700	0.14118600	1.58163600
C	1.20628000	0.76632700	2.45760700
C	2.56920800	0.85110200	2.08304800
C	2.94711600	0.39360500	0.79556200
C	2.03647000	-0.18176800	-0.06356400
H	-0.74713000	0.07524800	1.90750300
C	3.49552600	1.46879500	3.03726700
H	3.97278600	0.50775700	0.48073800
C	1.63240200	1.96185600	4.33873700
H	1.25991000	2.45604800	5.23671100
N	2.94380100	2.09123100	4.12421100
N	0.72931300	1.30691100	3.62719600
C	5.63694500	0.66026700	2.28465000
C	6.78625300	1.11970700	1.59416000
C	5.48163700	-0.74728600	2.40394600
C	7.70052800	0.23463500	1.03715500
H	6.93962900	2.19045900	1.50523100
C	6.41442100	-1.60027900	1.83786900
H	4.63504700	-1.14977400	2.94693400
C	7.53442900	-1.15022000	1.14413200
H	8.56532000	0.62313000	0.50756800
H	8.24623400	-1.84322200	0.71370200
Cl	6.17335100	-3.35467000	2.01665700
N	4.81429600	1.56053700	2.91073100
O	-0.14516800	-0.93636600	-0.55109000
O	2.32044000	-0.63466500	-1.32024500
C	3.65579900	-0.49090300	-1.79869700
H	3.65735200	-0.90912000	-2.80314500
H	3.94927500	0.56202900	-1.84180500
H	4.36271900	-1.04233500	-1.17238000
C	-1.51875400	-1.11127600	-0.20234800
H	-1.97705200	-1.61309700	-1.05168200
H	-1.62213400	-1.73375500	0.69049400
H	-2.00911700	-0.14807400	-0.03814700

Figure S1: Theoretical absorption spectra of studied AG1478 structures in water using B3LYP/6-311+G* model. All spectra are plotted using the same scale.

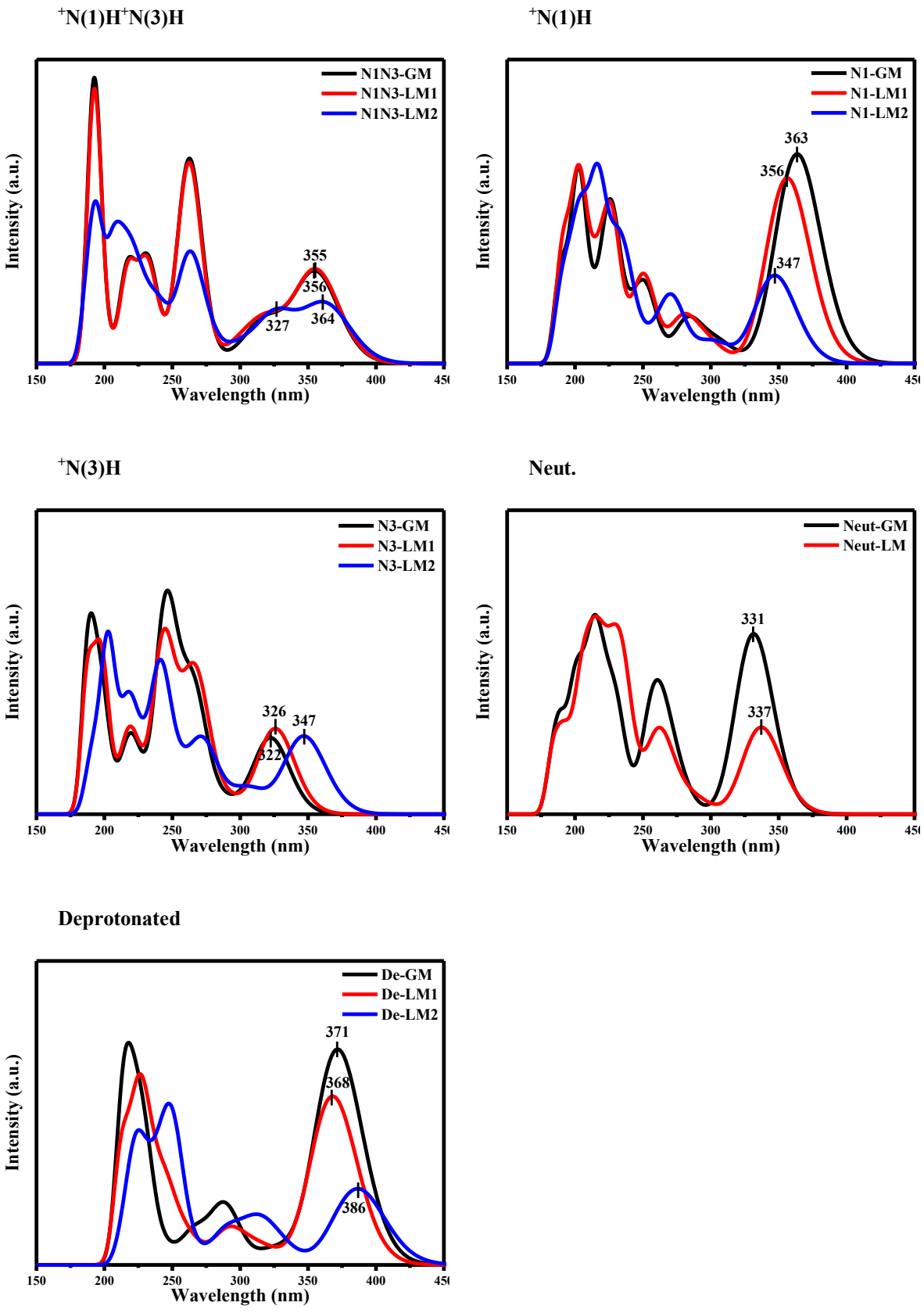

Chapter VI

Probing Structural Flexibility of AG1478 in Kinase Domain

Results obtained from the previous chapters give valuable information about AG1478 conformations and the impact of environment on AG1478 spectra. For instance, the AG1478 conformation (planar or twisted) was inferred from the fluorescence excitation spectrum and the polarity of the local environment of AG1478 was deduced from the fluorescence emission spectrum. This information are exploited herein to investigate the structure of AG1478 and the polarity and heterogeneity of AG1478 binding site in two AG1478-protein complexes.

Based on excitation and emission spectra of AG1478 complexed with two different proteins, the conformational states of AG1478 and binding site polarity were found quite different in the two protein complexes. The red-edge excitation shift (REES) probed the heterogeneity of the binding site (protein conformation and hydration) distributions in the protein conformational ensemble which differed significantly in the two protein complexes. The results were compared with X-ray crystal data of AG1478 and its structural analogue in the two proteins. A good agreement between our results, computations and literature was deduced demonstrating that our tool of combining UV-Vis spectroscopy with quantum chemical calculations is effective for probing the spatial and electronic properties of the environmentally-sensitive tyrosine kinase inhibitor, AG1478.

This chapter is presented in the form of a submitted paper, **Muhammad Khattab**, Feng Wang and Andrew H.A. Clayton, *Conformational Plasticity in TKI-kinase Interactions Revealed with Fluorescence Spectroscopy and Theoretical Calculations*.

Conformational Plasticity in TKI-kinase Interactions Revealed with Fluorescence Spectroscopy and Theoretical Calculations

Journal:	*The Journal of Physical Chemistry*
Manuscript ID	jp-2018-015303
Manuscript Type:	Article
Date Submitted by the Author:	12-Feb-2018
Complete List of Authors:	Khattab, Muhammad; Swinburne University of Technology, Wang, Feng; Swinburne University of Technology, Molecular Model Discovery Laboratory, Faculty of Science, Engineering and Technology Clayton, Andrew; Swinburne University of Technology, Centre for Microphotonics

Conformational Plasticity in TKI-kinase Interactions Revealed with Fluorescence Spectroscopy and Theoretical Calculations

Muhammad Khattab[a], Feng Wang[b*] and Andrew H. A. Clayton[a*]

[a] *Centre for Micro-Photonics, Faculty of Science, Engineering and Technology, Swinburne University of Technology, Melbourne, Victoria, 3122, Australia*

[b] *Molecular Model Discovery Laboratory, Department of Chemistry and Biotechnology, Engineering and Technology, Swinburne University of Technology, Melbourne, Victoria, 3122, Australia*

*Corresponding authors: aclayton@swin.edu.au

fwang@swin.edu.au

Abstract

To understand drug-protein dynamics, it is necessary to account for drug molecular flexibility and binding site plasticity. Herein, we exploit fluorescence from a tyrosine kinase inhibitor, AG1478, as a reporter of its conformation and binding-site environment when complexed with its cognate kinase. Water-soluble kinases, aminoglycoside phosphotransferase APH(3`)-Ia and mitogen activated protein kinase 14 (MAPK 14), were chosen for this study. Based on our prior work, the AG1478 conformation (planar or twisted) was inferred from the fluorescence excitation spectrum, the polarity of the AG1478 binding site was deduced from the fluorescence emission spectrum, while red-edge excitation shift (REES) probed the heterogeneity of the binding site (protein conformation and hydration) distributions in the protein conformational ensemble. In the AG1478-APH(3`)-Ia complex both twisted (or partially-twisted) and planar AG1478 conformations were evidenced from emission wavelength-dependent excitation spectra. The binding site environment provided by the APH(3`)-Ia was moderately polar (λ_{max}= 480nm) with evidence for considerable heterogeneity (REES= 34nm). In contrast, in the AG1478-MAPK14 complex, AG1478 was in a predominantly planar conformation with a lower degree of conformational heterogeneity. The binding site environment provided by the MAPK14 protein was of relatively low polarity (λ_{max}= 430nm) with a smaller-degree of heterogeneity (REES= 11nm). The results are compared with available literature x-ray data and discussed in the context of our current understanding of TKI conformation and protein conformational ensembles.

Keyword: Tyrosine kinase inhibitor; Anticancer drug; UV-Vis spectroscopy; Red edge excitation shift (REES); Quantum mechanical calculations; Structural heterogeneity; Occupancy factor; B-factor; Protein ruggedness.

1. Introduction

The free energy landscape (FEL) model of a protein structure defines the molecular heterogeneity as an array of equilibrated energetic minima on a multidimensional free energy surface.[1] Proteins exhibiting various conformational states have a *rugged* FEL, hence understanding how FEL is altered upon agonist/inhibitor binding is crucial for modulating biological/remedial function of a protein.[2]

Kinase conformational plasticity is a paramount factor for understanding ligand binding, enzymatic switching and biological function. Kinases were found adopting extensive array of conformations in their crystal structures.[3,4] Flexibility of activation loop regulates substrate/inhibitor access to ATP-binding site, hence conformational perturbations in a part or in a whole of kinase structure would alter kinase activity.[5,6] Upon binding of a kinase inhibitor to the target protein, a perturbation of dynamic ensemble of kinase conformations and biased stabilization of distinct conformation(s) can take place.[7] For instance, epidermal growth factor receptor (EGFR) plasticity enables it to accommodate Gefitinib in multiple conformations. Gefitinib exhibits 20-fold higher affinity to the active conformation of mutant EGFR than to the wild type.[8,9] Similarly, binding of ATP-competitive inhibitors to mitogen-activated protein kinase (MAPK14) is modulated through conformationally selective inhibition.[10,11] Therefore, many patients develop resistance against ATP-competitive kinase inhibitors due to conformational/hydrophobicity changes in the kinase gatekeeper triggered by single-point mutation. These changes were found introducing a steric clashes for an inhibitor to access and bind to the gatekeeper.[12]

The domain motion at hinge region (gatekeeper) is in fact constrained unless the kinase is phosphorylated.[13] Upon phosphorylation, conformational changes of target protein that precede ligand binding impede or accelerate the inhibitor-receptor association. Intriguingly, it was found that the binding rate is pH-dependent while the binding affinity is not.[7]

Identifying inhibitors that target distinct conformation is a cumbersome task and requires detailed conformational analysis of the inhibitor and protein-binding site.[7] Several approaches are extensively applied to address this problem such as fluorescent labels in kinases (FLiK),[14-19] optical second-harmonic generation,[20-22] NMR residual dipolar coupling,[23] and surface plasmon resonance studies.[24,25] In FLiK method, a fluorophore that is a reporter to its local environment is exploited to probe kinase conformational changes.[7] All the aforementioned techniques are used as a binding assay for *in vitro* studies. But for studying changes in drug conformations and medium heterogeneity in solution, REES measurements have been widely applied in literature for solutions of drug-protein complexes.[2,26-29]

Steady-state red edge excitation shift (REES) spectroscopy is a reliable quantitative measure for protein FEL and conformational equilibria of ligand-protein complexes.[2] REES is a phenomenon where low-energy excitation beam selectively excites discrete fluorophore molecules hence potentially reflects the conformational equilibrium of a fluorophore and its binding site.[28,30] REES is observed depending on the rate of solvent relaxation during excitation and the triggered changes in a fluorophore dipole moment following excitation. The emission wavelength becomes independent of excitation wavelength when the environmental relaxation is faster than the fluorescence lifetime. But in a rigid environment, the delayed solvent relaxation causes a blue-shifted fluorescence spectrum when excited in the blue due to the emission from solvent-unrelaxed excited state of the fluorophore. While a red-shifted emission is observed when the fluorophore is excited in the red due to the emission from solvent-relaxed state. Therefore, REES can be observed with fluorophores in viscous or cooled solutions or complexed with a folded protein states.[31,32] Hence, REES is a powerful tool for tackling contemporary challenges in biophysics and structural biology.

On the other hand, it has been revealed that small molecules do not necessarily adopt the global minimum conformation upon binding to their receptors.[33-35] Analyses of myriad ligand-protein cocrystals have reportedly demonstrated that many of ligand molecules do not even adopt the local minima structures.[36,37] Data from a library of 100 ligand-protein crystals showed that bound ligand structures are *nearly* identical to the local minima conformations.[38]

Aminoglycoside phosphotransferases are group of enzymes responsible for phosphorylation/activation of aminoglycoside antibiotics.[39,40] Many studies have been concerned with characterization of interaction modes between enzyme, nucleotide substrate and aminoglycoside. Detailed analyses revealed structural conservation of nucleotide triphosphate, ATP or GTP, binding site in the studied aminoglycoside phosphotransferases.[41-45] A high structural similarity of nucleotide triphosphate binding site was noted between aminoglycoside phosphotransferases and eukaryotic protein kinases.[46] Therefore, the inhibition potential of protein kinase inhibitors has been tested against aminoglycoside phosphotransferases.[46,47] One of these studies was conducted using AG1478 as a potential inhibitor for aminoglycoside phosphotransferase APH(3`)-Ia.[46]

AG1478 (**Fig. 1**) is a tyrosine kinase inhibitor[48-50] and its electronic and conformational properties have been studied by our group.[51-54] Our studies revealed that the medium pH, polarity and hydration significantly affects AG1478 conformation. We have also evaluated the topological and electronic properties of AG1478 under different conditions. Therefore our earlier results can be exploited to estimate the polarity of AG1478-binding site and structural flexibility (conformations) of AG1478 when bound to a target protein.

Figure 1. Molecular structure of *N*-(3-chlorophenyl)-6,7-dimethoxyquinazolin-4-amine (AG1478).

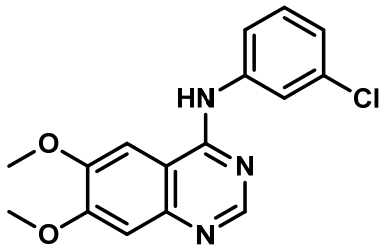

In the present work, we probe the binding environment of AG1478 in two proteins. The two proteins are aminoglycoside phosphotransferase and MAPK14. The x-ray crystal structure of aminoglycoside phosphotransferase APH(3`)-Ia in complex with AG1478 and kanamycin has been published previously.[46] Although AG1478 was proven as an inhibitor to MAPK14 (p38-α) through competitive binding to ATP-binding pocket (IC_{50}= 560 nM),[55] no x-ray data on this complex has been reported. However, the x-ray crystal structure of MAPK14 with MSQ (an AG1478 analogue) has been published.[56]

We aim to examine conformational plasticity and polarity of AG1478-binding site utilizing our previous spectroscopic results of AG1478 in various solvents. To this end, we performed steady-state fluorescence spectroscopy including REES measurements. We also conducted analyses for amino acids of AG1478 binding site using PDB data such as B-factor. In addition, a comparative theoretical study between different structures of AG1478 in the co-crystal forms deposited in PDB were performed. Our study provides a deep insight into the intrinsic and extrinsic structural and electronic property changes in AG1478 molecules at ATP-binding site helping to understand the nature of AG1478-binding pocket.

2. Materials and Methods

2.1. Materials

AG1478 was purchased from AdooQ Bioscience. Recombinant *danio rerio* aminoglycoside phosphotransferase domain-containing protein 1 (APH(3`)-Ia) and mitogen-activated protein kinase 14 isoform 2 (MAPK14) were obtained from MyBioSource, Inc. and used as received. Millipore deionized water was used in reconstitution of proteins. A pair of matched quartz cuvette of 1cm path length was purchased from Starna Pty Ltd.

2.2. Methods

2.2.1. UV-Vis spectroscopy

Solutions of the two proteins, APH(3`)-Ia and MAPK14, were prepared according to the manufacturer's instructions. The lyophilized powder of APH(3`)-Ia was reconstituted as specified in the product datasheet by adding 2mL deionized water

to give a final concentration of 8 μM APH(3`)-Ia. Reconstitution of MAPK14 was performed by adding 1mL 20mM Tris-HCl buffer (pH 8.0) to give a concentration of 5 $\mu$M MAPK14. We also prepared a 4mM stock solution of AG1478 in DMSO. The APH(3`)-Ia -AG1478 complex was formed by adding 3.3μL of 4mM AG1478 stock solution to the 2mL of the 8 μM APH(3`)-Ia solution. The MAPK14-AG1478 complex was formed by adding 1.7$\mu$L of 4mM AG1478 stock solution to the 2mL of the 5 $\mu$M APH(3`)-Ia solution.

Fluorescence and REES measurements were conducted on a Perkin Elmer LS55 spectrophotometer. Fluorescence spectra were recorded using a fixed excitation wavelength (in 5nm intervals in the range of 330nm-360nm) and scanning the emission from 400-600nm. Two types of spectral information were obtained from the fluorescence spectra recorded as a function of excitation wavelength. 1) The average fluorescence spectrum was obtained by integrating (or summing up) the individual fluorescence spectra recorded at different excitation wavelengths. 2) REES plots were obtained by plotting the emission maximum of the fluorescence spectrum as a function of the excitation wavelength. Fluorescence excitation spectra were recorded using a fixed emission wavelength (in 10nm intervals in the range of 400nm-550nm) and scanning the excitation from 300-390nm. The temperature (10–37 °C) of the sample was regulated using Perkin Elmer Peltier Temperature Programmer PTP-1. All spectra were corrected for background scatter from proteins and buffer. Fluorescence maxima, spectra averaging and error bars were obtained using Originlab software. Normalized spectra were produced by normalizing the wavelength maximum of excitation and emission to one.

2.2.2. Computational details

Structure coordinates were downloaded from Protein Databank www.rcsb.org. The missing hydrogen on the nitrogen linking quinazoline to anilino moiety was added using Gaussview software. Energy optimization was performed only for the added hydrogen while keeping all other atoms frozen. Five entries of AG1478 (four X-ray resolved structures + one calculated structure (entry-5)) were used with no further geometry optimization for calculating excitation spectrum. Time dependant density functional theory (TD-DFT)[57] was used for excitation energy calculation using the same model and basis set employed for AG1478 in our previous published studies.[52-54] Becke three-parameters Lee-Yang-Parr hybrid functional (B3LYP)[58,59] in combination with 6-311+G* basis set and conductor-like polarizable continuum model (CPCM)[60] were employed in all calculations. Dielectric continuum of water (ε= 78.3) was used to approximately describe the polarity of AG1478 environment. We used the dielectric continuum of water as approximation for AG1478 environment since our earlier results showed trivial changes in excitation energy calculations with varying the dielectric constant of implicit model.[52] The UV-Vis excitation (absorption) spectra of AG1478 structures were calculated for the

singlet–singlet transitions of the lowest 60 excited states. All simulations were performed on the uncomplexed AG1478 structures using GAUSSIAN 09 Revision C.01[61] on Swinburne supercomputing facilities.

3. Results

3.1. Spectroscopy study

3.1.1. AG1478-aminoglycoside phosphotransferase complex

Our previous work reported that the UV-Vis spectrum of AG1478 in solution consisted of two bands in the 300-360nm region, one at 330nm attributed to the planar conformer of AG1478 and a second band at 340nm attributed to the twisted conformer.[52] To determine the distribution of twisted versus planar conformer of AG1478 when bound to a protein kinase, we measured the excitation spectra of AG1478-APH(3`)-Ia complex in a buffer solution of pH 8 as a function of emission wavelength. The excitation spectrum of the AG1478-APH(3`)-Ia complex consisted primarily of two bands, one at 333nm and the other at 344nm, as expected. However, the relative proportion of the two band intensities was dependent on the monitoring wavelength of emission. A significant change (*i.e.* by 30%) in the relative intensity of 333nm and 344nm can be seen in the normalized excitation spectra depicted in **Fig. 2a** and in the plot of the ratio of the two band intensities shown in **Fig. 2b**. These results reveal that the AG1478 exists in different conformations within the ensemble of proteins. In the context of our prior work, our results could be interpreted as the twisted conformer being dominant relative to the planar conformer near the blue-edge of the emission (400-450nm), while both conformers contribute to the emission nearly equally from 460nm-550nm.

Figure 2. A) Normalized excitation spectra of AG1478-APH(3`)-Ia complex scanned at different emission wavelengths (400–550 nm); B) Plot of relative intensity of 333/344 nm bands as a function of emission wavelength fitted to Boltzmann model.

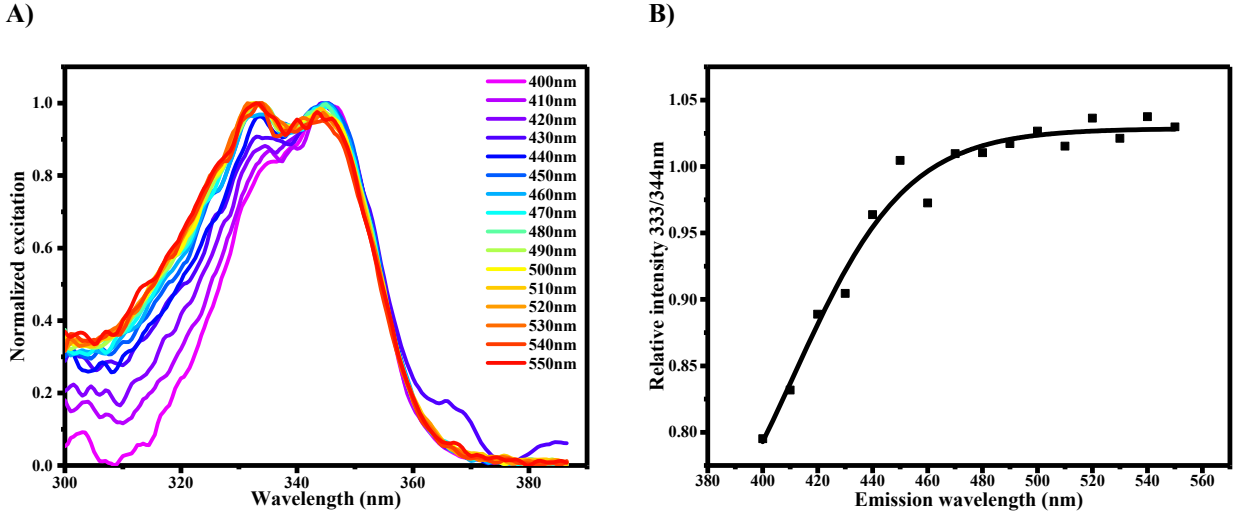

Our prior work also revealed the exquisite sensitivity of the fluorescence emission of AG1478 to solution polarity.[51] We use this sensitivity here to examine the environmental heterogeneity and dynamics provided by the protein close to the AG1478 moiety in the protein binding pocket.

Integrated fluorescence spectra of the AG1478-APH(3`)-Ia complex are shown in **Fig. 3a** recorded at several temperatures and information about the intensity of emission and position of the emission maximum are depicted in **Fig. 3b** and **Fig. 3c**. Interestingly, the intensity of fluorescence increased from 10 to 15 to 20 ºC but then decreased from 20 to 30 to 37 ºC. A decrease in fluorescence due to an increase in temperature is expected based on an increase in the non-radiative rates of deactivation from the excited state or dynamic quenching processes. An increase in fluorescence with temperature is unusual but was reported by us previously for the AG1478-water complex in acetonitrile:water solutions due to a release of static quenching.[53] This unorthodox temperature dependence of emission could be tentatively explained by both static and dynamic quenching mechanisms in the binding site of the protein or a temperature-dependent conformational change. However, we note that more work is needed to properly explain this behaviour. The wavelength of emission maximum revealed an increasing shift by 8nm with increasing temperature from 10 ºC to 37 ºC. This could result from an increase in solvent relaxation around the probe with increasing temperature, or alternatively, an increase in the hydration of the binding pocket with increasing temperature. To distinguish these two possibilities, we turn to REES measurements to gain an idea about the relative dynamics of the protein around the AG1478 probe, the relative dynamics of the excited-state and the nature of the protein FEL sensed by the AG1478 probe.

Emission spectra were recorded as a function of excitation wavelength in the range 330-360nm. The results are depicted in **Fig. 3d**. It is remarkable that the emission spectrum is highly dependent on the excitation wavelength with shifts exceeding 30nm. A slight increase in REES magnitude was observed upon changing temperature from 10, 15 to 20 ºC but a decrease was observed from 20 to 25 then a plateau. Aside from the measurements at 20 ºC, the REES measurement were nearly independent on temperature. An increase in dynamics of the protein with temperature should increase solvent relaxation giving a red-shifted emission but a smaller REES value, however temperature appears to affect the emission wavelength but not the REES value. This could be explained when the temperature increases, the hydration of the binding site is also increased (due to a conformational change opening up the binding pocket) but the dynamics of the protein matrix is too slow to cause significant solvent relaxation about the AG1478 chromophore during the excited-state lifetime. A temperature insensitive REES is consistent with a rugged landscape of the FEL sensed by the AG1478 probe.

Figure 3. A) Normalized summed spectra for all emissions of AG1478-APH(3`)-Ia complex obtained by exciting at 330, 335, 340, 345, 350, 355 and 360 nm at six different temperatures. B) and C) Plots of fluorescence intensity and fluorescence maximum as a function of temperature respectively. The solid line is to ease data points tracking. D) Plot of fluorescence maximum as a function of excitation wavelength of AG1478-APH(3`)-Ia complex recorded at different temperatures. Error bars are obtained from three replications. Inset indicates fitting of a selected plot to Boltzmann function. $\Delta\lambda_{em}^{max}$ defines the shift of emission maximum at λ_{exc}= 360nm relative to that obtained from λ_{exc}= 330nm.

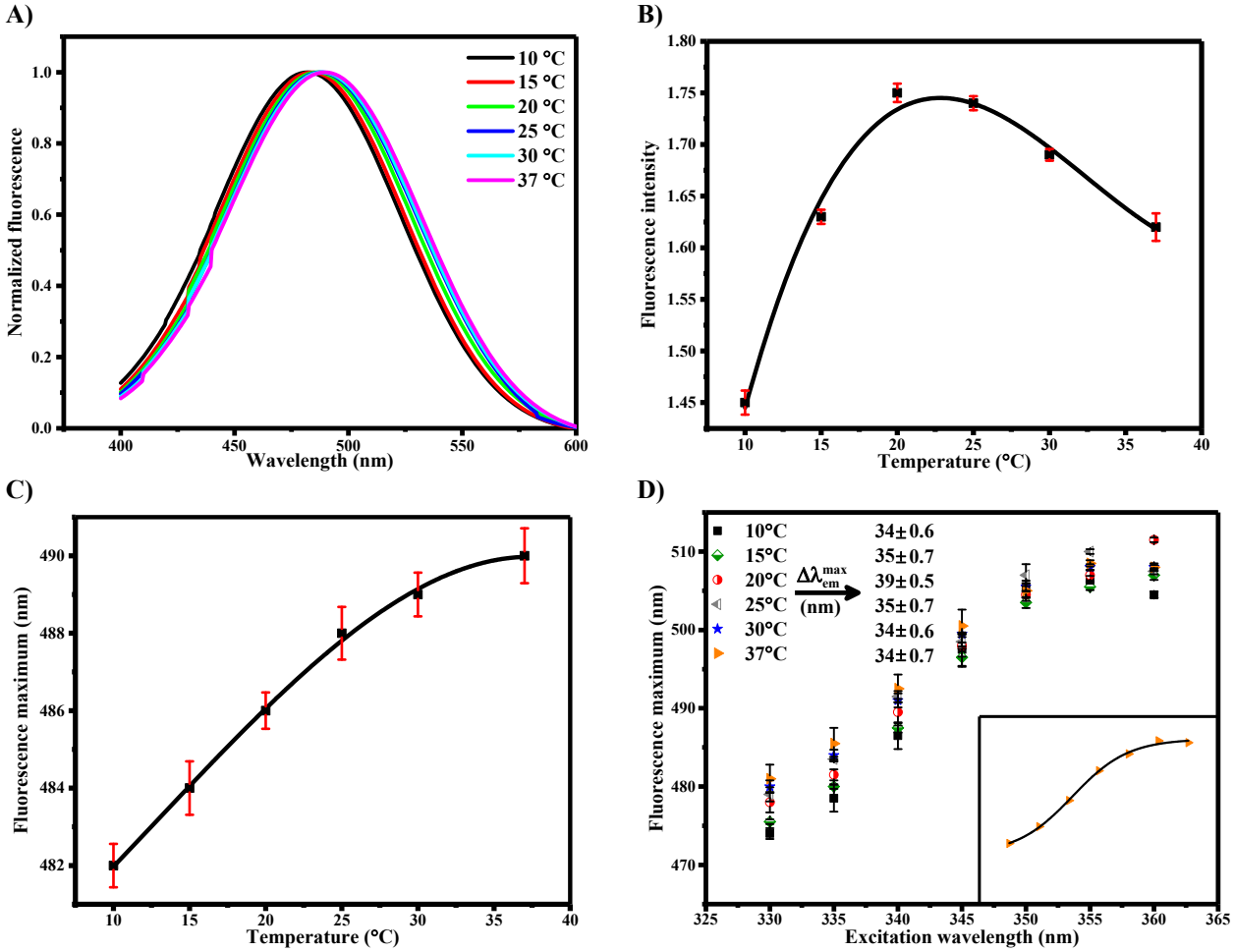

It was found that REES data fits well (R^2= 0.99) with a Boltzmann model $A = A_2 + \frac{A_1 - A_2}{1 + exp\frac{x - x_0}{dx}}$ where A stands for measured fluorescence, A_1 for minimum value for λ_{max}, A_2 for maximum value for λ_{max}, x for excitation wavelength, x_0 for the excitation wavelength value at midpoint between the maximum and minimum values of fluorescence maximum and dx for the width in (nm) of the most significant change in fluorescence. The calculated parameters from fitting of AG1478-APH(3`)-Ia complex fluorescence to Boltzmann model are summarized in **Table 1**. We noticed that the increase in temperature yielded increase in the min and max emission wavelength (A_1 and A_2) values. However REES magnitude was almost constant (around 34nm) insensitive to temperature change.

Table 1. Boltzmann fitting parameters calculated from the observed emission of AG1478-APH(3`)-Ia complex at different temperatures.

	10 ºC	15 ºC	20 ºC	25 ºC	30 ºC	37 ºC
A_1	473.4 ± 1.8	473.1 ± 0.9	473.1 ± 3.5	477.1 ± 3.5	478.2 ± 0.8	478.2 ± 1.5
A_2	506.1 ± 1.0	507.5 ± 0.5	512.3 ± 2.0	509.7 ± 1.8	508.8 ± 0.4	509.0 ± 0.7
x_0	341.3 ± 0.7	341.4 ± 0.3	342.0 ± 1.1	341.3 ± 1.3	341.4 ± 0.3	340.6 ± 0.6
dx	3.3 ± 0.6	4.5 ± 0.3	5.9 ± 1.3	4.3 ± 1.3	4.2 ± 0.3	4.7 ± 0.6

3.1.2. AG1478-MAPK14 complex

The excitation spectra of AG1478 in the AG1478-MAPK14 complex are depicted in **Fig. 4a**. The predominant band is at 330nm consistent with a predominant planar conformation of AG1478 in the AG1478-MAPK14 complex. The 340nm band appears as a shoulder in the excitation spectrum. The relative proportion of the two bands is somewhat dependent on emission observation wavelength, varying from 1.26 to 1.38 or by 10% across the range of emission as shown in **Fig. 4b**. This suggests some degree of conformational heterogeneity of AG1478 in the population of protein-drug complexes.

Figure 4. A) Normalized excitation spectra of AG1478 bound to MAPK14 in Tris buffer solution recorded at different emission wavelength (400–550 nm). B) Plot of relative intensity of 333nm and 344nm bands as a function of emission wavelength. Solid line is used to guide reader's eye.

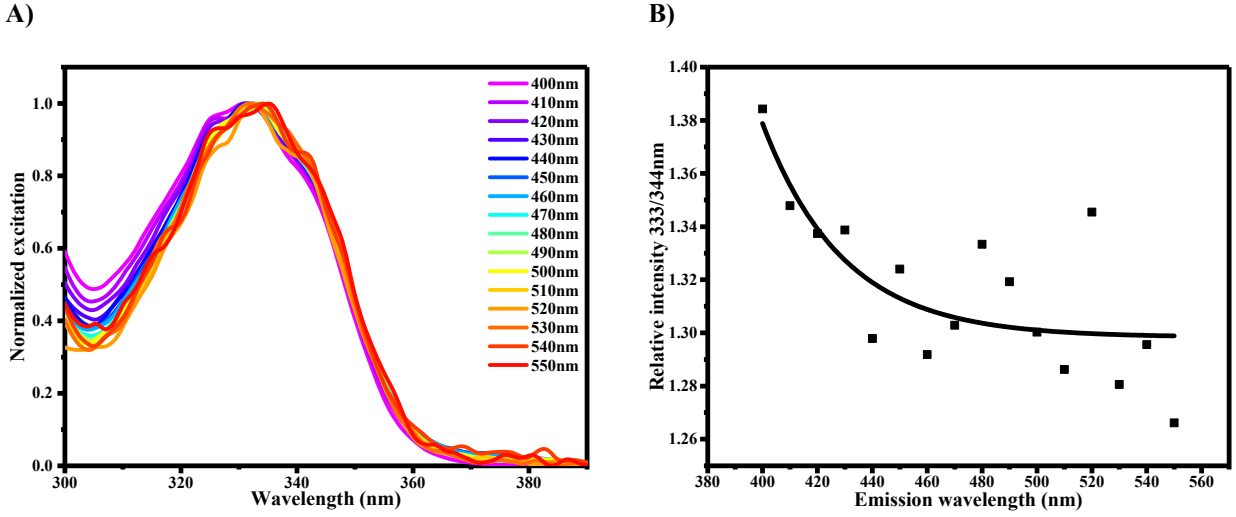

The emission spectrum of AG1478 in the AG1478-MAPK14 complex revealed an emission maximum near 427nm at all temperatures examined (**Fig. 5a**). Increase in temperature resulted in a decrease in emission from AG1478 consistent with conventional dynamic-type quenching processes (**Fig. 5b**). However, the position of the emission spectrum only changed slightly from 427nm at 15 ºC to 426 nm at 37 ºC (**Fig. 5c**). Taken together, these results suggest that the binding site for AG1478 in MAPK14 is relatively low in polarity.

The REES experiments on AG1478-MAPK14 revealed interesting behaviour as shown in **Fig. 5d**. The magnitude of the REES was only 11-14 nm and a slight increase in REES was observed upon heating the solutions. These observations are consistent with a rugged FEL, however we interpret the smaller REES and blue emission compared to AG1478-APH(3`)-Ia complex owing to a reduced polarity of the binding site in MAPK14. The existence of significant REES could be due to water molecules in an otherwise non-polar binding pocket.

Figure 5. A) Normalized summed spectra for all emissions obtained by exciting at 315, 320, 325, 330, 335, 340, 345, 350, 355 and 360 nm at six different temperatures. B) and C) Plots of fluorescence intensity and fluorescence maximum as a function of temperature respectively. Solid line is to guide reader's eye. D) Plot showing fluorescence maximum of AG1478 bound to MAPK14 in Tris buffer solution as a function of excitation wavelength. Error bars are obtained from three replications. Inset indicates fitting of a selected plot to Boltzmann function. $\Delta\lambda_{em}^{max}$ defines the shift of emission maximum at λ_{exc}= 360nm relative to that obtained from λ_{exc}= 330nm.

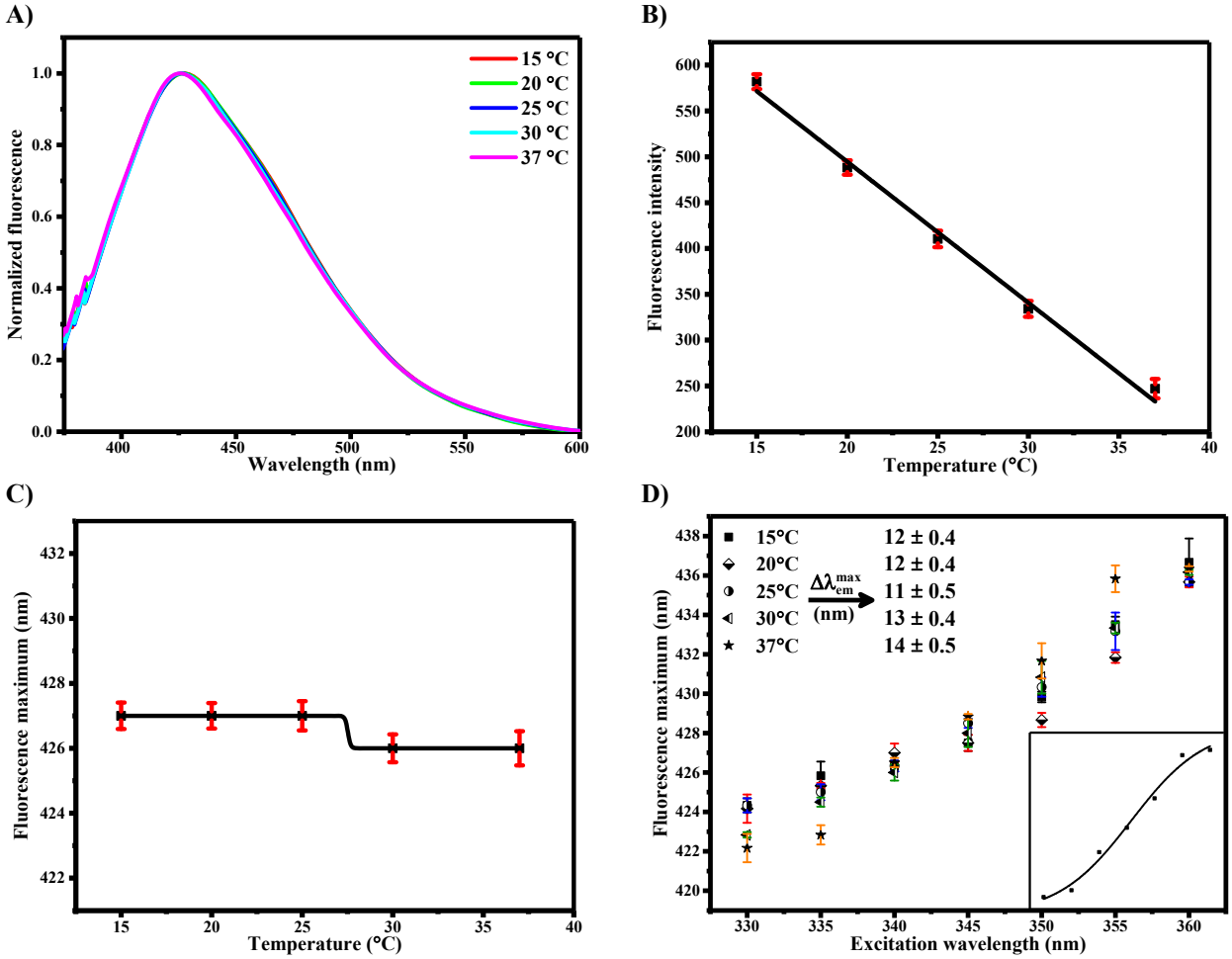

We also found that REES data of AG1478-MAPK14 fits well (R^2= 0.99) to Boltzmann model. The calculated parameters from fitting of AG1478-MAPK14 complex fluorescence to Boltzmann model are summarized in **Table 2**. In contrast to data of AG1478-APH(3`)-Ia complex, we noticed a decrease in A_1 and A_2 values with the increase in temperature. In the next section we make a quantitative estimation of the binding site polarity of the two proteins.

Table 2. Boltzmann fitting parameters calculated from the observed emission of AG1478-MAPK14 complex at different temperatures.

	15 ºC	20 ºC	25 ºC	30 ºC	37 ºC
A_1	424.2 ± 0.9	423.2 ± 0.8	422.8 ± 0.8	419.1 ± 2.0	420.5 ± 2.3
A_2	446.3 ± 11.2	444.7 ± 5.6	442.9 ± 4.1	450.1 ± 9.8	438.6 ± 2.6
x_0	357.9 ± 7.6	355.3 ± 1.1	354.5 ± 3.5	357.2 ± 7.2	345.8 ± 2.0
dx	7.7 ± 3.1	6.2 ± 1.3	9.5 ± 2.2	13.8 ± 4.4	6.6 ± 2.7

3.1.3. Estimation of binding site polarity using Reichardt $E_T(30)$ scale

In our earlier published manuscript,[51] emission energy of AG1478 fluorescence in hydrogen-donating and aprotic solvents exhibited a good correlation with Reichardt transition energy $E_T(30)$ scale. It is well known that Reichardt model takes into account both the solvent polarity and hydrogen bonding strength.[62-64] Therefore, we herein exploited our published model to determine $E_T(30)$ of AG1478 binding site within APH(3`)-Ia and MAPK14 proteins. By extrapolating the best fit model of AG1478 in aprotic solvents and using the maximum emission wavelength of AG1478-protein complex ($\lambda_{exc}$= 350) at 25 ºC, we obtained $E_T(30)$ of 52.8 and 34.8 kcal/mol for AG1478 bound to APH(3`)-Ia and MAPK14 respectively. These values mean that colligative properties of AG1478 binding site in APH(3`)-Ia and MAPK14 closely resembles *N*-methylformamide and 1,4-dioxane respectively. However, we could not use AG1478-protic model to estimate $E_T(30)$ of AG1478 in complex with the two proteins. This is because extrapolation of the fit line lies below the minimum value of the extreme nonpolar solvent (trimethylsilane) $E_T(30)$= 30.7 kcal/mol and the maximum value of the most polar solvent (water) $E_T(30)$= 63.1 kcal/mol.

Figure 6. Emission wavenumber of AG1478 in cm^{-1} as a function of Reichardt transition energy $E_T(30)$ in kcal/mol of AG1478 in two sets of solvents, aprotic and protic, adopted from [51]. Extrapolation of fitted lines is done to calculate $E_T(30)$ of AG1478-APH(3`)-Ia and AG1478-MAPK14 complexes. AG1478-APH(3`)-Ia and AG1478-MAPK14 emit at 430nm and 507nm respectively using λ_{exc}= 350 at 25 ºC. The figure is reproduced from [51].

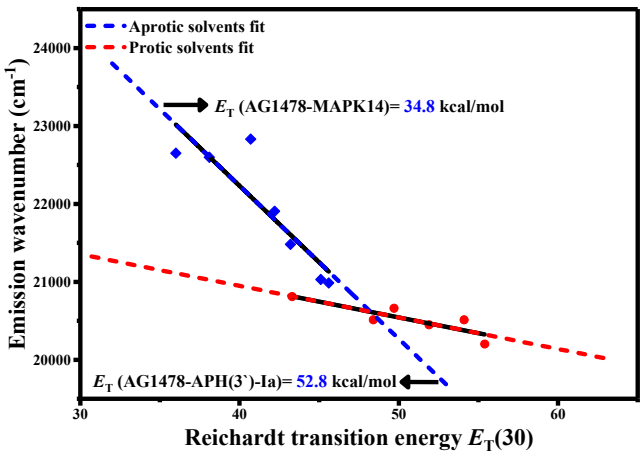

3.2. Computational study-comparison with x-ray crystallography models

3.2.1. Average conformation of AG1478

The two lowest energy excitation maxima were calculated for the five entries of AG1478 coordinates downloaded from PDB for AG1478 (PDB ID: 0TO) complexed with APH(3`)-Ia (PDB ID: 4FEX). The topological difference between AG1478 structures is due to the difference in torsional angle between quinazoline and aniline moiety. In spite of small variations in dihedral angle, a significant difference in excitation maxima was calculated as indicated in **Table 3**. The lowest energy excitation maximum was computed within 348–364 nm range while the second transition was calculated at 335–350 nm. The experimental excitation spectrum maxima of AG1478-APH(3`)-Ia complex was observed at 333nm and 344nm. By comparing the excitation spectra maxima of our experiment and entry-4 structure, we noticed a good agreement between our experimental results and the calculated excitation maxima for the obtained x-ray crystal structure (entry-4). The observed lowest energy transition and the second transition in AG1478-APH(3`)-Ia complex are shifted by 4nm and 2nm to the blue relative to entry-4.

We noticed that the entry-5 structure is substantially different from AG1478 x-ray structures regarding its geometrical and electronic properties as indicated in **Table 3**. Despite the entry-5 structure represents the most energy minimized structure (global minimum), it is far likely to be populated in AG1478-APH(3`)-Ia crystal. Only one major electronic transition was calculated in 300-360 nm range which cannot account for the experimental spectrum. By examining the oscillator strength and the main molecular orbital contribution to the electronic transitions within the four x-ray entries, entry-4 showed distinct electronic characteristics. In contrary to all other entries, the oscillator strength of lowest energy transition is lower than that of the higher energy transition. In addition the molecular orbital contribution to the two electronic transitions are quite different in entry-4 from other entries, refer to **Table 3**. Calculations revealed that HOMO-1→LUMO transition in entry-4 contributes to the first and second electronic excitations unlike in other entries. By taking entry-1 energy as a reference, energy calculations showed that the entry-5 structure is the most energetically stable structure while entry-2< entry-4< entry-3 are less stable than entry-1 in the same order.

Table 3. Comparison of excitation maxima and torsional angle calculated for AG1478 structures retrieved from PDB (four experimental entries + one calculated entry).[65] Exp. (AG1478-APH(3`)-Ia) denotes the observed excitation maxima of AG1478 bound to aminoglycoside phosphotransferase. e-transition (L) and (H) denote electronic transitions encountered in the lowest and higher energy excitation maximum respectively. Δ*E* stands for change in molecular energy relative to entry-1.

PDB entries		**Entry-1**	**Entry-2**	**Entry-3**	**Entry-4**	**Entry-5**
	Torsion angle	-15.1	-13.5	-15.7	-10.1	32.8
	Excit. max. (nm)	341/351	350/364	346/357	**335/348**	338
	Osc. str.	0.1718/0.1894	0.1542/0.2048	0.1195/0.2529	0.2733/0.1214	0.3834
	e-transition (L)	H→L (61%)	H→L (68%)	H→L (74%)	H-1→L (53%)	H→L (89%)
		H-2→L (26%)	H-2→L (27%)	H-2→L (17%)	H→L (42%)	
	e-transition (H)	H→L (36%)	H-2→L (62%)	H-2→L (57%)	H→L (54%)	
		H-2→L (31%)	H→L (30%)	H→L (23%)	H-1→L (39%)	
		H-3→L (18%)		H-4→L (13%)		
	Δ*E* (kcal/mol)	0.00	1.97	11.21	7.53	-28.62
Exp. (AG1478-APH(3`)-Ia)	Excit. max. (nm)	**333/344**				

3.2.2. Heterogeneity of AG1478 conformations

We searched for anilinoquinazoline-based compounds deposited in PDB to scrutinize the coplanarity between quinazoline core and aniline moiety in this family of active compounds. Compound name, protein name, and torsional angle between quinazoline and aniline rings for every PDB entry structure are compiled in Supplementary Materials **Table S1**. Four out of thirty-nine PDB entries showed a torsional angle less than 10º indicating that the planar conformation is not favoured and that the twisted conformation is the conformationally favoured protein-bound structure for anilinoquinazoline class kinase inhibitors. The four X-ray entries of AG1478 exhibited torsional angles in range of (-10.1º) – (-15.7º) revealing existence of AG1478 in twisted conformations at ATP-binding pocket of APH(3`)-Ia protein. The same finding was obtained from our experimental excitation spectra (**Fig. 2a** and **2b**). The structural heterogeneity of AG1478 may also contribute to the observed REES *i.e.* if different conformers have distinct absorbance and emission spectra.

Occupancy and temperature (Debye-Waller) factors are essential parameters to evaluate X-ray crystals. Occupancy factor has values ranging from 0 to 1, where values closest to 1 indicate a precise positioning of atom in the crystal. The temperature factor is defined as the mean-square displacement of an atom from its position in the model. It is an isotropic measure of static and dynamic disorder within the crystal. The static disorder is mainly due to different conformations of the drug in different unit cells of the protein. While the dynamic disorder originates from the atomic vibrations and translocations in the crystal. Lattice defects, restraints and model errors contribute also to calculation of temperature

factor.[66-68] Although the X-ray crystal resolution is 2.71Å and data collection was performed at temperature of 100K, it was noted that individual and average values of temperature factor are greater than 50Å^2 (rmsd> 0.90Å) indicating high structural disorder (heterogeneity) of AG1478 atoms within protein-binding site, refer to **Table 4**. It is in agreement with our experimental excitation spectra, since the structural flexibility of AG1478 atoms point out the existence of multiple conformations of AG1478 in two proteins accounting for the change in relative intensity of 333nm and 344nm excitation bands as a function of emission wavelength.

Table 4. Occupancy and temperature (B-factor) values in (Å^2) for non-hydrogen atoms of four copies of AG1478 (PDB: 0TO) obtained from its X-ray cocrystal with APH(3`)-Ia (PDB: 4FEX).

Atom type	**Entry-1**		**Entry-2**		**Entry-3**		**Entry-4**	
	Occupancy	**B-factor**	**Occupancy**	**B-factor**	**Occupancy**	**B-factor**	**Occupancy**	**B-factor**
C	0.74	62.84	0.79	76.27	0.83	72.47	0.87	78.62
C	0.74	74.15	0.79	81.74	0.83	88.69	0.87	85.47
Cl	0.74	82.11	0.79	86.89	0.83	89.30	0.87	80.81
C	0.74	67.68	0.79	76.13	0.83	77.89	0.87	65.99
C	0.74	75.27	0.79	76.93	0.83	82.56	0.87	74.35
C	0.74	76.06	0.79	73.40	0.83	77.80	0.87	72.86
C	0.74	62.77	0.79	76.79	0.83	66.75	0.87	63.67
N	0.74	54.99	0.79	74.21	0.83	63.06	0.87	53.42
C	0.74	62.28	0.79	73.97	0.83	63.93	0.87	58.36
N	0.74	60.25	0.79	65.33	0.83	64.95	0.87	52.88
C	0.74	55.94	0.79	63.48	0.83	57.57	0.87	56.73
N	0.74	50.00	0.79	68.53	0.83	53.70	0.87	50.11
C	0.74	56.84	0.79	65.70	0.83	56.09	0.87	61.68
C	0.74	46.34	0.79	62.61	0.83	51.54	0.87	50.99
C	0.74	60.87	0.79	71.06	0.83	63.39	0.87	59.11
C	0.74	65.60	0.79	78.53	0.83	68.24	0.87	64.08
O	0.74	77.28	0.79	74.87	0.83	63.66	0.87	78.97
C	0.74	63.77	0.79	64.95	0.83	73.05	0.87	67.21
C	0.74	67.93	0.79	77.49	0.83	67.50	0.87	60.73
C	0.74	60.66	0.79	67.43	0.83	54.74	0.87	50.91
O	0.74	63.72	0.79	65.02	0.83	66.57	0.87	66.83
C	0.74	55.00	0.79	73.98	0.83	56.82	0.87	59.74
Average	---	64	---	72	---	67	---	64
r.m.s. (Å)	---	0.91	---	0.96	---	0.93	---	0.91

The 4-anilinoquinazoline compound (PDB-ID: MSQ) complexed with MAPK14 (PDB-ID: 1DI9) showed occupancy value of 1 for all of its atoms as depicted in Supplementary Materials **Table S2**. The average temperature factor value is 28Å^2 (rmsd 0.60Å) indicating presence of MSQ, hence possibly for AG1478, in a more rigid (less disordered) environment than with APH(3`)-Ia (PDB-ID: 4FEX).

3.2.3. Average polarity of the AG1478 binding site from X-ray data

Five structurally and functionally identical copies comprises the asymmetric unit of aminoglycoside phosphotransferase APH(3`)-Ia. These copies are named chain A, B, C, D and E. Four different copies of AG1478 were resolved from chain A, C, D and E. A trivial change in amino acids sequence was noted at AG1478 binding site. The amino acid (aa) sequence similarity relative to binding site within chain A is given in **Table 5**. Although the binding site within four chains are highly conserved, a small change in binding site polarity, hydration and hydrophobicity might also be a contributing factor for variations in the excitation maxima of four AG1478 entries if included in calculations. Since molecular dynamics calculations are not within the scope of this manuscript, the interactions between AG1478 and protein are not discussed. Hereafter, we shed the light on some *isolated* physicochemical properties of AG1478 binding pocket in various chains of APH(3`)-Ia and in MAPK14 protein.

Table 5. Amino acid (aa) sequence of binding pocket within four chains of aminoglycoside phosphotransferase APH(3`)-Ia involved in interactions with the four entries of AG1478. Data in bold are for aa not found in chain A. Data are retrieved from PDB.[65]

Parameter	Chain A	Chain C	Chain D	Chain E
	V33	I40	**D31**	**E51**
	I40	F53	I40	F53
	F53	K55	F53	K55
	K55	E68	K55	E68
	E68	L72	E68	L72
	L72	P82	**L96**	P82
	P82	T98	T98	T98
	T98	T99	T99	T99
	T99	A100	A100	A100
	A100	I101	I101	I101
	I101	G103	**P102**	**P102**
	G103	K104	G103	G103
	K104	T105	K104	K104
	T105	**Q108**	T105	T105
	D202	D202	**Q108**	**Q108**
	I205	I205	I205	D202
	I215	I215	I215	I205
	D216	D216	D216	I215
	----	----	----	D216
Sequence similarity	100%	89%	78%	89%
No. of polar aa	8	9	9	10
No. of non-polar aa	10	9	9	9
No. of waters	1 (flexible)	0	0	1 (restricted)
Hydrophobicity[69] (kcal/mol)	-0.26	-0.29	-0.29	-0.42

The binding site in chain A contains 10 non-polar aa and 8 polar aa. While chain E is marked with the highest distribution of polar (10) aa relative to 8 non-polar aa. Chain C and D have equal distribution of polar and nonpolar aa. AG1478-binding site in chain A and E comprises one molecule of confined water. Water molecules was resolved at vicinity of methoxy groups and chlorine atom in chain A and E respectively. Hydrophobicity scale developed by Wimley *et al* was utilized to calculate hydrophobicity of AG1478 binding site. The hydrophobicity parameter (free energy of partitioning of aa) ranges from (1.85) for the most hydrophobic tryptophan to (-2.02) for the most hydrophilic glutamic acid.[69] The midpoint of the scale is at (-0.085). The average hydrophobicity of binding site aa in chain E has a value of (-0.42) which is lower in magnitude than in chain A (-0.26), chain C (-0.29) and chain D (-0.29) indicating that AG1478-binding site in chain E is significantly more hydrophilic than in other chains. The average hydrophobicity of AG1478-binding site in chain E was found identical to asparagine (-0.42). Whereas the average hydrophobicity of binding sites in chains A, C and D is intermediate between alanine (-0.17) and asparagine (-0.42). The polarity deduced from the analysis of the side chains proximal to AG1478 agrees well with our experimentally measured polarity from the AG1478 fluorescence spectrum. The emission maximum of AG1478 in the protein complex was similar to that observed for AG1478 in DMF and *N*-methylformamide.

X-ray crystallographic data of AG1478 with MAPK14 is not deposited in PDB. Fortunately, we found a structurally similar compound (PDB ID: MSQ), where the chlorine atom of AG1478 is replaced with methylsulfanyl group, deposited in PDB. Structural analysis of inhibitor-binding site revealed that MAPK14 (PDB ID: 1DI9) binding site is significantly less polar than APH(3`)-Ia inhibitor-binding site. The ratio of nonpolar to polar amino acids at inhibitor-binding site is 12:5 respectively as depicted in **Table 6**. The binding site within MAPK14 is more hydrated than in APH(3`)-Ia. Two confined water molecules were resolved at the vicinity of N(3) and 4-anilino substituent of MSQ. The hydrophobicity scale confirmed that inhibitor-binding site in the single chain crystal of MAPK14 is more hydrophobic (-0.18) than in all chains of APH(3`)-Ia. The average hydrophobicity of binding pocket is closely similar to alanine hydrophobicity (-0.17). This agrees also well with our results where the polarity of AG1478-MAPK14 complex was estimated lower than the polarity of AG1478-APH(3`)-Ia.

Table 6. Amino acid (aa) sequence of binding pocket of structurally and functionally similar compound to AG1478 (PDB-ID: MSQ) in MAPK14 protein. Data are adopted from protein data bank website.[65]

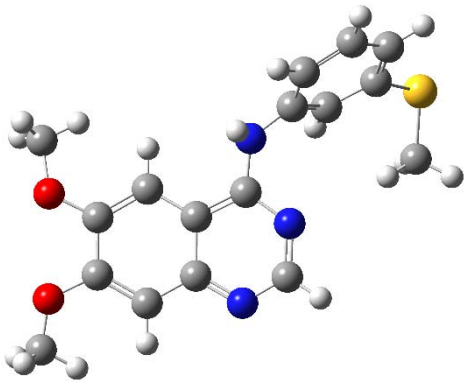

4-[3-Methylsulfanylanilino]-6,7-Dimethoxyquinazoline (MSQ)

Parameter	MAPK14
	V30 G31 V38 A51 V52 K53 E71 L75 I84 L104 V105 T106 H107 L108 M109 L167 D168
No. of polar aa	5
No. of non-polar aa	12
No. of waters	2
Hydrophobicity[69] (kcal/mol)	-0.18

3.2.4. Disorder of AG1478-binding site from X-ray structure

It is noteworthy that the majority of aa atoms at AG1478 binding site in APH(3`)-Ia and MAPK14 are assigned occupancy value of 1. This means the crystal backbone is precisely fortified, whereas the inhibitor (AG1478) atoms are disordered (occupancy factor 0.87-0.74) in APH(3`)-Ia (**Table 4**). In MAPK14, the inhibitor (MSQ) occupancy factor was equal to 1 indicating precise positioning and restricted movement of inhibitor within a well-defined binding pocket (**Table S2**).

We examined the B-factor values, deposited in PDB, of aa comprising AG1478 binding site in APH(3`)-Ia and MSQ in MAPK14. The average value of B-factor in APH(3`)-Ia is 52Å^2 (rmsd> 0.84Å) indicating a significant structural disorder (heterogeneity) of AG1478-binding site in APH(3`)-Ia. This structural disorder in AG1478- binding site could be a factor that contributes to the observed REES. The average value of B-factor for binding pocket in MAPK14 is estimated at 18Å^2 (rmsd> 0.47Å). This value implies slighter structural disorder within binding site which might account for the lesser magnitude of REES with AG1478-MAPK14.

We found that aa in APH(3`)-Ia have higher B-factor values than in MAPK14 as can be seen in **Fig. 7**, however the crystal data were collected at the same temperature (100K) and the resolution was nearly equal (2.71Å for AG1478-APH(3`)-Ia and 2.60Å for AG1478-MAPK14). This indicates that the environment around AG1478 in APH(3`)-Ia is more conformationally disordered than for MSQ in MAPK14. While in case of MAPK14, atoms vibrational movement are more constrained. Referring to our experimental results, this can account for the higher REES magnitude in AG1478-APH(3`)-Ia complex than in AG1478-MAPK14 complex. Because when the medium surrounding AG1478 is more disordered, it somehow reflects increase in environment dynamics which in turn affects emission process (REES and fluorescence quenching). Overall, binding site polarity and disorder (occupancy factor and B-factor) are both responsible for the red shifted emission with AG1478-APH(3`)-Ia than in MSQ-MAPK14.

Figure 7. Color map of temperature (B-factor) factor of amino acid residues in AG1478-binding site in APH(3`)-Ia (upper panel) and MSQ-binding site in MAPK14 (lower panel).

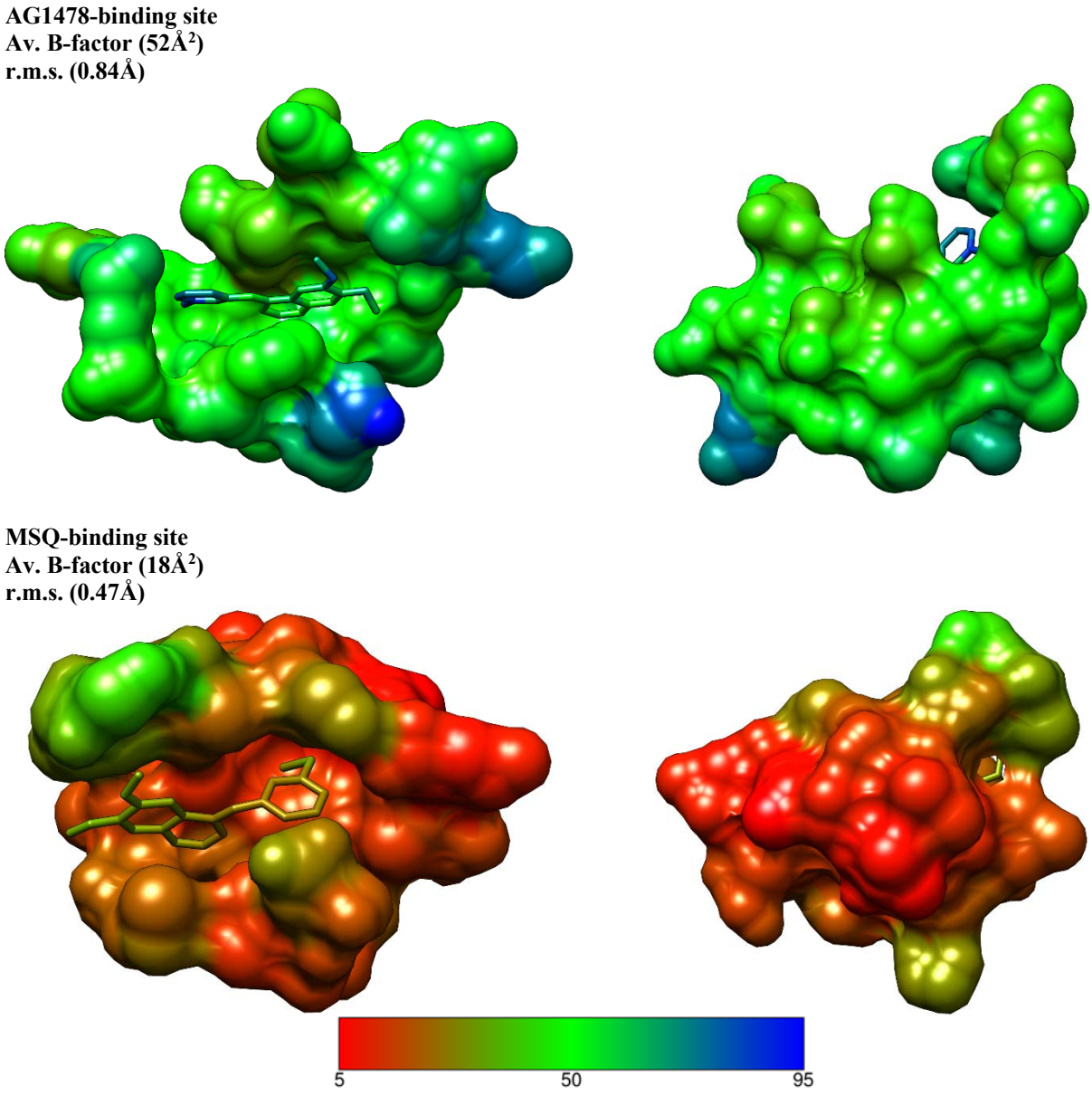

4. Discussion

The conformational states of AG1478, and the environment (structural plasticity and polarity) of the AG1478 protein binding site in two enzymes, APH(3`)-Ia and MAPK14, were examined using fluorescence spectroscopy techniques. We compared our fluorescence data with AG1478 conformers proposed in the literature using quantum chemical calculations. We also performed detailed analysis of X-ray data obtained from PDB to unravel polarity, hydrophobicity, and disorder of amino acids constituting the inhibitor binding site of APH(3`)-Ia and MAPK14. Our analyses on PDB data can be

taken as approximations for studying AG1478 conformations and environment in MAPK14 and should be exercised with caution. This is because we used the AG1478 derivative (MSQ) and its binding site on MAPK14 instead of AG1478.

The conformational states of AG1478 were deduced from the fluorescence excitation spectrum of the AG1478 in complex with each protein. In accordance with our prior work, an absorbance near 330nm is associated with a planar form of AG1478 while the presence of an additional band near 340nm is evidence for a twisted conformation of AG1478. In the APH(3`)-Ia-AG1478 complex both transitions were present, which is evidence for some degree of twisting in the AG1478 structure. Comparison of AG148 five conformers from the literature X-ray crystal structures of the APH(3`)-Ia-AG1478 complex revealed that the excitation spectrum from td-DFT calculations was very sensitive to AG1478 conformation, as expected. However, we found that one conformer, with a torsional angle of -10.1 degrees gave a better agreement with the observed wavelength positions of the experimental transitions, than the other conformers (with torsional angles of -14, -15, -16 and +33 degrees). Conformational heterogeneity was observed experimentally in the APH(3`)-Ia-AG1478 through an emission wavelength-dependent excitation spectrum. Both transitions at 330nm and 340nm persisted as a function of emission wavelength, but their relative amplitudes differed markedly with monitoring emission wavelength. This is evidence that there are multiple conformations of AG1478 in the APH(3`)-Ia-AG1478 complex in solution probably contributed by mixtures of planar and twisted (or slightly twisted) AG1478 structures.

The corresponding fluorescence excitation spectrum of AG1478-MAPK14 complex differed from the APH(3`)-Ia-AG1478 complex which is an indication for a different conformation or conformational distribution of AG1478 in the AG1478-MAPK14 complex. Based on the relatively larger 330nm band amplitude compared to the 340nm band amplitude in the excitation spectrum, we reasoned that the AG1478 conformation is more biased towards the planar conformation in the AG1478-MAPK14 complex. Moreover, the heterogeneity of conformations were less than in the APH(3`)-Ia-AG1478 complex as deduced from the fluorescence excitation spectrum as a function of emission wavelength. Examination of the X-ray B-factors for an AG1478 derivative in complex with MAPK14, showed that the AG1478 derivative was fairly rigid in the binding site, while the corresponding B-factors for AG1478 in the APH(3`)-Ia-AG1478 indicated more conformational disorder. These results suggest that AG1478 can adopt different conformational distributions depending on the target enzyme.

The environment provided by the protein at the AG1478 binding pocket was assessed by several spectroscopic parameters. Polarity was inferred from the wavelength of the emission peak, while a distribution of solvent environments around the

AG1478 (protein conformations, water) was deduced from red-edge excitation shift experiments. The emission from APH(3`)-Ia-AG1478 indicated a moderately polar environment surrounding AG1478, consistent with an analysis of the amino acid side chains comprising the binding site in the APH(3`)-Ia-AG1478 complex. The APH(3`)-Ia-AG1478 complex showed a significant REES of 34-39 nm indicating a distribution of micro-environments around the AG1478 in the protein complex suggestive of multiple conformational states of the protein. This conclusion is supported by the large B-factors in the X-ray crystal structure of the APH(3`)-Ia-AG1478 complex. In contrast for AG1478-MAPK14, the emission was more indicative of a less polar environment around the AG1478, in good qualitative agreement with an analysis of the amino acid side chains comprising the binding site in a AG1478-derivative in complex with MAPK14. Moreover, the REES observed in the AG1478-MAPK14 was markedly less (11-14 nm) than for AG1478- APH(3`)-Ia perhaps indicating a lower degree of heterogeneity of binding site environments (protein conformational states). This latter conclusion is consistent with the smaller B-factors in the X-ray crystal structure of the AG1478 derivative-MAPK14 complex.

It is important to note that for both AG1478-protein complexes, the REES values were largely independent of temperature over the temperature range examined. In analogy with Demchenko's analysis of tryptophan-containing proteins,[70,71] this suggests that solvent relaxation (i.e. protein) around the AG1478 is restricted somewhat on the fluorescence timescale of nanoseconds. This is in agreement with other reports of conformational plasticity of kinases. The combined millisecond molecular dynamics with Markov state models revealed conformational plasticity of the apo kinase domain of Bruton tyrosine kinase (BTK).[72] Simulations predicted several conformations for Imatinib (a tyrosine kinase inhibitor) binding site on Abelson tyrosine kinase (Abl). It was found that kinase domain (ATP binding site) plasticity modulates various landscapes available for binding with ligands. Based on free energy surface calculations, four main populations of the kinase were inferred along with other intermediate states pertaining conformational plasticity to the kinase.[72] The diversity in conformational states of kinase domain was earlier reported for many tyrosine kinases such as MAPK14[73], ERK2,[13] Aurora kinase A[74] and protein kinase A.[73] Taken together, these results indicate that the free energy landscape of solvated kinase domain is diffuse (rugged) which agrees well with our REES observations for AG1478 in APH(3`)-Ia and MAPK14.

Conclusions

Our experimental results are consistent with computations and literature demonstrating reasonable reliability and accuracy of using UV-Vis spectroscopy in probing fluorophore environment. The interplay between our applied methodologies (UV-Vis spectroscopy and quantum chemical calculations) introduced a new tool to monitor the spatial and electronic scenes for important class of anticancer drugs in the free and bound forms to target protein.

Plasticity of structural elements of ATP-binding site is critical for determining inhibitor conformation and binding mode. The binding interaction of AG1478 with either APH(3`)-Ia or MAPK14 can result in a discrete change in AG1478 conformation on a rugged matrix of protein backbone. Our UV-Vis spectra reveal that the interactions between AG1478 and APH(3`)-Ia protein are different from the interactions between AG1478 and MAPK14 protein. The former indicates that AG1478 exists in two distinguishable and competitive conformations at APH(3`)-Ia binding pocket. The presence of the conformers of AG1478 shows dependence on the emission wavelength. While in MAPK14 binding site, the AG1478 ligand may experience distortion with more than one conformers which are not very different from the most stable structures, and they are not very much emission wavelength dependent. The results suggest that AG1478 binds to ATP-binding site where conformational selection is protein-dependent. Polarity and hydrophobicity of amino acids at vicinity of AG1478 play significant role in determining AG1478 structure. To this end, our results along with extensive analyses of PDB data pave the way for studying the molecular dynamics of AG1478 binding to ATP pocket.

References

1 Tsai, C. J., Ma, B. Y., Sham, Y. Y., Kumar, S. & Nussinov, R. Structured disorder and conformational selection. *Proteins-Structure Function and Genetics* **44**, 418-427 (2001).

2 Catici, D. A. M., Amos, H. E., Yang, Y., van den Elsen, J. M. H. & Pudney, C. R. The red edge excitation shift phenomenon can be used to unmask protein structural ensembles: implications for NEMO-ubiquitin interactions. *Febs Journal* **283**, 2272-2284 (2016).

3 Masterson, L. R. *et al.* Dynamics connect substrate recognition to catalysis in protein kinase A. *Nat. Chem. Biol.* **6**, 821-828 (2010).

4 Huse, M. & Kuriyan, J. The conformational plasticity of protein kinases. *Cell* **109**, 275-282 (2002).

5 Endicott, J. A., Noble, M. E. M. & Johnson, L. N. The Structural Basis for Control of Eukaryotic Protein Kinases. *Annual Review of Biochemistry, Vol 81* **81**, 587-613 (2012).

6 Kar, G., Keskin, O., Gursoy, A. & Nussinov, R. Allostery and population shift in drug discovery. *Curr. Opin. Pharmacol.* **10**, 715-722 (2010).

7 Tong, M. & Seeliger, M. A. Targeting Conformational Plasticity of Protein Kinases. *ACS Chem. Biol.* **10**, 190-200 (2015).

8 Yun, C. H. *et al.* Structures of lung cancer-derived EGFR mutants and inhibitor complexes: Mechanism of activation and insights into differential inhibitor sensitivity. *Cancer Cell* **11**, 217-227 (2007).

9 Stamos, J., Sliwkowski, M. X. & Eigenbrot, C. Structure of the epidermal growth factor receptor kinase domain alone and in complex with a 4-anilinoquinazoline inhibitor. *J. Biol. Chem.* **277**, 46265-46272 (2002).

10 Rodriguez, J. & Crespo, P. Working Without Kinase Activity: Phosphotransfer-Independent Functions of Extracellular Signal-Regulated Kinases. *Science Signaling* **4** (2011).
11 Hari, S. B., Merritt, E. A. & Maly, D. J. Conformation-Selective ATP-Competitive Inhibitors Control Regulatory Interactions and Noncatalytic Functions of Mitogen-Activated Protein Kinases. *Chem. Biol.* **21**, 628-635 (2014).
12 Azam, M., Seeliger, M. A., Gray, N. S., Kuriyan, J. & Daley, G. Q. Activation of tyrosine kinases by mutation of the gatekeeper threonine. *Nat. Struct. Mol. Biol.* **15**, 1109-1118 (2008).
13 Xiao, Y. *et al.* Phosphorylation releases constraints to domain motion in ERK2. *Proc. Natl. Acad. Sci. U. S. A.* **111**, 2506-2511 (2014).
14 Yin, D. S. M. *et al.* Studying the Conformation of a Receptor Tyrosine Kinase in Solution by Inhibitor-Based Spin Labeling. *Angewandte Chemie-International Edition* **56**, 8417-8421 (2017).
15 Wang, L., Yan, X. & Su, X. G. A label-free and sensitive fluorescent assay for one step detection of protein kinase activity and inhibition. *Anal. Chim. Acta* **935**, 224-230 (2016).
16 Pezzato, C. *et al.* Label-free fluorescence detection of kinase activity using a gold nanoparticle based indicator displacement assay. *Org. Biomol. Chem.* **13**, 1198-1203 (2015).
17 Zhou, F. *et al.* One-strand oligonucleotide probe for fluorescent label-free "turn-on" detection of T4 polynucleotide kinase activity and its inhibition. *Analyst* **140**, 5650-5655 (2015).
18 Simard, J. R. *et al.* Development of a Fluorescent-Tagged Kinase Assay System for the Detection and Characterization of Allosteric Kinase Inhibitors. *J. Am. Chem. Soc.* **131**, 13286-13296 (2009).
19 Simard, J. R. *et al.* High-Throughput Screening To Identify Inhibitors Which Stabilize Inactive Kinase Conformations in p38 alpha. *J. Am. Chem. Soc.* **131**, 18478-18488 (2009).
20 Butko, M. T., Moree, B., Mortensen, R. B. & Salafsky, J. Detection of Ligand-Induced Conformational Changes in Oligonucleotides by Second-Harmonic Generation at a Supported Lipid Bilayer Interface. *Anal. Chem.* **88**, 10482-10489 (2016).
21 Salafsky, J. S. Detection of protein conformational change by optical second-harmonic generation. *J. Chem. Phys.* **125** (2006).
22 Nucciotti, V. *et al.* Probing myosin structural conformation in vivo by second-harmonic generation microscopy. *Proc. Natl. Acad. Sci. U. S. A.* **107**, 7763-7768 (2010).
23 Vajpai, N. *et al.* Solution conformations and dynamics of ABL kinase-inhibitor complexes determined by NMR substantiate the different binding modes of imatinib/nilotinib and dasatinib. *J. Biol. Chem.* **283**, 18292-18302 (2008).
24 Kitagawa, D., Gouda, M. & Kirii, Y. Quick Evaluation of Kinase Inhibitors by Surface Plasmon Resonance Using Single-Site Specifically Biotinylated Kinases. *Journal of Biomolecular Screening* **19**, 453-461 (2014).
25 Navratilova, I. *et al.* Biosensor-Based Approach to the Identification of Protein Kinase Ligands with Dual-Site Modes of Action. *Journal of Biomolecular Screening* **17**, 183-193 (2012).
26 Moradi, N., Ashrafi-Kooshk, M. R., Chamani, J., Shackebaei, D. & Norouzi, F. Separate and simultaneous binding of tamoxifen and estradiol to human serum albumin: Spectroscopic and molecular modeling investigations. *J. Mol. Liq.* **249**, 1083-1096 (2018).
27 Abdollahpour, N., Soheili, V., Saberi, M. R. & Chamani, J. Investigation of the Interaction Between Human Serum Albumin and Two Drugs as Binary and Ternary Systems. *Eur. J. Drug Metab. Pharmacokinet.* **41**, 705-721 (2016).
28 Chattopadhyay, A. & Haldar, S. Dynamic Insight into Protein Structure Utilizing Red Edge Excitation Shift. *Acc. Chem. Res.* **47**, 12-19 (2014).
29 Guha, S., Rawat, S. S., Chattopadhyay, A. & Bhattacharyya, B. Tubulin conformation and dynamics: A red edge excitation shift study. *Biochemistry* **35**, 13426-13433 (1996).
30 Demchenko, A. P. The red-edge effects: 30 years of exploration. *Luminescence* **17**, 19-42 (2002).
31 Weber, G. & Shinitzky, M. Failure of Energy Transfer between Identical Aromatic Molecules on Excitation at Long Wave Edge of Absorption Spectrum. *Proc. Natl. Acad. Sci. U. S. A.* **65**, 823-+ (1970).
32 Galley, W. C. & Purkey, R. M. Role of Heterogeneity of Solvation Site in Electronic Spectra in Solution. *Proc. Natl. Acad. Sci. U. S. A.* **67**, 1116-& (1970).

33 Kuzmanic, A. *et al.* Changes in the free-energy landscape of p38 alpha MAP kinase through its canonical activation and binding events as studied by enhanced molecular dynamics simulations. *Elife* **6** (2017).

34 Yu, S. C., Park, J. G., Kahn, J. N., Tumer, N. E. & Pang, Y. P. Common Pharmacophore of Structurally Distinct Small-Molecule Inhibitors of Intracellular Retrograde Trafficking of Ribosome Inactivating Proteins. *Sci. Rep.* **3** (2013).

35 Price, S. L. Predicting crystal structures of organic compounds. *Chem. Soc. Rev.* **43**, 2098-2111 (2014).

36 Perola, E. & Charifson, P. S. Conformational analysis of drug-like molecules bound to proteins: An extensive study of ligand reorganization upon binding. *J. Med. Chem.* **47**, 2499-2510 (2004).

37 Nicklaus, M. C., Wang, S. M., Driscoll, J. S. & Milne, G. W. A. Conformational-Changes of Small Molecules Binding to Proteins. *Biorg. Med. Chem.* **3**, 411-428 (1995).

38 Wang, Q. & Pang, Y. P. Preference of Small Molecules for Local Minimum Conformations when Binding to Proteins. *PLoS One* **2** (2007).

39 Shi, K. & Berghuis, A. M. Structural Basis for Dual Nucleotide Selectivity of Aminoglycoside 2 ''-Phosphotransferase IVa Provides Insight on Determinants of Nucleotide Specificity of Aminoglycoside Kinases. *J. Biol. Chem.* **287**, 13094-13102 (2012).

40 Toth, M., Chow, J. W., Mobashery, S. & Vakulenko, S. B. Source of Phosphate in the Enzymic Reaction as a Point of Distinction among Aminoglycoside 2 ''-Phosphotransferases. *J. Biol. Chem.* **284**, 6690-6696 (2009).

41 Fong, D. H., Xiong, B., Hwang, J. Y. & Berghuis, A. M. Crystal Structures of Two Aminoglycoside Kinases Bound with a Eukaryotic Protein Kinase Inhibitor. *PLoS One* **6** (2011).

42 Stogios, P. J., Shakya, T., Evdokimova, E., Savchenko, A. & Wright, G. D. Structure and Function of APH(4)-Ia, a Hygromycin B Resistance Enzyme. *J. Biol. Chem.* **286**, 1966-1975 (2011).

43 Toth, M., Frase, H., Antunes, N. T., Smith, C. A. & Vakulenko, S. B. Crystal structure and kinetic mechanism of aminoglycoside phosphotransferase-2 ''-IVa. *Protein Sci.* **19**, 1565-1576 (2010).

44 Nurizzo, D. *et al.* The crystal structure of aminoglycoside-3 '-phospho-transferase-IIa, an enzyme responsible for antibiotic resistance. *J. Mol. Biol.* **327**, 491-506 (2003).

45 Hon, W. C. *et al.* Structure of an enzyme required for aminoglycoside antibiotic resistance reveals homology to eukaryotic protein kinases. *Cell* **89**, 887-895 (1997).

46 Stogios, P. J. *et al.* Structure-guided optimization of protein kinase inhibitors reverses aminoglycoside antibiotic resistance. *Biochem. J.* **454**, 191-200 (2013).

47 Shakya, T. *et al.* A Small Molecule Discrimination Map of the Antibiotic Resistance Kinome. *Chem. Biol.* **18**, 1591-1601 (2011).

48 Weglicki, W. B., Kramer, J. H., Spurney, C. F., Chmielinska, J. J. & Mak, I. T. The EGFR tyrosine kinase inhibitor tyrphostin AG-1478 causes hypomagnesemia and cardiac dysfunction. *Can. J. Physiol. Pharmacol.* **90**, 1145-1149 (2012).

49 Shushan, A. *et al.* The AG1478 tyrosine kinase inhibitor is an effective suppressor of leiomyoma cell growth. *Hum. Reprod.* **19**, 1957-1967 (2004).

50 Zhu, X. F. *et al.* EGFR tyrosine kinase inhibitor AG1478 inhibits cell proliferation and arrests cell cycle in nasopharyngeal carcinoma cells. *Cancer Lett.* **169**, 27-32 (2001).

51 Khattab, M., Wang, F. & Clayton, A. H. UV–Vis spectroscopy and solvatochromism of the tyrosine kinase inhibitor AG-1478. *Spectrochim. Acta. A Mol. Biomol. Spectrosc.* **164** 128–132 (2016).

52 Khattab, M., Chatterjee, S., Clayton, A. H. A. & Wang, F. Two conformers of a tyrosine kinase inhibitor (AG-1478) disclosed using simulated UV-Vis absorption spectroscopy. *New J. Chem.* **40**, 8296-8304 (2016).

53 Khattab, M., Wang, F. & Clayton, A. H. A. Micro-solvation of tyrosine-kinase inhibitor AG1478 explored with fluorescence spectroscopy and computational chemistry. *Rsc Advances* **7**, 31725-31735 (2017).

54 Khattab, M., Wang, F. & Clayton, A. H. A. A pH-induced conformational switch in a tyrosine kinase inhibitor identified by electronic spectroscopy and quantum chemical calculations. *Sci. Rep.* **7**, 16271 (2017).

55 Diller, D. J., Lin, T. H. & Metzger, A. The discovery of novel chemotypes of p38 kinase inhibitors. *Curr. Top. Med. Chem.* **5**, 953-965 (2005).
56 Shewchuk, L. *et al.* Binding mode of the 4-anilinoquinazoline class of protein kinase inhibitor: X-ray crystallographic studies of 4-anilinoquinazolines bound to cyclin-dependent kinase 2 and p38 kinase. *J. Med. Chem.* **43**, 133-138 (2000).
57 Runge, E. & Gross, E. K. U. Density-Functional Theory for Time-Dependent Systems. *Phys. Rev. Lett.* **52**, 997-1000 (1984).
58 Becke, A. D. A New Mixing of Hartree-Fock and Local Density-Functional Theories. *J. Chem. Phys.* **98**, 1372-1377 (1993).
59 Becke, A. D. Density-Functional Thermochemistry .3. The Role of Exact Exchange. *J. Chem. Phys.* **98**, 5648-5652 (1993).
60 Cossi, M., Rega, N., Scalmani, G. & Barone, V. Energies, structures, and electronic properties of molecules in solution with the C-PCM solvation model. *J. Comput. Chem.* **24**, 669-681 (2003).
61 Gaussian 09, Revision C.01 (Gaussian, Inc., Wallingford CT, 2009).
62 Reichardt, C. Solvatochromic Dyes as Solvent Polarity Indicators. *Chem. Rev.* **94**, 2319-2358 (1994).
63 Reichardt, C. & Harbuschgornert, E. Pyridinium N-Phenoxide Betaines and Their Application for the Characterization of Solvent Polarities .10. Extension, Correction, and New Definition of the Et Solvent Polarity Scale by Application of a Lipophilic Penta-Tert-Butyl-Substituted Pyridinium N-Phenoxide Betaine Dy. *Liebigs Ann. Chem.*, 721-743 (1983).
64 Reichardt, C. & Welton, T. *Solvents and solvent effects in organic chemistry*. (John Wiley & Sons, 2011).
65 Berman, H. M. *et al.* The Protein Data Bank. *Nucleic Acids Res.* **28**, 235-242 (2000).
66 Wlodawer, A., Minor, W., Dauter, Z. & Jaskolski, M. Protein crystallography for non-crystallographers, or how to get the best (but not more) from published macromolecular structures. *Febs Journal* **275**, 1-21 (2008).
67 Touw, W. G. & Vriend, G. BDB: Databank of PDB files with consistent B-factors. *Protein Engineering Design & Selection* **27**, 457-462 (2014).
68 Carugo, O. Correlation between occupancy and B factor of water molecules in protein crystal structures. *Protein Eng.* **12**, 1021-1024 (1999).
69 Wimley, W. C. & White, S. H. Experimentally determined hydrophobicity scale for proteins at membrane interfaces. *Nat. Struct. Biol.* **3**, 842-848 (1996).
70 Demchenko, A. P. Fluorescence Molecular Relaxation Studies of Protein Dynamics - the Probe Binding-Site of Melittin Is Rigid on the Nanosecond Time Scale. *FEBS Lett.* **182**, 99-102 (1985).
71 Demchenko, A. P. On the Nanosecond Mobility in Proteins - Edge Excitation Fluorescence Red Shift of Protein-Bound 2-(Para-Toluidinylnaphthalene)-6-Sulfonate. *Biophys. Chem.* **15**, 101-109 (1982).
72 Sultan, M. M., Denny, R. A., Unwalla, R., Lovering, F. & Pande, V. S. Millisecond dynamics of BTK reveal kinome-wide conformational plasticity within the apo kinase domain. *Sci. Rep.* **7** (2017).
73 Xiao, Y., Liddle, J. C., Pardi, A. & Ahn, N. G. Dynamics of Protein Kinases: Insights from Nuclear Magnetic Resonance. *Acc. Chem. Res.* **48**, 1106-1114 (2015).
74 Cyphers, S., Ruff, E. F., Behr, J. M., Chodera, J. D. & Levinson, N. M. A water-mediated allosteric network governs activation of Aurora kinase A. *Nat. Chem. Biol.* **13**, 402-+ (2017).

Supplementary Materials

Conformational Plasticity in TKI-kinase Interactions Revealed with Fluorescence Spectroscopy and Theoretical Calculations

Muhammad Khattab[a], Feng Wang[b*] and Andrew H. A. Clayton[a*]

[a] *Centre for Micro-Photonics, Faculty of Science, Engineering and Technology, Swinburne University of Technology, Melbourne, Victoria, 3122, Australia*

[b] *Molecular Model Discovery Laboratory, Department of Chemistry and Biotechnology, Engineering and Technology, Swinburne University of Technology, Melbourne, Victoria, 3122, Australia*

*Corresponding authors: aclayton@swin.edu.au

fwang@swin.edu.au

Table S1. Ligand and protein names along with the corresponding PDB-ID and torsion angles between quinazoline moiety and aniline group of the reported 4-anilinoquinazoline based tyrosine kinase inhibitors retrieved from protein data bank.[65] Terms between brackets indicate mutation within protein sequence. The red highlights within 2D structure denotes measured torsional angle.

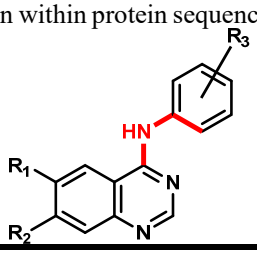

Compound	PDB-ID	Protein	PDB-ID	Torsion angle					
				Entry-1	Entry-2	Entry-3	Entry-4	Entry-5	Entry-6
Afatinib	0WN	EGFR (T790M)	4G5P	12.3	**1.9**				
	0WM	EGFR	4G5J						
AG1478	0TO	APH(3`)-Ia	4FEX	-15.1	-13.5	-15.7	-10.1		
Dacomitinib	1C9	EGFR	4I23	28.5	27.2	44.0			
		EGFR (T790M)	4I24						
Erlotinib	AQ4	EGFR	1M17	41.2	39.5	41.6			
		EGFR (V924R)	4HJO						
Gefitinib	IRE	EGFR (T790M, L858R, V948R)	4I22	52.9	49.1	35.5	35.3	45.7	55.2
		EGFR	4WKQ						
		EGFR (G719S, T790M)	3UG2						
		EGFR (T790M, L858R, V948R)	4I1Z						
		EGFR (G719S)	2ITO						
		EGFR	2ITY						
		EGFR (L858R)	2ITZ						
Lapatinib	FMM	ErbB-4	3BBT	68.1	67.1	55.3			
		EGFR	1XKK						
PD168393	DJK	EGFR (L858R)	4LQM	34.6	30.8	32.8	32.4	**-0.5**	**-0.7**
		EGFR (S345C)	2HWP						
		EGFR (T338M, S345C)	3LOK						
	YUN	EGFR	4LRM						
		EGFR (T790M, L858R)	4LL0						
Sarcatinib	H8H	Myt1	5VCX	52.4	50.4	66.3	52.3		
		Myt1	5VD3						
		MST3	4QMX						
		SRC1	2H8H						
Vandetanib	ZD6	RET	2IVU	61.1					
WHI-P180	DTQ	TTBK1	4BTK	36.0	-34.4	42.5	**0.5**		
		RET	5AMN						
		CDPK1	3NYV						
a	MSQ	P38-α	1DI9	57.4					
b	PFE	FBP (E20Q, S96T, D199N)	1KZ8	32.3	37.0				
c	6U7	KSR2	5KKR	92.3					
d	0N5	GlmU	4E1K	-50.7					

[a] 4-[3-Methylsulfanylanilino]-6,7-Dimethoxyquinazoline
[b] [4-[3-[(6,7-diethoxyquinazolin-4-yl)amino]phenyl]-1,3-thiazol-2-yl]methanol
[c] 6,7-dimethoxy-N-(2-methyl-4-phenoxy-phenyl)quinazolin-4-amine
[d] N-[4-[(6-methoxy-7-oxidanyl-quinazolin-4-yl)amino]phenyl]benzamide

Table S2. Occupancy and temperature (B-factor) values for non-hydrogen atoms of PDB-ID: MSQ obtained from its X-ray cocrystal (PDB: 1DI9). Occupancy value ranges from 0–1 and indicates the amount of each conformation observed in the crystal. Given a value of 1 means that the atom is found in all of the molecules in the same place in the crystal, while lower values denotes uncertainty for atom position. B-factor is indicative for atomic motion and smearing of electron density. Values under 10 indicates sharp positioning of the atom in all molecules in the crystal while values greater than 50 indicates the dynamic movement of the atoms.

Atom type	Occupancy	B-factor
N	1	23.98
C	1	26.59
N	1	27.52
C	1	28.34
C	1	27.62
C	1	25.72
C	1	29.70
C	1	30.67
C	1	30.34
C	1	29.33
N	1	25.53
C	1	24.30
C	1	24.91
C	1	25.78
C	1	25.23
C	1	25.74
C	1	24.98
S	1	30.22
C	1	27.37
O	1	32.32
C	1	31.38
O	1	31.89
C	1	30.60
Average		28
r.m.s. (Å)		0.60

Figure S1. Emission spectra of AG1478-APH3I` complex collected at different temperatures a) 10º C, b) 15º C, c) 20º C, d) 25º C, e) 30º C, and f) 37º C using excitation wavelengths between 315-360 nm.

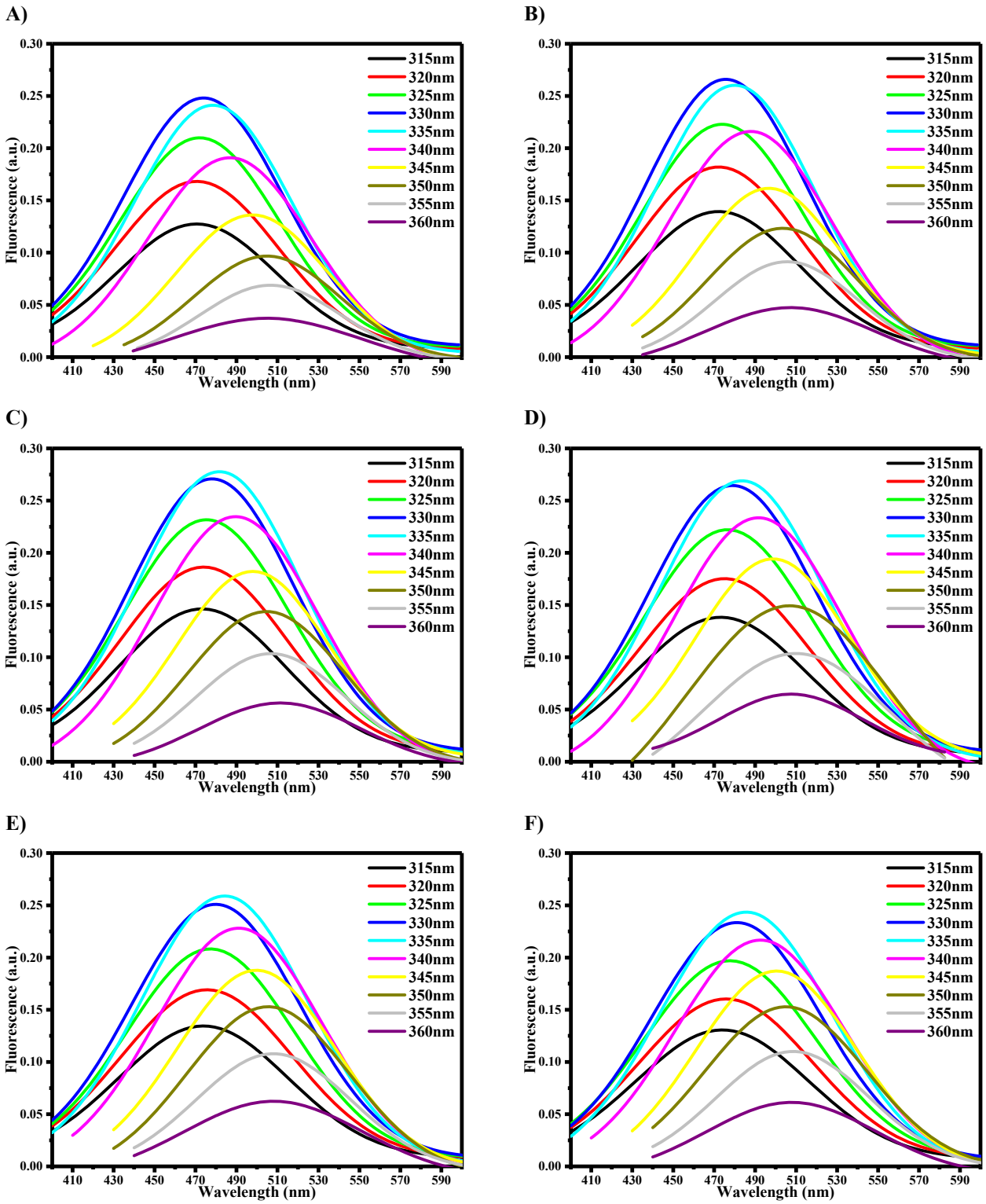

Figure S2. Normalized fluorescence spectra (upper panel) and excitation spectra (lower panel) of AG1478 bound to MAPK14 in Tris buffer solution at 25 ºC, 30 ºC and 37 ºC.

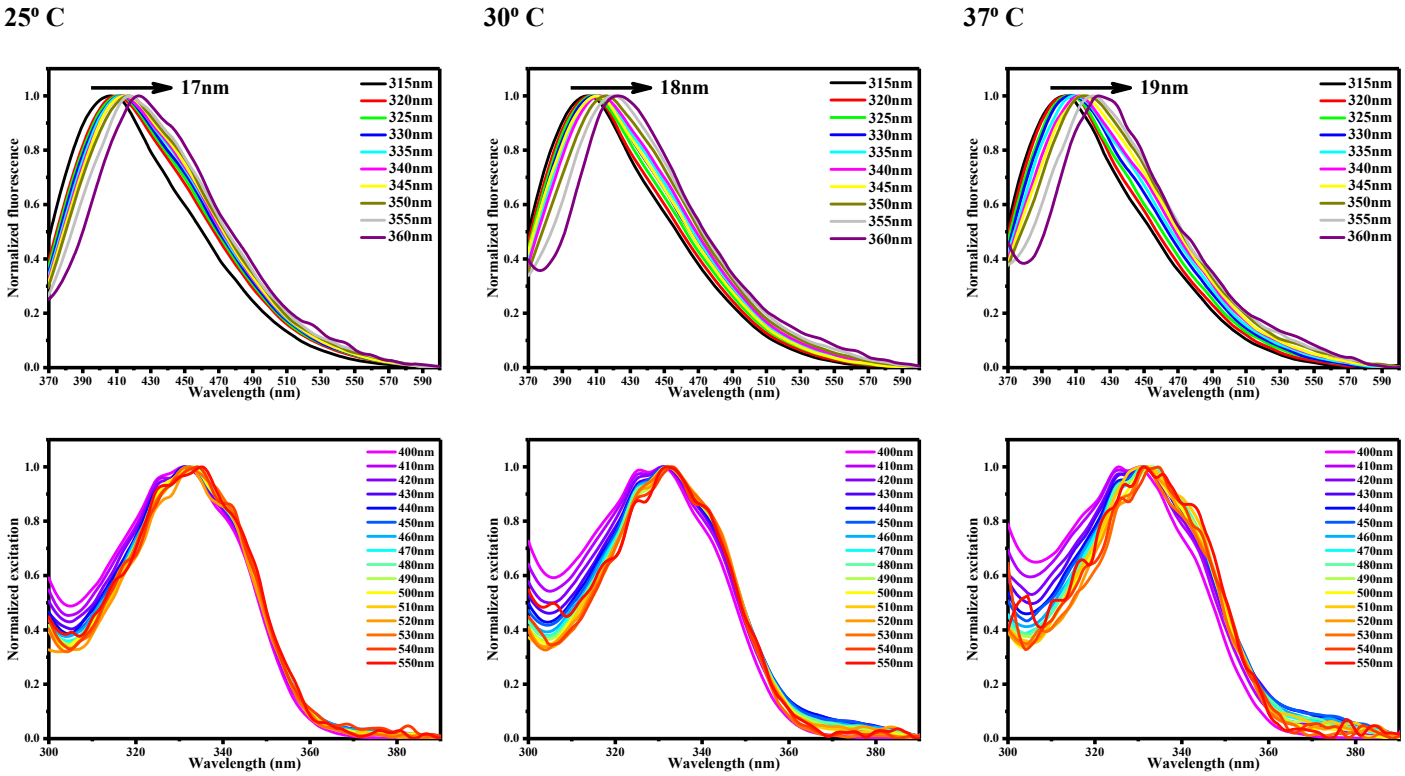

Chapter VII

Solvatochromism and Conformational Analysis of SKF86002

Another important ligand in the TKIs class is SKF86002 (PTC299). It exhibits anti-inflammatory and protein kinase inhibitory activity. Its hydrogenated imidazo-thiazole pharmacophore besides the fluorophenyl and pyridine rings play important role in binding to target proteins. Solvatochromism studies revealed that SKF86002 absorption and fluorescence are sensitive to solvent media. As a result, SKF86002 can be used as a self-reporter of its own environment. The fluorophenyl and pyridine moieties are connected to the chromophore through single bonds. Hence potential energy surface scan is required to identify the most stable conformers of SKF86002. The simulated UV-Vis spectrum of the two calculated structures were compared together with one structure from protein data bank and another from pubchem. Computations revealed that SKF86002 ground and excited states are conformation-dependent. Therefore, studying the electronic and geometrical properties of SKF86002 gave insights into predicting the anisotropic and topological changes occurring at SKF86002-binding pocket.

The experimental part was done by Muhammad while mentoring Madeline on her project. All theoretical calculations were performed by Madeline and included in her honours thesis. I greatly acknowledge her contribution to the work done on SKF86002. This chapter is presented in the form of two published papers,

- **Muhammad Khattab**, Madeline Van Dongen, Feng Wang, Andrew H.A. Clayton, *Solvatochromism and linear solvation energy relationship of the kinase inhibitor SKF86002*, Spectrochim. Acta A Mol. Biomol. Spectrosc. 170 (2017), 226-33.

- Madeline Van Dongen, **Muhammad Khattab**, Feng Wang, Andrew H.A. Clayton, *Exploring optical reporting characteristics of drugs: UV-Vis spectra and conformation of tyrosine kinase inhibitor SKF86002*, New J. Chem. 41 (**2017**), 14567-73.

Spectrochimica Acta Part A: Molecular and Biomolecular Spectroscopy 170 (2017) 226–233

Contents lists available at ScienceDirect

Spectrochimica Acta Part A: Molecular and Biomolecular Spectroscopy

journal homepage: www.elsevier.com/locate/saa

Solvatochromism and linear solvation energy relationship of the kinase inhibitor SKF86002

Muhammad Khattab [a], Madeline Van Dongen [b], Feng Wang [b,*], Andrew H.A. Clayton [a,*]

[a] Centre for Micro-Photonics, Faculty of Science, Engineering and Technology, Swinburne University of Technology, Melbourne, Victoria 3122, Australia
[b] Molecular Model Discovery Laboratory, Department of Chemistry and Biotechnology, School of Science, Faculty of Science, Engineering and Technology, Swinburne University of Technology, Melbourne, Victoria 3122, Australia

ARTICLE INFO

Article history:
Received 17 May 2016
Received in revised form 15 July 2016
Accepted 15 July 2016
Available online 17 July 2016

Keywords:
Solvatochromism
Photophysics
UV–Vis spectroscopy
SKF86002
Kinase inhibitor
Anti-inflammatory drug

ABSTRACT

We studied the spectroscopic characteristics of SKF86002, an anti-inflammatory and tyrosine kinase inhibitor drug candidate. Two conformers SKF86002A and SKF86002B are separated by energy barriers of 19.68 kJ·mol^{-1} and 6.65 kJ·mol^{-1} due to H-bonds, and produce the three major UV–Vis absorption bands at 325 nm, 260 nm and 210 nm in cyclohexane solutions. This environment-sensitive fluorophore exhibited emission in the 400–500 nm range with a marked response to changes in environment polarity. By using twenty-two solvents for the solvatochromism study, it was noticed that solvent polarity, represented by dielectric constant, was well correlated with the emission wavelength maxima of SKF86002. Thus, the SKF86002 fluorescence peak red shifted in aprotic solvents from 397.5 nm in cyclohexane to 436 nm in DMSO. While the emission maximum in hydrogen donating solvents ranged from 420 nm in *t*-butanol to 446 nm in *N*-methylformamide. Employing Lippert-Mataga, Bakhshiev and Kawski models, we found that one linear correlation provided a satisfactory description of polarity effect of 18 solvents on the spectral changes of SKF86002 with R^2 values 0.78, 0.80 and 0.80, respectively. Additionally, the multicomponent linear regression analysis of Kamlet-Taft ($R^2 = 0.94$) revealed that solvent acidity, basicity and polarity accounted for 31%, 24% and 45% of solvent effects on SKF86002 emission, respectively. While Catalán correlation ($R^2 = 0.92$) revealed that solvatochromic change of SKF86002 emission was attributed to changes in solvent dipolarity (71%), solvent polarity (12%), solvent acidity (11%) and solvent basicity (6%). Plot of Reichardt transition energies and emission energies of SKF86002 in 18 solvents showed also a linear correlation with $R^2 = 0.90$. The dipole moment difference between excited and ground state was calculated to be 3.4–3.5 debye.

1. Introduction

SKF86002, given a IUPAC name 6-(4-fluorophenyl)-2,3-dihydro-5-(4-pyridinyl)-imidazo[2,1-*b*]thiazole, is a low molecular weight heterocycle. It was first synthesized by Bender et al., and was tested for its anti-inflammatory activity [1,2]. Later, it was identified as p38α inhibitor [3]. Pargellis et al., demonstrated that SKF86002 can act as a fluorescent marker upon binding to the ATP active pocket of p38α [4]. It was revealed that not only is SKF86022 able to bind to the mitogen-activated protein kinase (p38α), but also to other kinases viz. Pim1, ASK1, HCK and AMPH [5]. Hence, SKF86002 is a small kinase inhibitor, able to act as a self-fluorescent reporter and/or probe for candidate ATP-competitive inhibitors [5].

Photophysical studies have recently received much attention, since the spectral parameters are very sensitive to the change in microenvironment [6]. Therefore, different models have been progressively developed for analyzing the photophysical properties of fluorescent compounds. Lippert-Mataga (L-M) [7,8], Bakhshiev [9], and Bilot-Kawski [10,11] (often called Kawski-Chamma-Viallet) [12,13] models are commonly applied to investigate solvent effects on the spectral characteristics of dye molecule and to estimate the change in dipole moment between the ground and excited state [14]. They are easily employed, however cannot account for stabilization of dyes based on hydrogen bonding [15,16]. However, it was later discovered that if aprotic and protic solvents were plotted separately using Kawski model, then dipole moment differences for H-bond and non-H-bond environments could be evaluated [17,18] This has opened the door for studying compounds capable of strong H-bond formation [19].

Models which can separately evaluate different modes of solute-solvent interactions have also been developed. By using Kamlet-Taft and Catalán models, one can qualitatively and quantitatively investigate the specific (H-bond) and non-specific (due to change in dipolarity and polarizability) interactions [20]. Since SKF86002 is an ATP competitive inhibitor, investigating the mechanism of its binding to target protein relies on understanding of its physicochemical characteristics. This

* Corresponding authors.
E-mail addresses: mkhattab@swin.edu.au (M. Khattab), fwang@swin.edu.au (F. Wang), aclayton@swin.edu.au (A.H.A. Clayton).

http://dx.doi.org/10.1016/j.saa.2016.07.027
1386-1425/

would be beneficial for optimizing the drug efficacy and minimizing side effects for newly developed drugs.

To the best of our knowledge, there are no detailed UV–Vis spectroscopic studies on SKF86002 (Fig. 1). The reported studies showed that SKF86002 exhibits fluorescence which was greatly enhanced upon binding to the target protein [21]. Therefore, we present an intensive spectral study on SKF86002 in solvents with varying polarity and hydrogen bond strength.

2. Experimental and computational

2.1. Materials

All solvents were of spectroscopic or HPLC grade. They were selected to cover a broad range of solvent polarity and hydrogen bond strength. Cyclohexane (CH), dichloromethane (DCM), ethanol (EtOH), 2-propanol (iPrOH), and dimethyl sulfoxide (DMSO) were purchased from Sigma-Aldrich Pty Ltd. Methanol (MeOH), *t*-butanol (*t*-But), ethylene glycol (EG), allyl alcohol (allyl), *N*-methylformamide (NMF), toluene (Tol), xylene (Xyl), pyridine (Pyd), acetonitrile (ACN), *N*,*N*-dimethylformamide (DMF), 1,4-dioxane (Diox), tetrahydrofuran (THF), ethylacetate (EtAc), 1,2-dichloroethane (DCE), acetone (Act), and chloroform ($CHCl_3$) were obtained from Thermo Fisher Scientific Inc. Water used was double-distilled deionized water. SKF86002 was purchased from Sapphire Bioscience Pty Ltd. Quartz cuvettes with a path length of 1 cm were purchased from Starna Pty Ltd.

2.2. Methods

All solutions of SKF86002 were prepared and left overnight for equilibration. A matched pair of quartz cuvette was loaded with a 3 μM of SKF86002 for absorbance measurement. For excitation and emission measurements, 0.3 μM solutions of SKF86002 were used. The absorption measurements were conducted at room temperature using a Perkin-Elmer LAMBDA 1050 UV/Vis/NIR spectrophotometer. While the excitation and emission experiments were done on a Perkin Elmer LS55 Fluorescence Spectrometer at room temperature as well. Blank samples devoid of SKF86002 were used for background absorbance, scatter and fluorescence corrections.

2.3. Computational details

Density functional theory (DFT) based Becke three-parameters Lee-Yang-Parr hybrid functional (B3LYP) [25] in combination with B3LYP/6-31 + G(d) basis set was employed in the calculations. The geometry of SKF86002 was originally optimized using B3LYP/6-31G(d) model and reoptimized using the B3LYP/6-31 + G(d) model (B3LYP/6-31G(d)// B3LYP/6-31 + G(d)). The UV–Vis spectrum in cyclohexane solution was calculated using time dependent density functional theory (TD-DFT) and conductor-like polarizable continuum model (CPCM) [26]. Absorption UV–Vis spectrum in methanol were calculated for the lowest 30 excited states of singlet–singlet transitions. All calculations performed using Gaussian 09 computational chemistry package [27] on Swinburne University Supercomputing Facility.

3. Results and discussion

3.1. The UV–Vis absorption spectrum in cyclohexane solution and the role of hydrogen bond

The measured absorption spectrum of SKF86002 is composed of three absorption bands. The wavelengths of absorption maxima are listed in Table 1. Using a 3 μM solution of SKF86002 in cyclohexane, we could reveal only two absorption peaks at 253.5 nm and 216.5 nm, as shown in Fig. 2 (solid black spectrum). These two maxima have a high optical density in all studied solvents ranging from 0.5 to 3.2, however we observed a small band around 320 nm (OD < 0.1). Therefore, we used a higher concentration of SKF86002 which helped to resolve it into a distinct absorption peak, refer to the inset of Fig. 2. Generally, SKF86002 absorption maxima in different solvents can be shown, with an order of increasing optical density, at approximately $\lambda_1 = 325$ nm, $\lambda_2 = 260$ nm and $\lambda_3 = 210$ nm.

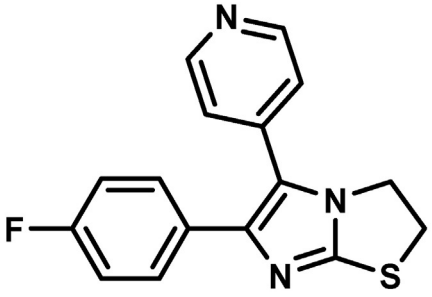

Two-dimensional (2D) chemical Structure

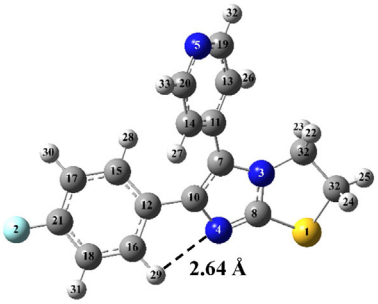

Optimized 3D structure of SKF86002 isomer A.

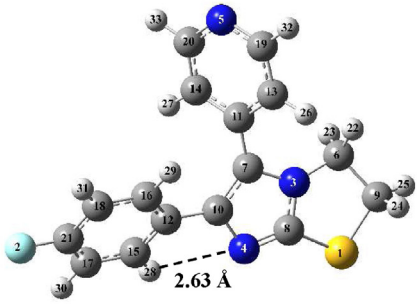

Optimized 3D structure of SKF86002 isomer B.

Fig. 1. Chemical structure of SKF86002 (2D) and quantum mechanically optimized isoenergy isomers (A) and (B) of SKF86002 in three-dimensional (3D) space in cyclohexane solution (pale blue shows the positions of the possible H-bond). (For interpretation of the references to color in this figure legend, the reader is referred to the web version of this article.)

Table 1
Absorbance and emission wavelength maxima (at excitation wavelength = 350 nm) of SKF86002 in studied solvents and stokes shift in both wavelength (nm) and wavenumber (cm^{-1}) units. Solvents are listed in order of increasing dielectric constants.

Solvent	Absorbance	Emission		Stokes shift	
	λ_{ab}	λ_{em}	AUC	$\Delta\lambda$ (nm)	$\Delta\nu$ (cm^{-1})
Aprotic					
CH	328	397.5	10,280	69.5	5331
Diox	328.5	412	68,534	83.5	6170
Tol	333.5	412	54,265	78.5	5713
Xyl	332	411.5	63,687	79.5	5819
$CHCl_3$	329	413.5	38,258	84.5	6211
EtAc	319	414	36,221	95	7193
THF	328.5	414	67,220	85.5	6287
DCM	326	415	56,195	89	6578
Pyd	–	434	60,312	–	–
Act	–	418	67,423	–	–
ACN	319	420	33,291	101	7538
DMF	326.5	426	61,082	99.5	7154
DMSO	329	436	56,396	107	7459
Protic					
t-But	329.5	420	90,372	90.5	6539
Allyl	327.5	438.5	299	111	7729
iPrOH	328	436	36,217	108	7552
EtOH	325	438	1117	113	7938
MeOH	322.5	439	322	116.5	8229
EG	330	440.5	96	110.5	7602
Water	322	415	78	93	6960
NMF	325.5	446	11,009	120.5	8300

The structure of SKF86002 as shown in Fig. 1 consists of a fluorophenyl ring, a pyridinyl ring and a imidazo[2,1-*b*]thiazole ring which are connected by two C—C bonds as C(7)—C(11) and C(10)—C(12). Rotation of these C—C bonds will produce local minima conformers, SKF86002A and SKF86002B. Among all the atoms in the conformers, N(4) in both conformers exhibit the most negative atomic charge of −0.534e for SKF86002A and −0.536e for SKF86002B (Mulliken) and form strong hydrogen bond with the hydrogen in the fluorophenyl ring. The H-bond distance of C(16)—H(29)···N(4) is 2.643 Å for SKF86002A whereas the H-bond distance of C(15)—H(28)···N(4) is 2.633 Å for SKF86002B, as marked on the structures in Fig. 1. Rotation of the C(7)—C(11) bond connecting the pyridyl ring with the imidazo[2,1-*b*]thiazole ring involves the formation and breaking of a hydrogen bond and therefore, producing an energy barrier of approximately 19.68 kJ·mol^{-1}. The conformers can also be produced through rotation of the C(10)—C(12) bond connection of the pyridinyl ring and the imidazo[2,1-*b*]thiazole thiazole ring, but with a lot lower energy barrier of approximately 6.56 kJ·mol^{-1} using the same model in the calculations. The spectral band positions are calculated at λ_1 = 345 nm, λ_2 = 255 nm and λ_3 = 225 nm for SKF86002A and λ_1 = 344 nm, λ_2 = 255 nm and λ_3 = 228 nm for SKF86002B. All the absorption transitions λ_1, λ_2 and λ_3 are dominated by frontier orbitals with λ_1 is purely due to the highest occupied molecular orbital (HOMO) and lowest unoccupied molecular orbital (LUMO) of the compound.

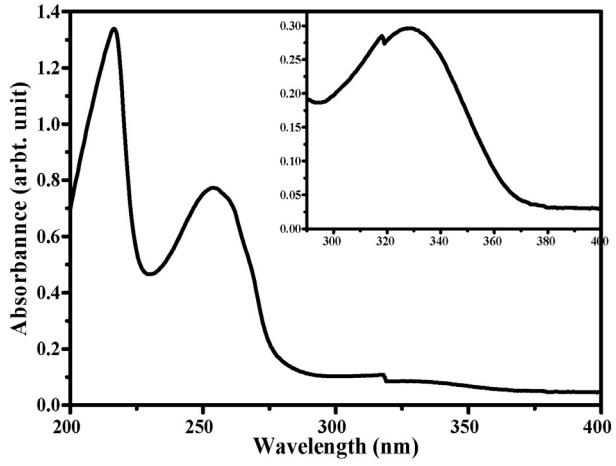

Fig. 2. Representative of the measured absorption spectrum of 3 μM solution of SKF86002 in cyclohexane; inset shows the absorption maximum in the 290–400 nm region using higher concentrated solution of the compound.

3.2. Solvent effect on absorption and fluorescence spectra

In solvents of differing polarities, the low energy absorption band varied from 322 to 333.5 nm (shift of 1071 cm^{-1}), while the higher energy absorption peak varied from 253.5–263.5 nm (shift of 1497 cm^{-1}). The shortest wavelength absorption band can only be shown in cyclohexane, 2-propanol and water, due to the higher UV cut-off of other solvents, where the absorption maxima were recorded at 216.5 nm, 216 nm and 201 nm, respectively.

Emission spectra of SKF86002 measured at excitation wavelength of 350 nm are shown in Fig. 3. The emission maximum recorded in the non-polar cyclohexane was at 397.5 nm, while it was at 446 nm in *N*-methylformamide, the most polar of studied solvents. Therefore, a total solvatochromic shift of a magnitude of 2736 cm^{-1} discloses the environmental impact on SKF86002 fluorescence. Also, it was noticed that the bathochromic shift of fluorescence maxima increases with the increase in the solvent dielectric constant. This was observed in both aprotic and protic solvents except with pyridine (aprotic) and water (protic) solvents, as compiled in Table 1. The heteroaromatic nature of pyridine may contribute to additional specific interactions with SKF86002 and the dual H-donating and accepting behaviour of water molecule may contribute to two opposite solvatochromic effects.

In aprotic solvents, the solvatochromic shift of emission peak was estimated 2221 cm^{-1}, from 397.5 nm in cyclohexane to 436 nm in DMSO. While the emission maxima in hydrogen donating solvents were recorded between 420 nm and 446 nm, giving rise to a solvatochromic shift of 1388 cm^{-1}. Moreover, SKF86002 fluorescence was observed highly quenched in protic solvents relative to aprotic solvents as indicated by area under the curve (AUC) of fluorescence spectra. Enhancement of non-radiative decay due to solute-solvent specific (H-bond) interactions could be a contributing factor for fluorescence quenching of SKF86002.

The Stokes shift was calculated for SKF86002 solutions exhibiting absorption peak in the range of 319–333.5 nm. Values for the Stokes shift ranged from 69.5–120 nm, that is, from 5331 to 8300 cm^{-1} on the wavenumber energy scale. This magnitude of Stokes shift was indicative of a significant change in the electronic configuration of the excited state relative to the ground state. In the next section, we evaluate the solvatochromic change in Stokes shift of SKF86002 using the three commonly used solvatochromism models.

3.3. Solvatochromism models

To gain insight into the solvatochromism of SKF86002, the spectral parameters were plotted against Lippert-Mataga (L-M), Bakhshiev and Bilot-Kawski solvent polarity functions. To begin with L-M method, the solvent polarity function is given by:

$$F_1(\varepsilon, n) = \frac{\varepsilon - 1}{2\varepsilon + 1} - \frac{n^2 - 1}{2n^2 + 1} \quad (1)$$

where ε is the solvent dielectric constant and n is the solvent refractive index. A linear solvent energy relationship was obtained between the solvent polarity function F_1 (ε, n) and the Stokes shift (ν_{st}) as illustrated in Fig. 4. Linear correlations were established for 11 aprotic solvents and 7 protic solvents with coefficient of determination (R^2) values of 0.82 and 0.68, respectively. When we did not plot the aprotic and protic

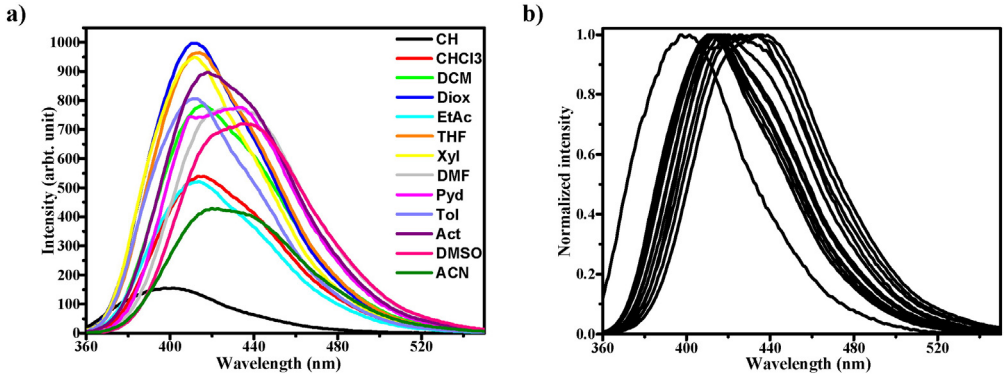

Fig. 3. Emission spectra (a) and its normalized set (b) of 0.3 μM solution of SKF86002 obtained in 13 aprotic solvents using excitation wavelength 350 nm.

lines separately, we obtained a single linear correlation for all 18 solvents with $R^2 = 0.78$, as shown in Fig. 4.

By employing Bakhshiev model (Eq. 2), we also obtained linear correlations for both aprotic and protic solvents, as illustrated in Fig. 5. Surprisingly, the hydrogen-donating solvents showed a better correlation between Stokes shift (ν_{st}) and Bakhshiev polarity function F_2 (ε, n) than with aprotic solvents. The R^2 values in the case of aprotic solvents and protic solvents corresponded to 0.82 and 0.93, respectively. Interestingly, combined solvents data points showed a good correlation with a value ($R^2 = 0.8$) slightly lower than the individual values, but higher than that obtained by applying L-M model, as indicated in Fig. 5. These results showed that solvent polarity function developed by Bakhshiev model correlates better with the change in stokes shift of SKF86002, regardless whether solvents were protic or aprotic. This indicates that inclusion of solute-solvent interactions in the Bakhshiev model that are not present in the L-M model appear to be warranted.

$$F_2(\varepsilon, n) = \frac{2n^2+1}{n^2+2}\left(\frac{\varepsilon-1}{\varepsilon+2} - \frac{n^2-1}{n^2+2}\right) \quad (2)$$

The more complicated solvent model of Bilot-Kawski (Eq. 3), which describes solvent polarizability by two separate functions, was also explored. By plotting Stokes shift versus Δg function, we obtained linear correlations for both aprotic and protic solvents similar to Bakhshiev correlation, refer to Fig. 6. We also obtained a linear correlation for all solvents with $R^2 = 0.8$, slightly smaller than the separated solvents correlations. However, the linear plot of ($\nu_{ab} + \nu_{em}$) against (Δg + 2Δh) function showed very weak correlations for the separated and combined solvent sets, as shown in Fig. 6.

$$F_3(\varepsilon, n) = \Delta g + 2\Delta h = \frac{2n^2+1}{(n^2+2)}\left(\frac{\varepsilon-1}{\varepsilon+2} - \frac{n^2-1}{n^2+2}\right) + \frac{3(n^4-1)}{(n^2+2)^2} \quad (3)$$

The lack of improvement when comparing Bilot-Kawski to Kawski indicates that in the context of the dielectric continuum model, inclusion of two solvent polarizability functions does not seem to be warranted.

Plot of emission energies of SKF86002 and Reichardt-Dimorth transition energies exhibited linear correlations for aprotic and protic solvents which were almost on the same line. By plotting the 18 solvents together, we obtained a good linear correlation with $R^2 = 0.90$, as presented in Fig. 7. The quality of the linear regression for this solvent parameter set is significantly higher than for the models that employ a dielectric continuum model for the solvent-solute interactions. This suggests that contributions of specific solvent-solute interactions, such as H-bond interactions are required to account for the changes in fluorescence from SKF86002. In the next section we obtained estimates of the relative contributions of H-bonding versus polarity/polarizability to the solvatochromism of SKF86002.

3.4. Multicomponent linear regression analysis

To account for hydrogen bonding and solvent polarity effects on photophysics of SKF86002, we applied multiple linear regression (MLR) analysis using Kamlet-Taft model. In this model, a spectral parameter can be evaluated in terms of solvent Lewis acidity (α), solvent Lewis basicity (β) and polarity/polarizability (π^*) scales. We obtained

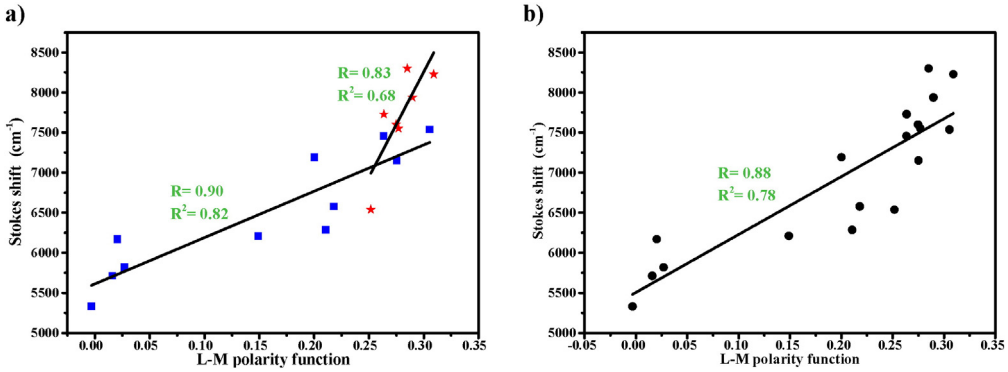

Fig. 4. Plot between stokes shift in cm^{-1} and Lippert-Mataga solvent polarity function of SKF86002 in a) **11** aprotic (blue squares) solvents and **7** protic (red stars) solvents; b) **18** solvents. (For interpretation of the references to color in this figure legend, the reader is referred to the web version of this article.)

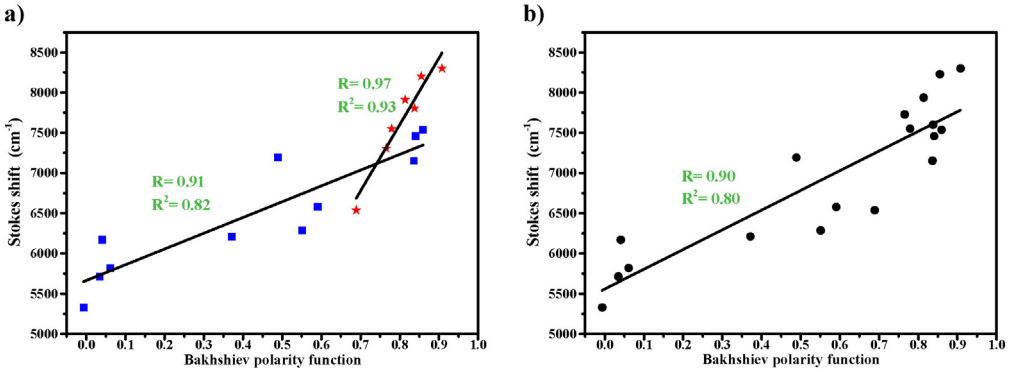

Fig. 5. Plot between stokes shift in cm^{-1} and Bakhshiev solvent polarity function of SKF86002 in a) **11** aprotic (blue squares) solvents and **7** protic (red stars) solvents; b) **18** solvents. (For interpretation of the references to color in this figure legend, the reader is referred to the web version of this article.)

a linear solvation energy relationship (LSER) by solving for the coefficients of Kamlet-Taft parameters viz.;

$$\nu_{em} = 25,226(\pm 155) - 1002(\pm 185)\alpha - 758(\pm 214)\beta - 1430(\pm 241)\pi * \left(R^2 = 0.94\right) \quad (4)$$

By plotting the theoretical emission wavenumber versus the measured one, we obtained a linear correlation with $R^2 = 0.94$, as shown in Fig. 8. It is well known that Kamlet-Taft solvent parameters are not normalized. Therefore, the analysis of LSER reveals roughly that solvent polarity has nearly equal impact on stabilization of SKF86002 excited state as H-bond interactions. It accounted for 45% of solvent effects on SKF86002 emission. While solvent acidity and basicity accounted for 31% and 24% of solvent effects, respectively.

Subsequently, we used Catalán model, where all solvent parameters are normalized, for reliable quantification of solvent effects on SKF86002. The linear equation which best describes the solvent interactions was deducted from;

$$\nu_{em} = 25,224(\pm 348) - 1832(\pm 405)SA - 813(\pm 371)SB - 1247(\pm 528)SPP \left(R^2 = 0.84\right) \quad (5)$$

From this linear correlation, the solvent Brønsted acidity effect accounts quantitatively for 47% of solvent effects on SKF86002 emission. While solvent Brønsted basicity contributes by 21% of total solvent effects. The solvent polarity/polarizability parameter affects spectral emission by 32% of total solvent effects.

Since solvent polarity plays a noticeable role on stabilizing SKF86002 excited state, the new Catalán model which separates solvent polarity/polarizability (SPP) into solvent polarizability (SP) and solvent dipolarity parameters (SdP) was employed. This model also evaluates the impact of solvent H-donating interactions (SA) and solvent H-

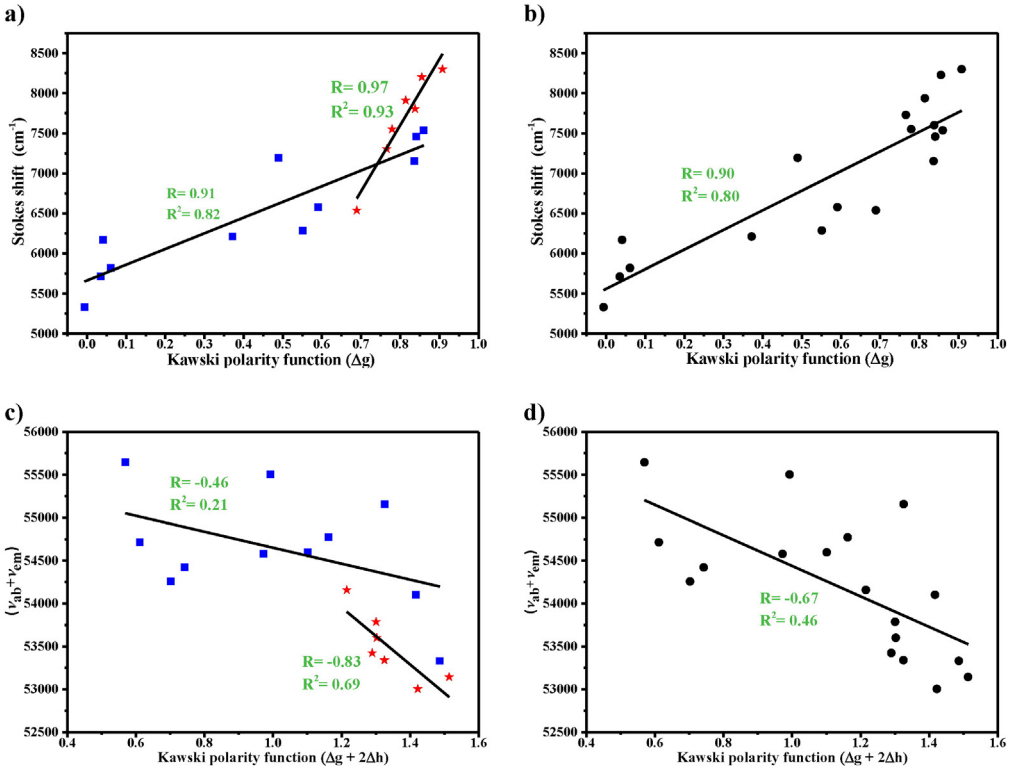

Fig. 6. Plot between stokes shift in cm^{-1} and Δg of Kawski solvent polarity function of SKF86002 in a) **11** aprotic (blue squares) solvents and **7** protic (red stars) solvents; b) **18** solvents. Plot of summation of emission and absorption wavenumbers against Δg + 2Δh of Kawski solvent polarity function in a) **11** aprotic (blue squares) solvents and **7** protic (red stars) solvents. (For interpretation of the references to color in this figure legend, the reader is referred to the web version of this article.)

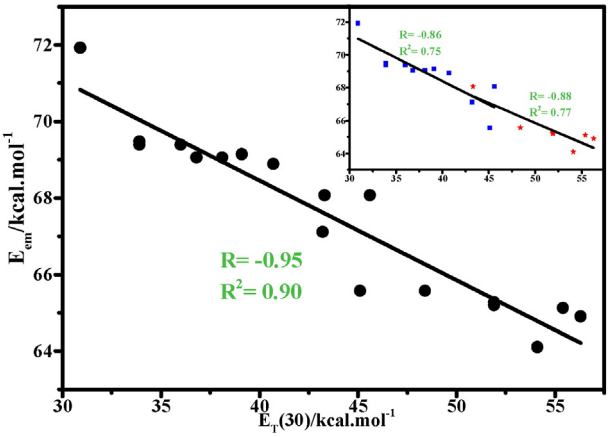

Fig. 7. Plot between emission energies of SKF86002 in 18 solvents and Reichardt transition energies in kcal/mol. Inset shows the separate linear correlation in 11 aprotic solvents (blue, squares) and 7 protic solvents (red, stars). (For interpretation of the references to color in this figure legend, the reader is referred to the web version of this article.)

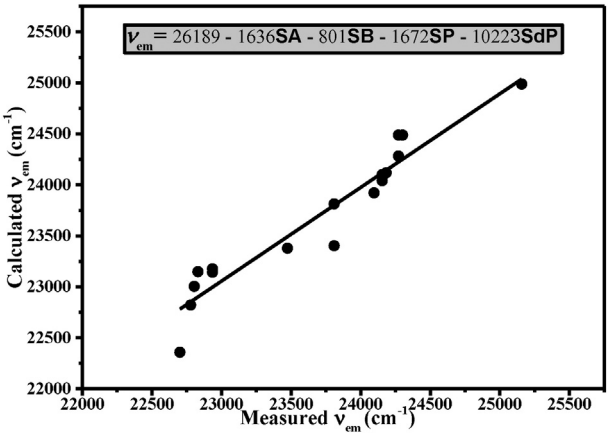

Fig. 9. Plot between the calculated wavenumber obtained by multiple linear regression analysis of Catalán solvent energy linear relationship and the observed emission wavenumber in cm^{-1}.

accepting interactions (SB). The MLR analysis of parameterized Catalán scales gave us the following linear solvent energy relationship;

$$\nu_{em} = 26,189(\pm 734) - 1636(\pm 313)SA - 801(\pm 318)SB - 1672(\pm 957) \quad (5)$$
$$SP - 10,223(\pm 276)SdP \left(R^2 = 0.92\right)$$

From which, the hydrogen-donating and accepting power of solvent can only account for 11% and 6% of solvent effects on SKF86002 emission. The solvent polarizability represents 12% of total solvent effects. While solvent dipolarity contributes by 71% to the total solvent impact on SKF86002 emission. This means the total solvent polarization contributes by 83% of total solvent effects on SKF86002 emission, while solvent specific interactions contribute only by 17%. Plot of the calculated emission wavenumber and the observed values showed a linear correlation with R^2 equal to 0.92, as shown in Fig. 9.

A pronounced difference between contribution of solvent polarity to stabilization of SKF86002 excited state using Kamlet-Taft and Catalán models was noted. In Catalán model, the solvent polarity/polarizability term is resolved into two separate parameters (solvent polarizability and solvent dipolarity). Besides, solvent parameters in Catalán scale are normalized. Therefore, the MLR results obtained by employing Catalán model should be more accurate and reliable than that obtained by Kamlet-Taft scale.

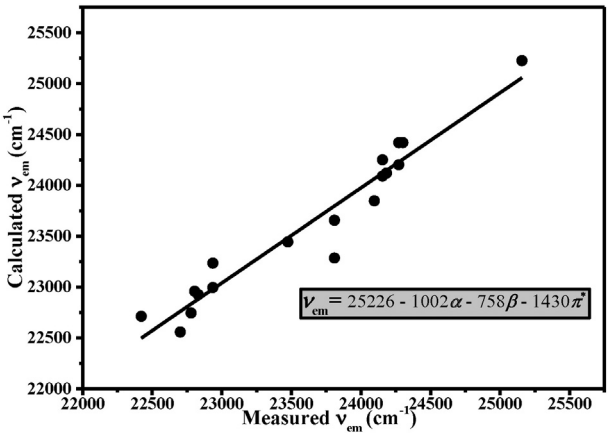

Fig. 8. Plot between the calculated wavenumbers obtained by multiple linear regression analysis of Kamlet-Taft solvent energy linear relationship and the observed emission wavenumber in cm^{-1}.

3.5. Estimation of dipole moment

In order to account for the magnitude of the Stokes shift, we determined the dipole moment difference between the excited and ground state. As indicated earlier, we plotted stokes shift versus to F_1 (ε, n), Eq. (1), stokes shift versus to F_2 (ε, n), Eq. (2), ($\nu_{ab} + \nu_{em}$) versus to F_3 (ε, n), Eq. (3), and stokes shift versus to solvent polarity parameter E_T^N by using Lippert-Mataga, Bakhshiev, Kawski-Chamma-Viallet and Reichardt equations, respectively (Figs. 4–6). The corresponding values of intercept, slope, Pearson's correlation (R) and corresponding standard errors are compiled in.

As can be noted in Table 2, the dipole moment of excited state was found higher than ground state dipole moment with all employed approaches. This indicates that a significant electronic rearrangement of SKF86002 excited state took place. Using L-M model, the dipole moment difference obtained from the 18 studied solvents was estimated (7.0 D). This value was nearly close to that obtained from the individual slope of 11 aprotic solvents (6.3 D). However, the slope of 7 protic solvents revealed a higher dipole difference value of (13.4 D). This is due to L-M model does not account for the specific interactions between solute and solvent molecules.

By applying Bakhshiev model, we obtained dipole moment difference value of (4.1 D) using the 18 solvents. The dipole moment difference here is apparently lower than that obtained from L-M equation. The advantage of Bahshiev model is that it considers both solvent polarity and induction polarization for treating spectral changes of solute molecules. Therefore, the value of dipole moment difference should be more accurate than by using L-M model. Dipole moment values of 3.7 and 7.5 debye were estimated from aprotic and protic solvents lines, respectively.

Kawski-Chamma-Viallet equations allow distinct determination of the ground state and excited state dipole moments. The GS dipole moment was calculated as 1.4, 3.5 and 0.7 debye using the 11 aprotic, 7 protic and all 18 solvents, respectively. While the dipole moment of excited state was estimated at 3.9, 8.3 and 4.2 debye, respectively. The dipole moment differences were also listed in Table 2. Taken together, we noticed the dipole moment difference between the ground and excited state become smaller going from L-M equation to the more descriptive Kawski model.

The Reichardt model, which accounts for the change in transition energy based on both the specific and non-specific interaction, was also employed. The difference in dipole moment between ES and GS was calculated as 3.9, 3.4 and 3.4 debye in aprotic, protic and total solvent used, respectively. It is clear that the values are similar indicating the reliability of using Reichardt model for estimation of dipole moment difference

Table 2
Spectral treatment of Lippert-Mataga, Bakhshiev, Kawski-Chamma-Viallet and Reichardt correlations of SKF86002. (Onsager cavity radius = 4.8 Å).

	Correlation	Intercept	SE[a]	Slope	SE	R[b]	N[c]	$\Delta\mu$[d]	μ_g[d]	μ_e[d]
L-M										
Aprotic	$(\nu_{ab} - \nu_{fl})$	5612	173	5781	914	0.90	11	6.3 (±0.5)	–	–
Protic	/	391	2235	26,219	8005	0.83	7	13.4 (±2.2)	–	–
All	$F_1(\varepsilon, n)$	5506	221	7223	966	0.88	18	7.0 (±0.5)	–	–
Bakh.										
Aprotic	$(\nu_{ab} - \nu_{fl})$	5664	163	1960	303	0.91	11	3.7 (±0.3)	–	–
Protic	/	1003	795	8249	983	0.97	7	7.5 (±0.5)	–	–
All	$F_2(\varepsilon, n)$	5560	199	2449	304	0.90	18	4.1 (±0.3)	–	–
Kaws.										
Aprotic	$(\nu_{ab} + \nu_{fl})$	55,580	628	−930	596	−0.46	11	2.5	1.4 (±0.6)	3.9 (±0.1)
Protic	/	57,946	1328	−3326	990	−0.83	7	4.8	3.5 (±0.7)	8.3 (±0.2)
All	$F_3(\varepsilon, n)$	56,214	567	−1776	483	−0.68	18	3.5	0.7 (±0.3)	4.2 (±0.2)
Reich.										
Aprotic	$(\nu_{ab} - \nu_{fl})$	5371	176	4681	632	0.93	11	3.9 (±0.3)	–	–
Protic	/	5432	692	3513	1052	0.83	7	3.4 (±0.6)	–	–
All	E_T^N	5614	158	3392	340	0.93	18	3.4 (±0.2)	–	–

[a] Standard error.
[b] Pearson's correlation coefficient.
[c] Number of data.
[d] μ_g is the ground state dipole moment, μ_e is the excited state dipole moment, and $\Delta\mu$ is the difference in the dipole moment between two states. (all in debye).

of solute molecules. Also, it is worth mentioning that the dipole moment difference between GS and ES using 18 data points was nearly the same (3.4 D) as the value obtained with the Kawski (3.5 D) and Reichardt models (3.4). Taken together, the experimental dipole moment difference appears to be in the range of 3.4–3.5 debye.

It is noted that the previous solvatochromic models evaluated solvatochromism based on finding a linear correlation between specified spectral parameters and solvent polarity functions which took into account the dielectric constant and refractive index of environment [22]. In Lippert-Mataga model, solvent polarizability is not sufficiently treated and therefore, the estimated $\Delta\mu$ values are larger compared to other models [23]. Polarizability function, embedded in Bakhshiev and Kawski models, permits more accurate determination of dipole moment difference. However, Kawski scale has the advantageous of being able to evaluate separately the dipole moment of the ground and excited state. All of three models do not consider solvent H-bond interactions. Therefore, the significant difference between the $\Delta\mu$ in protic and aprotic solvents indicates significant contribution of solvent H-bonding, besides solvent polarity, to stabilization of SKF86002 ground and excited states. On the other hand, Reichardt $E_T(30)$ parameter was measured from solvatochromism of betaine dye 30, a dye exhibiting strong H-bonding capabilities. This means values of $E_T(30)$ took into account both solvent specific and non-specific interactions, rendering the estimation of $\Delta\mu$ more reliable.

Overall, the results reveal that SKF86002 can be a fluorescent reporter of its interactions with target proteins and macromolecules. Generally, our results pave the way for understanding the binding mode of SKF86602 to the ATP pocket of target tyrosine kinases. It can also help in investigating the drug pharmacokinetics through recording the change in its spectral parameters upon binding to plasma proteins, phospholipids and DNA.

4. Conclusion

A solvatochromic study of the anti-inflammatory and kinase inhibitor, SKF86002, was made. SKF86002 appeared to be a promising fluorescent tracer for the estimation of protein binding site polarity, due to its wide solvatochromic emission shift. It displayed several spectral properties including three UV absorption maxima, broad excitation ranges and emission in the blue region of visible light from two isoenergy conformers of SKF8002. A strong H-bond formed produces a significant higher energy barrier of 19.68 $kJ \cdot mol^{-1}$ and a weaker H-bond results in only approximately 6.65 $kJ \cdot mol^{-1}$. It was found that solvent polarity and polarizability played a significant role in the solvatochromism studies of SKF86002. The electrostatic interaction contributes more or less to stabilization of SKS86002 excited state, in addition to H-bond interactions. Altogether, SKF86002 can be used as a fluorescent marker of its biological binding to target receptors and plasma proteins.

Acknowledgment

M. Khattab acknowledges Swinburne University Postgraduate Research Award (SUPRA).

References

[1] P.E. Bender, I. Lantos, Pyridyl substituted 2, 3-dihydroimidazo [2, 1-b] thiazoles, in, US 4175127 Patent, 1979.
[2] I. Lantos, P.E. Bender, K.A. Razgaitis, B.M. Sutton, M.J. DiMartino, D.E. Griswold, D.T. Walz, Antiinflammatory activity of 5,6-diaryl-2,3-dihydroimidazo[2,1-*b*]thiazoles. Isomeric 4-pyridyl and 4-substituted phenyl derivatives, J. Med. Chem. 27 (1984) 72–75.
[3] T.F. Gallagher, G.L. Seibel, S. Kassis, J.T. Laydon, M.J. Blumenthal, J.C. Lee, D. Lee, J.C. Boehm, S.M. Fier-Thompson, J.W. Abt, M.E. Soreson, J.M. Smietana, R.F. Hall, R.S. Garigipati, P.E. Bender, K.F. Erhard, A.J. Krog, G.A. Hofmann, P.L. Sheldrake, P.C. McDonnell, S. Kumar, P.R. Young, J.L. Adams, Regulation of stress-induced cytokine production by pyridinylimidazoles; inhibition of CSBP kinase, Bioorg. Med. Chem. 5 (1997) 49–64.
[4] C. Pargellis, L. Tong, L. Churchill, P.F. Cirillo, T. Gilmore, A.G. Graham, P.M. Grob, E.R. Hickey, N. Moss, S. Pav, J. Regan, Inhibition of p38 MAP kinase by utilizing a novel allosteric binding site, Nat. Struct. Biol. 9 (2002) 268–272.
[5] L.J. Parker, S. Taruya, K. Tsuganezawa, N. Ogawa, J. Mikuni, K. Honda, Y. Tomabechi, N. Handa, M. Shirouzu, S. Yokoyama, A. Tanaka, Kinase crystal identification and ATP-competitive inhibitor screening using the fluorescent ligand SKF86002, Acta Crystallogr. D Biol. Crystallogr. 70 (2014) 392–404.
[6] R.R. Dogonadze, E. Kálmán, A.A. Kornyshev, J. Ulstrup, The chemical physics of solvation, Pt. B (1986).
[7] E. Lippert, Dipolmoment Und Elektronenstruktur Von Angeregten Molekulen, Zeitschrift Fur Naturforschung Part a-Astrophysik Physik Und Physikalische Chemie 10 (1955) 541–545.
[8] N. Mataga, Y. Kaifu, M. Koizumi, Solvent effects upon fluorescence spectra and the dipole moments of excited molecules, Bull. Chem. Soc. Jpn. 29 (1956) 465–470.
[9] N.G. Bakhshiev, Universal Intermolecular Interactions and Their Effect on the Position of the Electronic Spectra of Molecules in 2-Component Solutions, 7. Theory (General Case for Isotopic Solution), 16, Opt Spektrosk, 1964 821–832.
[10] L. Bilot, A. Kawski, Zur Theorie Des Einflusses Von Losungsmitteln Auf Die Elektroenspektren Der Molekule, Zeitschrift Fur Naturforschung Part a-Astrophysik Physik Und Physikalische Chemie, A 17 (1962) (621-&).
[11] A. Kawski, J. Rabek, Progress in Photochemistry and Photophysics, Boca Raton, Boston, 1992 1–47.
[12] A. Kawski, Der Wellenzahl von elecktronenbanden lumineszierenden moleküle, Acta Phys. Polon. 29 (1966) 507–518.
[13] A. Chamma, P. Viallet, Determination of dipole moment of molecule in singlet excited state - application to indole, benzimidazole and indazole, Comptes Rendus Hebdomadaires Des Seances De L Academie Des Sciences Serie C 270 (1970) (1901-&).

[14] A. Giussani, R. Pou-Amerigo, L. Serrano-Andres, A. Freire-Corbacho, C. Martinez-Garcia, M.I. Fernandez, M. Sarakha, M. Canle, J.A. Santaballa, Combined theoretical and experimental study of the photophysics of Asulam, J. Phys. Chem. A 117 (2013) 2125–2137.
[15] A.G. Gilani, S.E. Hosseini, M. Moghadam, E. Alizadeh, Excited state electric dipole moment of nile blue and brilliant cresyl blue: a comparative study, Spectrochim. Acta A Mol. Biomol. Spectrosc. 89 (2012) 231–237.
[16] R. Rautela, N.K. Joshi, H.C. Joshi, N. Tewari, S. Pant, Solvatochromic study of 2-hydroxy-4-methylquinoline for the determination of dipole moments and solute-solvent interactions, J. Mol. Liq. 154 (2010) 47–51.
[17] S. Jana, S. Dalapati, N. Guchhait, Excited state intramolecular charge transfer suppressed proton transfer process in 4-(diethylamino)-2-hydroxybenzaldehyde, J. Phys. Chem. A 117 (2013) 4367–4376.
[18] G. Kodali, M. Narayanan, R.J. Stanley, Excited-state electronic properties of 6-methylisoxanthopterin (6-MI): an experimental and theoretical study, J. Phys. Chem. B 116 (2012) 2981–2989.
[19] C.J. Talone, J.Y. Gao, J.R. Lynch, R.M. Tanu, S.T. Deyrup, Determination of the ground- and excited-state dipole moments of bromocresol purple in protic and aprotic solvents, Spectrochim. Acta A Mol. Biomol. Spectrosc. 156 (2016) 138–142.
[20] M. Shannigrahi, R. Pramanik, S. Bagchi, Studies of solvation in homogeneous and heterogeneous media by electronic spectroscopic method, Spectrochim. Acta A Mol. Biomol. Spectrosc. 59 (2003) 2921–2933.
[21] D. Falck, J.S. de Vlieger, W.M. Niessen, J. Kool, M. Honing, M. Giera, H. Irth, Development of an online p38alpha mitogen-activated protein kinase binding assay and integration of LC-HR-MS, Anal. Bioanal. Chem. 398 (2010) 1771–1780.
[22] C. Reichardt, T. Welton, Solvents and Solvent Effects in Organic Chemistry, John Wiley & Sons, 2011.
[23] U.S. Raikar, V.B. Tangod, S.R. Mannopantar, B.M. Mastiholi, Ground and excited state dipole moments of coumarin 337 laser dye, Opt. Commun. 283 (2010) 4289–4292.

NJC

PAPER

View Article Online
View Journal | View Issue

Cite this: *New J. Chem.*, 2017, **41**, 14567

Exploring the optical reporting characteristics of drugs: UV-Vis spectra and conformations of the tyrosine kinase inhibitor SKF86002†

Madeline Van Dongen,[a] Muhammad Khattab,[b] Andrew H. A. Clayton[b] and Feng Wang*[a]

Received 5th September 2017,
Accepted 18th October 2017

DOI: 10.1039/c7nj03361c

rsc.li/njc

The ultimate understanding of drug–protein interactions relies on understanding drug behaviours in solution, at the molecular level. The conformation of a drug contributes to drug–protein docking, hence, drug potency and spectroscopy. Some drugs, such as the anti-cancer drug SKF86002, are chromophores, which are promising tools for optical reporting, as they may change colour or fluorescence when interacting with cells. In the present study, four conformers of the tyrosine kinase inhibitor SKF86002 (stability: **B** > **A** > **C** > **D**) were obtained with **B** and **A** from this study through optimisation, and **C** and **D** from the literature. As the global energy minimum structure, SKF86002**B** is 0.17 kcal mol^{-1}, 10.75 kcal mol^{-1} and 12.52 kcal mol^{-1} lower in energy than **A**, **C** and **D**, respectively. Although the total energy difference is small between **B** and **A**, the orientation of the fluorophenyl and the pyridinyl rings with respect to the heterocyclic imidazothiazole ring *i.e.*, the shape, is quite different. The UV-Vis spectra of the conformers in dichloromethane solution were calculated using time dependent density functional theory. The absorption spectra of **A**, **B** and **C** exhibit two major bands at 325.3 nm and 240.4 nm, in the vicinity of the measured bands, whereas **D** displays one major band (249.1 nm). In addition, the calculations assign the major bands to different transitions of the conformers, indicating that the UV-Vis spectrum of SKF86002 is, in fact, conformation dependent. The UV-Vis spectra of SFK86002 may serve as a useful optical reporting property for drug conformational changes in cells.

1. Introduction

Recent studies indicate that activation of p38 mitogen-activated protein kinase (MAPK) results in cancer cell apoptosis initiated by retinoids, cisplatin and other chemotherapeutic agents.[1] Pharmaceutical developments related to p38α MAPK pathways, therefore, have focused on molecules that inhibit MAPKs.[1] An anti-inflammatory compound, SKF86002, with the IUPAC name of 6-(4-fluorophenyl)-2,3-dihydro-5-(4-pyridinyl)-imidazo[2,1-*b*]thiazole (given in Fig. 1), was first reported in 1988 for the inhibition of interleukin-1 beta (IL-1b).[2] Its relatively low affinity and specificity allow binding to other kinases such as Pim1, ASK1, AMPK and HCK.[3] The p38α kinase is activated by phosphorylation with the ATP co-factor as a result of external stimuli, where the nature of the upstream and downstream signals in the cascade is dependent on the cell type.[4] In monocytes, activation of p38α MAPK was found to associate with the release of proinflammatory cytokines, which are the key mediators of immune or inflammation processes.[4–6] By preventing the phosphorylation of p38α MAPK, SKF86002 can inhibit the production of cytokines and therefore the inflammation.[6]

As a pyridyl-imidazole derivative, SKF86002 binds a wide variety of kinases.[3] Most pyridyl-imidazole derivatives were explored as potential MAPK inhibitors and were classified as non-steroidal anti-inflammatory drugs (NSAIDs), or more specifically, cytokine suppressive anti-inflammatory drugs (CSAIDs).[7,8] Therefore, SKF86002 has been applied in the treatment of shock, fever, cellular damage or cachexia, which is diagnosed due to excessive cytokine release.[5,9] The chemical structure (in two-dimensional, 2D) of SKF86002 is given in Fig. 1. Studies reveal that the central pharmacophores connecting to the 5-pyridyl and 4-fluorophenyl ring moieties of SKF86002 have been identified as the main contributors to interact with the MAPK kinase ATP co-factor binding pocket.[6,10,11] To date, several inhibitors fulfilling these criteria have been advanced into clinical trials.[10] As a small kinase inhibitor, SKF86002 lacks

[a] *Molecular Model Discovery Laboratory, Department of Chemistry and Biotechnology, Faculty of Science, Engineering and Technology, Swinburne University of Technology, Melbourne, Victoria 3122, Australia. E-mail: fwang@swin.edu.au*

[b] *Centre for Micro-Photonics, Faculty of Science, Engineering and Technology, Swinburne University of Technology, Melbourne, Victoria 3122, Australia*

† Electronic supplementary information (ESI) available. See DOI: 10.1039/c7nj03361c

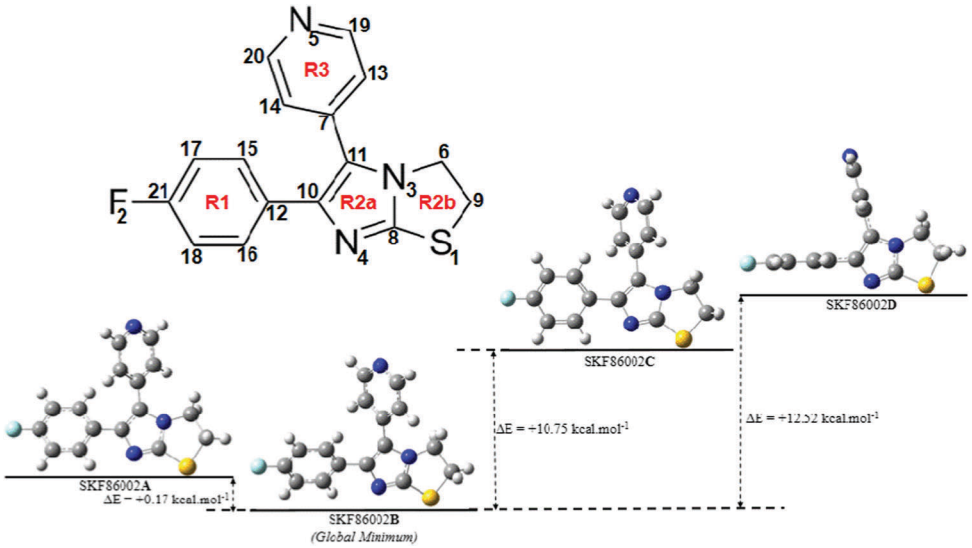

Fig. 1 The three-dimensional structures of the four conformers of SKF86002 under vacuum, SKF86002**A** (local minimum) and SKF86002**B** (global minimum) as well as PDB ligand structure SKF86002**C** and PubChem structure SKF86002**D** using the DFT based B3LYP/6-31G* model. The 2D chemical structure of SKF86002 (upper panel). All relevant energies (ΔE) refer to the total energy of **B** which was set to 0.0 kcal mol^{-1}.

intrinsic fluorescence but becomes fluorescent upon binding to the ATP binding sites of p38 MAPK.[3] However, the co-crystals of this compound with various kinases were distinguishable by their strong fluorescence. That is, the co-crystals of SKF86002 with p38α, Pim1, ASK1, HCK and MAPK are also fluorescent.[3] Parker *et al.*[3] identified the apo-Pim1-SKF86002 crystal structure which was deposited into the RCSB Protein Data Bank (PDB) (entry for the 'SK8' ligand of the Pim-1 MAP Kinase docking structure; 4LL5).[3] Thus, for a broad range of kinases, SKF86002 is useful as a crystal marker and stabilizer to identify ligand co-crystals for structural analysis.

As indicated that SKF86002 is an important drug, crystal marker, crystal stabilizer and a marker to identify ligand co-crystals for structural analysis,[3] information about the small drug at the molecular level has been rare. To our knowledge, no detailed molecular electronic structural and spectroscopic information is available for this drug molecule. It is noted that the pyridylimidazole moiety has been notably reported to constitute a broad class of mitogen activated protein kinase inhibitors.[12–15] The reported properties and characteristics of SKF86002 are related to the chemical and electronic structures in space. Recently, Selig *et al.*[10] reported the strong conformational effects on inhibitor potency, caused by steric hindrance of the *S*-methyl group in the well-known class of pyridyl thioimidazoles of SKF86002 derivatives.[10] We recently revealed that solvatochromic changes affect the fluorescence and UV-Vis spectrum of AG1478 (another anti-cancer drug), which were mainly attributed to a change in solvent dipolarity and drug conformation, as supported by our accurate quantum mechanical calculations.[16] The results agree well with the study of Hofener *et al.* using combined theory and experimental methods for the UV-Vis spectra of bis-triazin-pyridine (BTP) ligands in solution.[25] Based on the information of our previous photophysical study on SKF86002 in a variety of solvents,[17] the present study proceeds to calculate the UV-Vis spectra in solution from its molecular structure in isolation and in solution using accurate quantum mechanical based density functional theory (DFT). The study explores the relationships between the molecular structure, conformation and solvent effect with the experimental measurements of UV-Vis/fluorescence spectra of SKF86002.

2. Spectroscopic measurements and computational details

Absorption measurements were performed at room temperature using a UV-1601 Shimadzu UV-Visible Spectrophotometer. A series of aprotic and protic solvents with different range of polarities were selected to assess the contribution of specific hydrogen bonding and bulk properties on the SKF86002 absorption spectra. The selected solvents were cyclohexane (CH), dichloromethane (DCM), ethanol (EtOH), methanol (MeOH), 2-propanol (iPrOH) and deionized water and all are of either HPLC or spectroscopic grade. All solvents were purchased from Sigma-Aldrich Pty Ltd, except methanol, which was bought from Thermo Fisher Scientific Inc. The SKF86002 compound was obtained from Sapphire Bioscience Pty Ltd. Samples and blanks were loaded in a matched pair of quartz cuvettes with 1 cm path length. All samples and solvents were directly used without purification. For more details, refer to our previous study.[17]

In theory, geometry optimisation is carried out using the density functional theory (DFT) based B3LYP/6-31+G* model. After the optimised structure was obtained, a potential energy scan is performed through rotating around the flexible C–C single bonds of the optimised structure of SKF86002 using the same model. Time-dependent (TD)-DFT calculations were employed using the B3LYP/6-31G*,[18] B3LYP/6-31+G*,[18] PBE0/6-31G*[19,20] and PBE0/6-31+G*[19,20] models, respectively. The implicit solvent

conductor-like polarizable continuum solvent model (CPCM)[21] was employed. Absorption UV-Vis spectra in solutions were calculated for up to the lowest 30 excited states of singlet–singlet transitions. All quantum mechanical calculations were performed on the Swinburne University Supercomputing Facility using the Gaussian 09 computational chemistry package.[22] The calculated UV-Vis spectra of the conformers using the PBE0/6-31G* model agree the best with our measurements and therefore, only the UV-Vis spectra calculated using the PBE0/6-31G* model are presented in this study.

3. Results and discussion

The two-dimensional (2D) chemical structure of the SKF86002 molecule and the nomenclature are given in Fig. 1. Four rings, *i.e.*, the fluorophenyl (R1) ring, the pyridinyl (R3) ring as well as the imidazole (R2a) and thiazole (R2b) heterocyclic imidazothiazole rings, are connected by C–C single bonds. An initial SKF86002 structure was optimised using B3LYP/6-31G* and resulted in a local structure of SKF86002**A** (Fig. 1). Based on this SKF86002**A** structure, we performed potential energy surface (PES) scans by rotations of the flexible C(11)–C(7) and C(12)–C(10) single bonds (connecting the rings of R3–R2a/R2b and R1–R2a/R2b, respectively, as shown in Fig. 1) while freezing the rings in the optimised structures. The positions of the pyridinyl (R2b) and fluorophenyl (R1) rings of SKF86002 are of significant structural and functional interest due to their mobility and role in binding to the ATP pocket.[8,9] In the PES scan, the C(11)–C(7) and C(10)–C(12) single C–C bonds were rotated, which corresponds to a change in the dihedral angles of C(13)–C(11)–C(7)–N(3) and N(4)–C(10)–C(12)–C(15), respectively, in steps of 10° at a time. The calculations led to the determination of a global minimal structure of SKF86002**B** and this structure was further optimised.

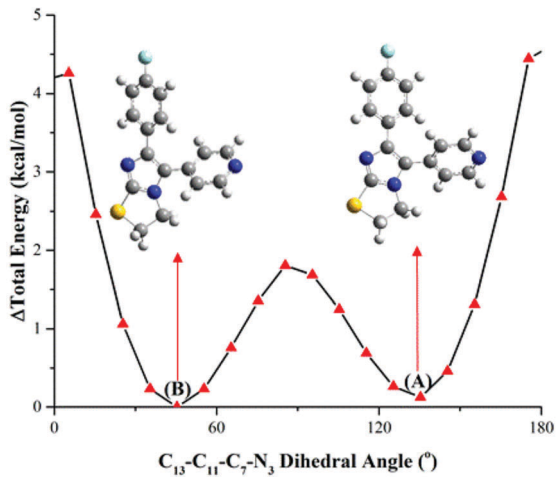

Fig. 2 Potential energy surface (PES) scan of SKF86002 through rotation of the C(7)–C(11) bond (*i.e.*, C(13)–C(7)–C(11)–N(3) dihedral angle) *i.e.*, relative positions of the pyridinyl (R3) ring and the imidazothiophenyl (R2a/b) ring at the B3LYP/6-31G* level of theory.

Four energy structures of SKF86002 are obtained and their structures in 3D are also given in Fig. 1. Structures **A** and **B** were obtained from energy minimization and potential energy surface (PES) scans in this study, as shown in Fig. 2. Although **B** and **A** differ by a small energy of 0.17 kcal mol^{-1}, there is an energy barrier of approximately 2 kcal mol^{-1} so that **A** and **B** are stable structures at low temperatures. Two additional structures, **C** and **D**, are obtained from the literature,[3,23] where **C** of Parker *et al.*[3] was obtained from the RCSB Protein Data Bank (PDB) entry for the 'SK8' ligand of the Pim-1 MAP Kinase docking structure, which was determined using an R-AXIS VII imaging plate detector and the Australian Synchrotron micro-crystallography beamline.[3] **D**[23] is a structure obtained from PubChem3D, determined using the OMEGA software package from OpenEye Scientific Software, Inc.[23]

All structures of SKF86002 are shown in Fig. 1. SKF86002**B** is the global minimum structure, which is energetically favoured over **A** by 0.17 kcal mol^{-1} using the present quantum mechanical B3LYP/6-31+G* model. The crystal structure **C**[3] and the modelling structure **D**[23] were then calculated using the same DFT model with 10.75 kcal mol^{-1} and 12.52 kcal mol^{-1}, respectively, higher in energy than **B**. Table S1 (ESI†) gives the calculated geometric and other properties of the four conformers. In general, the isotropic properties of the conformers do not change apparently, but anisotropic properties change more obviously. For example, the bond lengths and ring perimeters, R1, R2a, R2b and R3, which are the ring perimeters of the fluorophenyl (R1) ring, the pyridinyl (R3) ring as well as the imidazole (R2a) and thiazole (R2b) heterocyclic imidazothiazole rings,[17] are almost the same. The perimeters of the fluorophenyl (R1) ring are given as 8.382 Å, 8.381 Å, 8.352 Å and 8.391 Å, for **B**, **A**, **C** and **D**, respectively. However, properties such as bond angles and dihedral angles of the conformers are noticeably different.

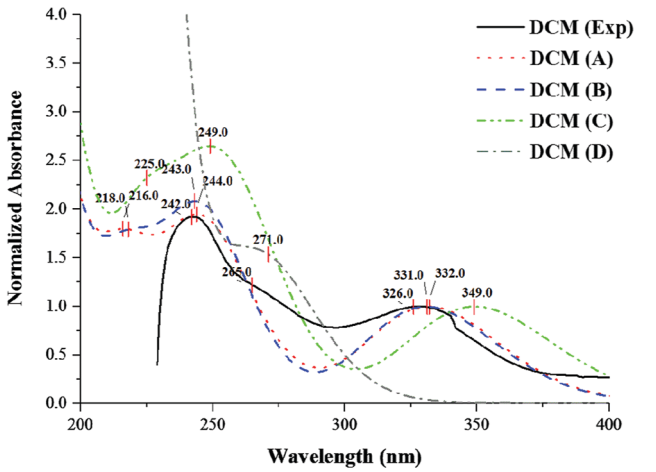

Fig. 3 Comparison of the measured[17] and calculated UV-Vis absorbance of SKF86002 conformers using the TD-DFT PBE0/6-31G* model and the CPCM solvent model. The measured UV-Vis absorbance of SKF86002 in 1.36 μM dichloromethane (DCM) solution. The calculated spectra were normalized to the intensity of λ_1 at 326 nm of the measurement. The spectrum of **D** shows quite different profiles from the experiment and the other conformers of SKF86002.

Table 1 Important transitions of the absorption bands of **B**, **A**, **C** and **D** with measurements in DCM solvent[a]

	SKF-86002B			SKF-86002A			SKF-86002C			SKF-86002D			Exp.
	Excitation energy (nm)	Oscillator strength	Major contributors	Excitation energy (nm)	Oscillator strength	Major contributors	Excitation energy (nm)	Oscillator strength	Major contributors	Excitation energy (nm)	Oscillator strength	Major contributors	DCM
λ_1	332.28	0.2587	H → L (70%)	333.81	0.2453	H → L (70%)	348.32	0.2141	H → L (70%)	324.60	0.0001	H → L (70%)	325.3
λ_2	256.37	0.1164	H−3 → L (20%)	N/A	N/A	N/A	N/A	N/A	N/A	276.93	0.0159	H → L+1 (70%)	262.4
λ_3	245.38	0.3528	H−1 → L (63%)	245.27	0.3223	H−1 → L (60%)	249.00	0.2344	H−1 → L (52%)	249.09	0.2344	H−1 → L (52%)	240.4
			H → L+2 (23%)			H → L+2 (26%)							
λ_4	221.91	0.1363	H → L+5 (66%)	216.87	0.2756	H−5 → L (51%),	227.42	0.1607	H → L+5 (65%)	227.42	0.1607	H → L+5 (65%)	N/A
			H−6 → L (15%)				222.46	0.1613	H−6 → L (26%)	214.69	0.2993	H → L+5 (67%)	
									H−5 → L (61%)				

[a] Oscillator strengths ($f > 0.10$) and major contributing electronic transition configurations (> 15%) (nm) are shown. Calculated using the PBE0/6-31G* model.

Perhaps the most noticeable property difference between the conformers is the electronic spatial extent, $\langle R^2 \rangle$, which relates to the shape, *i.e.*, "spatial volume" of the conformers. For example, the measured structure **C**[3] is approximately 260 a.u. smaller than the global minimum structure **B**.

Fig. 3 compares the measured UV-Vis spectrum of SKF86002 in dilute dichloromethane (DCM) solution,[17] with the calculated UV-Vis spectra of the four conformers **A**, **B**, **C** and **D** using the PBE0/6-31G* model. Good agreement between the measured and calculated spectra of **B** and **A** for the region above 230 nm is achieved in the DCM solution. The two observed absorption band positions λ_1 and λ_3 at 332 nm and 240 nm, respectively agree to within ±6 nm (*i.e.* 2% of λ) with the calculated bands at 326 nm and 242 nm, respectively, for **B** (blue dashed line) using the PBE0/6-31G* model. As seen in this figure, the UV-Vis spectra of **A** (red dotted line) and **B** (blue dashed line) are almost the same and both agree well with the measurements. The calculated UV-Vis spectral bands based on the crystal structure **C**[3] need to shift 23 nm and 7 nm for λ_1 and λ_3, respectively to agree with the measured spectrum in DCM. The UV-Vis spectrum calculated from the **C** structure[3] shows the major features present in the experimental spectrum. However, the λ_1 band of the UV-Vis spectrum based on **C** shifts by a significant 23 nm. As this band is dominated by the HOMO → LUMO transition of **C**, this indicates that losing the flexibility of **C** in the crystal structure may cause large changes in the electronic structure particularly in the HOMO and LUMO states. On the other hand, the calculated UV-Vis spectrum of the structure of **D** obtained from modelling seems to be significantly different from the measurement in DCM solution. Therefore, electron distributions in **D**[23] are significantly different from the structures when the drug is "free" in the DCM solvent. With very different orientation

Fig. 4 Molecular electrostatic potentials (MEP) of the SKF86002 conformers calculated using the DFT-PBE0/6-31G* level of theory. The MEPs indeed show that the shape of the **A**, **B** and **C** conformers is quite different from that of the **D** conformer.

of the rings, R1 and R2a&b, and R3 and R2a&b in **D** from other conformers, **D** may only exist in a confined environment such as docked with a protein, rather than independently existing in solution.

Table 1 collects the calculated oscillator strength (>0.10) and major transitions (>15%) to the UV-Vis bands of the spectra of **B**, **A**, **C** and **D** in Fig. 3. It is clear that the energy gap between the highest occupied molecular orbital (HOMO) and the lowest unoccupied molecular orbital (LUMO) of each conformer is the smallest possible transition of the drug, which leads to the longest wavelength band in nm (*e.g.*, λ_1) of their UV-Vis spectra above 330 nm (70%). The shorter wavelength band in nm (λ_3) in the absorption spectrum is dominated by transitions from HOMO−1 to the LUMO, and HOMO to LUMO+2. For example, conformers **A** and **B** exhibit transitions such as HOMO−1 → LUMO (>60%), and HOMO → LUMO+2 (>20%), whereas conformer **C** leads to only a single dominant transition of HOMO−1 → LUMO (52%). The spectrum of **D** shows very different profiles from the spectra produced by the other conformers (**B**, **A** and **C**) for the measurement in the same region. This suggests that this conformer, **D**, is unlikely to exist in such a solution environment as a free compound but rather it may exist under constrained conditions such as when docked with a protein.

In order to further explore the properties of SKF86002 related to its conformers, Fig. 4 reports the molecular electrostatic potential (MEP) contours of SKF86002. The molecular plane is through the plane formed by C(7)–N(3)–C(8) of the imidazothiophene ring (the central pharmacophore of the drug). The MEPs show that the molecular electrostatic potential distribution crosses the molecular surface of the SKF86002 conformers and hence allows better comparison of the 3D shape in space associated with their electrostatic properties.[24] The MEPs of the conformers exhibit apparent polarized structures and **D** exhibits a Y-shape, which is a very different electrostatic potential compared to the other SKF86002 conformers. The experimentally obtained structure of **C** exhibits a similar shape and electrostatic potential to the structures obtained through optimisation in this study, in particular to **B**, the lower energy structure of SKF86002. The relative orientations of the pyridine ring (R3 in Fig. 1) and the imidazothiophene ring (R2a and R2b in Fig. 1)

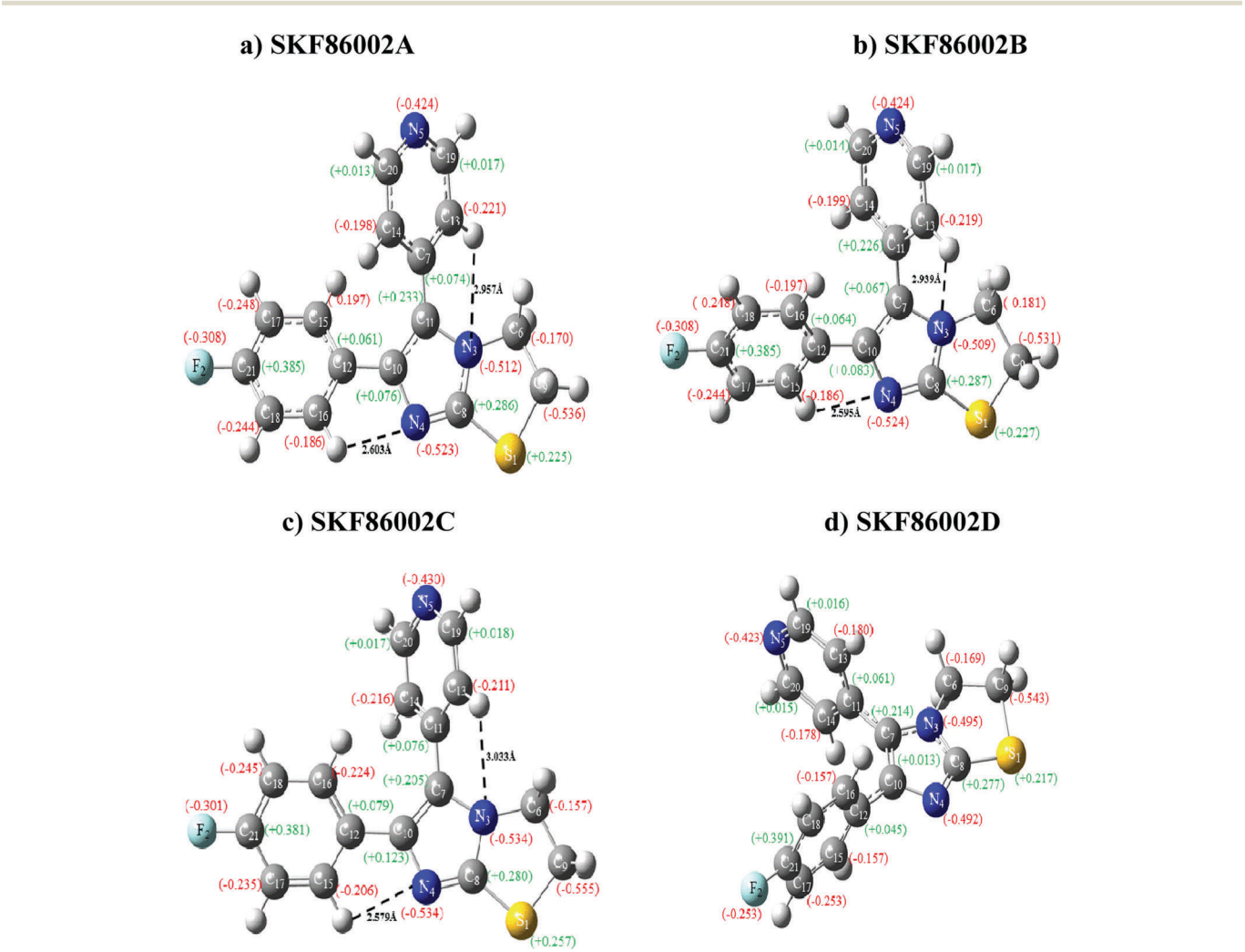

Fig. 5 Atomic natural bond order (NBO) charge analysis of heavy atoms of the SKF86002 conformers using the model at the PBE0/6-31G* level of theory.

reveal the most obvious similarities of conformers **B**, **A** and **C**, indicating that the free drug molecule can be quite flat rather than in full 3D space. Nevertheless, the MEPs indicate that all conformers exhibit negative electrostatic potentials and, therefore, contain electron donating sites at the same positions at N(4), F and N(5) (orange color spots).

The charge distributions are revealed using the natural bond orbital (NBO) analysis of the conformers, calculated using the same PBE0/6-31G* model. Fig. 5 shows the calculated NBO of the conformers on the atoms. The crystal structure of **C** is more polarized than the other structures obtained from the present calculations. For example, the most negative–positive sites in **C** are C(9) of $-0.555e$ (in the S–C(9) bond) and C(21) of $+0.381e$ (in the C(21)–F bond). C(9) and C(10) are located at the extremities of the R1 and R2b ring systems and therefore have the largest separation of any pair of carbons atom in conformer C. Interestingly, the S atoms on the imidazothiophene ring of the conformers possess a positive charge of above $+2.0e$, whereas all the N and F atoms exhibit negative charges in the conformers. For example, the charges of the S atom are $+0.225e$, $+0.227e$, $+0.257e$ and $+0.217e$, respectively, for **B**, **A**, **C** and **D**. On the other hand, the charge on the F atom in **C** (crystal structure) is given by $-0.301e$, whereas this F site in **B** and **A** results in the same charge of $-0.308e$. Although the N atoms in the imidazothiophene ring of the crystal structure, **C**, N(4) and N(3), do not have the same chemical environment, they possess the same charge of $-0.534e$. This may be an accident as the NBOs of the same nitrogen sites in other conformers show slightly different charges.

The role of the carbon atoms is different from S, N and F, which are all negatively charged. The carbon atoms in the SKF86002 conformers are either positively or negatively charged, depending on the local chemical environment of the carbon atoms. Among the obtained four conformers, the three flat conformers **A**, **B** and **C** are able to form possible intramolecular hydrogen bonds (as indicated by dashed lines in the structures), but the twisted structure of **D** is unlikely to form such intramolecular hydrogen bonds. For example, the distance between C(13)–H$\cdots$N(3) is approximately 3.0 Å whereas the distance between C(16)–H$\cdots$N(4) is approximately 2.6 Å, slightly shorter than C(13)–H$\cdots$N(3), which are illustrated in the structures of the flat conformers, *i.e.*, **A**, **B** and **C**. These intramolecular hydrogen bonds again indicate that **B** and **A** are likely the measured structures of SKF86002.

4. Conclusion

Understanding the structure and conformational states of tyrosine kinase inhibitors such as SKF86002 in isolation and *in vitro* is essential, before we are able to reveal the drug–environment interactions and to understand how the drug behaves in a native/protein environment. The flexibility of the structure of SKF86002 allows various conformational states to be populated in a physiological environment. In addition to solvent effects as revealed by our earlier experimental studies of SKF86002 in a variety of solvents,[17] conformational and structural information as well as their impact on the optical reporting characteristics of the drug are important. The stability of the conformers is in the order **B** > **A** > **C** > **D** under vacuum. Conformers **B** and **A** represent the global and local minimum structures, respectively, with a small energy difference of 0.17 kcal mol^{-1}. The measured crystal structure **C** is 10.75 kcal mol^{-1} above **B** and conformer **D** is 12.52 kcal mol^{-1} above **B**. In dichloromethane (DCM) solution, **B**, **A** and **C** are able to produce two major absorption bands in the vicinity of the measured UV-Vis spectrum of SKF86002[17] in the same solution. Further, the present study assigns the transition band λ_1 to the HOMO → LUMO transition and the transition band λ_3 (λ_2 is a small shoulder near λ_1) to the HOMO−1 → LUMO and HOMO → LUMO+2 transitions. The findings indicate that the conformations of SKF86002 affect the ground and excited states of the conformers and therefore their UV-Vis absorption spectra. As a result, when the drug is in binding with proteins and/or co-crystallized with proteins, solvents and other media, possible conformational changes and charge transfer of SKF86002 may lead to significant ground and excited states changes.

Conflicts of interest

There are no conflicts to declare.

Acknowledgements

MVD is an undergraduate (honours) student. MK acknowledges Swinburne University Postgraduate Research Award (SUPRA). FW acknowledges the Swinburne University Supercomputing Facilities. FW acknowledges Swinburne University of Technology for financial support of her Academic Sabbatical Award hosted by School of Chemistry (Bio21 Institute) and School of Physics, The University of Melbourne.

References

1 J. M. Olson and A. R. Hallahan, p38 MAP kinase: a convergence point in cancer therapy, *Trends Mol. Med.*, 2004, **10**(3), 125–129.
2 J. C. Lee, D. E. Griswold, B. Votta and N. Hanna, Inhibition of monocyte IL-1 production by the anti-inflammatory compound, SK&F 86002, *Int. J. Immunopharmacol.*, 1988, **10**, 835–843.
3 L. J. Parker, S. Taruya, K. Tsuganezawa, N. Ogawa, J. Mikuni and K. Honda, *et al.*, Kinase crystal identification and ATP-competitive inhibitor screening using the fluorescent ligand SKF86002, *Acta Crystallogr., Sect. D: Biol. Crystallogr.*, 2014, **70**, 392–404.
4 T. Zarubin and J. Han, Activation and signaling of the p38 MAP kinase pathway, *Cell Res.*, 2005, **15**(1), 11–18.
5 M. L. D. Barbosa, M. M. Fumian, A. L. P. d. Miranda, E. J. Barreiro and L. M. Lima, Therapeutic approaches for tumor necrosis factor inhibition, *Braz. J. Pharm. Sci.*, 2011, **47**(3), 427–447.

6 G. Wagner and S. Laufer, Small Molecular Anti-Cytokine Agents, *Med. Res. Rev.*, 2006, **26**(1), 1–62.
7 I. Lantos, P. E. Bender, K. A. Razgaitis, B. M. Sutton, M. J. Dimantino and D. E. Griswold, *et al.*, Antiinflamatory Activity of 5,6-Diaryl-2,3-Dihydroimidazo[2,1-*b*]Thiazoles. Isomeric 4-Pyridyl and 4-substituted Phenyl Derivatives, *J. Med. Chem.*, 1984, **27**(1), 72–75.
8 J. C. Lee, J. T. Laydon, P. C. Mcdonnell, T. F. Gallagher, S. Kumar and D. Green, *et al.*, A Protein-Kinase Involved in the Regulation of Inflammatory Cytokine Biosynthesis, *Nature*, 1994, **372**, 739–746.
9 U. Prabhakar, D. Lipshutz and A. Traneh, Inhibition of CD44, CD45 and LFA-3 mediated cytokine release from human monocytes by SK&F 86002 and pentoxifylline, *Int. J. Immunopharmacol.*, 1993, **15**(2), 205–209.
10 R. Selig, V. Schattel, M. Goettert, D. Schollmeyer, W. Albrecht and S. Laufer, Conformational effects on potency of thioimidazoles and dihydrothiazolines, *MedChemComm*, 2011, **2**(4), 261–269.
11 N. A. Todorova, V. Doseeva, J. Ramprakash and F. P. Schwartz, Effect of the distal C162S mutation on the energetics of drug binding to p38a MAP kinase, *Arch. Biochem. Biophys.*, 2008, **469**, 232–242.
12 T. Scior, D. M. Domeyer, K. Cuanalo-Contreras and S. A. Laufer, Pharmacophore Design of p38 alpha MAP Kinase Inhibitors with Either 2,4,5-Trisubstituted or 1,2,4,5-Tetrasubstituted Imidazole Scaffold, *Curr. Med. Chem.*, 2011, **18**, 1526–1539.
13 M. Shibazaki, T. Takeuchi, S. Ahmed and H. Kikuchi, Suppression by p38 MAP kinase inhibitors (pyridinyl imidazole compounds) of Ah receptor target gene activation by 2,3,7,8-tetrachlorodibenzo-p-dioxin and the possible mechanism, *J. Biol. Chem.*, 2004, **279**, 3869–3876.
14 K. P. Wilson, P. G. McCaffrey, K. Hsiao, S. Pazhanisamy and V. Galullo, *et al.*, The structural basis for the specificity of pyridinylimidazole inhibitors of p38 MAP kinase, *Chem. Biol.*, 1997, **4**, 423–431.
15 P. R. Young, M. M. McLaughlin, S. Kumar, S. Kassis and M. L. Doyle, *et al.*, Pyridinyl imidazole inhibitors of p38 mitogen-activated protein kinase bind in the ATP site, *J. Biol. Chem.*, 1997, **272**, 12116–12121.
16 M. Khattab, S. Chatterjee, A. H. A. Clayton and F. Wang, Two conformers of a tyrosine kinase inhibitor (AG-1478) disclosed using simulated UV-Vis absorption spectroscopy, *New J. Chem.*, 2016, **40**, 8296–8304.
17 M. Khattab, M. T. V. Dongen, F. Wang and A. H. Clayton, Solvatochromism and linear solvation energy relationship of the kinase inhibitor SKF86002, *Spectrochim. Acta, Part A*, 2017, **170**, 226–233.
18 A. D. Becke, Density-Functional Thermochemistry 3. The Role of Exact Exchange, *J. Chem. Phys.*, 1993, **98**, 5648–5652.
19 J. P. Perdew, M. Ernzerhof and K. Burke, Rationale for mixing exact exchange with density functional approximations, *J. Chem. Phys.*, 1996, **105**(22), 9982–9985.
20 C. Adamo and V. Barone, Toward reliable density functional methods without adjustable parameters: The PBE0 model, *J. Chem. Phys.*, 1999, **110**(13), 6158–6170.
21 M. Cossi, N. Rega, G. Scalmani and V. Barone, Energies, structures, and electronic properties of molecules in solution with the C-PCM solvation model, *J. Comput. Chem.*, 2003, **24**, 669–681.
22 G. W. T. M. J. Frisch, H. B. Schlegel, G. E. Scuseria, M. A. Robb, J. R. Cheeseman, G. Scalmani, V. Barone, B. Mennucci, G. A. Petersson, H. Nakatsuji, M. Caricato, X. Li, H. P. Hratchian, A. F. Izmaylov, J. Bloino, G. Zheng, J. L. Sonnenberg, M. Hada, M. Ehara, K. Toyota, R. Fukuda, J. Hasegawa, M. Ishida, T. Nakajima, Y. Honda, O. Kitao, H. Nakai, T. Vreven, J. A. Montgomery, Jr., J. E. Peralta, F. Ogliaro, M. Bearpark, J. J. Heyd, E. Brothers, K. N. Kudin, V. N. Staroverov, R. Kobayashi, J. Normand, K. Raghavachari, A. Rendell, J. C. Burant, S. S. Iyengar, J. Tomasi, M. Cossi, N. Rega, J. M. Millam, M. Klene, J. E. Knox, J. B. Cross, V. Bakken, C. Adamo, J. Jaramillo, R. Gomperts, R. E. Stratmann, O. Yazyev, A. J. Austin, R. Cammi, C. Pomelli, J. W. Ochterski, R. L. Martin, K. Morokuma, V. G. Zakrzewski, G. A. Voth, P. Salvador, J. J. Dannenberg, S. Dapprich, A. D. Daniels, Ö. Farkas, J. B. Foresman, J. V. Ortiz, J. Cioslowski and D. J. Fox, *Gaussian 09, Revision C.01*, Gaussian, Inc., Wallingford CT, 2009.
23 S. Kim, P. A. Thiessen, E. E. Bolton, J. Chen, G. Fu and A. Gindulyte, *et al.*, PubChem Substance and Compound databases, *Nucleic Acids Res.*, 2016, **44**, D1202–D1213.
24 J. D. Mottishaw, A. R. Erck, J. H. Kramer, H. Sun and M. Koppang, Electrostatic Potential Maps and Natural Bond Orbital Analysis: Visualization and Conceptualization of Reactivity in Sanger's Reagent, *J. Chem. Educ.*, 2015, **92**, 1846–1852.
25 S. Höfener, M. Trumm, C. Koke, J. Heuser, U. Ekström, A. Skerencak-Frech, B. Schimmelpfennig and P. J. Panak, *Phys. Chem. Chem. Phys.*, 2016, **18**, 7728–7736.

Supplementary Materials

Table S1. Selected geometrical parameters and other properties of the global minimum structure, SKF86002**B**, compared with conformers SKF86002**A**, SKF86002**C** and SKF86002**D***

Parameters	SKF86002B	SKF86002A (Δ)	SKF86002C (Δ)	SKF86002D (Δ)
R1[a]	8.382	8.383 (-0.001)	8.412 (-0.030)	8.373 (+0.009)
R2a[a]	6.856	6.852 (+0.004)	7.007 (-0.151)	6.78 (+0.076)
R2b[a]	7.987	7.985 (+0.002)	7.959 (+0.028)	7.896 (+0.091)
R3[a]	8.283	8.283 (0.000)	8.341 (-0.058)	8.256 (+0.027)
Bond length (Å)				
$C_{(21)}$-$F_{(2)}$	1.361	1.361 (0.000)	1.349 (+0.012)	1.34 (+0.021)
$C_{(10)}$-$C_{(12)}$	1.474	1.474 (0.000)	1.512 (-0.038)	1.43 (+0.044)
$C_{(8)}$-$N_{(4)}$	1.308	1.309 (-0.001)	1.336 (-0.028)	1.31 (-0.002)
$C_{(8)}$-$N_{(3)}$	1.366	1.362 (+0.004)	1.402 (-0.036)	1.36 (+0.006)
$C_{(8)}$-$S_{(1)}$	1.765	1.766 (-0.001)	1.730 (+0.035)	1.72 (+0.045)
$C_{(9)}$-$S_{(1)}$	1.856	1.857 (-0.001)	1.791 (+0.065)	1.84 (+0.016)
$C_{(7)}$-$C_{(11)}$	1.468	1.468 (0.000)	1.491 (-0.023)	1.44 (+0.028)
$C_{(20)}$-$N_{(5)}$	1.342	1.342 (0.000)	1.361 (-0.019)	1.35 (-0.008)
$C_{(19)}$-$N_{(5)}$	1.340	1.339 (+0.001)	1.355 (-0.015)	1.35 (-0.010)
$C_{(10)}$-$C_{(7)}$	1.395	1.397 (-0.002)	1.431 (-0.036)	1.39 (+0.005)
$N_{(3)}$-$C_{(6)}$	1.460	1.458 (+0.002)	1.491 (-0.031)	1.45 (+0.01)
Bond angle (°)				
$C_{(8)}$-$S_{(1)}$-$C_{(9)}$	88.94	88.63 (+0.31)	93.74 (-4.80)	91.72 (-2.78)
$N_{(3)}$-$C_{(6)}$-$C_{(9)}$	104.33	104.67 (-0.34)	109.66 (-5.33)	106.45 (-2.12)
$C_{(10)}$-$N_{(4)}$-$C_{(8)}$	104.86	104.92 (-0.06)	106.54 (-1.68)	103.06 (+1.80)
$C_{(7)}$-$N_{(3)}$-$C_{(6)}$	134.44	136.21 (-1.77)	141.45 (-7.01)	133.45 (+0.99)
$N_{(4)}$-$C_{(8)}$-$S_{(1)}$	132.86	133.4 (-0.54)	132.42 (+0.44)	134.40 (-1.54)
Dihedral angle (°)				
$C_{(14)}$-$C_{(11)}$-$C_{(7)}$-$C_{(10)}$	-47.90	42.63 (-90.53)	-52.78 (+4.88)	-90.15 (+42.25)
$C_{(16)}$-$C_{(12)}$-$C_{(10)}$-$N_{(4)}$	148.12	30.35 (+117.77)	164.89 (-16.77)	90.34 (+57.78)
$N_{(3)}$–$C_{(8)}$–$S_{(1)}$–$C_{(9)}$	9.99	15.1 (-5.11)	-1.70 (+11.69)	10.16 (-0.17)
$C_{(10)}$-$N_{(4)}$-$C_{(8)}$-$N_{(3)}$	1.66	0.32 (+1.34)	-0.19 (+1.85)	-0.17 (+1.83)

$C_{(8)}$-$S_{(1)}$-$C_{(9)}$-$C_{(6)}$	-25.42	-26.8 (+1.38)	2.84 (-28.26)	-18.56 (-6.86)
$N_{(3)}$-$C_{(6)}$-$C_{(9)}$-$S_{(1)}$	33.75	31.44 (+2.31)	-3.28 (+37.03)	21.85 (+11.90)
$N_{(4)}$-$C_{(8)}$-$S_{(1)}$-$C_{(9)}$	-175.55	-166.14 (-9.41)	178.43 (-353.98)	-169.42 (-6.13)
$C_{(11)}$-$C_{(7)}$-$N_{(3)}$-$C_{(6)}$	-19.65	-8.51 (-11.14)	-0.39 (-19.26)	-1.94 (-17.71)
$C_{(12)}$-$C_{(10)}$-$C_{(7)}$-$C_{(11)}$	-4.85	6.53 (-11.38)	1.95 (-6.80)	-0.19 (-4.66)
$\langle R^2 \rangle$ (a.u.)	7310.6635	7311.3428 (-0.6793)	7569.4695 (-258.8060)	6976.9344 (+333.7291)
***μ* (D)**	5.34	5.37 (-0.03)	5.92 (-0.58)	5.34 (0.00)
***E* (E_h)**	-1279.243354	-1279.2433 (-0.00008)	-1278.0769 (-1.16645)	-1278.082 (-1.16132)
ZPE (kcal·mol^{-1})	157.14303	157.09623 (+0.04680)	155.64052 (+1.50251)	157.43193 (-0.28890)
***E* + ZPE (E_h)**	-1278.993197	-1278.9929 (-0.00027)	-1278.9761 (-0.01713)	-1278.9733 (-0.01995)
HOMO-LUMO gap (eV)	0.17	0.16 (+0.01)	0.16 (+0.01)	0.18 (-0.01)
Rotational Const. A (GHz)	0.3550	0.3560 (-0.0010)	0.3451 (+0.0099)	0.3771 (-0.0221)
B (GHz)	0.2098	0.2095 (+0.0003)	0.2029 (+0.0069)	0.2091 (+0.0007)
C (GHz)	0.1374	0.1373 (+0.0001)	0.1318 (+0.0056)	0.1486 (-0.0112)

***** Using the B3LYP/6-31+G* level of theory.

[a] Perimeters [17] of the fluorophenyl (R1), imidazolyl (R2a), thiophenyl (R2b) and pyridinyl (R3) aromatic rings, respectively.

Chapter VIII

Conclusion and Perspectives

8.1. Summary and Conclusion

To date, cancer is one of the gravest threats prevailing worldwide and morbidity rate is brutally rising. Several approaches have been applied for the clinical detection of cancer, targeting cancer cells and characterization of the binding interactions between anticancer drugs and targeted receptors in the infected cells. These methods are such as magnetic resonance imaging, immunofluorescence assay, protein chip technology and others. However these methods have serious drawbacks such as high operating cost, poor sensitivity to experimental factors, time consuming and so on. Herein the combined UV-Vis spectroscopy and computational chemistry methods is proven as a powerful tool for monitoring the spatial and electronic properties of two different pharmacophore of anticancer compounds.

The 4-anilinoquinazoline-based TKIs have been intensively studied leading to a number of FDA-approved drugs such as Afatinib, Erlotinib, Gefitinib, Lapatinib, and Vandetanib. Although AG1478 is a promising anticancer agent, the spatial and electronic properties of the free compound and when bound to a target protein have not received sufficient attention. Based on our experimental studies, the absorption, fluorescence excitation and fluorescence emission properties of AG1478 and SKF86002 were clearly defined in solutions with different polarities, hydration and pH. The results revealed that the two anticancer drug candidates are sensitive to environmental changes, hence they can be exploited as a self-reporter for their environments.

The thesis aimed to develop a meticulous approach for studying the two anticancer compounds, AG1478 and SKF86002. More work was done on the tyrosine kinase inhibitor AG1478 than on the MAPK inhibitor SKF86002. The detailed solvatochromic study, in *Chapter II*, was conducted on AG1478 in twenty-one organic solvents. The change in absorption and emission spectra of AG1478 proved that the solvent has a measurable effect on the electronic stabilization of AG1478 ground and excited states. Most notably, the fluorescence quantum yield was found higher in aprotic than in protic solvents in contrary to AG1478 optical density. Linear solvation energy relationship models helped us to qualitatively and quantitatively evaluate the change in AG1478 spectral properties based on the change in the explicit solvent parameters. In general, our analyses revealed sensitivity of AG1478 to the change in physiochemical properties of its bulk environment. We therefore foresee using AG1478 as a reporter of its own environment in the *in vitro* and *in vivo* studies.

Our experimental results revealed that AG1478 has a spectral signature that can be potentially useful in characterization of relevant protein targets and binding interactions. In *Chapter III*, we employed quantum mechanical based DFT calculations to assign the UV-Vis spectral signature of AG1478 to a relevant structural geometry. A potential energy surface scan was performed from which two stable conformers of AG1478 are located, one is coplanar (global minimum) and the other is twisted (local minimum). The measured absorption spectrum of AG1478 was adequately reproduced by the simulated UV-Vis spectra of the two conformers of AG1478. The calculated absorption spectrum for the planar structure of AG1478 suggested that it is responsible to the experimentally observed peak at *ca.* 330nm. The other rotamer where aniline group is tilted relative to quinazoline moiety gives the absorption peak at *ca.* 340nm. The energy gap between the coplanar and twisted isomers was estimated at $\Delta E = 1.58$ kcal.mol^{-1} suggesting that the two structures might exist in equilibrium in solutions. Our detailed computational study showed that each conformer has its own structural and electronic properties which in turn would affect the binding interactions with target protein.

In *Chapter IV*, the specific interactions between AG1478 and water molecules were explored experimentally and theoretically. AG1478 absorbance and fluorescence spectra were found sensitive to H-bond interactions between water molecules and AG1478 in the

ground and excited states. Potential AG1478-nH_2O (n= 3-5) complexes were investigated computationally. The planar and twisted conformers of AG1478 can favourably form 3–5 H-bonds with clustered waters, where the hydrated twisted rotamers of AG1478 were predicted more energetically favoured than the planar counterparts in contrast to the dehydrated AG1478. Accordingly, determination of AG1478 conformation at protein binding site could be dependent on the extent of hydration at binding pocket. In this regard, AG1478 can be also used as a microhydration probe in fluorescent protein assays.

During transit of AG1478 to its target kinase, different pH environments are encountered that could have a major impact on AG1478 structure and electronic properties. Therefore we reported the UV-Vis absorption spectra and computational study on AG1478 in buffer solutions with different pH. In *Chapter V*, the absorption spectra of AG1478 were blue shifted from acidic to neutral pH and split in two overlapping bands at strongly alkaline pH. Due to dependence of AG1478 absorption on the change in pH, we were able to determine the ionization constant (pka) of AG1478 molecule. We theoretically calculated the absorption spectrum of different prototropic forms of AG1478. Hence, we were able to assign the observed absorption spectrum in acidic pH to a two twisted protonated isomers of AG1478. While the neutral planar structure of AG1478 was responsible for experimental absorption in pH range 7–12. The absorption spectra in pH≥ 13 were ascribed to a two neutral rotamers and a two deprotonated isomers of AG1478. Taken altogether, AG1478 can be also used as a reporter of the pH of its environment.

In *chapter VI*, our results in the previous chapters were exploited to define the structural conformations of AG1478 at the binding sites of two kinases and to estimate the polarity of binding site. It was found that AG1478 adapts various conformations where the equilibria between twisted and planar conformations are varied depending on the protein. Based on our experiments and detailed analyses of X-ray data deposited in PDB, the AG1478 binding site in two proteins has a rugged free energy landscape exhibiting a higher polarity in APH(3`)-Ia than in MAPK14. These results pave the way for studying the molecular dynamics of AG1478 binding to the ATP pocket.

SKF86002 is a TKI and serine kinase inhibitor. Its chemical entities are a chief chromophores for many anticancer drugs. In *chapter VII*, the solvatochromic study conducted on SKF86002 revealed that SKF86002 is also a good reporter of its own environment. The absorption and fluorescence spectra of SKF86002 in twenty-two solvents varied significantly with the change in solvent polarity and H-bond strength. Stokes shift was estimated in the range of 5331–8300 cm^{-1} which is also large in magnitude as reported earlier for AG1478 (4536-9210 cm^{-1}). A satisfactory fits to various linear solvation energy models were obtained even without separating the protic and aprotic solvents into two sets. The dipole moment difference between GS and ES of SKF86002 was determined between 3.4–3.5 debye. On the other hand, the theoretical study on four conformers of SKF86002 revealed that only two structures can contribute to the experimental absorption spectrum. Generally, the structural flexibility and optical reporting characteristics of SKF86002 are very important features that can be exploited for defining the drug interactions with macromolecules.

Overall, theoretical analyses of the structural conformations and electronic absorption hallmarks of the two compounds revealed dependence of optical properties on the structural configurations of the drug. That means, during monitoring the TKI in *in-vitro* or *in-vivo* systems, the distinctive conformation of the TKI dissolved in a biological medium, can be easily determined based on the observed absorption spectrum. In addition, the nature of environment at the vicinity of the TKI can be deduced from the observed emission spectrum. The combined UV-Vis spectroscopy and computational chemistry are herein proven a reliable, precise and reproducible tool to pursue conformational characterization of fluorescent TKI. Hence, the other invasive and destructive procedures for structural characterization can be avoided.

8.2. Perspectives

We foresee the possible separation of the two conformers of AG1478 at low temperatures. Given that the small energy barrier between the planar and twisted structures of AG1478 can be overcome in favour of one conformer, we would be able to discretely isolate and characterize each conformer. We also believe that the lifetime measurements would give deeper insights in understanding the electronic properties of the two conformers of AG1478. This is because lifetime measurements can sense the subtle changes in the relaxation dynamics of the excited states. Hence the excited molecules of the two conformers of AG1478 would emit fluorescence at different radiative rates. In other words, dynamic quenching reduces the apparent fluorescent lifetime while static quenching does not change the lifetime of the excited state.

Our results have ramifications for studying the binding interactions of TKIs at the ATP binding pocket. The H-bond formation between AG1478 or SKF86002 and amino acid residue would alter drug conformation and absorption spectrum. Also, the interaction between AG1478 and confined water molecules at binding site would alter its structural and electronic configurations. In addition, the polarity and folding state of a protein matrix would also have an impact. Therefore, an informative picture of the drug conformation and the micro- and macro- properties of a target macromolecule can be obtained through measuring the optical spectrum and comparing it to the theoretical spectrum of a corresponding conformer. The dependence of AG1478 spectrum on solution pH can be exploited for identifying its dissolution profile which is crucial for the drug formulation. It can also help in probing AG1478 pharmacokinetics extracellularly and intracellularly. The acid dissociation constant of AG1478 is experimentally determined for the first time. The future work would be to identify the binding constant between AG1478 molecule and target proteins.

Bibliography

1. Torre, L.A., F. Bray, R.L. Siegel, J. Ferlay, J. Lortet-Tieulent, and A. Jemal, *Global Cancer Statistics, 2012.* Ca-a Cancer Journal for Clinicians, 2015. **65**(2): p. 87-108.
2. Yang, M., K. Sunderland, and C. Mao, *Virus-Derived Peptides for Clinical Applications.* Chem Rev, 2017. **117**(15): p. 10377-10402.
3. Stratton, M.R., P.J. Campbell, and P.A. Futreal, *The cancer genome.* Nature, 2009. **458**(7239): p. 719-724.
4. Carmeliet, P. and R.K. Jain, *Angiogenesis in cancer and other diseases.* Nature, 2000. **407**(6801): p. 249-257.
5. Chambers, A.F., A.C. Groom, and I.C. MacDonald, *Dissemination and growth of cancer cells in metastatic sites.* Nature Reviews Cancer, 2002. **2**(8): p. 563-572.
6. Zhao, Y., H. Li, Y.Y. Zhang, L.L. Li, R.P. Fang, Y.H. Li, Q. Liu, W.Y. Zhang, L.Y. Qiu, F.B. Liu, X.D. Zhang, and L.H. Ye, *Oncoprotein HBXIP Modulates Abnormal Lipid Metabolism and Growth of Breast Cancer Cells by Activating the LXRs/SREBP-1c/FAS Signaling Cascade.* Cancer Research, 2016. **76**(16): p. 4696-4707.
7. Chand, M., S. Rasheed, R. Heald, I. Swift, N. West, S. Rao, P. Tekkis, and G. Brown, *Adjuvant chemotherapy may improve disease-free survival in patients with rectal cancer positive for MRI-detected extramural venous invasion following chemoradiation.* Colorectal Disease, 2017. **19**(6): p. 537-543.
8. Reck, M., D. Rodriguez-Abreu, A.G. Robinson, R.N. Hui, T. Csoszi, A. Fulop, M. Gottfried, N. Peled, A. Tafreshi, S. Cuffe, M. O'Brien, S. Rao, K. Hotta, M.A. Leiby, G.M. Lubiniecki, Y. Shentu, R. Rangwala, J.R. Brahmer, and K.-. Investigators, *Pembrolizumab versus Chemotherapy for PD-L1-Positive Non-Small-Cell Lung Cancer.* New England Journal of Medicine, 2016. **375**(19): p. 1823-1833.
9. Negrao, M.V., L.S.D. Rocha, D.D. Girardi, and O. Feher, *Perioperative chemotherapy with and without high-dose methotrexate in adult osteosarcoma.* Anti-Cancer Drugs, 2017. **28**(8): p. 915-921.
10. Gershenson, D.M., D.C. Bodurka, R.L. Coleman, K.H. Lu, A. Malpica, and C.C. Sun, *Hormonal maintenance therapy for women with low grade serous carcinoma of the ovary or peritoneum.* Journal of Clinical Oncology, 2016. **34**(15).
11. Kwan, M.L., J.M. Roh, C.A. Laurent, J. Lee, L. Tang, D. Hershman, L.H. Kushi, and S. Yao, *Patterns and reasons for switching classes of hormonal therapy among women with early-stage breast cancer.* Cancer Causes & Control, 2017. **28**(6): p. 557-562.
12. Bluethmann, S.M., C.M. Alfano, J.D. Clapp, G. Luta, B.J. Small, A. Hurria, H.J. Cohen, S. Sugarman, B.M. H, C. Isaacs, and J.S. Mandelblatt, *Cognitive function and discontinuation of adjuvant hormonal therapy in older breast cancer survivors: CALGB 369901 (Alliance).* Breast Cancer Res Treat, 2017.
13. Yuan, B.Y., Y. Hu, L. Zhang, Y.H. Chen, Y.Y. Dong, and Z.C. Zeng, *Radiotherapy for adrenal gland metastases from hepatocellular carcinoma.* Clinical & Translational Oncology, 2017. **19**(9): p. 1154-1160.
14. De, B., O. Cahlon, I.J. Dunkel, K.C. De Braganca, Y. Khakoo, S.W. Gilheeney, M.M. Souweidane, and S.L. Wolden, *Reduced-volume radiotherapy for patients with localized intracranial nongerminoma germ cell tumors.* Journal of Neuro-Oncology, 2017. **134**(2): p. 349-356.
15. Stumpf, P.K., A. Amini, B.L. Jones, M. Koshy, D.J. Sher, C.H. Lieu, T.E. Schefter, K.A. Goodman, and C.G. Rusthoven, *Adjuvant Radiotherapy Improves Overall Survival in Patients With Resected Gastric Adenocarcinoma: A National Cancer Data Base Analysis.* Cancer, 2017. **123**(17): p. 3402-3409.

16. Mohanty, S., R. Rajaram, K.Y. Bilimoria, R. Salem, T.M. Pawlik, and D.J. Bentrem, *Assessment of non-surgical versus surgical therapy for localized hepatocellular carcinoma.* J Surg Oncol, 2016. **113**(2): p. 175-80.
17. Zwick, E., J. Bange, and A. Ullrich, *Receptor tyrosine kinase signalling as a target for cancer intervention strategies.* Endocr Relat Cancer, 2001. **8**(3): p. 161-73.
18. Hubbard, S.R. and W.T. Miller, *Receptor tyrosine kinases: mechanisms of activation and signaling.* Curr Opin Cell Biol, 2007. **19**(2): p. 117-23.
19. Tsai, C.J. and R. Nussinov, *The molecular basis of targeting protein kinases in cancer therapeutics.* Semin Cancer Biol, 2013. **23**(4): p. 235-42.
20. Shah, D.R., R.R. Shah, and J. Morganroth, *Tyrosine kinase inhibitors: their on-target toxicities as potential indicators of efficacy.* Drug Saf, 2013. **36**(6): p. 413-26.
21. Aman, P., *Fusion oncogenes in tumor development.* Semin Cancer Biol, 2005. **15**(3): p. 236-43.
22. Hojjat-Farsangi, M., *Small-molecule inhibitors of the receptor tyrosine kinases: promising tools for targeted cancer therapies.* Int J Mol Sci, 2014. **15**(8): p. 13768-801.
23. Eglen, R. and T. Reisine, *Drug discovery and the human kinome: recent trends.* Pharmacol Ther, 2011. **130**(2): p. 144-56.
24. Anreddy, N., P. Gupta, R.J. Kathawala, A. Patel, J.N. Wurpel, and Z.S. Chen, *Tyrosine kinase inhibitors as reversal agents for ABC transporter mediated drug resistance.* Molecules, 2014. **19**(9): p. 13848-77.
25. Cozza, G., A. Bortolato, E. Menta, E. Cavalletti, S. Spinelli, and S. Moro, *ATP non-competitive Ser/Thr kinase inhibitors as potential anticancer agents.* Anticancer Agents Med Chem, 2009. **9**(7): p. 778-86.
26. Finn, R.S., *Targeting Src in breast cancer.* Ann Oncol, 2008. **19**(8): p. 1379-86.
27. Brown, M.T. and J.A. Cooper, *Regulation, substrates and functions of src.* Biochim Biophys Acta, 1996. **1287**(2-3): p. 121-49.
28. Cohen, P., *Protein kinases--the major drug targets of the twenty-first century?* Nat Rev Drug Discov, 2002. **1**(4): p. 309-15.
29. Duong-Ly, K.C. and J.R. Peterson, *The human kinome and kinase inhibition.* Curr Protoc Pharmacol, 2013. **Chapter 2**: p. Unit2 9.
30. Al-Obeidi, F.A., J.J. Wu, and K.S. Lam, *Protein tyrosine kinases: Structure, substrate specificity, and drug discovery.* Biopolymers, 1998. **47**(3): p. 197-223.
31. Robinson, D.R., Y.M. Wu, and S.F. Lin, *The protein tyrosine kinase family of the human genome.* Oncogene, 2000. **19**(49): p. 5548-57.
32. Ullrich, A. and J. Schlessinger, *Signal transduction by receptors with tyrosine kinase activity.* Cell, 1990. **61**(2): p. 203-12.
33. Johnson, L.N., *Protein kinase inhibitors: contributions from structure to clinical compounds.* Q Rev Biophys, 2009. **42**(1): p. 1-40.
34. Blume-Jensen, P. and T. Hunter, *Oncogenic kinase signalling.* Nature, 2001. **411**(6835): p. 355-65.
35. Sullivan, I. and D. Planchard, *Next-Generation EGFR Tyrosine Kinase Inhibitors for Treating EGFR-Mutant Lung Cancer beyond First Line.* Frontiers in Medicine, 2017. **3**.
36. Su, S. and Y.L. Wu, *Clinical trials of tyrosine kinase inhibitors for lung cancer in China: a review.* Journal of Hematology & Oncology, 2017. **10**.
37. Gharwan, H. and H. Groninger, *Kinase inhibitors and monoclonal antibodies in oncology: clinical implications.* Nature Reviews Clinical Oncology, 2016. **13**(4): p. 209-227.
38. Wu, P., T.E. Nielsen, and M.H. Clausen, *Small-molecule kinase inhibitors: an analysis of FDA-approved drugs.* Drug Discovery Today, 2016. **21**(1): p. 5-10.
39. Blanc, J., R. Geney, and C. Menet, *Type II kinase inhibitors: an opportunity in cancer for rational design.* Anticancer Agents Med Chem, 2013. **13**(5): p. 731-47.

40. Zhang, J., P.L. Yang, and N.S. Gray, *Targeting cancer with small molecule kinase inhibitors.* Nat Rev Cancer, 2009. **9**(1): p. 28-39.
41. Liu, Y. and N.S. Gray, *Rational design of inhibitors that bind to inactive kinase conformations.* Nat Chem Biol, 2006. **2**(7): p. 358-64.
42. Davis, M.I., J.P. Hunt, S. Herrgard, P. Ciceri, L.M. Wodicka, G. Pallares, M. Hocker, D.K. Treiber, and P.P. Zarrinkar, *Comprehensive analysis of kinase inhibitor selectivity.* Nat Biotechnol, 2011. **29**(11): p. 1046-51.
43. Garuti, L., M. Roberti, and G. Bottegoni, *Non-ATP competitive protein kinase inhibitors.* Curr Med Chem, 2010. **17**(25): p. 2804-21.
44. Fasano, M., C.M. Della Corte, R. Califano, A. Capuano, T. Troiani, E. Martinelli, F. Ciardiello, and F. Morgillo, *Type III or allosteric kinase inhibitors for the treatment of non-small cell lung cancer.* Expert Opin Investig Drugs, 2014. **23**(6): p. 809-21.
45. Lamba, V. and I. Ghosh, *New directions in targeting protein kinases: focusing upon true allosteric and bivalent inhibitors.* Curr Pharm Des, 2012. **18**(20): p. 2936-45.
46. Dar, A.C. and K.M. Shokat, *The evolution of protein kinase inhibitors from antagonists to agonists of cellular signaling.* Annu Rev Biochem, 2011. **80**: p. 769-95.
47. Gower, C.M., M.E. Chang, and D.J. Maly, *Bivalent inhibitors of protein kinases.* Crit Rev Biochem Mol Biol, 2014. **49**(2): p. 102-15.
48. Barf, T. and A. Kaptein, *Irreversible protein kinase inhibitors: balancing the benefits and risks.* J Med Chem, 2012. **55**(14): p. 6243-62.
49. Leproult, E., S. Barluenga, D. Moras, J.M. Wurtz, and N. Winssinger, *Cysteine mapping in conformationally distinct kinase nucleotide binding sites: application to the design of selective covalent inhibitors.* J Med Chem, 2011. **54**(5): p. 1347-55.
50. Gonzales, A.J., K.E. Hook, I.W. Althaus, P.A. Ellis, E. Trachet, A.M. Delaney, P.J. Harvey, T.A. Ellis, D.M. Amato, J.M. Nelson, D.W. Fry, T. Zhu, C.M. Loi, S.A. Fakhoury, K.M. Schlosser, K.E. Sexton, R.T. Winters, J.E. Reed, A.J. Bridges, D.J. Lettiere, D.A. Baker, J. Yang, H.T. Lee, H. Tecle, and P.W. Vincent, *Antitumor activity and pharmacokinetic properties of PF-00299804, a second-generation irreversible pan-erbB receptor tyrosine kinase inhibitor.* Mol Cancer Ther, 2008. **7**(7): p. 1880-9.
51. Hug, B., R. Abbas, C. Leister, J. Burns, and D. Sonnichsen, *A single-dose, crossover, placebo- and moxifloxacin-controlled study to assess the effects of neratinib (HKI-272) on cardiac repolarization in healthy adult subjects.* Clin Cancer Res, 2010. **16**(15): p. 4016-23.
52. Yaish, P., A. Gazit, C. Gilon, and A. Levitzki, *Blocking of EGF-dependent cell proliferation by EGF receptor kinase inhibitors.* Science, 1988. **242**(4880): p. 933-5.
53. Gazit, A., P. Yaish, C. Gilon, and A. Levitzki, *Tyrphostins I: synthesis and biological activity of protein tyrosine kinase inhibitors.* J Med Chem, 1989. **32**(10): p. 2344-52.
54. Gazit, A., N. Osherov, I. Posner, P. Yaish, E. Poradosu, C. Gilon, and A. Levitzki, *Tyrphostins .2. Heterocyclic and Alpha-Substituted Benzylidenemalononitrile Tyrphostins as Potent Inhibitors of Egf Receptor and Erbb2/Neu Tyrosine Kinases.* Journal of Medicinal Chemistry, 1991. **34**(6): p. 1896-1907.
55. Caja, L., P. Sancho, E. Bertran, C. Ortiz, J.S. Campbell, N. Fausto, and I. Fabregat, *The tyrphostin AG1478 inhibits proliferation and induces death of liver tumor cells through EGF receptor-dependent and independent mechanisms.* Biochemical Pharmacology, 2011. **82**(11): p. 1583-1592.
56. Bojko, A., K. Reichert, A. Adamczyk, J. Ligeza, J. Ligeza, and A. Klein, *The effect of tyrphostins AG494 and AG1478 on the autocrine growth regulation of A549 and DU145 cells.* Folia Histochemica Et Cytobiologica, 2012. **50**(2): p. 186-195.
57. Ma, L., H.Q. Yan, and Q.H. Zhou, *AG1478 inhibits the migration and invasion of cisplatin-resistant human lung adenocarcinoma cells via the cell cycle regulation by matrix*

metalloproteinase-9. Oncology Letters, 2014. **8**(2): p. 921-927.

58. Zhu, X.F., Z.C. Liu, B.F. Xie, Z.M. Li, G.K. Feng, D.J. Yang, and Y.X. Zeng, *EGFR tyrosine kinase inhibitor AG1478 inhibits cell proliferation and arrests cell cycle in nasopharyngeal carcinoma cells.* Cancer Letters, 2001. **169**(1): p. 27-32.
59. Baba, Y., T. Maeda, A. Suzuki, S. Takada, M. Fujii, and Y. Kato, *Deguelin Potentiates Apoptotic Activity of an EGFR Tyrosine Kinase Inhibitor (AG1478) in PIK3CA-Mutated Head and Neck Squamous Cell Carcinoma.* International Journal of Molecular Sciences, 2017. **18**(2).
60. Takezawa, K., T. Ogawa, S. Shimizu, and T. Shimizu, *Epidermal growth factor receptor inhibitor AG1478 inhibits mucus hypersecretion in airway epithelium.* American Journal of Rhinology & Allergy, 2016. **30**(1): p. E1-E6.
61. Dorobantu, C.M., C. Harak, R. Klein, L. van der Linden, J.R.P.M. Strating, H.M. van der Schaar, V. Lohmann, and F.J.M. van Kuppeveld, *Tyrphostin AG1478 Inhibits Encephalomyocarditis Virus and Hepatitis C Virus by Targeting Phosphatidylinositol 4-Kinase III alpha.* Antimicrobial Agents and Chemotherapy, 2016. **60**(10): p. 6402-6406.
62. Liu, B., H.Y. Chen, T.G. Johns, and A.H. Neufeld, *Epidermal growth factor receptor activation: An upstream signal for transition of quiescent astrocytes into reactive astrocytes after neural injury.* Journal of Neuroscience, 2006. **26**(28): p. 7532-7540.
63. Robinson, R., S.R. Viviano, J.M. Criscione, C.A. Williams, L. Jun, J.C. Tsai, and E.B. Lavik, *Nanospheres Delivering the EGFR TKI AG1478 Promote Optic Nerve Regeneration: The Role of Size for Intraocular Drug Delivery.* Acs Nano, 2011. **5**(6): p. 4392-4400.
64. Bondi, M.L., A. Azzolina, E.F. Craparo, C. Botto, E. Amore, G. Giammona, and M. Cervello, *Entrapment of an EGFR inhibitor into nanostructured lipid carriers (NLC) improves its antitumor activity against human hepatocarcinoma cells.* Journal of Nanobiotechnology, 2014. **12**.
65. Lavik, E., Y.H. Kwon, M. Kuehn, S. Saluja, J. Bertram, and J. Huang, *Sustained intraocular delivery of drugs from biodegradable polymeric microparticles*. 2013, Google Patents.
66. Ishiguro, Y., H. Ishiguro, and H. Miyamoto, *Epidermal Growth Factor Receptor Tyrosine Kinase Inhibition Up-regulates Interleukin-6 in Cancer Cells and Induces Subsequent Development of Interstitial Pneumonia.* Oncotarget, 2013. **4**(4): p. 550-559.
67. Gazel, A. and M. Blumenberg, *Transcriptional effects of inhibiting epidermal growth factor receptor in keratinocytes.* Dermatologica Sinica, 2013. **31**(3): p. 107-119.
68. Weglicki, W.B., J.H. Kramer, C.F. Spurney, J.J. Chmielinska, and I.T. Mak, *The EGFR tyrosine kinase inhibitor tyrphostin AG-1478 causes hypomagnesemia and cardiac dysfunction.* Canadian Journal of Physiology and Pharmacology, 2012. **90**(8): p. 1145-1149.
69. Al-Obeidi, F.A. and K.S. Lam, *Development of inhibitors for protein tyrosine kinases.* Oncogene, 2000. **19**(49): p. 5690-5701.
70. Gan, H.K., A.W. Burgess, F. Walker, A.M. Scott, and T.G. Johns, *The epidermal growth factor receptor (EGFR) exists as an inactive dimer conformation that is reactive with mAb 806 and distinct from the "back-to-back" ligated dimer.* Clinical Cancer Research, 2005. **11**(24): p. 8995s-8995s.
71. Stogios, P.J., P. Spanogiannopoulos, E. Evdokimova, O. Egorova, T. Shakya, N. Todorovic, A. Capretta, G.D. Wright, and A. Savchenko, *Structure-guided optimization of protein kinase inhibitors reverses aminoglycoside antibiotic resistance.* Biochemical Journal, 2013. **454**: p. 191-200.
72. Berman, H.M., J. Westbrook, Z. Feng, G. Gilliland, T.N. Bhat, H. Weissig, I.N. Shindyalov, and P.E. Bourne, *The Protein Data Bank.* Nucleic Acids Research, 2000. **28**(1): p. 235-242.
73. Lantos, I., P.E. Bender, K.A. Razgaitis, B.M. Sutton, M.J. DiMartino, D.E. Griswold, and

D.T. Walz, *Antiinflammatory activity of 5,6-diaryl-2,3-dihydroimidazo[2,1-b]thiazoles. Isomeric 4-pyridyl and 4-substituted phenyl derivatives.* J Med Chem, 1984. **27**(1): p. 72-5.

74. Lee, J.C., J.T. Laydon, P.C. Mcdonnell, T.F. Gallagher, S. Kumar, D. Green, D. Mcnulty, M.J. Blumenthal, J.R. Heys, S.W. Landvatter, J.E. Strickler, M.M. Mclaughlin, I.R. Siemens, S.M. Fisher, G.P. Livi, J.R. White, J.L. Adams, and P.R. Young, *A Protein-Kinase Involved in the Regulation of Inflammatory Cytokine Biosynthesis.* Nature, 1994. **372**(6508): p. 739-746.
75. Lee, J.C., D.E. Griswold, B. Votta, and N. Hanna, *Inhibition of monocyte IL-1 production by the anti-inflammatory compound, SK&F 86002.* Int J Immunopharmacol, 1988. **10**(7): p. 835-43.
76. Selig, R., V. Schattel, M. Goettert, D. Schollmeyer, W. Albrecht, and S. Laufer, *Conformational effects on potency of thioimidazoles and dihydrothiazolines.* Medchemcomm, 2011. **2**(4): p. 261-269.
77. Todorova, N.A., V. Doseeva, J. Ramprakash, and F.P. Schwarz, *Effect of the distal C162S mutation on the energetics of drug binding to p38 alpha MAP kinase.* Archives of Biochemistry and Biophysics, 2008. **469**(2): p. 232-242.
78. Parker, L.J., S. Taruya, K. Tsuganezawa, N. Ogawa, J. Mikuni, K. Honda, Y. Tomabechi, N. Handa, M. Shirouzu, S. Yokoyama, and A. Tanaka, *Kinase crystal identification and ATP-competitive inhibitor screening using the fluorescent ligand SKF86002.* Acta Crystallogr D Biol Crystallogr, 2014. **70**(Pt 2): p. 392-404.
79. Zarubin, T. and J. Han, *Activation and signaling of the p38 MAP kinase pathway.* Cell Res, 2005. **15**(1): p. 11-8.
80. Barbosa, M.L.D., M.M. Fumian, A.L.P. de Miranda, E.J. Barreiro, and L.M. Lima, *Therapeutic approaches for tumor necrosis factor inhibition.* Brazilian Journal of Pharmaceutical Sciences, 2011. **47**(3): p. 427-446.
81. Wagner, G. and S. Laufer, *Small molecular anti-cytokine agents.* Medicinal Research Reviews, 2006. **26**(1): p. 1-62.
82. Aspnes, D.E., *Linear and nonlinear optical spectroscopy of surfaces and interfaces.* Physica Status Solidi a-Applied Research, 2001. **188**(4): p. 1353-1360.
83. Volkmer, A., P.P. Radi, A.M. Zheltikov, and A. Zumbusch, *New trends and recent advances in coherent Raman microscopy and nonlinear optical spectroscopy: introduction to the special issue.* Journal of Raman Spectroscopy, 2009. **40**(7): p. 712-713.
84. Albani, J.R., *Principles and Applications of Fluorescence Spectroscopy*. 2008, Wiley,: Hoboken. p. 1 online resource (270 p.).
85. Sauer, M., J. Hofkens, and J. Enderlein, *Basic Principles of Fluorescence Spectroscopy*, in *Handbook of Fluorescence Spectroscopy and Imaging*. 2011, Wiley-VCH Verlag GmbH & Co. KGaA. p. 1-30.
86. Skoog, D.A., F.J. Holler, and S.R. Crouch, *Principles of instrumental analysis*. 6th ed ed. 2007, Belmont, CA: Thomson. xv, 1039 p.
87. Brown, J.Q., K. Vishwanath, G.M. Palmer, and N. Ramanujam, *Advances in quantitative UV-visible spectroscopy for clinical and pre-clinical application in cancer.* Curr Opin Biotechnol, 2009. **20**(1): p. 119-31.
88. Pundak, S. and R.S. Roche, *Steady-State and Nanosecond Spectroscopy of Tyrosine-Tyrosinate Fluorescence in Spinach and Bovine Testis Calmodulin.* Biophysical Journal, 1983. **41**(2): p. A220-A220.
89. Yue, X.L., Z. Armijo, K. King, M.V. Bondar, A.R. Morales, A. Frazer, I.A. Mikhailov, O.V. Przhonska, and K.D. Belfield, *Steady-State and Femtosecond Transient Absorption Spectroscopy of New Two-Photon Absorbing Fluorene-Containing Quinolizinium Cation Membrane Probes.* Acs Applied Materials & Interfaces, 2015. **7**(4): p. 2833-2846.

90. Catici, D.A.M., H.E. Amos, Y. Yang, J.M.H. van den Elsen, and C.R. Pudney, *The red edge excitation shift phenomenon can be used to unmask protein structural ensembles: implications for NEMO-ubiquitin interactions.* Febs Journal, 2016. **283**(12): p. 2272-2284.
91. Chattopadhyay, A. and S. Haldar, *Dynamic Insight into Protein Structure Utilizing Red Edge Excitation Shift.* Accounts of Chemical Research, 2014. **47**(1): p. 12-19.
92. Demchenko, A.P., *The red-edge effects: 30 years of exploration.* Luminescence, 2002. **17**(1): p. 19-42.
93. Weber, G. and M. Shinitzky, *Failure of Energy Transfer between Identical Aromatic Molecules on Excitation at Long Wave Edge of Absorption Spectrum.* Proceedings of the National Academy of Sciences of the United States of America, 1970. **65**(4): p. 823-+.
94. Galley, W.C. and R.M. Purkey, *Role of Heterogeneity of Solvation Site in Electronic Spectra in Solution.* Proceedings of the National Academy of Sciences of the United States of America, 1970. **67**(3): p. 1116-&.
95. Lakowicz, J.R., *Principles of fluorescence spectroscopy*. 2013: Springer Science & Business Media.
96. Jacobkhed, *Jablonski diagram of absorbance, non-radiative decay, and fluorescence.* https://en.wikipedia.org/wiki/Jablonski_diagram, viewed January 27, 2018.
97. Trummer, B.J., V. Iyer, S.V. Balu-Iyer, R. O'Connor, and R.M. Straubinger, *Physicochemical properties of epidermal growth factor receptor inhibitors and development of a nanoliposomal formulation of gefitinib.* J Pharm Sci, 2012. **101**(8): p. 2763-76.
98. Hemalatha, K., G. Madhumitha, C.S. Vasavi, and P. Munusami, *2,3-Dihydroquinazolin-4(1H)-ones: visible light mediated synthesis, solvatochromism and biological activity.* J Photochem Photobiol B, 2015. **143**: p. 139-47.
99. Gaudette, F., S. Raeppel, H. Nguyen, N. Beaulieu, C. Beaulieu, I. Dupont, A.R. Macleod, J.M. Besterman, and A. Vaisburg, *Identification of potent and selective VEGFR receptor tyrosine kinase inhibitors having new amide isostere headgroups.* Bioorg Med Chem Lett, 2010. **20**(3): p. 848-52.
100. Wilson, J.N., W. Liu, A.S. Brown, and R. Landgraf, *Binding-induced, turn-on fluorescence of the EGFR/ERBB kinase inhibitor, lapatinib.* Org Biomol Chem, 2015.
101. Grante, I., A. Actins, and L. Orola, *Protonation effects on the UV/Vis absorption spectra of imatinib: A theoretical and experimental study.* Spectrochimica Acta. Part A: Molecular and Biomolecular Spectroscopy, 2014. **129**: p. 326-332.
102. Huang, Y., Q.H. Hu, G.X. Song, Z. Tao, S.F. Xue, Q.J. Zhu, Q.D. Zhouc, and G. Wei, *Cucurbit[7,8]urils binding to gefitinib and the effect of complex formation on the solubility and dissolution rate of the drug.* RSC Adv., 2014. **4**(7): p. 3348-3354.
103. Sirajuddin, M., S. Ali, and A. Badshah, *Drug-DNA interactions and their study by UV-Visible, fluorescence spectroscopies and cyclic voltametry.* J Photochem Photobiol B, 2013. **124**: p. 1-19.
104. Berts, A. and K.P. Minneman, *Tyrosine kinase inhibitors and Ca2+ signaling: direct interactions with fura-2.* Eur J Pharmacol, 2000. **389**(1): p. 35-40.
105. Lu, Z., L. Qi, G.X. Li, Q. Li, G.H. Sun, and R.Z. Xie, *In Vitro Characterization for Human Serum Albumin Binding Sorafenib, A Multi Kinase Inhibitor: Spectroscopic Study.* Journal of Solution Chemistry, 2014. **43**(11): p. 2010-2025.
106. Liu, Y., M.M. Chen, and L. Song, *Comparing the effects of Fe(III) and Cu(II) on the binding affinity of erlotinib to bovine serum albumin using spectroscopic methods.* Journal of Luminescence, 2013. **134**: p. 515-523.
107. Vadia, N. and S. Rajput, *Development of colorimetric method for determination of dasatinib in bulk and in tablet formulation.* Int J Pharm Pharm Sci, 2011. **3**(2): p. 188-190.

108. Ruan, L., D. Su, C. Shao, J. Wang, C. Dong, X. Huang, and J. Ren, *A sensitive and microscale method for drug screening combining affinity probes and single molecule fluorescence correlation spectroscopy.* Analyst, 2015. **140**(4): p. 1207-14.
109. Clayton, A.H., M.A. Perugini, J. Weinstock, J. Rothacker, K.G. Watson, A.W. Burgess, and E.C. Nice, *Fluorescence and analytical ultracentrifugation analyses of the interaction of the tyrosine kinase inhibitor, tyrphostin AG 1478-mesylate, with albumin.* Anal Biochem, 2005. **342**(2): p. 292-9.
110. Jensen, F., *Introduction to computational chemistry*. 2013: John Wiley & Sons.
111. Foresman, J.B., A.E. Frisch, and I. Gaussian, *Exploring Chemistry with Electronic Structure Methods, 3rd ed.* 2015: Gaussian, Incorporated.
112. Swart, M., *A new family of hybrid density functionals.* Chemical Physics Letters, 2013. **580**: p. 166-171.
113. Grimme, S., *Density functional theory with London dispersion corrections.* Wiley Interdisciplinary Reviews-Computational Molecular Science, 2011. **1**(2): p. 211-228.
114. Becke, A.D., *Density-Functional Thermochemistry .3. The Role of Exact Exchange.* Journal of Chemical Physics, 1993. **98**(7): p. 5648-5652.
115. Zhao, Y. and D.G. Truhlar, *Density functionals with broad applicability in chemistry.* Acc Chem Res, 2008. **41**(2): p. 157-67.
116. Adamo, C. and D. Jacquemin, *The calculations of excited-state properties with Time-Dependent Density Functional Theory.* Chemical Society Reviews, 2013. **42**(3): p. 845-856.
117. Runge, E. and E.K.U. Gross, *Density-Functional Theory for Time-Dependent Systems.* Physical Review Letters, 1984. **52**(12): p. 997-1000.
118. Cintron, M.S., G.P. Johnson, and A.D. French, *Quantum mechanics models of the methanol dimer: OHcdots, three dots, centeredO hydrogen bonds of beta-d-glucose moieties from crystallographic data.* Carbohydr Res, 2017. **443-444**: p. 87-94.
119. Sudhi, G., S.R. Rajina, S.G. Praveen, T.S. Xavier, P.T.M. Kenny, D. Jaiswal-Nagar, and J. Binoy, *Investigations of vibrational spectra and bioactivity of novel anticancer drug N-(6-ferrocenyl-2-naphthoyl)-gamma-amino butyric acid ethyl ester.* Spectrochimica Acta Part a-Molecular and Biomolecular Spectroscopy, 2017. **185**: p. 234-244.
120. Mamais, M., A.D. Esposti, V. Kouloumoundra, T. Gustavsson, F. Monti, A. Venturini, E.D. Chrysina, D. Markovitsi, and T. Gimisis, *A New Potent Inhibitor of Glycogen Phosphorylase Reveals the Basicity of the Catalytic Site.* Chemistry-a European Journal, 2017. **23**(37): p. 8800-8805.
121. Perez, M., R. Concu, M. Ornelas, M.N.D.S. Cordeiro, M. Azenha, and A.F. Silva, *Measurement artifacts identified in the UV-vis spectroscopic study of adduct formation within the context of molecular imprinting of naproxen.* Spectrochimica Acta Part a-Molecular and Biomolecular Spectroscopy, 2016. **153**: p. 661-668.
122. Sheikhi, M., S. Shahab, L. Filippovich, H. Yahyaei, E. Dikusar, and M. Khaleghian, *New derivatives of (E,E)-azomethines: Design, quantum chemical modeling, spectroscopic (FT-IR, UV/Vis, polarization) studies, synthesis and their applications: Experimental and theoretical investigations.* Journal of Molecular Structure, 2018. **1152**: p. 368-385.
123. Joshi, B.D., A. Srivastava, P. Tandon, S. Jain, and A.P. Ayala, *A combined experimental (IR, Raman and UV-Vis) and quantum chemical study of canadine.* Spectrochim Acta A Mol Biomol Spectrosc, 2018. **191**: p. 249-258.
124. Barone, V., J. Bloino, S. Monti, A. Pedone, and G. Prampolini, *Fluorescence spectra of organic dyes in solution: a time dependent multilevel approach.* Physical Chemistry Chemical Physics, 2011. **13**(6): p. 2160-2166.
125. Lin, Y.L., Y.L. Meng, L. Huang, and B. Roux, *Computational Study of Gleevec and G6G Reveals Molecular Determinants of Kinase Inhibitor Selectivity.* Journal of the American

Chemical Society, 2014. **136**(42): p. 14753-14762.
126. Banavath, H.N., O.P. Sharma, M.S. Kumar, and R. Baskaran, *Identification of novel tyrosine kinase inhibitors for drug resistant T315I mutant BCR-ABL: a virtual screening and molecular dynamics simulations study.* Scientific Reports, 2014. **4**.
127. Yang, Y.L., G.H. Li, D.Y. Zhao, H.Y. Yu, X.L. Zheng, X.D. Peng, X. Zhang, T. Fu, X.Q. Hu, M.S. Niu, X.F. Ji, L.B. Zou, and J. Wang, *Computational discovery and experimental verification of tyrosine kinase inhibitor pazopanib for the reversal of memory and cognitive deficits in rat model neurodegeneration.* Chemical Science, 2015. **6**(5): p. 2812-2821.
128. Santillan, M.B., F. Tomas-Vert, J.M. Aullo, E.A. Jauregui, and G.M. Ciuffo, *Structural and electronic properties of tyrosine kinases inhibitors.* Cell Mol Biol (Noisy-le-grand), 2003. **49**(6): p. 929-37.
129. Rohe, A., C. Gollner, K. Wichapong, F. Erdmann, G.M.A. Al-Mazaideh, W. Sippl, and M. Schmidt, *Evaluation of potential Myt1 kinase inhibitors by TR-FRET based binding assay.* European Journal of Medicinal Chemistry, 2013. **61**: p. 41-48.
130. Wichapong, K., A. Rohe, C. Platzer, I. Slynko, F. Erdmann, M. Schmidt, and W. Sippl, *Application of Docking and QM/MM-GBSA Rescoring to Screen for Novel Myt1 Kinase Inhibitors.* Journal of Chemical Information and Modeling, 2014. **54**(3): p. 881-893.
131. Ahamed, G., S. Batuta, D. Ghosh, N.A. Begum, and D. Mandal, *Photophysical studies on a photoactive yellow protein fluorophore analog with the 4-Hydroxy group replaced by 4-Dimethylamino group.* Journal of Photochemistry and Photobiology a-Chemistry, 2017. **335**: p. 86-93.
132. Grimsdale, A.C., K.L. Chan, R.E. Martin, P.G. Jokisz, and A.B. Holmes, *Synthesis of Light-Emitting Conjugated Polymers for Applications in Electroluminescent Devices.* Chemical Reviews, 2009. **109**(3): p. 897-1091.
133. Tainaka, K., K. Tanaka, S. Ikeda, K. Nishiza, T. Unzai, Y. Fujiwara, I. Saito, and A. Okamoto, *PRODAN-conjugated DNA: Synthesis and photochemical properties.* Journal of the American Chemical Society, 2007. **129**(15): p. 4776-4784.
134. Hantzsch, A., *Review of halochromy and "salvatochromic" of the dibenzalacetone and simple ketone, as well as their ketochloride.* Berichte Der Deutschen Chemischen Gesellschaft, 1922. **55**: p. 953-979.
135. Ungnade, H.E., *The Effect of Solvents on the Absorption Spectra of Aromatic Compounds.* Journal of the American Chemical Society, 1953. **75**(2): p. 432-434.
136. Ketskemety, I., L. Szalay, and Z. Varkonyi, *Effect of Solvent on Absorption and Fluorescence Spectra of Alcoholic Solutions of Trypaflavine.* Acta Physica Et Chemica, 1965. **11**(1-2): p. 15-+.
137. Makitra, R.G. and Y.M. Tsikantchuk, *Solvent Effects on the Organic-Complexes .2. The Uv-Spectrophotometrical Investigation of Interaction between Dimethylformamide and Iodine.* Organic Reactivity, 1979. **16**(4): p. 505-511.
138. Novaki, L.P. and O.A. El Seoud, *Solvatochromism in aqueous micellar solutions: effects of the molecular structures of solvatochromic probes and cationic surfactants.* Physical Chemistry Chemical Physics, 1999. **1**(8): p. 1957-1964.
139. Matsui, M., T. Yamamoto, K. Kakitani, S. Biradar, Y. Kubota, and K. Funabiki, *UV-vis absorption and fluorescence spectra, solvatochromism, and application to pH sensors of novel xanthene dyes having thienyl and thieno[3,2-b]thienyl rings as auxochrome.* Dyes and Pigments, 2017. **139**: p. 533-540.
140. Reichardt, C., *Solvatochromic Dyes as Solvent Polarity Indicators.* Chemical Reviews, 1994. **94**(8): p. 2319-2358.
141. Marini, A., A. Munoz-Losa, A. Biancardi, and B. Mennucci, *What is Solvatochromism?* Journal of Physical Chemistry B, 2010. **114**(51): p. 17128-17135.
142. Lakowicz, J.R., *Principles of fluorescence spectroscopy*. 3rd ed. 2006, New York: Springer.

xxvi, 954 p.

143. Matei, I., S. Ionescu, and M. Hillebrand, *Solute–Solvent Hydrogen Bond Formation in the Excited State. Experimental and Theoretical Evidence*, in *Hydrogen Bonding and Transfer in the Excited State*. 2010, John Wiley & Sons, Ltd. p. 79-123.
144. Bilot, L. and A. Kawski, *Zur Theorie Des Einflusses Von Losungsmitteln Auf Die Elektroenspektren Der Molekule.* Zeitschrift Fur Naturforschung Part a-Astrophysik Physik Und Physikalische Chemie, 1962. **A 17**(7): p. 621-&.
145. Lippert, E., *Habilitationsschrift Zur Erlangung Der Lehrberichtigung (Venia Legendi) Fur Das Fach Physikalische Chemie Ander Techischen-Hochschule-Stuttgart - Spektroskopische Bestimmung Des Dipolmomentes Aromatischer Verbindungen Im Ersten Angeregten Singulettzustand.* Zeitschrift Fur Elektrochemie, 1957. **61**(8): p. 962-975.
146. Mataga, N., Y. Kaifu, and M. Koizumi, *Solvent Effects Upon Fluorescence Spectra and the Dipolemoments of Excited Molecules.* Bulletin of the Chemical Society of Japan, 1956. **29**(4): p. 465-470.
147. Bakhshiev, N.G., *Universal Intermolecular Interactions and Their Effect on the Position of the Electronic Spectra of Molecules in 2-Component Solutions .7. Theory (General Case for Isotopic Solution).* Optika I Spektroskopiya, 1964. **16**(5): p. 821-832.
148. Kawski, A., *On the estimation of excited-state dipole moments from solvatochromic shifts of absorption and fluorescence spectra.* Zeitschrift Fur Naturforschung Section a-a Journal of Physical Sciences, 2002. **57**(5): p. 255-262.
149. Chamma, A. and P. Viallet, *Determination of Dipole Moment of Molecule in Singlet Excited State - Application to Indole, Benzimidazole and Indazole.* Comptes Rendus Hebdomadaires Des Seances De L Academie Des Sciences Serie C, 1970. **270**(24): p. 1901-&.
150. Lee, S.C., N.Y. Kang, S.J. Park, S.W. Yun, Y. Chandran, and Y.T. Chang, *Development of a fluorescent chalcone library and its application in the discovery of a mouse embryonic stem cell probe.* Chemical Communications, 2012. **48**(53): p. 6681-6683.
151. Prabu, S., R. Nagalakshmi, and P. Srinivasan, *Investigations on the physico chemical properties of 4-bromochalcone single crystals for nonlinear optical applications.* Spectrochimica Acta Part a-Molecular and Biomolecular Spectroscopy, 2013. **103**: p. 45-52.
152. Reichardt, C. and T. Welton, *Solvents and solvent effects in organic chemistry*. 2011: John Wiley & Sons.
153. Reichardt, C. and E. Harbuschgornert, *Pyridinium N-Phenoxide Betaines and Their Application for the Characterization of Solvent Polarities .10. Extension, Correction, and New Definition of the Et Solvent Polarity Scale by Application of a Lipophilic Penta-Tert-Butyl-Substituted Pyridinium N-Phenoxide Betaine Dy.* Liebigs Annalen Der Chemie, 1983(5): p. 721-743.
154. Olivares, S.P., S. Risso, and M.I. Gutierrez, *Solvent effects on the spectroscopic properties of 4-hexylresorcinol.* Spectrochimica Acta Part a-Molecular and Biomolecular Spectroscopy, 2008. **71**(2): p. 336-339.
155. Nikolov, P. and I. Timtcheva, *Photophysical properties of some derivatives of 3-arylmethylene-1(3H)-isobenzofuranone - Indication of intermolecular hydrogen-bond formation in the singlet excited state.* Journal of Photochemistry and Photobiology a-Chemistry, 2000. **131**(1-3): p. 23-26.
156. Kamlet, M.J., J.L.M. Abboud, M.H. Abraham, and R.W. Taft, *Linear Solvation Energy Relationships .23. A Comprehensive Collection of the Solvatochromic Parameters, Pi-Star, Alpha and Beta, and Some Methods for Simplifying the Generalized Solvatochromic Equation.* Journal of Organic Chemistry, 1983. **48**(17): p. 2877-2887.

157. Catalan, J., *On the pi* solvent scale.* Journal of Organic Chemistry, 1995. **60**(25): p. 8315-8317.
158. Abe, T., *Improvements of the Empirical Pistar Solvent Polarity Scale.* Bulletin of the Chemical Society of Japan, 1990. **63**(8): p. 2328-2338.
159. Sjostrom, M. and S. Wold, *Statistical-Analysis of Solvatochromic Shift Data.* Journal of the Chemical Society-Perkin Transactions 2, 1981(1): p. 104-109.
160. Catalan, J., *Toward a generalized treatment of the solvent effect based on four empirical scales: dipolarity (SdP, a new scale), polarizability (SP), acidity (SA), and basicity (SB) of the medium.* J Phys Chem B, 2009. **113**(17): p. 5951-60.
161. Laurence, C., J. Legros, A. Chantzis, A. Planchat, and D. Jacquemin, *A Database of Dispersion-Induction DI, Electrostatic ES, and Hydrogen Bonding alpha 1 and beta 1 Solvent Parameters and Some Applications to the Multiparameter Correlation Analysis of Solvent Effects.* Journal of Physical Chemistry B, 2015. **119**(7): p. 3174-3184.
162. Schnupf, U., J.L. Willett, W.B. Bosma, and F.A. Momany, *DFT study of alpha- and beta-D-allopyranose at the B3LYP/6-311++G ** level of theory.* Carbohydr Res, 2007. **342**(2): p. 196-216.
163. Khajehzadeh, M. and M. Moghadam, *Molecular structure, FT IR, NMR, UV, NBO and HOMO-LUMO of 1-(3-(dimethylamino)propyl)-1-(4-fluorophenyl)-1,3-dihydroisobenzofuran-5-carboni trile by DFT/B3LYP and PBEPBE methods with LanL2DZ and 6-311++G(d,2p) basis sets.* Spectrochim Acta A Mol Biomol Spectrosc, 2017. **180**: p. 51-66.
164. Mahmood, A., S.U.D. Khan, and F.U. Rehman, *Assessing the quantum mechanical level of theory for prediction of UV/Visible absorption spectra of some aminoazobenzene dyes.* Journal of Saudi Chemical Society, 2015. **19**(4): p. 436-441.
165. Jacquemin, D., E.A. Perpete, G.E. Scuseria, I. Ciofini, and C. Adamo, *TD-DFT performance for the visible absorption spectra of organic dyes: Conventional versus long-range hybrids.* Journal of Chemical Theory and Computation, 2008. **4**(1): p. 123-135.
166. Lee, M.H., J.H. Han, J.H. Lee, N. Park, R. Kumar, C. Kang, and J.S. Kim, *Two-Color Probe to Monitor a Wide Range of pH Values in Cells.* Angewandte Chemie-International Edition, 2013. **52**(24): p. 6206-6209.
167. Tian, J.W., L. Ding, H.J. Xu, Z. Shen, H.X. Ju, L. Jia, L. Bao, and J.S. Yu, *Cell-Specific and pH-Activatable Rubyrin-Loaded Nanoparticles for Highly Selective Near-Infrared Photodynamic Therapy against Cancer.* Journal of the American Chemical Society, 2013. **135**(50): p. 18850-18858.
168. Shi, W., X.H. Li, and H.M. Ma, *A Tunable Ratiometric pH Sensor Based on Carbon Nanodots for the Quantitative Measurement of the Intracellular pH of Whole Cells.* Angewandte Chemie International Edition, 2012. **51**(26): p. 6432-6435.
169. Tang, B., F. Yu, P. Li, L.L. Tong, X. Duan, T. Xie, and X. Wang, *A Near-Infrared Neutral pH Fluorescent Probe for Monitoring Minor pH Changes: Imaging in Living HepG2 and HL-7702 Cells.* Journal of the American Chemical Society, 2009. **131**(8): p. 3016-3023.
170. Wang, F.L., R.G. Widejko, Z.Q. Yang, K.T. Nguyen, H.Y. Chen, L.P. Fernando, K.A. Christensen, and J.N. Anker, *Surface-Enhanced Raman Scattering Detection of pH with Silica-Encapsulated 4-Mercaptobenzoic Acid-Functionalized Silver Nanoparticles.* Analytical Chemistry, 2012. **84**(18): p. 8013-8019.
171. Cao, Y., R.C. Qian, D.W. Li, and Y.T. Long, *Raman/fluorescence dual-sensing and imaging of intracellular pH distribution.* Chemical Communications, 2015. **51**(99): p. 17584-17587.
172. Hou, H., Y.Y. Zhao, C.P. Li, M.M. Wang, X.L. Xu, and Y.D. Jin, *Single-cell pH imaging and detection for pH profiling and label-free rapid identification of cancer-cells.* Scientific Reports, 2017. **7**.

173. Casey, J.R., S. Grinstein, and J. Orlowski, *Sensors and regulators of intracellular pH.* Nature Reviews Molecular Cell Biology, 2010. **11**(1): p. 50-61.
174. Srivastava, J., D.L. Barber, and M.P. Jacobson, *Intracellular pH sensors: Design principles and functional significance.* Physiology, 2007. **22**: p. 30-39.
175. Webb, B.A., M. Chimenti, M.P. Jacobson, and D.L. Barber, *Dysregulated pH: a perfect storm for cancer progression.* Nature Reviews Cancer, 2011. **11**(9): p. 671-677.
176. Wan, Q.Q., S.M. Chen, W. Shi, L.H. Li, and H.M. Ma, *Lysosomal pH Rise during Heat Shock Monitored by a Lysosome-Targeting Near-Infrared Ratiometric Fluorescent Probe.* Angewandte Chemie-International Edition, 2014. **53**(41): p. 10916-10920.
177. Chen, S.J., Y.N. Hong, Y. Liu, J.Z. Liu, C.W.T. Leung, M. Li, R.T.K. Kwok, E.G. Zhao, J.W.Y. Lam, Y. Yu, and B.Z. Tang, *Full-Range Intracellular pH Sensing by an Aggregation-Induced Emission-Active Two-Channel Ratiometric Fluorogen.* Journal of the American Chemical Society, 2013. **135**(13): p. 4926-4929.
178. Hulikova, A., A.L. Harris, R.D. Vaughan-Jones, and P. Swietach, *Regulation of intracellular pH in cancer cell lines under normoxia and hypoxia.* Journal of Cellular Physiology, 2013. **228**(4): p. 743-752.

Appendices

A1. Copyright Statement

I warrant that I have obtained, where necessary, permission from the copyright owners to use any third party copyright material reproduced in the thesis (such as artwork, images, unpublished documents), or to use any of my own published work (such as journal articles) in which the copyright is held by another party (such as publisher, co-author).

Signed:

Muhammad Khattab

A2. Subject to Permission from the Publisher

Copyright

Describes the rights related to the publication and distribution of research. It governs how authors (as well as their employers or funders), publishers and the wider general public can use, publish and distribute articles or books.

Journal author rights | Government employees | Elsevier's rights | Protecting author rights | Open access

Journal author rights

In order for Elsevier to publish and disseminate research articles, we need publishing rights. This is determined by a publishing agreement between the author and Elsevier. This agreement deals with the transfer or license of the copyright to Elsevier and authors retain significant rights to use and share their own published articles. Elsevier supports the need for authors to share, disseminate and maximize the impact of their research and these rights, in Elsevier proprietary journals* are defined below:

For subscription articles	For open access articles
Authors transfer copyright to the publisher as part of a journal publishing agreement, but have the right to: • Share their article for Personal Use, Internal Institutional Use and Scholarly Sharing purposes, with a DOI link to the version of record on ScienceDirect (and with the Creative Commons CC-BY-NC- ND license for author manuscript versions) • Retain patent, trademark and other intellectual property rights (including research data). • Proper attribution and credit for the published work.	Authors sign an exclusive license agreement, where authors have copyright but license exclusive rights in their article to the publisher**. In this case authors have the right to: • Share their article in the same ways permitted to third parties under the relevant user license (together with Personal Use rights) so long as it contains a CrossMark logo, the end user license, and a DOI link to the version of record on ScienceDirect. • Retain patent, trademark and other intellectual property rights (including research data). • Proper attribution and credit for the published work.

***Please note that society or third party owned journals may have different publishing agreements. Please see the journal's guide for authors for journal specific copyright information.**

****This includes the right for the publisher to make and authorize commercial use, please see "Rights granted to Elsevier" for more details.**

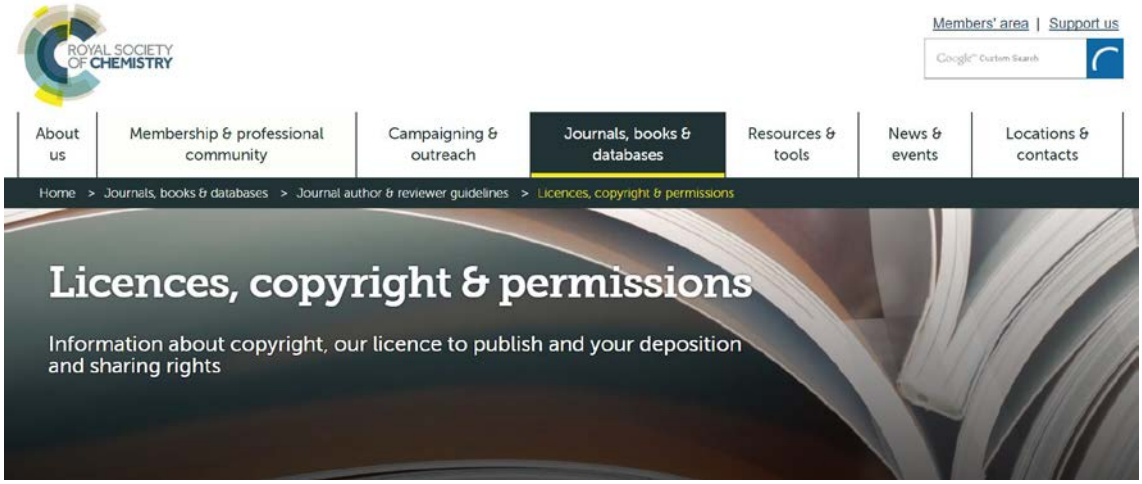

Author reusing their own work published by the Royal Society of Chemistry

You do not need to request permission to reuse your own figures, diagrams, etc, that were originally published in a Royal Society of Chemistry publication. However, permission should be requested for use of the whole article or chapter except if reusing it in a thesis. If you are including an article or book chapter published by us in your thesis please ensure that your co-authors are aware of this.

Reuse of material that was published originally by the Royal Society of Chemistry must be accompanied by the appropriate acknowledgement of the publication. The form of the acknowledgement is dependent on the journal in which it was published originally, as detailed in 'Acknowledgements'.

SWINBURNE UNIVERSITY OF TECHNOLOGY

Swinburne Research

Authorship Indication Form

For PhD (including associated papers) candidates

NOTE

This Authorship Indication form is a statement detailing the percentage of the contribution of each author in each associated 'paper'. This form must be signed by each co-author and the Principal Coordinating Supervisor. This form must be added to the publication of your final thesis as an appendix. Please fill out a separate form for each associated paper to be included in your thesis.

DECLARATION

We hereby declare our contribution to the publication of the 'paper' entitled:

UV–Vis spectroscopy and solvatochromism of the tyrosine kinase inhibitor AG-1478

First Author

Name: **Muhammad Khattab** Signature: Muhammad

Percentage of contribution: **80%** Date: 19/01/2018

Brief description of contribution to the 'paper' and your central responsibilities/role on project:
Conception/design of experiments, data collection/analysis and drafting the article

Second Author

Name: **Feng Wang** Signature:

Percentage of contribution: **10%** Date: 19/01/2018

Brief description of your contribution to the 'paper':
Designing/supervision of research and critical revision/final approval of the article to be published

Third Author

Name: **Andrew H.A. Clayton** Signature:

Percentage of contribution: **10%** Date: 23/01/2018

Brief description of your contribution to the 'paper':
Designing/supervision of research and critical revision/final approval of the article to be published

Fourth Author

Name: _____ Signature: _____

Percentage of contribution: ____% Date: __/__/____

Brief description of your contribution to the 'paper':

Principal Coordinating Supervisor Name: **Andrew Clayton** Signature:

Date: 23/01/2018

In the case of more than four authors please attach another sheet with the names, signatures and contribution of the authors.

SWINBURNE UNIVERSITY OF TECHNOLOGY

Swinburne Research

Authorship Indication Form

For PhD (including associated papers) candidates

NOTE

This Authorship Indication form is a statement detailing the percentage of the contribution of each author in each associated 'paper'. This form must be signed by each co-author and the Principal Coordinating Supervisor. This form must be added to the publication of your final thesis as an appendix. Please fill out a separate form for each associated paper to be included in your thesis.

DECLARATION

We hereby declare our contribution to the publication of the 'paper' entitled:

Two Conformers of a Tyrosine Kinase Inhibitor (AG-1478) Disclosed Using Simulated UV-Vis Absorption Spectroscopy

First Author

Name: **Muhammad Khattab** Signature: Muhammad

Percentage of contribution: **80%** Date: 19/01/2018

Brief description of contribution to the 'paper' and your central responsibilities/role on project:
Conception/design of experiments, data collection/analysis and drafting the article

Second Author

Name: **Subhojyoti Chatterjee** Signature: Chatterjee

Percentage of contribution: **5%** Date: 21/11/2017

Brief description of your contribution to the 'paper':
As an expert user of Gaussian software, he taught the first author how to use Gaussian for doing theoretical calculations

Third Author

Name: **Andrew H.A. Clayton** Signature:

Percentage of contribution: **5%** Date: 23/01/2018

Brief description of your contribution to the 'paper':
Critical revision/final approval of the article to be published

Fourth Author

Name: **Feng Wang** Signature:

Percentage of contribution: **10%** Date: 19/01/2018

Brief description of your contribution to the 'paper':
Designing/supervision of research and critical revision/final approval of the article to be published

Principal Coordinating Supervisor Name: **Andrew Clayton** Signature:

Date: 23/01/2018

In the case of more than four authors please attach another sheet with the names, signatures and contribution of the authors.

SWINBURNE UNIVERSITY OF TECHNOLOGY

Swinburne Research

Authorship Indication Form

For PhD (including associated papers) candidates

NOTE

This Authorship Indication form is a statement detailing the percentage of the contribution of each author in each associated 'paper'. This form must be signed by each co-author and the Principal Coordinating Supervisor. This form must be added to the publication of your final thesis as an appendix. Please fill out a separate form for each associated paper to be included in your thesis.

DECLARATION

We hereby declare our contribution to the publication of the 'paper' entitled:

Micro-Solvation of Tyrosine-Kinase Inhibitor AG1478 Explored with Fluorescence Spectroscopy and Computational Chemistry

First Author

Name: **Muhammad Khattab** Signature: Muhammad

Percentage of contribution: **80%** Date: 19/01/2018

Brief description of contribution to the 'paper' and your central responsibilities/role on project:
Conception/design of experiments, data collection/analysis and drafting the article

Second Author

Name: **Feng Wang** Signature:

Percentage of contribution: **10%** Date: 19/01/2018

Brief description of your contribution to the 'paper':
Designing/supervision of research and critical revision/final approval of the article to be published

Third Author

Name: **Andrew H.A. Clayton** Signature:

Percentage of contribution: **10%** Date: 23/01/2018

Brief description of your contribution to the 'paper':
Designing/supervision of research and critical revision/final approval of the article to be published

Fourth Author

Name: _____ Signature: _____

Percentage of contribution: ____% Date: __/__/____

Brief description of your contribution to the 'paper':

Principal Coordinating Supervisor Name: **Andrew Clayton** Signature:

Date: 23/01/2018

In the case of more than four authors please attach another sheet with the names, signatures and contribution of the authors.

SWINBURNE UNIVERSITY OF TECHNOLOGY

Swinburne Research

Authorship Indication Form

For PhD (including associated papers) candidates

NOTE

This Authorship Indication form is a statement detailing the percentage of the contribution of each author in each associated 'paper'. This form must be signed by each co-author and the Principal Coordinating Supervisor. This form must be added to the publication of your final thesis as an appendix. Please fill out a separate form for each associated paper to be included in your thesis.

DECLARATION

We hereby declare our contribution to the publication of the 'paper' entitled:

A pH-induced conformational switch in a tyrosine kinase inhibitor identified by electronic spectroscopy and quantum chemical calculations

First Author

Name: **Muhammad Khattab** Signature: Muhammad

Percentage of contribution: **80%** Date: 19/01/2018

Brief description of contribution to the 'paper' and your central responsibilities/role on project:
Conception/design of experiments, data collection/analysis and drafting the article

Second Author

Name: **Feng Wang** Signature:

Percentage of contribution: **10%** Date: 19/01/2018

Brief description of your contribution to the 'paper':
Designing/supervision of research and critical revision/final approval of the article to be published

Third Author

Name: **Andrew H.A. Clayton** Signature:

Percentage of contribution: **10%** Date: 23/01/2018

Brief description of your contribution to the 'paper':
Designing/supervision of research and critical revision/final approval of the article to be published

Fourth Author

Name: _____ Signature: _____

Percentage of contribution: ____% Date: __/__/____

Brief description of your contribution to the 'paper':

Principal Coordinating Supervisor Name: **Andrew Clayton** Signature:

Date: 23/01/2018

In the case of more than four authors please attach another sheet with the names, signatures and contribution of the authors.

SWINBURNE UNIVERSITY OF TECHNOLOGY

Swinburne Research

Authorship Indication Form

For PhD (including associated papers) candidates

NOTE

This Authorship Indication form is a statement detailing the percentage of the contribution of each author in each associated 'paper'. This form must be signed by each co-author and the Principal Coordinating Supervisor. This form must be added to the publication of your final thesis as an appendix. Please fill out a separate form for each associated paper to be included in your thesis.

DECLARATION

We hereby declare our contribution to the publication of the 'paper' entitled:

Solvatochromism and linear solvation energy relationship of the kinase inhibitor SKF86002

First Author

Name: **Muhammad Khattab** Signature: Muhammad

Percentage of contribution: **80%** Date: 19/01/2018

Brief description of contribution to the 'paper' and your central responsibilities/role on project:
Conception/design of experiments, data collection/analysis and drafting the article

Second Author

Name: **Madeline Van Dongen** Signature: MVDongen

Percentage of contribution: **5%** Date: 20/11/2017

Brief description of your contribution to the 'paper':
Performing theoretical calculations recommended by manuscript reviewers

Third Author

Name: **Feng Wang** Signature:

Percentage of contribution: **5%** Date: 19/01/2018

Brief description of your contribution to the 'paper':
Critical revision/final approval of the article to be published

Fourth Author

Name: **Andrew H.A. Clayton** Signature:

Percentage of contribution: **10%** Date: 23/01/2018

Brief description of your contribution to the 'paper':
Designing/supervision of research and critical revision/final approval of the article to be published

Principal Coordinating Supervisor Name: **Andrew Clayton** Signature:

Date: 23/01/2018

In the case of more than four authors please attach another sheet with the names, signatures and contribution of the authors.

SWINBURNE UNIVERSITY OF TECHNOLOGY

Swinburne Research

Authorship Indication Form

For PhD (including associated papers) candidates

NOTE

This Authorship Indication form is a statement detailing the percentage of the contribution of each author in each associated 'paper'. This form must be signed by each co-author and the Principal Coordinating Supervisor. This form must be added to the publication of your final thesis as an appendix. Please fill out a separate form for each associated paper to be included in your thesis.

DECLARATION

We hereby declare our contribution to the publication of the 'paper' entitled:

Exploring optical reporting characteristics of drugs: UV-Vis spectra and conformation of tyrosine kinase inhibitor SKF86002

First Author

Name: **Madeline Van Dongen** Signature: MVDongen

Percentage of contribution: **50%** Date: 20/11/2017

Brief description of contribution to the 'paper' and your central responsibilities/role on project:
Conception/design of computations and data collection/analysis

Second Author

Name: **Muhammad Khattab** Signature: Muhammad

Percentage of contribution: **30%** Date: 19/01/2018

Brief description of your contribution to the 'paper':
Drafting the article and helping in experiments

Third Author

Name: **Andrew H.A. Clayton** Signature:

Percentage of contribution: **10%** Date: 23/01/2018

Brief description of your contribution to the 'paper':
Designing/supervision of research and critical revision/final approval of the article to be published

Fourth Author

Name: **Feng Wang** Signature:

Percentage of contribution: **10%** Date: 19/01/2018

Brief description of your contribution to the 'paper':
Designing/supervision of research and critical revision/final approval of the article to be published

Principal Coordinating Supervisor Name: **Andrew Clayton** Signature:

Date: 23/01/2018

In the case of more than four authors please attach another sheet with the names, signatures and contribution of the authors.

A4. Addendum

- The computational details in the associated manuscripts of **Chapter III**, **IV**, **VI** and **VII** should include the following statement "*The calculated vibrational frequencies showed that all optimized structures are true local minima.*"

- In page 14572 of the second published manuscript in **Chapter VII**, the typo in the value of positive charge in the following phrase should be corrected to be *+0.2e* "Interestingly, the S atoms on the imidazo thiophene ring of the conformers possess a positive charge of above +2.0e".

- The submitted manuscript in **Chapter VI** is now published as **Muhammad Khattab**, Feng Wang and Andrew H.A. Clayton, *Conformational Plasticity in Tyrosine Kinase Inhibitor–Kinase Interactions Revealed with Fluorescence Spectroscopy and Theoretical Calculations*, J. Phys. Chem. B 122 (2018), 4667−79.

THE JOURNAL OF PHYSICAL CHEMISTRY B

Article

Cite This: J. Phys. Chem. B 2018, 122, 4667−4679

pubs.acs.org/JPCB

Conformational Plasticity in Tyrosine Kinase Inhibitor−Kinase Interactions Revealed with Fluorescence Spectroscopy and Theoretical Calculations

Muhammad Khattab,[†] Feng Wang,*[,‡] and Andrew H. A. Clayton*[,†]

[†]Centre for Micro-Photonics, Faculty of Science, Engineering and Technology, and [‡]Molecular Model Discovery Laboratory, Department of Chemistry and Biotechnology, Engineering and Technology, Swinburne University of Technology, Melbourne, Victoria 3122, Australia

Supporting Information

ABSTRACT: To understand drug−protein dynamics, it is necessary to account for drug molecular flexibility and binding site plasticity. Herein, we exploit fluorescence from a tyrosine kinase inhibitor, AG1478, as a reporter of its conformation and binding site environment when complexed with its cognate kinase. Water-soluble kinases, aminoglycoside phosphotransferase APH(3′)-Ia and mitogen-activated protein kinase 14 (MAPK14), were chosen for this study. On the basis of our prior work, the AG1478 conformation (planar or twisted) was inferred from the fluorescence excitation spectrum and the polarity of the AG1478-binding site was deduced from the fluorescence emission spectrum, while red-edge excitation shift (REES) probed the heterogeneity of the binding site (protein conformation and hydration) distributions in the protein conformational ensemble. In the AG1478−APH(3′)-Ia complex, both twisted (or partially twisted) and planar AG1478 conformations were evidenced from emission wavelength-dependent excitation spectra. The binding site environment provided by APH(3′)-Ia was moderately polar (λ_{max} = 480 nm) with evidence for considerable heterogeneity (REES = 34 nm). In contrast, in the AG1478−MAPK14 complex, AG1478 was in a predominantly planar conformation with a lower degree of conformational heterogeneity. The binding site environment provided by the MAPK14 protein was of relatively low polarity (λ_{max} = 430 nm) with a smaller degree of heterogeneity (REES = 11 nm). The results are compared with the available X-ray data and discussed in the context of our current understanding of tyrosine kinase inhibitor conformation and protein conformational ensembles.

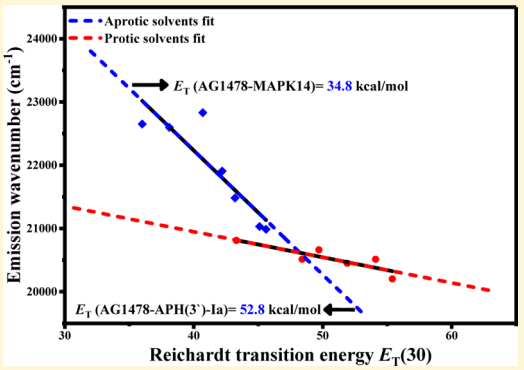

1. INTRODUCTION

Kinase conformational plasticity is a paramount factor for understanding ligand binding, enzymatic switching, and biological function. Kinases were found to adopt an extensive array of conformations in their crystal structures.[1,2] Flexibility of the activation loop regulates substrate/inhibitor access to the ATP-binding site; hence, conformational perturbations in a part or in a whole of kinase structure would alter kinase activity.[3,4] Upon binding of a kinase inhibitor to the target protein, a perturbation of dynamic ensemble of kinase conformations and biased stabilization of distinct conformation(s) can take place.[5] For instance, epidermal growth factor receptor (EGFR) plasticity enables it to accommodate gefitinib in multiple conformations. Gefitinib exhibits 20-fold higher affinity to the active conformation of the mutant EGFR than to the wild type.[6,7] Similarly, binding of ATP-competitive inhibitors to mitogen-activated protein kinase (MAPK14) is modulated through conformationally selective inhibition.[8,9] Therefore, many patients develop resistance against ATP-competitive kinase inhibitors because of conformational/hydrophobicity changes in the kinase gatekeeper triggered by single-point mutation. These changes were found to introduce steric clashes for an inhibitor to access and bind to the gatekeeper.[10]

The domain motion at the hinge region (gatekeeper) is in fact constrained unless the kinase is phosphorylated.[11] Upon phosphorylation, conformational changes of the target protein that precede ligand binding impede or accelerate the inhibitor−receptor association. The free-energy landscape (FEL) model of a protein structure defines the molecular heterogeneity as an array of equilibrated energetic minima on a multidimensional free-energy surface.[12] Proteins exhibiting various conformational states have a rugged FEL; hence, understanding how FEL is altered upon agonist/inhibitor binding is crucial for modulating the biological/remedial function of a protein.[13]

Identifying inhibitors that target distinct conformation is a cumbersome task and requires detailed conformational analysis of the inhibitor and protein-binding site.[5] Several approaches are extensively applied to address this problem such as fluorescent labels in kinases (FLiK),[14−19] optical second-

Received: February 12, 2018
Revised: April 8, 2018
Published: April 9, 2018

DOI: 10.1021/acs.jpcb.8b01530
J. Phys. Chem. B 2018, 122, 4667−4679

harmonic generation,[20−22] NMR residual dipolar coupling,[23] and surface plasmon resonance studies.[24,25] In the FLiK method, a fluorophore that is a reporter to its local environment is exploited to probe kinase conformational changes.[5] All the aforementioned techniques are used as a binding assay for in vitro studies. However, for studying changes in drug conformations and medium heterogeneity in solution, red-edge excitation shift (REES) measurements have been widely applied in the literature for solutions of drug−protein complexes.[13,26−29]

Steady-state REES spectroscopy is a reliable quantitative measure for protein FEL and conformational equilibria of ligand−protein complexes.[13] REES is a phenomenon where low-energy excitation beam selectively excites discrete fluorophore molecules, hence potentially reflecting the conformational equilibrium of a fluorophore and its binding site.[28,30] REES is observed depending on the rate of solvent relaxation during excitation and the triggered changes in a fluorophore dipole moment following excitation. The emission wavelength becomes independent of the excitation wavelength when the environmental relaxation is faster than the fluorescence lifetime. However, in a rigid environment, the delayed solvent relaxation causes a blue-shifted fluorescence spectrum when excited in the blue region because of the emission from the solvent-unrelaxed excited state of the fluorophore, whereas a red-shifted emission is observed when the fluorophore is excited in the red region because of the emission from the solvent-relaxed state. Therefore, REES can be observed with fluorophores in viscous or cooled solutions or complexed with a folded protein state.[31,32] Hence, REES is a powerful tool for tackling contemporary challenges in biophysics and structural biology.

On the other hand, it has been revealed that small molecules do not necessarily adopt the global minimum conformation upon binding to their receptors.[33−35] Analyses of myriad ligand−protein cocrystals have reportedly demonstrated that many of the ligand molecules do not even adopt the local minima structures.[36,37] Data from a library of 100 ligand−protein crystals showed that bound ligand structures are nearly identical to the local minima conformations.[38]

Aminoglycoside phosphotransferases are a group of enzymes responsible for phosphorylation/activation of aminoglycoside antibiotics.[39,40] Many studies have been concerned with characterization of interaction modes between enzymes, nucleotide substrates, and aminoglycosides. Detailed analyses revealed structural conservation of nucleotide triphosphate, ATP or GTP, binding site in the studied aminoglycoside phosphotransferases.[41−45] A high structural similarity of nucleotide triphosphate-binding site was noted between aminoglycoside phosphotransferases and eukaryotic protein kinases.[46] Therefore, the inhibition potential of protein kinase inhibitors has been tested against aminoglycoside phosphotransferases.[46,47] One of these studies was conducted using AG1478 as a potential inhibitor for aminoglycoside phosphotransferase APH(3′)-Ia.[46]

AG1478 (Figure 1) is a tyrosine kinase inhibitor,[48−50] and its electronic and conformational properties have been studied by our group.[51−54] Our studies revealed that the medium pH, polarity, and hydration significantly affect AG1478 conformation. We have also evaluated the topological and electronic properties of AG1478 under different conditions. Therefore, our earlier results can be exploited to estimate the polarity of the AG1478-binding site and structural flexibility (conformations) of AG1478 when bound to a target protein.

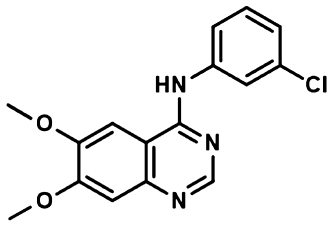

Figure 1. Molecular structure of *N*-(3-chlorophenyl)-6,7-dimethoxyquinazolin-4-amine (AG1478).

In the present work, we probe the binding environment of AG1478 in two proteins. The two proteins are aminoglycoside phosphotransferase and MAPK14. The X-ray crystal structure of aminoglycoside phosphotransferase APH(3′)-Ia in complex with AG1478 and kanamycin has been published previously.[46] Although AG1478 was proven as an inhibitor to MAPK14 (p38-α) through competitive binding to the ATP-binding pocket (IC_{50} = 560 nM),[55] no X-ray data on this complex have been reported. However, the X-ray crystal structure of MAPK14 with MSQ (an AG1478 analogue) has been published.[56]

We aim to examine the conformational plasticity and polarity of the AG1478-binding site utilizing our previous spectroscopic results of AG1478 in various solvents. To this end, we performed steady-state fluorescence spectroscopy including REES measurements. We also conducted analyses for amino acids of the AG1478-binding site using Protein Data Bank (PDB) data such as B-factor. In addition, a comparative theoretical study between different structures of AG1478 in the cocrystal forms deposited in PDB was performed. Our study provides a deep insight into the intrinsic and extrinsic structural and electronic property changes in AG1478 molecules at the ATP-binding site helping to understand the nature of the AG1478-binding pocket.

2. MATERIALS AND METHODS

2.1. Materials. AG1478 was purchased from AdooQ Bioscience. Recombinant *Danio rerio* aminoglycoside phosphotransferase domain-containing protein 1 (APH(3′)-Ia) and MAPK14 isoform 2 (MAPK14) were obtained from MyBioSource, Inc. and used as received. Millipore deionized water was used in reconstitution of proteins. A pair of matched quartz cuvette of a 1 cm path length was purchased from Starna Pty Ltd.

2.2. Methods. *2.2.1. UV−Vis Spectroscopy.* Solutions of the two proteins, APH(3′)-Ia and MAPK14, were prepared according to the manufacturer's instructions. The lyophilized powder of APH(3′)-Ia was reconstituted as specified in the product datasheet by adding 2 mL of deionized water to give a final concentration of 8 μM APH(3′)-Ia. Reconstitution of MAPK14 was performed by adding 1 mL 20 mM Tris−HCl buffer (pH 8.0) to give a concentration of 5 μM MAPK14. We also prepared a 4 mM stock solution of AG1478 in dimethyl sulfoxide. The APH(3′)-Ia−AG1478 complex was formed by adding 3.3 μL of 4 mM AG1478 stock solution to 2 mL of the 8 μM APH(3′)-Ia solution. The MAPK14−AG1478 complex was formed by adding 1.7 μL of 4 mM AG1478 stock solution to 2 mL of the 5 μM MAPK14 solution.

Fluorescence and REES measurements were conducted on a PerkinElmer LS55 spectrophotometer. Fluorescence spectra

DOI: 10.1021/acs.jpcb.8b01530
J. Phys. Chem. B 2018, 122, 4667−4679

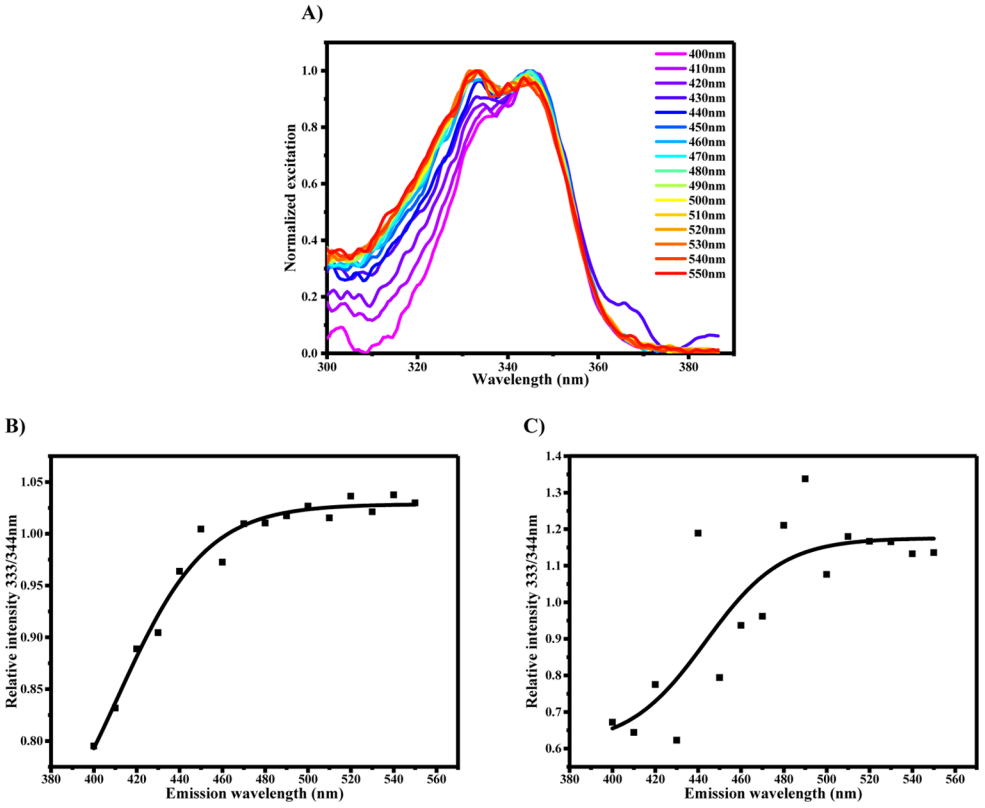

Figure 2. (A) Normalized excitation spectra of the AG1478−APH(3′)-Ia complex scanned at different emission wavelengths (400−550 nm); (B) plot of relative intensity of 333 nm excitation to 344 nm excitation as a function of emission wavelength fitted to the Boltzmann model and (C) plot of relative intensity of resolved 333 and 344 nm bands as a function of emission wavelength obtained from decomposing the experimental spectrum into the sum of three Gaussian bands. The solid line is to guide the eye.

were recorded using a fixed excitation wavelength (in 5 nm intervals in the range of 330−360 nm) and scanning the emission from 400 to 600 nm. Two types of spectral information were obtained from the fluorescence spectra recorded as a function of excitation wavelength. (1) The average fluorescence spectrum was obtained by integrating (or summing up) the individual fluorescence spectra recorded at different excitation wavelengths. (2) REES plots were obtained by plotting the emission maximum of the fluorescence spectrum as a function of the excitation wavelength. Fluorescence excitation spectra were recorded using a fixed emission wavelength (in 10 nm intervals in the range of 400−550 nm) and scanning the excitation from 300 to 390 nm. The temperature (10−37 °C) of the sample was regulated using PerkinElmer Peltier temperature programmer PTP-1. All spectra were corrected for background scattering from proteins and buffer. Fluorescence maxima, spectra averaging, and error bars were obtained using OriginLab software. Normalized spectra were produced by normalizing the wavelength maximum of excitation and emission to one.

2.2.2. Computational Details. Structure coordinates were downloaded from PDB http://www.rcsb.org. The missing hydrogen on the nitrogen-linking quinazoline to the anilino moiety was added using GaussView software. Energy optimization was performed only for the added hydrogen while keeping all other atoms frozen. Five entries of AG1478 [four X-ray resolved structures + one calculated structure (entry 5)] were used with no further geometry optimization for calculating the excitation spectrum. Time-dependent density functional theory (TD-DFT)[57] was used for excitation energy calculation using the same model and basis set employed for AG1478 in our previous published studies.[52−54] Becke three-parameter Lee−Yang−Parr hybrid functional[58,59] in combination with the 6-311+G* basis set and a conductor-like polarizable continuum model[60] were employed in all calculations. Dielectric continuum of water (ε = 78.3) was used to approximately describe the polarity of the AG1478 environment. We used the dielectric continuum of water as approximation for the AG1478 environment because our earlier results showed trivial changes in excitation energy calculations with varying the dielectric constant of the implicit model.[52] The UV−vis excitation (absorption) spectra of AG1478 structures were calculated for the singlet−singlet transitions of the lowest 60 excited states. All simulations were performed using Gaussian 09 revision C.01[61] on Swinburne supercomputing facilities.

3. RESULTS

3.1. Spectroscopy Study. *3.1.1. AG1478−Aminoglycoside Phosphotransferase Complex.* Our previous work reported that the UV−vis spectrum of AG1478 in solution consisted of two bands in the 300−360 nm region, one at 330 nm attributed to the planar conformer of AG1478 and the other at 340 nm attributed to the twisted conformer.[52] To determine the distribution of twisted versus planar conformer of AG1478 when bound to a protein kinase, we measured the excitation spectra of the AG1478−APH(3′)-Ia complex in a buffer solution of pH 8 as a function of emission wavelength. The excitation spectrum of the AG1478−APH(3′)-Ia complex consisted primarily of two bands, one at 333 nm and the other

DOI: 10.1021/acs.jpcb.8b01530
J. Phys. Chem. B 2018, 122, 4667−4679

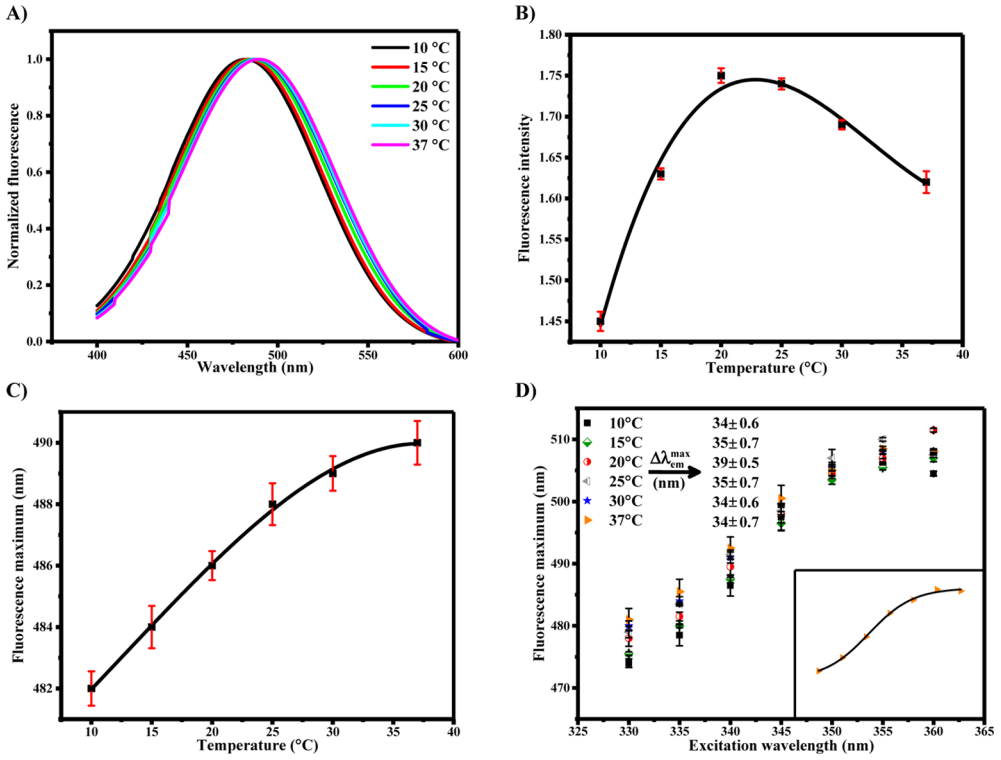

Figure 3. (A) Normalized summed spectra for all emissions of the AG1478−APH(3′)-Ia complex obtained by exciting at 330, 335, 340, 345, 350, 355, and 360 nm at six different temperatures. (B,C) Plots of fluorescence intensity and fluorescence maximum as a function of temperature. The solid line is to ease data point tracking. (D) Plot of fluorescence maximum as a function of excitation wavelength of the AG1478−APH(3′)-Ia complex recorded at different temperatures. Error bars are obtained from three replications. The inset indicates fitting of a selected plot to Boltzmann function. $\Delta\lambda_{em}^{max}$ defines the shift of the emission maximum at λ_{exc} = 360 nm relative to that obtained from λ_{exc} = 330 nm.

at 344 nm, as expected. However, the relative proportion of the two band intensities was dependent on the monitoring wavelength of emission. A significant change (i.e., by greater than 30%) in the relative intensity of 333 and 344 nm can be seen in the normalized excitation spectra depicted in Figure 2a and in the plot of the ratio of the two band intensities shown in Figure 2b. Deconvolution of the excitation spectra into the sum of three Gaussian bands revealed similar trends in the relative contributions of the 333 and 344 nm bands (Figure 2c). These results reveal that AG1478 exists in different conformations within the ensemble of proteins. In the context of our prior work, our results could be interpreted as the twisted conformer being dominant relative to the planar conformer near the blue edge of the emission (400−450 nm), while both conformers contribute to the emission nearly equally from 460 to 550 nm.

Our prior work also revealed the exquisite sensitivity of the fluorescence emission of AG1478 to solution polarity.[51] We use this sensitivity here to examine the environmental heterogeneity and dynamics provided by the protein close to the AG1478 moiety in the protein-binding pocket.

Integrated fluorescence spectra of the AG1478−APH(3′)-Ia complex are shown in Figure 3a recorded at several temperatures, and information about the intensity of emission and position of the emission maximum is depicted in Figure 3b,c. Interestingly, the intensity of fluorescence increased from 10 to 15 to 20 °C but then decreased from 20 to 30 to 37 °C. A decrease in fluorescence due to an increase in temperature is expected based on an increase in the nonradiative rates of deactivation from the excited state or dynamic quenching processes. An increase in fluorescence with temperature is unusual but was reported by us previously for the AG1478−water complex in acetonitrile/water solutions because of a release of static quenching.[53] This unorthodox temperature dependence of emission could be tentatively explained by both static and dynamic quenching mechanisms in the binding site of the protein or a temperature-dependent conformational change. However, we note that more work is needed to properly explain this behavior. The wavelength of emission maximum revealed an increasing shift by 8 nm with increasing temperature from 10 to 37 °C. This could result from an increase in solvent relaxation around the probe with increasing temperature, or alternatively, an increase in the hydration of the binding pocket with increasing temperature. To distinguish these two possibilities, we turn to REES measurements to gain an idea about the relative dynamics of the protein around the AG1478 probe, the relative dynamics of the excited state, and the nature of the protein FEL sensed by the AG1478 probe.

Emission spectra were recorded as a function of excitation wavelength in the range of 330−360 nm. The results are depicted in Figure 3d. It is remarkable that the emission spectrum is highly dependent on the excitation wavelength with shifts exceeding 30 nm. A slight increase in REES magnitude was observed upon changing temperature from 10 and 15 to 20 °C, but a decrease was observed from 20 to 25 until reaching a plateau. Aside from the measurements at 20 °C, the REES measurement was nearly independent of temperature. An increase in dynamics of the protein with temperature should increase solvent relaxation giving a red-shifted emission but a smaller REES value; however, the temperature appears to affect the emission wavelength but not the REES value. This could be explained when the temperature increases; the hydration of the binding site is also increased (because of a conformational

DOI: 10.1021/acs.jpcb.8b01530
J. Phys. Chem. B 2018, 122, 4667−4679

Table 1. Boltzmann Fitting Parameters Calculated from the Observed Emission of the AG1478−APH(3′)-Ia Complex at Different Temperatures

	10 °C	15 °C	20 °C	25 °C	30 °C	37 °C
A_1	473.4 ± 1.8	473.1 ± 0.9	473.1 ± 3.5	477.1 ± 3.5	478.2 ± 0.8	478.2 ± 1.5
A_2	506.1 ± 1.0	507.5 ± 0.5	512.3 ± 2.0	509.7 ± 1.8	508.8 ± 0.4	509.0 ± 0.7
x_0	341.3 ± 0.7	341.4 ± 0.3	342.0 ± 1.1	341.3 ± 1.3	341.4 ± 0.3	340.6 ± 0.6
dx	3.3 ± 0.6	4.5 ± 0.3	5.9 ± 1.3	4.3 ± 1.3	4.2 ± 0.3	4.7 ± 0.6

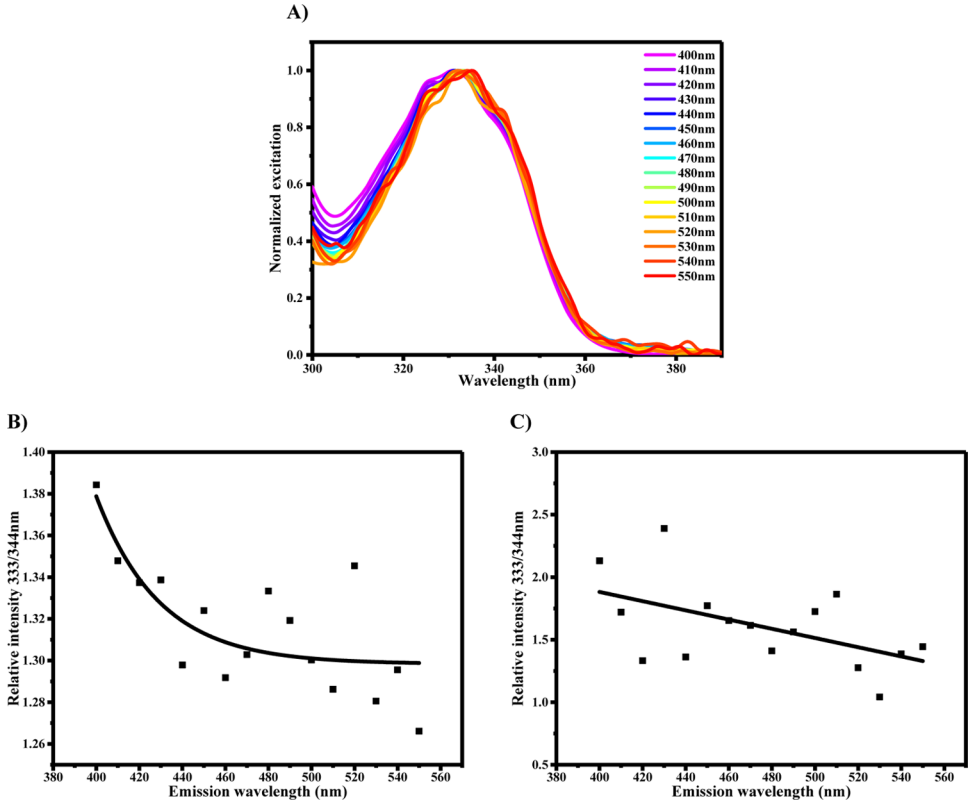

Figure 4. (A) Normalized excitation spectra of AG1478 bound to MAPK14 in Tris buffer solution recorded at different emission wavelengths (400−550 nm). (B) Plot of relative intensity of 333 and 344 nm bands as a function of emission wavelength. The solid line is used to guide the reader's eye. (C) Plot of relative intensity of 333/344 nm bands as a function of emission wavelength obtained from decomposing the experimental spectrum into the sum of three Gaussian bands. The solid line is to guide the eye.

change opening up the binding pocket), but the dynamics of the protein matrix is too slow to cause significant solvent relaxation about the AG1478 chromophore during the excited-state lifetime. A temperature-insensitive REES is consistent with a rugged landscape of the FEL sensed by the AG1478 probe.

It was found that REES data fit well (R^2 = 0.99) with a Boltzmann model $A = A_2 + \frac{A_1 - A_2}{1 + \exp^{(x-x_0)/dx}}$, where A stands for the measured fluorescence, A_1 for the minimum value for λ_{max}, A_2 for the maximum value for λ_{max}, x for the excitation wavelength, x_0 for the excitation wavelength value at the midpoint between the maximum and minimum values of fluorescence maximum, and dx for the width in nanometer of the most significant change in fluorescence. The calculated parameters from the fitting of the AG1478−APH(3′)-Ia complex fluorescence to the Boltzmann model are summarized in Table 1. We noticed that the increase in temperature yielded increase in the minimum and maximum emission wavelength (A_1 and A_2) values. However, REES magnitude was almost constant (around 34 nm) insensitive to temperature change.

3.1.2. AG1478−MAPK14 Complex. The excitation spectra of AG1478 in the AG1478−MAPK14 complex are depicted in Figure 4a. The predominant band is at 330 nm consistent with a predominant planar conformation of AG1478 in the AG1478−MAPK14 complex. The 340 nm band appears as a shoulder in the excitation spectrum. The relative proportion of the two bands is slightly dependent on the emission observation wavelength, varying from 1.26 to 1.38 or by 10% across the range of emission as shown in Figure 4b. The same trend in relative amplitude was observed using deconvoluted Gaussian bands, as shown in Figure 4c. This suggests some degree of conformational heterogeneity of AG1478 in the population of protein−drug complexes.

The emission spectrum of AG1478 in the AG1478−MAPK14 complex revealed an emission maximum near 427 nm at all temperatures examined (Figure 5a). Increase in temperature resulted in a decrease in emission from AG1478 consistent with conventional dynamic-type quenching processes (Figure 5b). However, the position of the emission spectrum only changed slightly from 427 nm at 15 °C to 426 nm at 37 °C (Figure 5c). Taken together, these results suggest that the binding site for AG1478 in MAPK14 is relatively low in polarity.

DOI: 10.1021/acs.jpcb.8b01530
J. Phys. Chem. B 2018, 122, 4667−4679

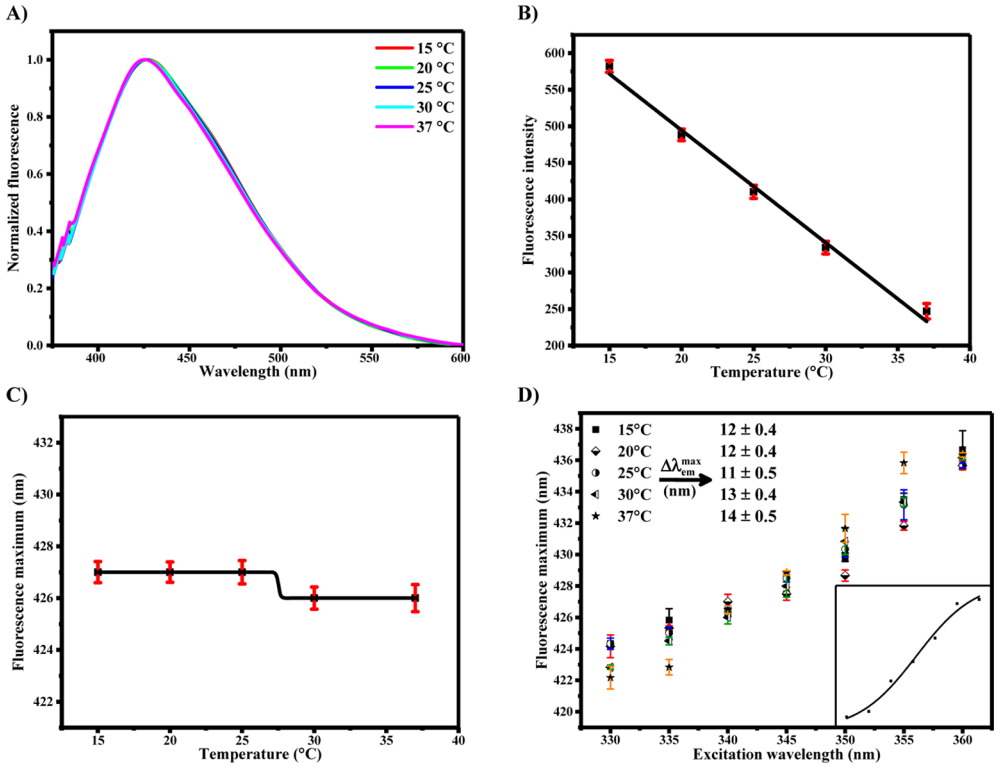

Figure 5. (A) Normalized summed spectra for all emissions obtained by exciting at 315, 320, 325, 330, 335, 340, 345, 350, 355, and 360 nm at six different temperatures. (B,C) Plots of fluorescence intensity and fluorescence maximum as a function of temperature. The solid line is to guide the reader's eye. (D) Plot showing fluorescence maximum of AG1478 bound to MAPK14 in Tris buffer solution as a function of excitation wavelength. Error bars are obtained from three replications. The inset indicates fitting of a selected plot to Boltzmann function. $\Delta\lambda_{em}^{max}$ defines the shift of emission maximum at λ_{exc} = 360 nm relative to that obtained from λ_{exc} = 330 nm.

Table 2. Boltzmann Fitting Parameters Calculated from the Observed Emission of the AG1478−MAPK14 Complex at Different Temperatures

	15 °C	20 °C	25 °C	30 °C	37 °C
A_1	424.2 ± 0.9	423.2 ± 0.8	422.8 ± 0.8	419.1 ± 2.0	420.5 ± 2.3
A_2	446.3 ± 11.2	444.7 ± 5.6	442.9 ± 4.1	450.1 ± 9.8	438.6 ± 2.6
x_0	357.9 ± 7.6	355.3 ± 1.1	354.5 ± 3.5	357.2 ± 7.2	345.8 ± 2.0
dx	7.7 ± 3.1	6.2 ± 1.3	9.5 ± 2.2	13.8 ± 4.4	6.6 ± 2.7

The REES experiments on AG1478−MAPK14 revealed an interesting behavior, as shown in Figure 5d. The magnitude of the REES was only 11−14 nm, and a slight increase in REES was observed upon heating the solutions. These observations are consistent with a rugged FEL; however, we interpret the smaller REES and blue emission compared to the AG1478−APH(3′)-Ia complex owing to a reduced polarity of the binding site in MAPK14. The existence of significant REES could be due to water molecules in an otherwise nonpolar binding pocket.

We also found that the REES data of AG1478−MAPK14 fit well (R^2 = 0.99) to the Boltzmann model. The calculated parameters from the fitting of the AG1478−MAPK14 complex fluorescence to the Boltzmann model are summarized in Table 2. In contrast to the data of the AG1478−APH(3′)-Ia complex, we noticed a decrease in A_1 and A_2 values with the increase in temperature. In the next section, we make a quantitative estimation of the binding site polarity of the two proteins.

3.1.3. Estimation of Binding Site Polarity Using a Reichardt E_T(30) Scale. In our earlier published work,[51] the emission energy of AG1478 fluorescence in hydrogen-donating and aprotic solvents exhibited a good correlation with a Reichardt transition energy E_T(30) scale. It is well-known that the Reichardt model takes into account both the solvent polarity and hydrogen bonding strength.[62−64] Therefore, we herein exploited our published model to determine E_T(30) of the AG1478-binding site within APH(3′)-Ia and MAPK14 proteins. By extrapolating the best fit model of AG1478 in aprotic solvents and using the maximum emission wavelength of the AG1478−protein complex (λ_{exc} = 350) at 25 °C, we obtained E_T(30) of 52.8 and 34.8 kcal/mol for AG1478 bound to APH(3′)-Ia and MAPK14, respectively. These values mean that the colligative properties of the AG1478-binding site in APH(3′)-Ia and MAPK14 closely resemble *N*-methylformamide and 1,4-dioxane, respectively. However, we could not use the AG1478-protic model to estimate E_T(30) of AG1478 in complex with the two proteins. This is because extrapolation of the fit line lies below the minimum value of the extreme nonpolar solvent (trimethylsilane) E_T(30) = 30.7 kcal/mol and the maximum value of the most polar solvent (water) E_T(30) = 63.1 kcal/mol (Figure 6).

3.2. Computational Study Comparison with X-ray Crystallography Models. *3.2.1. Average Conformation of AG1478.* The two lowest energy excitation maxima were

DOI: 10.1021/acs.jpcb.8b01530
J. Phys. Chem. B 2018, 122, 4667−4679

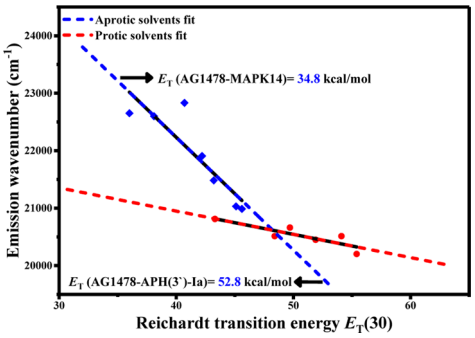

Figure 6. Emission wavenumber of AG1478 in cm^{-1} as a function of Reichardt transition energy E_T(30) in kcal/mol of AG1478 in two sets of solvents, aprotic and protic, adopted from ref 51. Extrapolation of fitted lines is done to calculate E_T(30) of the AG1478−APH(3′)-Ia and AG1478−MAPK14 complexes. AG1478−APH(3′)-Ia and AG1478−MAPK14 emit at 430 and 507 nm, respectively, using λ_{exc} = 350 at 25 °C. The figure is reproduced from ref 51.

calculated for the five entries of AG1478 coordinates downloaded from PDB for AG1478 (PDB ID: 0TO) complexed with APH(3′)-Ia (PDB ID: 4FEX). The topological difference between AG1478 structures is due to the difference in torsional angle between quinazoline and aniline moiety. In spite of small variations in dihedral angle, a significant difference in excitation maxima was calculated as indicated in Table 3. The lowest energy excitation maximum was computed within the 348−364 nm range, while the second transition was calculated at 335−350 nm. The experimental excitation spectrum maxima of the AG1478−APH(3′)-Ia complex were observed at 333 and 344 nm. By comparing the excitation spectra maxima of our experiment and entry 4 structure, we noticed a good agreement between our experimental results and the calculated excitation maxima for the obtained X-ray crystal structure (entry 4). The observed lowest energy transition and the second transition in the AG1478−APH(3′)-Ia complex are shifted by 4 and 2 nm to the blue region relative to entry 4.

We noticed that the entry 5 structure is substantially different from AG1478 X-ray structures regarding its geometrical and electronic properties as indicated in Table 3. Although the entry 5 structure represents the most energy-minimized structure (global minimum), it is far likely to be populated in the AG1478−APH(3′)-Ia crystal. Only one major electronic transition was calculated in the 300−360 nm range which cannot account for the experimental spectrum. By examining the oscillator strength and the main molecular orbital contribution to the electronic transitions within the four X-ray entries, entry 4 showed distinct electronic characteristics. In contrary to all other entries, the oscillator strength of the lowest energy transition is lower than that of the higher energy transition. In addition, the molecular orbital contribution to the two electronic transitions is quite different in entry 4 from other entries (refer to Table 3). Calculations revealed that the highest occupied molecular orbital − 1 → lowest unoccupied molecular orbital transition in entry 4 contributes to the first and second electronic excitations unlike in other entries. By taking entry 1 energy as a reference, energy calculations showed that the entry 5 structure is the most energetically stable structure, whereas entry 2 < entry 4 < entry 3 are less stable than entry 1 in the same order.

3.2.2. Heterogeneity of AG1478 Conformations. We searched for anilinoquinazoline-based compounds deposited in PDB to scrutinize the coplanarity between quinazoline core and aniline moiety in this family of active compounds. Compound name, protein name, and torsional angle between quinazoline and aniline rings for every PDB entry structure are compiled in Supporting Information Table S1. Four out of 39 PDB entries showed a torsional angle less than 10°, indicating that the planar conformation is not favored and that the twisted conformation is the conformationally favored protein-bound structure for anilinoquinazoline class kinase inhibitors. The four X-ray entries of AG1478 exhibited torsional angles in the range of (−10.1°)−(−15.7°), revealing the existence of AG1478 in twisted conformations at the ATP-binding pocket of the APH(3′)-Ia protein. The same finding was obtained from our experimental excitation spectra (Figure 2a,b). The structural heterogeneity of AG1478 may also contribute to the observed REES, that is, if different conformers have distinct absorbance and emission spectra.

Occupancy and temperature (Debye−Waller) factors are essential parameters to evaluate X-ray crystals. Occupancy factor has values ranging from 0 to 1, where values closest to 1 indicate a precise positioning of atoms in the crystal. The temperature factor is defined as the mean-square displacement of an atom from its position in the model. It is an isotropic measure of static and dynamic disorders within the crystal. The static disorder is mainly due to different conformations of the

Table 3. Comparison of Excitation Maxima and Torsional Angle Calculated for AG1478 Structures Retrieved from PDB (Four Experimental Entries + One Calculated Entry)[65]

PDB entries		entry 1	entry 2	entry 3	entry 4	entry 5
	torsion angle	−15.1	−13.5	−15.7	−10.1	32.8
	excit. max. (nm)	341/351	350/364	346/357	**335/348**	338
	osc. str.	0.1718/0.1894	0.1542/0.2048	0.1195/0.2529	0.2733/0.1214	0.3834
	e-transition (L)[a]	H → L (61%)	H → L (68%)	H → L (74%)	H − 1 → L (53%)	H → L (89%)
		H − 2 → L (26%)	H − 2 → L (27%)	H − 2 → L (17%)	H → L (42%)	
	e-transition (H)[b]	H → L (36%)	H − 2 → L (62%)	H − 2 → L (57%)	H → L (54%)	
		H − 2 → L (31%)	H → L (30%)	H → L (23%)	H − 1 → L (39%)	
		H − 3 → L (18%)		H − 4 → L (13%)		
	ΔE (kcal/mol)[c]	0.00	1.97	11.21	7.53	−28.62
exp. (AG1478−APH(3′)-Ia)[d]	excit. max. (nm)	**333/344**				

[a]Electronic transitions encountered in the lowest energy excitation maximum. [b]Electronic transitions encountered in the second lowest energy excitation maximum. [c]Change in molecular energy relative to entry 1. [d]Observed excitation maxima of AG1478 bound to aminoglycoside phosphotransferase.

DOI: 10.1021/acs.jpcb.8b01530
J. Phys. Chem. B 2018, 122, 4667−4679

Table 4. Occupancy and Temperature (B-Factor) Values in (Å^2) for Nonhydrogen Atoms of Four Copies of AG1478 (PDB: 0TO) Obtained from Its X-ray Cocrystal with APH(3′)-Ia (PDB: 4FEX)

	entry 1		entry 2		entry 3		entry 4	
atom type	occupancy	B-factor	occupancy	B-factor	occupancy	B-factor	occupancy	B-factor
C	0.74	62.84	0.79	76.27	0.83	72.47	0.87	78.62
C	0.74	74.15	0.79	81.74	0.83	88.69	0.87	85.47
Cl	0.74	82.11	0.79	86.89	0.83	89.30	0.87	80.81
C	0.74	67.68	0.79	76.13	0.83	77.89	0.87	65.99
C	0.74	75.27	0.79	76.93	0.83	82.56	0.87	74.35
C	0.74	76.06	0.79	73.40	0.83	77.80	0.87	72.86
C	0.74	62.77	0.79	76.79	0.83	66.75	0.87	63.67
N	0.74	54.99	0.79	74.21	0.83	63.06	0.87	53.42
C	0.74	62.28	0.79	73.97	0.83	63.93	0.87	58.36
N	0.74	60.25	0.79	65.33	0.83	64.95	0.87	52.88
C	0.74	55.94	0.79	63.48	0.83	57.57	0.87	56.73
N	0.74	50.00	0.79	68.53	0.83	53.70	0.87	50.11
C	0.74	56.84	0.79	65.70	0.83	56.09	0.87	61.68
C	0.74	46.34	0.79	62.61	0.83	51.54	0.87	50.99
C	0.74	60.87	0.79	71.06	0.83	63.39	0.87	59.11
C	0.74	65.60	0.79	78.53	0.83	68.24	0.87	64.08
O	0.74	77.28	0.79	74.87	0.83	63.66	0.87	78.97
C	0.74	63.77	0.79	64.95	0.83	73.05	0.87	67.21
C	0.74	67.93	0.79	77.49	0.83	67.50	0.87	60.73
C	0.74	60.66	0.79	67.43	0.83	54.74	0.87	50.91
O	0.74	63.72	0.79	65.02	0.83	66.57	0.87	66.83
C	0.74	55.00	0.79	73.98	0.83	56.82	0.87	59.74
average		64		72		67		64
rms (Å)		0.91		0.96		0.93		0.91

drug in different unit cells of the protein, whereas the dynamic disorder originates from the atomic vibrations and translocations in the crystal. Lattice defects, restraints, and model errors contribute also to the calculation of temperature factor.[66−68] Although the X-ray crystal resolution is 2.71 Å and data collection was performed at the temperature of 100 K, it was noted that individual and average values of the temperature factor are greater than 50 Å^2 (root-mean-square deviation (rmsd) > 0.90 Å), indicating a high structural disorder (heterogeneity) of AG1478 atoms within the protein-binding site (refer to Table 4). It is in agreement with our experimental excitation spectra because the structural flexibility of AG1478 atoms points out the existence of multiple conformations of AG1478 in two proteins accounting for the change in the relative intensity of 333 and 344 nm excitation bands as a function of emission wavelength.

The 4-anilinoquinazoline compound (PDB-ID: MSQ) complexed with MAPK14 (PDB-ID: 1DI9) showed an occupancy value of 1 for all of its atoms as depicted in Supporting Information Table S2. The average temperature factor value is 28 Å^2 (rmsd 0.60 Å), indicating the presence of MSQ, hence possibly for AG1478, in a more rigid (less disordered) environment than with APH(3′)-Ia (PDB-ID: 4FEX).

3.2.3. Average Polarity of the AG1478-Binding Site from X-ray Data. Five structurally and functionally identical copies comprise the asymmetric unit of aminoglycoside phosphotransferase APH(3′)-Ia. These copies are named chains A, B, C, D, and E. Four different copies of AG1478 were resolved from chains A, C, D, and E. A trivial change in amino acid (aa) sequence was noted at the AG1478-binding site. The aa sequence similarity relative to the binding site within chain A is given in Table 5. Although the binding site within four chains is

Table 5. Amino Acid Sequence of the Binding Pocket within Four Chains of Aminoglycoside Phosphotransferase APH(3′)-Ia Involved in Interactions with the Four Entries of AG1478[a]

parameter	chain A	chain C	chain D	chain E
	V33	I40	**D31**	**E51**
	I40	F53	I40	F53
	F53	K55	F53	K55
	K55	E68	K55	E68
	E68	L72	E68	L72
	L72	P82	**L96**	P82
	P82	T98	T98	T98
	T98	T99	T99	T99
	T99	A100	A100	A100
	A100	I101	I101	I101
	I101	G103	**P102**	**P102**
	G103	K104	G103	G103
	K104	T105	K104	K104
	T105	**Q108**	T105	T105
	D202	D202	**Q108**	**Q108**
	I205	I205	I205	D202
	I215	I215	I215	I205
	D216	D216	D216	I215
				D216
sequence similarity	100%	89%	78%	89%
no. of polar aa	8	9	9	10
no. of nonpolar aa	10	9	9	9
no. of waters	1 (flexible)	0	0	1 (restricted)
hydrophobicity[69] (kcal/mol)	−0.26	−0.29	−0.29	−0.42

[a]Data in bold are for aa not found in chain A. Data are retrieved from PDB.[65]

DOI: 10.1021/acs.jpcb.8b01530
J. Phys. Chem. B 2018, 122, 4667−4679

highly conserved, a small change in binding site polarity, hydration, and hydrophobicity might also be a contributing factor for variations in the excitation maxima of four AG1478 entries if included in calculations. Because molecular dynamics calculations are not within the scope of this work, the interactions between AG1478 and protein are not discussed. Hereafter, we shed the light on some isolated physicochemical properties of the AG1478-binding pocket in various chains of APH(3′)-Ia and in MAPK14 protein.

The binding site in chain A contains 10 nonpolar amino acids and 8 polar amino acids, while chain E is marked with the highest distribution of polar (10) aa relative to 8 nonpolar aa. Chains C and D have equal distribution of polar and nonpolar aa. The AG1478-binding site in chains A and E comprises one molecule of confined water. Water molecules were resolved at the vicinity of methoxy groups and chlorine atom in chains A and E, respectively. The hydrophobicity scale developed by Wimley and White was utilized to calculate the hydrophobicity of the AG1478-binding site. The hydrophobicity parameter (free energy of partitioning of aa) ranges from (1.85) for the most hydrophobic tryptophan to (−2.02) for the most hydrophilic glutamic acid.[69] The midpoint of the scale is at (−0.085). The average hydrophobicity of the binding site amino acid in chain E has a value of (−0.42) which is lower in magnitude than in chain A (−0.26), chain C (−0.29), and chain D (−0.29), indicating that the AG1478-binding site in chain E is significantly more hydrophilic than in other chains. The average hydrophobicity of the AG1478-binding site in chain E was found identical to asparagine (−0.42), whereas the average hydrophobicity of the binding sites in chains A, C, and D is intermediate between alanine (−0.17) and asparagine (−0.42). The polarity deduced from the analysis of the side chains proximal to AG1478 agrees well with our experimentally measured polarity from the AG1478 fluorescence spectrum. The emission maximum of AG1478 in the protein complex was similar to that observed for AG1478 in dimethylformamide and *N*-methylformamide.

X-ray crystallographic data of AG1478 with MAPK14 are not deposited in PDB. Fortunately, we found a structurally similar compound (PDB ID: MSQ), where the chlorine atom of AG1478 is replaced with the methylsulfanyl group, deposited in PDB. Structural analysis of the inhibitor-binding site revealed that the MAPK14 (PDB ID: 1DI9)-binding site is significantly less polar than the APH(3′)-Ia inhibitor-binding site. The ratio of nonpolar to polar amino acids at the inhibitor-binding site is 12:5, as depicted in Table 6. The binding site within MAPK14 is more hydrated than in APH(3′)-Ia. Two confined water molecules were resolved at the vicinity of N(3) and 4-anilino substituent of MSQ. The hydrophobicity scale confirmed that the inhibitor-binding site in the single-chain crystal of MAPK14 is more hydrophobic (−0.18) than in all chains of APH(3′)-Ia. The average hydrophobicity of the binding pocket is closely similar to alanine hydrophobicity (−0.17). This agrees also well with our results where the polarity of the AG1478−MAPK14 complex was estimated lower than the polarity of AG1478−APH(3′)-Ia.

3.2.4. Disorder of the AG1478-Binding Site from the X-ray Structure. It is noteworthy that the majority of aa atoms at the AG1478-binding site in APH(3′)-Ia and MAPK14 are assigned occupancy value of 1. This means the crystal backbone is precisely fortified, whereas the inhibitor (AG1478) atoms are disordered (occupancy factor 0.87−0.74) in APH(3′)-Ia (Table 4). In MAPK14, the inhibitor (MSQ) occupancy factor was equal to 1, indicating precise positioning and restricted movement of the inhibitor within a well-defined binding pocket (Table S2).

Table 6. aa Sequence of the Binding Pocket of Structurally and Functionally Similar Compound to AG1478 (PDB-ID: MSQ) in the MAPK14 Protein[a]

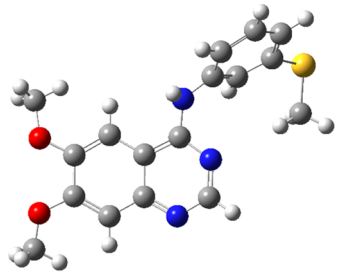

4-[3-Methylsulfanylanilino]-6,7-Dimethoxyquinazoline (MSQ)

parameter	MAPK14
	V30
	G31
	V38
	A51
	V52
	K53
	E71
	L75
	I84
	L104
	V105
	T106
	H107
	L108
	M109
	L167
	D168
no. of polar aa	5
no. of nonpolar aa	12
no. of waters	2
hydrophobicity[69] (kcal/mol)	−0.18

[a]Data are adopted from PDB website.[65]

We examined the B-factor values, deposited in PDB, of aa comprising AG1478-binding site in APH(3′)-Ia and MSQ in MAPK14. The average value of B-factor in APH(3′)-Ia is 52 Å^2 (rmsd > 0.84 Å), indicating a significant structural disorder (heterogeneity) of the AG1478-binding site in APH(3′)-Ia. This structural disorder in the AG1478-binding site could be a factor that contributes to the observed REES. The average value of B-factor for the binding pocket in MAPK14 is estimated at 18 Å^2 (rmsd > 0.47 Å). This value implies slighter structural disorder within the binding site, which might account for the lesser magnitude of REES with AG1478−MAPK14.

We found that amino acids in APH(3′)-Ia have higher B-factor values than in MAPK14 as can be seen in Figure 7; however, the crystal data were collected at the same temperature (100 K) and the resolution was nearly equal (2.71 Å for AG1478−APH(3′)-Ia and 2.60 Å for MSQ−MAPK14). This indicates that the environment around AG1478 in APH(3′)-Ia is more conformationally disordered than for MSQ in MAPK14. While in the case of MAPK14, the vibrational movement of atoms is more constrained. Referring to our experimental results, this can account for the higher REES magnitude in the AG1478−APH(3′)-Ia complex than in

DOI: 10.1021/acs.jpcb.8b01530
J. Phys. Chem. B 2018, 122, 4667−4679

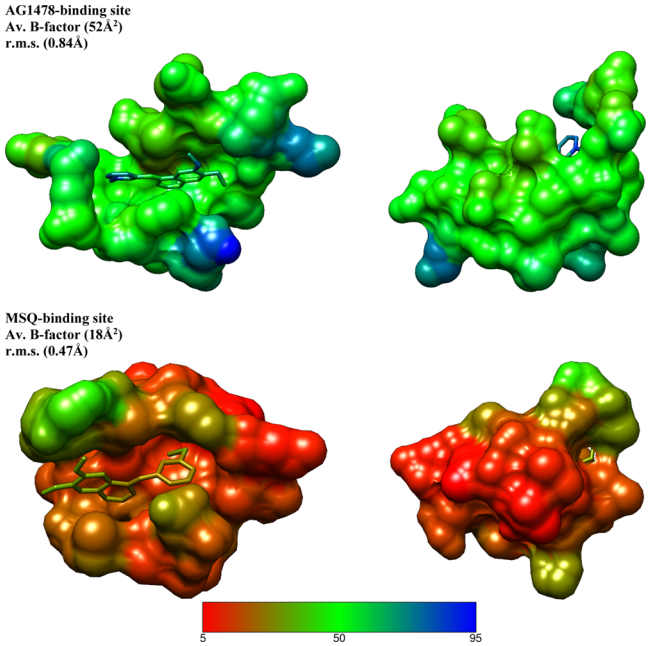

Figure 7. Color map of temperature (B-factor) factor of amino acid residues in the AG1478-binding site in APH(3′)-Ia (upper panel) and the MSQ-binding site in MAPK14 (lower panel).

the AG1478−MAPK14 complex. Because when the medium surrounding AG1478 is more disordered, it somehow reflects increase in environment dynamics which in turn affects the emission process (REES and fluorescence quenching). Overall, binding site polarity and disorder (occupancy factor and B-factor) are both responsible for the red-shifted emission in AG1478−APH(3′)-Ia than in MSQ−MAPK14.

Taking into account that B-factors for protein residues and inhibitor were estimated at 100 K, therefore we expect a higher structural disorder in AG1478 at room temperature (298 K). The higher dynamics of AG1478 molecules would significantly affect the equilibrium between the planar and twisted conformations of AG1478. This would be reflected in the change in relative absorption of 333 and 344 nm peaks in the absorption spectrum of AG1478.

4. DISCUSSION

The conformational states of AG1478, and the environment (structural plasticity and polarity) of the AG1478 protein-binding site in two enzymes, APH(3′)-Ia and MAPK14, were examined using fluorescence spectroscopy techniques. While the observed heterogeneity in fluorescence could, in principle, result from uncomplexed AG1478 species and uncomplexed protein species, the negligible quantum yield of AG1478 in buffer and the excitation wavelengths used (outside tryptophan absorbance) rule out these factors as potential causes of heterogeneity. We compared our fluorescence data with AG1478 conformers proposed in the literature using quantum chemical calculations. We also performed detailed analysis of X-ray data obtained from PDB to unravel polarity, hydrophobicity, and disorder of amino acids constituting the inhibitor-binding site of APH(3′)-Ia and MAPK14. Our analyses on PDB data can be taken as approximations for studying AG1478 conformations and environment in MAPK14 and should be exercised with caution. This is because we used the AG1478 derivative (MSQ) and its binding site on MAPK14 instead of AG1478.

The conformational states of AG1478 were deduced from the fluorescence excitation spectrum of the AG1478 in complex with each protein. In accordance with our prior work, an absorbance near 330 nm is associated with a planar form of AG1478, while the presence of an additional band near 340 nm is evidence for a twisted conformation of AG1478. In the APH(3′)-Ia−AG1478 complex, both transitions were present, which is evidence for some degree of twisting in the AG1478 structure. Comparison of AG148 five conformers from the literature X-ray crystal structures of the APH(3′)-Ia−AG1478 complex revealed that the excitation spectrum from TD-DFT calculations was very sensitive to the AG1478 conformation, as expected. However, we found that one conformer, with a torsional angle of −10.1°, gave a better agreement with the observed wavelength positions of the experimental transitions than the other conformers (with torsional angles of −14, −15, −16, and +33°). Conformational heterogeneity was observed experimentally in APH(3′)-Ia−AG1478 through an emission wavelength-dependent excitation spectrum. Both transitions at 330 and 340 nm persisted as a function of emission wavelength, but their relative amplitudes differed markedly with monitoring emission wavelength. This is evidence that there are multiple conformations of AG1478 in the APH(3′)-Ia−AG1478 complex in solution probably contributed by mixtures of planar and twisted (or slightly twisted) AG1478 structures.

The corresponding fluorescence excitation spectrum of the AG1478−MAPK14 complex differed from the APH(3′)-Ia−AG1478 complex, which is an indication for a different conformation or conformational distribution of AG1478 in the AG1478−MAPK14 complex. On the basis of a relatively larger 330 nm band amplitude compared to the 340 nm band amplitude in the excitation spectrum, we reasoned that the AG1478 conformation is more biased toward the planar conformation in the AG1478−MAPK14 complex. Moreover, the heterogeneity of conformations was less than in the APH(3′)-Ia−AG1478 complex as deduced from the fluorescence excitation spectrum as a function of emission wavelength. Examination of the X-ray B-factors for an AG1478 derivative in complex with MAPK14 showed that the AG1478 derivative was fairly rigid in the binding site, while the corresponding B-factors for AG1478 in the APH(3′)-Ia−AG1478 indicated more conformational disorder. These results suggest that AG1478 can adopt different conformational distributions depending on the target enzyme.

The environment provided by the protein at the AG1478-binding pocket was assessed by several spectroscopic parameters. Polarity was inferred from the wavelength of the emission peak, while a distribution of solvent environments around AG1478 (protein conformations, water) was deduced from REES experiments. The emission from APH(3′)-Ia−AG1478 indicated a moderately polar environment surrounding AG1478, consistent with an analysis of the amino acid side chains comprising the binding site in the APH(3′)-Ia−AG1478 complex. The APH(3′)-Ia−AG1478 complex showed a significant REES of 34−39 nm, indicating a distribution of microenvironments around AG1478 in the protein complex suggestive of multiple conformational states of the protein. This conclusion is supported by the large B-factors in the X-ray crystal structure of the APH(3′)-Ia−AG1478 complex. In contrast to AG1478−MAPK14, the emission was more indicative of a less polar environment around the AG1478, in

DOI: 10.1021/acs.jpcb.8b01530
J. Phys. Chem. B 2018, 122, 4667−4679

good qualitative agreement with an analysis of the amino acid side chains comprising the binding site in an AG1478 derivative in complex with MAPK14. Moreover, the REES observed in AG1478−MAPK14 was markedly less (11−14 nm) than for AG1478−APH(3′)-Ia, perhaps indicating a lower degree of heterogeneity of binding site environments (protein conformational states). This latter conclusion is consistent with the smaller B-factors in the X-ray crystal structure of the AG1478 derivative−MAPK14 complex.

It is important to note that for both AG1478−protein complexes, the REES values were largely independent of temperature over the temperature range examined. In analogy with Demchenko's analysis of tryptophan-containing proteins,[70,71] this suggests that solvent relaxation (i.e., protein) around AG1478 is restricted slightly on the fluorescence timescale of nanoseconds. This is in agreement with other reports of conformational plasticity of kinases. The combined millisecond molecular dynamics with Markov-state models revealed conformational plasticity of the apo kinase domain of Bruton tyrosine kinase.[72] Simulations predicted several conformations for imatinib (a tyrosine kinase inhibitor)-binding site on Abelson tyrosine kinase. It was found that the kinase domain (ATP-binding site) plasticity modulates various landscapes available for binding with ligands. On the basis of free-energy surface calculations, four main populations of the kinase were inferred along with other intermediate states pertaining conformational plasticity to the kinase.[72] The diversity in conformational states of the kinase domain was earlier reported for many tyrosine kinases such as MAPK14,[73] ERK2,[11] aurora kinase A,[74] and protein kinase A.[73] Taken together, these results indicate that the FEL of solvated kinase domain is diffuse (rugged), which agrees well with our REES observations for AG1478 in APH(3′)-Ia and MAPK14.

5. CONCLUSIONS

Our experimental results are consistent with computations and literature, demonstrating reasonable reliability and accuracy of using UV−vis spectroscopy in probing the fluorophore environment. The interplay between our applied methodologies (UV−vis spectroscopy and quantum chemical calculations) introduced a new tool to monitor the spatial and electronic scenes for important class of anticancer drugs in the free and bound forms to target protein.

The plasticity of structural elements of the ATP-binding site is critical for determining the inhibitor conformation and binding mode. The binding interaction of AG1478 with either APH(3′)-Ia or MAPK14 can result in a discrete change in AG1478 conformation on a rugged matrix of protein backbone. Our UV−vis spectra reveal that the interactions between AG1478 and APH(3′)-Ia protein are different from the interactions between AG1478 and MAPK14 protein. The former indicates that AG1478 exists in two distinguishable and competitive conformations at the APH(3′)-Ia-binding pocket. The presence of the conformers of AG1478 shows dependence on the emission wavelength. While in MAPK14-binding site, the AG1478 ligand may experience distortion with more than one conformers which are not very different from the most stable structures, and they are not very much emission-wavelength-dependent. The results suggest that AG1478 binds to the ATP-binding site where conformational selection is protein-dependent. Polarity and hydrophobicity of amino acids at the vicinity of AG1478 play a significant role in determining the AG1478 structure. To this end, our results along with extensive analyses of PDB data pave the way for studying the molecular dynamics of AG1478 binding to the ATP pocket.

■ ASSOCIATED CONTENT

Supporting Information

The Supporting Information is available free of charge on the ACS Publications website at DOI: 10.1021/acs.jpcb.8b01530.

Compound name, protein name, and torsional angle between quinazoline and aniline rings for every PDB entry structure and occupancy factors for atoms in MSQ and AG1478 obtained from PDB databank (PDF)

■ AUTHOR INFORMATION

Corresponding Authors

*E-mail: fwang@swin.edu.au (F.W.).
*E-mail: aclayton@swin.edu.au (A.H.A.C.).

ORCID

Muhammad Khattab: 0000-0002-9086-8983
Feng Wang: 0000-0002-6584-0516
Andrew H. A. Clayton: 0000-0002-6182-3049

Notes

The authors declare no competing financial interest.

■ ACKNOWLEDGMENTS

A.H.A.C. acknowledges the Australian Research Council for partial support of this work. M.K. thanks Swinburne University of Technology for a SUPRA scholarship. F.W. acknowledges supercomputer support from Swinburne University of Technology.

■ REFERENCES

(1) Masterson, L. R.; Cheng, C.; Yu, T.; Tonelli, M.; Kornev, A.; Taylor, S. S.; Veglia, G. Dynamics Connect Substrate Recognition to Catalysis in Protein Kinase A. *Nat. Chem. Biol.* **2010**, *6*, 821−828.

(2) Huse, M.; Kuriyan, J. The Conformational Plasticity of Protein Kinases. *Cell* **2002**, *109*, 275−282.

(3) Endicott, J. A.; Noble, M. E. M.; Johnson, L. N. The Structural Basis for Control of Eukaryotic Protein Kinases. *Annu. Rev. Biochem.* **2012**, *81*, 587−613.

(4) Kar, G.; Keskin, O.; Gursoy, A.; Nussinov, R. Allostery and Population Shift in Drug Discovery. *Curr. Opin. Pharmacol.* **2010**, *10*, 715−722.

(5) Tong, M.; Seeliger, M. A. Targeting Conformational Plasticity of Protein Kinases. *ACS Chem. Biol.* **2015**, *10*, 190−200.

(6) Yun, C.-H.; Boggon, T. J.; Li, Y.; Woo, M. S.; Greulich, H.; Meyerson, M.; Eck, M. J. Structures of Lung Cancer-Derived EGFR Mutants and Inhibitor complexes: Mechanism of Activation and Insights into Differential Inhibitor Sensitivity. *Cancer Cell* **2007**, *11*, 217−227.

(7) Stamos, J.; Sliwkowski, M. X.; Eigenbrot, C. Structure of the Epidermal Growth Factor Receptor Kinase Domain Alone and in Complex with a 4-Anilinoquinazoline Inhibitor. *J. Biol. Chem.* **2002**, *277*, 46265−46272.

(8) Rodriguez, J.; Crespo, P. Working Without Kinase Activity: Phosphotransfer-Independent Functions of Extracellular Signal-Regulated Kinases. *Sci. Signal.* **2011**, *4*, re3.

(9) Hari, S. B.; Merritt, E. A.; Maly, D. J. Conformation-Selective ATP-Competitive Inhibitors Control Regulatory Interactions and Noncatalytic Functions of Mitogen-Activated Protein Kinases. *Chem. Biol.* **2014**, *21*, 628−635.

(10) Azam, M.; Seeliger, M. A.; Gray, N. S.; Kuriyan, J.; Daley, G. Q. Activation of Tyrosine Kinases by Mutation of the Gatekeeper Threonine. *Nat. Struct. Mol. Biol.* **2008**, *15*, 1109−1118.

DOI: 10.1021/acs.jpcb.8b01530
J. Phys. Chem. B 2018, 122, 4667−4679

(11) Xiao, Y.; Lee, T.; Latham, M. P.; Warner, L. R.; Tanimoto, A.; Pardi, A.; Ahn, N. G. Phosphorylation Releases Constraints to Domain Motion in ERK2. *Proc. Natl. Acad. Sci. U.S.A.* **2014**, *111*, 2506−2511.
(12) Tsai, C.-J.; Ma, B.; Sham, Y. Y.; Kumar, S.; Nussinov, R. Structured Disorder and Conformational Selection. *Proteins Struct. Funct. Genet.* **2001**, *44*, 418−427.
(13) Catici, D. A. M.; Amos, H. E.; Yang, Y.; van den Elsen, J. M. H.; Pudney, C. R. The Red Edge Excitation Shift Phenomenon Can Be Used to Unmask Protein Structural Ensembles: Implications for NEMO-Ubiquitin Interactions. *FEBS J.* **2016**, *283*, 2272−2284.
(14) Yin, D. M.; Hannam, J. S.; Schmitz, A.; Schiemann, O.; Hagelueken, G.; Famulok, M. Studying the Conformation of a Receptor Tyrosine Kinase in Solution by Inhibitor-Based Spin Labeling. *Angew. Chem. Int. Ed.* **2017**, *56*, 8417−8421.
(15) Wang, L.; Yan, X.; Su, X. A Label-Free and Sensitive Fluorescent Assay for One Step Detection of Protein Kinase Activity and Inhibition. *Anal. Chim. Acta* **2016**, *935*, 224−230.
(16) Pezzato, C.; Zaramella, D.; Martinelli, M.; Pieters, G.; Pagano, M. A.; Prins, L. J. Label-Free Fluorescence Detection of Kinase Activity Using a Gold Nanoparticle Based Indicator Displacement Assay. *Org. Biomol. Chem.* **2015**, *13*, 1198−1203.
(17) Zhou, F.; Wang, G.; Shi, D.; Sun, Y.; Sha, L.; Qiu, Y.; Zhang, X. One-Strand Oligonucleotide Probe for Fluorescent Label-Free "Turn-On" Detection of T4 Polynucleotide Kinase Activity and its Inhibition. *Analyst* **2015**, *140*, 5650−5655.
(18) Simard, J. R.; Getlik, M.; Grütter, C.; Pawar, V.; Wulfert, S.; Rabiller, M.; Rauh, D. Development of a Fluorescent-Tagged Kinase Assay System for the Detection and Characterization of Allosteric Kinase Inhibitors. *J. Am. Chem. Soc.* **2009**, *131*, 13286−13296.
(19) Simard, J. R.; Grütter, C.; Pawar, V.; Aust, B.; Wolf, A.; Rabiller, M.; Wulfert, S.; Robubi, A.; Klüter, S.; Ottmann, C.; Rauh, D. High-Throughput Screening to Identify Inhibitors Which Stabilize Inactive Kinase Conformations In p38 Alpha. *J. Am. Chem. Soc.* **2009**, *131*, 18478−18488.
(20) Butko, M. T.; Moree, B.; Mortensen, R. B.; Salafsky, J. Detection of Ligand-Induced Conformational Changes In Oligonucleotides by Second-Harmonic Generation at a Supported Lipid Bilayer Interface. *Anal. Chem.* **2016**, *88*, 10482−10489.
(21) Salafsky, J. S. Detection of Protein Conformational Change by Optical Second-Harmonic Generation. *J. Chem. Phys.* **2006**, *125*, 074701.
(22) Nucciotti, V.; Stringari, C.; Sacconi, L.; Vanzi, F.; Fusi, L.; Linari, M.; Piazzesi, G.; Lombardi, V.; Pavone, F. S. Probing Myosin Structural Conformation in Vivo by Second-Harmonic Generation Microscopy. *Proc. Natl. Acad. Sci. U.S.A.* **2010**, *107*, 7763−7768.
(23) Vajpai, N.; Strauss, A.; Fendrich, G.; Cowan-Jacob, S. W.; Manley, P. W.; Grzesiek, S.; Jahnke, W. Solution Conformations and Dynamics of ABL Kinase-Inhibitor Complexes Determined by NMR Substantiate the Different Binding Modes of Imatinib/Nilotinib and Dasatinib. *J. Biol. Chem.* **2008**, *283*, 18292−18302.
(24) Kitagawa, D.; Gouda, M.; Kirii, Y. Quick evaluation of Kinase Inhibitors by Surface Plasmon Resonance Using Single-Site Specifically Biotinylated Kinases. *J. Biomol. Screen* **2014**, *19*, 453−461.
(25) Navratilova, I.; Macdonald, G.; Robinson, C.; Hughes, S.; Mathias, J.; Phillips, C.; Cook, A. Biosensor-Based Approach to the Identification of Protein Kinase Ligands with Dual-Site Modes of Action. *J. Biomol. Screen* **2012**, *17*, 183−193.
(26) Moradi, N.; Ashrafi-Kooshk, M. R.; Chamani, J.; Shackebaei, D.; Norouzi, F. Separate and Simultaneous Binding of Tamoxifen and Estradiol to Human Serum Albumin: Spectroscopic and Molecular Modeling Investigations. *J. Mol. Liq.* **2018**, *249*, 1083−1096.
(27) Abdollahpour, N.; Soheili, V.; Saberi, M. R.; Chamani, J. Investigation of the Interaction Between Human Serum Albumin and Two Drugs as Binary and Ternary systems. *Eur. J. Drug Metab. Pharmacokinet.* **2016**, *41*, 705−721.
(28) Chattopadhyay, A.; Haldar, S. Dynamic Insight into Protein Structure Utilizing Red Edge Excitation Shift. *Acc. Chem. Res.* **2014**, *47*, 12−19.
(29) Guha, S.; Rawat, S. S.; Chattopadhyay, A.; Bhattacharyya, B. Tubulin Conformation and Dynamics: A red edge excitation shift study. *Biochemistry* **1996**, *35*, 13426−13433.
(30) Demchenko, A. P. The Red-Edge Effects: 30 Years of Exploration. *Luminescence* **2002**, *17*, 19−42.
(31) Weber, G.; Shinitzky, M. Failure of Energy Transfer between Identical Aromatic Molecules on Excitation at the Long Wave Edge of the Absorption Spectrum. *Proc. Natl. Acad. Sci. U.S.A.* **1970**, *65*, 823.
(32) Galley, W. C.; Purkey, R. M. Role of Heterogeneity of Solvation Site in Electronic Spectra in Solution. *Proc. Natl. Acad. Sci. U.S.A.* **1970**, *67*, 1116.
(33) Kuzmanic, A.; Sutto, L.; Saladino, G.; Nebreda, A. R.; Gervasio, F. L.; Orozco, M. Changes in the Free-Energy Landscape of p38 Alpha MAP Kinase Through its Canonical Activation and Binding Events as Studied by Enhanced Molecular Dynamics Simulations. *Elife* **2017**, *6*, No. e22175.
(34) Yu, S.; Park, J. G.; Kahn, J. N.; Tumer, N. E.; Pang, Y.-P. Common Pharmacophore of Structurally Distinct Small-Molecule Inhibitors of Intracellular Retrograde Trafficking of Ribosome Inactivating Proteins. *Sci. Rep.* **2013**, *3*, 3397.
(35) Price, S. L. Predicting Crystal Structures of Organic Compounds. *Chem. Soc. Rev.* **2014**, *43*, 2098−2111.
(36) Perola, E.; Charifson, P. S. Conformational Analysis of Drug-Like Molecules Bound to Proteins: An Extensive Study of Ligand Reorganization Upon Binding. *J. Med. Chem.* **2004**, *47*, 2499−2510.
(37) Nicklaus, M. C.; Wang, S.; Driscoll, J. S.; Milne, G. W. A. Conformational Changes of Small Molecules Binding to Proteins. *Bioinorg. Med. Chem.* **1995**, *3*, 411−428.
(38) Wang, Q.; Pang, Y.-P. Preference of Small Molecules for Local Minimum Conformations When Binding to Proteins. *PLoS One* **2007**, *2*, No. e820.
(39) Shi, K.; Berghuis, A. M. Structural Basis for Dual Nucleotide Selectivity of Aminoglycoside 2′-Phosphotransferase IVa Provides Insight On Determinants of Nucleotide Specificity of Aminoglycoside Kinases. *J. Biol. Chem.* **2012**, *287*, 13094−13102.
(40) Toth, M.; Chow, J. W.; Mobashery, S.; Vakulenko, S. B. Source of Phosphate in the Enzymic Reaction as a Point of Distinction Among Aminoglycoside 2′-phosphotransferases. *J. Biol. Chem.* **2009**, *284*, 6690−6696.
(41) Fong, D. H.; Xiong, B.; Hwang, J.; Berghuis, A. M. Crystal Structures of Two Aminoglycoside Kinases Bound with a Eukaryotic Protein Kinase Inhibitor. *PLoS One* **2011**, *6*, No. e19589.
(42) Stogios, P. J.; Shakya, T.; Evdokimova, E.; Savchenko, A.; Wright, G. D. Structure and Function of APH(4)-Ia, a Hygromycin B Resistance Enzyme. *J. Biol. Chem.* **2011**, *286*, 1966−1975.
(43) Toth, M.; Frase, H.; Antunes, N. T.; Smith, C. A.; Vakulenko, S. B. Crystal Structure and Kinetic Mechanism of Aminoglycoside Phosphotransferase-2′-IVa. *Protein Sci.* **2010**, *19*, 1565−1576.
(44) Nurizzo, D.; Shewry, S. C.; Perlin, M. H.; Brown, S. A.; Dholakia, J. N.; Fuchs, R. L.; Deva, T.; Baker, E. N.; Smith, C. A. The Crystal Structure of Aminoglycoside-3′-phospho-transferase-IIa, an Enzyme Responsible for Antibiotic Resistance. *J. Mol. Biol.* **2003**, *327*, 491−506.
(45) Hon, W.-C.; McKay, G. A.; Thompson, P. R.; Sweet, R. M.; Yang, D. S. C.; Wright, G. D.; Berghuis, A. M. Structure of an Enzyme Required for Aminoglycoside Antibiotic Resistance Reveals Homology to Eukaryotic Protein Kinases. *Cell* **1997**, *89*, 887−895.
(46) Stogios, P. J.; Spanogiannopoulos, P.; Evdokimova, E.; Egorova, O.; Shakya, T.; Todorovic, N.; Capretta, A.; Wright, G. D.; Savchenko, A. Structure-Guided Optimization of Protein Kinase Inhibitors Reverses Aminoglycoside Antibiotic Resistance. *Biochem. J.* **2013**, *454*, 191−200.
(47) Shakya, T.; Stogios, P. J.; Waglechner, N.; Evdokimova, E.; Ejim, L.; Blanchard, J. E.; McArthur, A. G.; Savchenko, A.; Wright, G. D. A Small Molecule Discrimination Map of the Antibiotic Resistance Kinome. *Chem. Biol.* **2011**, *18*, 1591−1601.
(48) Weglicki, W. B.; Kramer, J. H.; Spurney, C. F.; Chmielinska, J. J.; Mak, I. T. The EGFR Tyrosine Kinase Inhibitor Tyrphostin AG-1478

DOI: 10.1021/acs.jpcb.8b01530
J. Phys. Chem. B 2018, 122, 4667−4679

Causes Hypomagnesemia and Cardiac dysfunction. *Can. J. Physiol. Pharmacol.* **2012**, *90*, 1145−1149.
(49) Shushan, A.; Rojansky, N.; Laufer, N.; Klein, B. Y.; Shlomai, Z.; Levitzki, R.; Hartzstark, Z.; Ben-Bassat, H. The AG1478 Tyrosine Kinase Inhibitor is an Effective Suppressor of Leiomyoma Cell Growth. *Hum. Reprod.* **2004**, *19*, 1957−1967.
(50) Zhu, X.-F.; Liu, Z.-C.; Xie, B.-F.; Li, Z.-M.; Feng, G.-K.; Yang, D.; Zeng, Y.-X. EGFR Tyrosine Kinase Inhibitor AG1478 Inhibits Cell Proliferation and Arrests Cell Cycle in Nasopharyngeal Carcinoma Cells. *Canc. Lett.* **2001**, *169*, 27−32.
(51) Khattab, M.; Wang, F.; Clayton, A. H. A. UV−Vis Spectroscopy and Solvatochromism of the Tyrosine Kinase Inhibitor AG-1478. *Spectrochim. Acta Mol. Biomol. Spectrosc.* **2016**, *164*, 128−132.
(52) Khattab, M.; Chatterjee, S.; Clayton, A. H. A.; Wang, F. Two Conformers of a Tyrosine Kinase Inhibitor (AG-1478) Disclosed Using Simulated UV-Vis Absorption Spectroscopy. *New J. Chem.* **2016**, *40*, 8296−8304.
(53) Khattab, M.; Wang, F.; Clayton, A. H. A. Micro-Solvation of Tyrosine-Kinase Inhibitor AG1478 Explored with Fluorescence Spectroscopy and Computational Chemistry. *RSC Adv.* **2017**, *7*, 31725−31735.
(54) Khattab, M.; Wang, F.; Clayton, A. H. A. A pH-Induced Conformational Switch in a Tyrosine Kinase Inhibitor Identified by Electronic Spectroscopy and Quantum Chemical Calculations. *Sci. Rep.* **2017**, *7*, 16271.
(55) Diller, D.; Lin, T.; Metzger, A. The Discovery of Novel Chemotypes of p38 Kinase Inhibitors. *Curr. Top. Med. Chem.* **2005**, *5*, 953−965.
(56) Shewchuk, L.; Hassell, A.; Wisely, B.; Rocque, W.; Holmes, W.; Veal, J.; Kuyper, L. F. Binding Mode of the 4-anilinoquinazoline Class of Protein Kinase Inhibitor: X-ray Crystallographic Studies of 4-Anilinoquinazolines Bound to Cyclin-Dependent Kinase 2 and P38 Kinase. *J. Med. Chem.* **2000**, *43*, 133−138.
(57) Runge, E.; Gross, E. K. U. Density-Functional Theory for Time-Dependent Systems. *Phys. Rev. Lett.* **1984**, *52*, 997−1000.
(58) Becke, A. D. New Mixing of Hartree-Fock and Local Density-Functional Theories. *J. Chem. Phys.* **1993**, *98*, 1372−1377.
(59) Becke, A. D. Density-Functional Thermochemistry. III. The Role of Exact Exchange. *J. Chem. Phys.* **1993**, *98*, 5648−5652.
(60) Cossi, M.; Rega, N.; Scalmani, G.; Barone, V. Energies, Structures, and Electronic Properties of Molecules in Solution with the C-PCM Solvation Model. *J. Comput. Chem.* **2003**, *24*, 669−681.
(61) Frisch, M. J.; Trucks, G. W.; Schlegel, H. B.; Scuseria, G. E.; Robb, M. A.; Cheeseman, J. R.; Scalmani, G.; Barone, V.; Mennucci, B.; Petersson, G. A.; et al. *Gaussian 09*, Revision C.01; Gaussian, Inc.: Wallingford, CT, 2009.
(62) Reichardt, C. Solvatochromic Dyes as Solvent Polarity Indicators. *Chem. Rev.* **1994**, *94*, 2319−2358.
(63) Reichardt, C.; Harbusch-Görnert, E. Pyridinium N-phenoxide Betaines and Their Application For The Characterization of Solvent Polarities. X. Extension, Correction, and New Definition of the ET Solvent Polarity Scale by Application of a Lipophilic Penta-Tert-Butyl-Substituted Pyridinium N-Phenoxide Betaine Dye. *Liebigs Ann. Chem.* **1983**, *1983*, 721−743.
(64) Reichardt, C.; Welton, T. *Solvents and Solvent Effects in Organic Chemistry*; John Wiley & Sons, 2011.
(65) Berman, H. M.; Westbrook, J.; Feng, Z.; Gilliland, G.; Bhat, T. N.; Weissig, H.; Shindyalov, I. N.; Bourne, P. E. The Protein Data Bank. *Nucleic Acids Res.* **2000**, *28*, 235−242.
(66) Wlodawer, A.; Minor, W.; Dauter, Z.; Jaskolski, M. Protein Crystallography for Non-Crystallographers, or How to Get the Best (But Not More) from Published Macromolecular Structures. *FEBS J.* **2008**, *275*, 1−21.
(67) Touw, W. G.; Vriend, G. BDB: Databank of PDB files with Consistent B-factors. *Protein Eng. Des. Sel.* **2014**, *27*, 457−462.
(68) Carugo, O. Correlation Between Occupancy and B Factor of Water Molecules in Protein Crystal Structures. *Protein Eng.* **1999**, *12*, 1021−1024.
(69) Wimley, W. C.; White, S. H. Experimentally Determined Hydrophobicity Scale for Proteins at Membrane Interfaces. *Nat. Struct. Biol.* **1996**, *3*, 842−848.
(70) Demchenko, A. P. Fluorescence Molecular Relaxation Studies of Protein Dynamics—The Probe Binding-Site of Melittin Is Rigid on the Nanosecond Time Scale. *FEBS Lett.* **1985**, *182*, 99−102.
(71) Demchenko, A. P. On the Nanosecond Mobility in Proteins—Edge Excitation Fluorescence Red Shift of Protein-Bound 2-(para-toluidinylnaphthalene)-6-sulfonate. *Biophys. Chem.* **1982**, *15*, 101−109.
(72) Sultan, M. M.; Denny, R. A.; Unwalla, R.; Lovering, F.; Pande, V. S. Millisecond Dynamics of BTK Reveal Kinome-Wide Conformational Plasticity Within the Apo Kinase Domain. *Sci. Rep.* **2017**, *7*, 15604.
(73) Xiao, Y.; Liddle, J. C.; Pardi, A.; Ahn, N. G. Dynamics of Protein Kinases: Insights from Nuclear Magnetic Resonance. *Acc. Chem. Res.* **2015**, *48*, 1106−1114.
(74) Cyphers, S.; Ruff, E. F.; Behr, J. M.; Chodera, J. D.; Levinson, N. M. A Water-Mediated Allosteric Network Governs Activation of Aurora Kinase A. *Nat. Chem. Biol.* **2017**, *13*, 402−408.

DOI: 10.1021/acs.jpcb.8b01530
J. Phys. Chem. B 2018, 122, 4667−4679

Supplementary Information

Conformational Plasticity in TKI-kinase Interactions Revealed with Fluorescence Spectroscopy and Theoretical Calculations

Muhammad Khattab[a], Feng Wang[b*] and Andrew H. A. Clayton[a*]

[a] *Centre for Micro-Photonics, Faculty of Science, Engineering and Technology, Swinburne University of Technology, Melbourne, Victoria, 3122, Australia*

[b] *Molecular Model Discovery Laboratory, Department of Chemistry and Biotechnology, Engineering and Technology, Swinburne University of Technology, Melbourne, Victoria, 3122, Australia*

*Corresponding authors: aclayton@swin.edu.au

fwang@swin.edu.au

Table S1. Ligand and protein names along with the corresponding PDB-ID and torsion angles between quinazoline moiety and aniline group of the reported 4-anilinoquinazoline based tyrosine kinase inhibitors retrieved from protein data bank.[1] Terms between brackets indicate mutation within protein sequence. The red highlights within 2D structure denotes measured torsional angle.

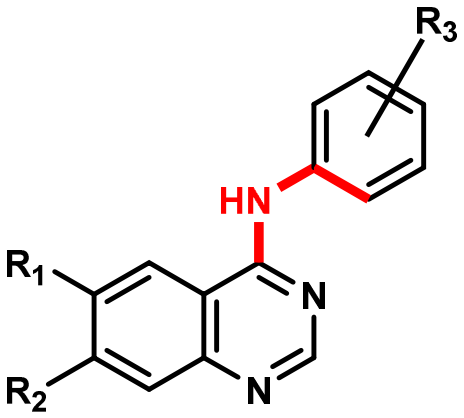

Compound	PDB-ID	Protein	PDB-ID	Torsion angle					
				Entry-1	Entry-2	Entry-3	Entry-4	Entry-5	Entry-6
Afatinib	0WN	EGFR (T790M)	4G5P	12.3	**1.9**				
	0WM	EGFR	4G5J						
AG1478	0TO	APH(3`)-Ia	4FEX	-15.1	-13.5	-15.7	-10.1		
Dacomitinib	1C9	EGFR	4I23	28.5	27.2	44.0			
		EGFR (T790M)	4I24						
Erlotinib	AQ4	EGFR	1M17	41.2	39.5	41.6			
		EGFR (V924R)	4HJO						
Gefitinib	IRE	EGFR (T790M, L858R, V948R)	4I22	52.9	49.1	35.5	35.3	45.7	55.2
		EGFR	4WKQ						
		EGFR (G719S, T790M)	3UG2						
		EGFR (T790M, L858R, V948R)	4I1Z						
		EGFR (G719S)	2ITO						
		EGFR	2ITY						
		EGFR (L858R)	2ITZ						
Lapatinib	FMM	ErbB-4	3BBT	68.1	67.1	55.3			
		EGFR	1XKK						
PD168393	DJK	EGFR (L858R)	4LQM	34.6	30.8	32.8	32.4	**-0.5**	**-0.7**
		EGFR (S345C)	2HWP						
		EGFR (T338M, S345C)	3LOK						
	YUN	EGFR	4LRM						
		EGFR (T790M, L858R)	4LL0						
Sarcatinib	H8H	Myt1	5VCX	52.4	50.4	66.3	52.3		
		Myt1	5VD3						
		MST3	4QMX						
		SRC1	2H8H						
Vandetanib	ZD6	RET	2IVU	61.1					
WHI-P180	DTQ	TTBK1	4BTK	36.0	-34.4	42.5	**0.5**		
		RET	5AMN						
		CDPK1	3NYV						
a	MSQ	P38-α	1DI9	57.4					
b	PFE	FBP (E20Q, S96T, D199N)	1KZ8	32.3	37.0				
c	6U7	KSR2	5KKR	92.3					
d	0N5	GlmU	4E1K	-50.7					

[a] 4-[3-Methylsulfanylanilino]-6,7-Dimethoxyquinazoline
[b] [4-[3-[(6,7-diethoxyquinazolin-4-yl)amino]phenyl]-1,3-thiazol-2-yl]methanol
[c] 6,7-dimethoxy-N-(2-methyl-4-phenoxy-phenyl)quinazolin-4-amine
[d] N-[4-[(6-methoxy-7-oxidanyl-quinazolin-4-yl)amino]phenyl]benzamide

Table S2. Occupancy and temperature (B-factor) values for non-hydrogen atoms of PDB-ID: MSQ obtained from its X-ray cocrystal (PDB: 1DI9). Occupancy value ranges from 0–1 and indicates the amount of each conformation observed in the crystal. Given a value of 1 means that the atom is found in all of the molecules in the same place in the crystal, while lower values denotes uncertainty for atom position. B-factor is indicative for atomic motion and smearing of electron density. Values under 10 indicates sharp positioning of the atom in all molecules in the crystal while values greater than 50 indicates the dynamic movement of the atoms.

Atom type	Occupancy	B-factor
N	1	23.98
C	1	26.59
N	1	27.52
C	1	28.34
C	1	27.62
C	1	25.72
C	1	29.70
C	1	30.67
C	1	30.34
C	1	29.33
N	1	25.53
C	1	24.30
C	1	24.91
C	1	25.78
C	1	25.23
C	1	25.74
C	1	24.98
S	1	30.22
C	1	27.37
O	1	32.32
C	1	31.38
O	1	31.89
C	1	30.60
Average		28
r.m.s. (Å)		0.60

Reference

1. Berman, H. M.; Westbrook, J.; Feng, Z.; Gilliland, G.; Bhat, T. N.; Weissig, H.; Shindyalov, I. N.; Bourne, P. E., The Protein Data Bank. *Nucleic Acids Res.* **2000,** *28* (1), 235-242.